Spontaneous down-conversion of microwave photons from a superconducting quantum impurity

Dorian Fraudet

Thèse pour obtenir le grade de

Docteur de l'Université Grenoble Alpes

Ecole doctorale : PHYS - Physique
Spécialité : Physique de la Matière Condensée et du Rayonnement
Unité de recherche : Institut Néel

Conversion spontanée de photons micro-ondes à partir d'une impureté quantique supraconductrice

Spontaneous down-conversion of microwave photons from a superconducting quantum impurity

Présentée par :
Dorian Fraudet

Direction de thèse :

Serge Florens Directeur de recherche, Université Grenoble Alpes	Directeur de thèse
Nicolas Roch Chargé de recherche, Université Grenoble Alpes	Co-directeur de thèse

Rapporteurs :

Takis Kontos
Directeur de recherche, Laboratoire de Physique de l'Ecole Normale Supérieure

Elisabetta Paladino
Associate professor, CNR, University of Catania

Thèse soutenue publiquement le **15 décembre 2023**, devant le jury composé de :

Serge Florens Directeur de recherche, Université Grenoble Alpes	Directeur de thèse
Takis Kontos Directeur de recherche, Laboratoire de Physique de l'Ecole Normale Supérieure	Rapporteur
Elisabetta Paladino Associate professor, CNR, University of Catania	Rapporteur
Benoît Boulanger Professeur des Universités, Université Grenoble Alpes	Président du jury
Nicolas Roch Chargé de recherche HDR, Institut Néel	Co-directeur de thèse
Fabian Hassler Professeur, JARA Institute for Quantum Information	Examinateur
Pol Forn-Díaz Assistant professor, Institut de Física d'Altes Energies	Examinateur

Aknowledgements

Je tiens tout d'abord à exprimer ma profonde gratitude envers les membres du jury pour avoir consacré une partie de leur précieux temps à évaluer mon travail de thèse et assister à ma soutenance. Je souhaite particulièrement remercier Elisabetta Paladino et Takis Kontos d'avoir accepté le rôle de rapporteurs et d'avoir pris le temps d'examiner attentivement mon manuscrit. Je remercie également Benoît Boulanger, Fabian Hassler et Pol Forn-Díaz d'avoir accepté d'être examinateurs et pour leur enthousiasme lors de ma soutenance. Recevoir des commentaires aussi positifs de chercheurs de ce calibre est extrêmement gratifiant et renforce indéniablement ma confiance en moi.

Les quatre années passées à l'Institut Néel ont été jalonnées de bien des épreuves, à la fois professionnelles et personnelles. C'est avec beaucoup de satisfaction que j'achève cette aventure en présentant des résultats que moi-même je n'attendais plus. En tant que physicien expérimentateur, mettre en évidence un effet physique jamais mesuré auparavant est particulièrement exaltant, et je suis conscient de la chance que j'ai eue de vivre cette expérience. Le chemin parcouru jusqu'ici a été parsemé de frustrations et de déceptions, et je n'aurais pas pu mener à bien ce projet sans le soutien que j'ai reçu au cours de ces trois années. Je tiens tout d'abord à souligner l'importance de l'environnement de travail exceptionnel de l'Institut Néel. Les femmes et les hommes remarquables qui y travaillent contribuent à faire de ce laboratoire un lieu de recherche d'une qualité exceptionnelle. Je pense notamment au pôle NanoFabrication, au cœur de l'activité de l'Institut, ainsi qu'aux pôles cryogénie, ingénierie expérimentale et électronique. Je remercie en particulier Sébastien Triqueneaux pour son aide précieuse lors du remplacement du compresseur du BlueFors, qui a permis de relancer l'expérience après plusieurs mois d'interruption au début de ma thèse. Un clin d'œil à Jean-Baptiste Cully pour l'installation du nouveau système de filtration d'eau, qui permettra au BlueFors d'avoir encore de beaux jours devant lui. Bien évidemment, je remercie également Éric Eyraud, le magicien de la cryogénie, pour son assistance précieuse lors des diverses tâches de maintenance du frigo. Merci à Julien Jarreau et Laurent Del-Rey pour leur aide lors de la fabrication de pièces mécaniques en tout genre. Un grand merci à Julien Minet pour le travail incroyable sur la RFSoC et l'aide apportée pour la compréhension et la prise en main de cet instrument.

J'espère que ce manuscrit reflète fidèlement l'importance des TWPAs, ces amplificateurs à très faible bruit conçus et fabriqués par mes collègues de l'équipe SQC, sans lesquels ce projet n'aurait tout simplement pas été possible. For this, I'd like to express my deepest gratitude to Arpit for designing and making the TWPA I used to get these results (and the many others I've tested...). People should know that your mere presence in an experimental room can make a stubborn TWPA finally work. Thanks to Martina for teaching me the rudiments of using a TWPA and for your warm welcome when I arrived in the lab. Merci à Gwen pour nos discussions passionnantes sur les éventuels effets secondaires du TWPA sur l'expérience. Ces échanges m'ont permis de mieux comprendre comment tirer le meilleur parti de ce dernier. Ton intérêt pour mon travail dès ton

arrivée au laboratoire a été extrêmement rafraîchissant et m'a définitivement redonné un élan de motivation. Les TWPAs rendent accessible tout un nouveau pan de recherche en optique quantique micro-ondes, et les résultats rapportés dans ce manuscrit constituent une démonstration pratique de la puissance de ces dispositifs.

Il est essentiel de souligner que le travail présenté dans ce manuscrit est le fruit d'une collaboration étroite avec quelques théoriciens. Ainsi, les nombreuses discussions scientifiques avec Denis Basko, Serge Florens, Izak Snyman, Théo Sépulcre et Nante Raveloarijaona ont été essentielles à l'avancement du projet. Merci pour votre pédagogie et votre patience lorsque vous avez dû répondre à mes questions naïves d'expérimentateur. Merci à toi Denis d'avoir pris le temps de m'expliquer les points de tes calculs qui m'échappaient. Thank you Izak for your dedication to the project and your impressive pedagogical skills. Parmi toutes les conversations scientifiques que j'ai eues au cours de ma thèse, il en est une qui se distingue nettement par son impact décisif. Je tiens donc à remercier chaleureusement Romain Albert pour avoir partagé son expérience avec moi lors d'une discussion improvisée près de l'expérience. Tu m'as permis de comprendre le détail qui me manquait pour transformer l'essai.

Je tiens à remercier chaleureusement Sébastien Léger. Mon travail de thèse fait directement suite au tien, alors autant dire que je te dois beaucoup pour m'avoir confié cette expérience exceptionnelle. Merci aussi d'avoir eu la patience de répondre à mes questions à mes débuts alors que tu étais en pleine rédaction de ton manuscrit. En plus d'être une personnalité remarquable, tes qualités en tant que scientifique sont impressionnantes, et, en ce sens, je n'ai eu d'autre choix que de déroger à l'adage qui prédit que l'élève doit dépasser le maître.

Un grand merci à tous les membres de l'équipe SQC avec qui j'ai partagé d'excellents moments, tant au laboratoire qu'en dehors. Côtoyer autant de personnes brillantes au quotidien est une expérience qui force à l'humilité. Merci Seb, Luca et Sam (et parfois Jovian et Giulio) pour nos courses aux Vouillants, au Jalla et au Rachais. J'espère pouvoir remettre ça bientôt ! Merci Tibo pour les nombreuses bouffes et les sessions guitare. Mention spéciale à Alexandre, ton passage au laboratoire restera un super souvenir, et grimper avec toi était toujours un immense plaisir. J'espère avoir l'occasion de te faire découvrir le massif des Écrins à nouveau ! Merci à Sam, Nicoló, Giulio, Cyril, Guilli am et Raphaël pour nos chouettes sessions d'escalade. Un clin d'œil à Philéas, tu m'as vraiment impressionné lors de ton stage. Thank you to Khartik for teaching me how to use the BlueFors and for your very good vibes! Jovian, your remarkable personality definitely helped me enjoy my time in the lab. Together with Seb and Luca, you formed an unforgettable trio! Merci également aux membres permanents de l'équipe, Wiebke, Cécile, Olivier, Nico et Quentin. Vous gérez tout cela avec brio. Wiebke, merci de m'avoir permis d'utiliser le BlueFors tout au long de ma thèse. Le temps de mesure sans contrainte dont j'ai bénéficié a été extrêmement précieux. Merci Olivier pour ta bienveillance et tes bons conseils. Je pense que tous les membres de l'équipe conviendront que tu es indispensable à l'équilibre du groupe.

Bien sûr, je tiens particulièrement à remercier mes directeurs de thèse, Serge et Nico. Je sais à quel point la réussite de ce projet était importante pour vous, et je vous remercie de m'avoir fait confiance et de m'avoir donné les moyens de le mener à bien.

J'ai énormément appris à vos côtés.

Enfin, je voudrais exprimer ma gratitude envers mes proches, dont le soutien a été indispensable à la réussite de ma thèse. Merci à mes parents pour m'avoir permis d'étudier la physique et pour leur soutien indéfectible. Merci à mon frère pour être une source d'inspiration constante. Merci à mes amis pour m'avoir aidé à décompresser et pour avoir écouté mes doutes et mes questionnements avec bienveillance. Et surtout, un grand merci à toi, Estelle, pour avoir toujours été présente pour moi au quotidien. Sans toi, je n'aurais jamais pu aller au bout de cette aventure. Merci pour tout ce que tu m'as fait découvrir pendant ces années et pour ta patience à mon égard. Ta rencontre a simplement changé ma vie.

Abstract

Français Les modèles d'impuretés quantiques sont d'une importance capitale en physique de la matière condensée car ils permettent de décrire les propriétés émergentes d'une grande collection de particules interagissant avec un système quantique unique. Les progrès récents en matière de techniques expérimentales ont largement été mis à profit afin d'implémenter ces modèles en laboratoire. Tout particulièrement, les avancées dans le domaine de l'électrodynamique quantique des circuits (circuit-QED) ont permis d'atteindre expérimentalement le régime d'impureté quantique, où un défaut unique, comme un qubit ou une jonction tunnel supraconductrice, est très fortement couplé à de nombreux modes d'un environnement électromagnétique. Dans ces systèmes, en raison de la forte non-linéarité de l'impureté, des interactions effectives commencent à se développer entre les modes initialement indépendants de l'environnement, parmis lesquels des processus qui ne conservent pas le nombre d'excitations – des photons micro-ondes dans ce contexte. La diffusion inélastique de ces derniers sur l'impureté est l'archétype de ces processus qui ne conservent pas le nombre d'excitations et a récemment été indirectement observée grâce à la spectroscopie micro-ondes de circuits supraconducteurs. Dans cette thèse, nous allons au-delà de la spectroscopie et rapportons l'observation directe des photons qui sont produits au cours de ces processus de diffusion inélastique. Plus précisément, en tirant parti de l'état de l'art en terme d'amplification proche de la limite quantique, le signal de fluorescence associé à la conversion spontanée des photons micro-ondes est directement mesuré. De plus, nous montrons que cette conversion des photons micro-ondes est directement liée à la dissipation du système, confirmant ainsi le scénario envisagé dans les études spectroscopiques précédant ce travail. Ce processus de conversion de photons nous permet également d'explorer les effets des quasiparticules – que sont les paires de Cooper brisées – sur les états excités du système. Nous rapportons l'observation d'effets de charge commensurables sur un état à trois photons, lequel est spectroscopiquement résolu grâce à son couplage à un état à un seul photon. Au-delà des motivations découlants de l'étude des modèles d'impuretés quantiques, ces résultats contribuent au domaine en plein essor de l'optique quantique à N-corps et offrent une signature directe du couplage ultra-fort entre la lumière et la matière. Ils présentent également un intérêt particulier pour la compréhension des propriétés de cohérence des qubits à haute impédance, tels que le Fluxonium ou le qubit 0-π, qui reposent sur des structures multi-modes.

English Quantum impurity models are of paramount importance in condensed matter physics, as they make it possible to describe the emergent properties of a large collection of particles interacting with a single quantum system. Recent progress in experimental techniques have been leveraged to emulate such models in the lab. In particular, recent advances in the field of circuit-quantum electrodynamics (circuit-QED) have made it possible to experimentally reach the quantum impurity regime where a single defect, like a qubit or a weak link, is ultra-strongly coupled to many modes of an electromagnetic environment. In such systems, owing to the strong non-linearity of the impurity, effective

interactions start to develop between the initially independent modes of the environment, including processes that do not conserve the number of excitations – microwave photons in that context. The inelastic scattering of these latter off the impurity is archetypical of such non-conserving processes and has been indirectly observed through the microwave spectroscopy of superconducting circuits in very recent experiments. In this thesis, we go beyond spectroscopy and report the direct experimental observation of the photons that are produced during these inelastic scattering processes. More specifically, taking advantage of state-of-the-art amplification near the quantum limit, the fluorescence signal associated to the spontaneous down-conversion of microwave photons was directly measured. Additionally, we show that this down-conversion of microwave photons is directly linked to the dissipation of the system, hence confirming the scenario envisioned in spectroscopic studies preceeding this work. This photon-conversion process also allows us to explore the effects of quasiparticles (also known as broken Cooper pairs) on the excited states of the system. We report the observation of commensurable charging effects on a three-photon state that we can spectroscopically resolve through its coupling to a single-photon state. Beyond the motivations inherited from the study of quantum impurity models, these results contribute to the booming field of many-body quantum optics and offer a direct signature of the ultra-strong light-matter coupling. They are also of particular interest in the understanding of the coherence properties of high-impedance qubits, such as the Fluxonium or the $0 - \pi$ qubit, that rely on multi-mode structures.

Contents

List of Figures

Tout chercheur sérieux éprouve un jour cette évidence douloureuse de la limitation. Malgré lui, il voit le cercle de son savoir se rétrécir de plus en plus. Il perd alors le sens des grandes architectures et se transforme en ouvrier aveugle dans un immense ensemble.

— *Albert Einstein*

1 Introduction and summary

Contents

1.1. Introduction

1.1.1. Radiative shifts in quantum electrodynamics

Quantum electrodynamics (QED) is one of the areas of research in modern physics that has made the greatest contributions to our understanding of the quantum world, by bringing theory face to face with many experimental situations. This quantum theory has its origins in the field of atomic physics and its development has allowed a better understanding of the structure of matter. An example of great historical importance is the understanding of the spectral series of the hydrogen atom (the fine structure of which was first measured by A. Michelson and E. Morley in 1887, long before it could actually be explained by theory [Michelson and Morley 1887]) where the Dirac equation correctly predicts the fine structure of the electron energy levels, going beyond the Bohr model of the atom and taking into account relativistic effects as well as the electron spin. Further theoretical refinement, taking into account the interactions between the proton spin and the internal electromagnetic field of the atom, reveals the hyperfine structure of hydrogen with, for example, the HI line (transition between the two non-degenerate spin states of the hydrogen ground state, $1S_{1/2}$), which is now extensively used

in astronomy. Although Dirac's theory gives a remarkably satisfactory estimate of the energy levels of hydrogen-like atoms, it fails to describe quantitatively the exact spectrum of the atom. While Dirac's theory predicts that the $2S_{1/2}$ and $2P_{1/2}$ orbitals are energy degenerate, experimental evidence showed the opposite, with an actual energy difference of $4.372 \times 10^{-6}\,\text{eV}$, the celebrated Lamb shift [Lamb and Retherford 1947; Lamb and Retherford 1951][1]. Although seemingly insignificant compared to the 10.2 eV transition from the $n = 2$ shell to the ground state of the atom, this degeneracy lift provided the motivation to further develop our understanding of the quantum processes at work in atoms and opened the door to the development of quantum electrodynamics, the study of the interactions between matter and the quantised electromagnetic field. The various corrections to the hydrogen energy levels discussed above are summarised in Figure 1.1.

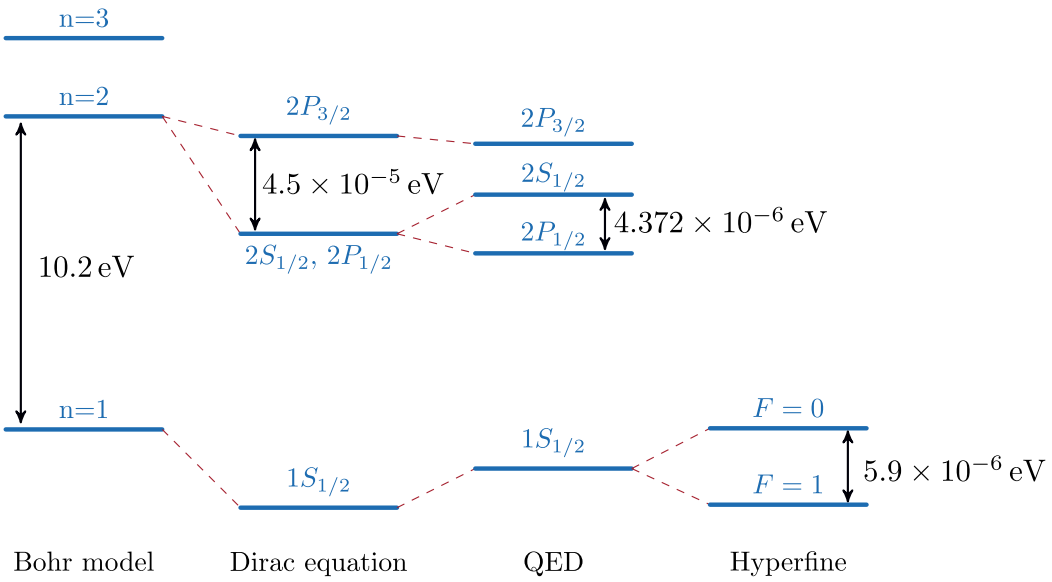

Figure 1.1.: Schematics of the first few levels of hydrogen as given by different theories. The energy transitions are not to scale. The energy levels are labelled by nL_J, where n is the principal quantum number, L is the orbital quantum number and J is the total angular momentum quantum number. In the Bohr model, the energy of the atom depends only on the principal quantum number. In the case of the hyperfine structure, the nuclear spin of the atom has to be considered in such a way that the total angular momentum, F, comes into play.

[1] Note that the fine and hyperfine structure effects also lead to very small yet measurable corrections to the Bohr model. For example, the fine structure corresponds to an energy difference of 4.5×10^{-5} eV between the $2P_{3/2}$ and $2P_{1/2}$ orbitals, and the hyperfine structure leads to a 5.9×10^{-6} eV difference between the two spin states of the $1S_{1/2}$ ground state of the atom.

In QED, the electromagnetic radiation is quantised and consists of discrete packets of energy corresponding to light particles called photons (the carriers of the electromagnetic force). Roughly speaking, the electromagnetic field is described as an ensemble of independent quantum harmonic oscillators, and the presence of a photon of energy $\hbar\omega$ corresponds to the associated oscillator being in its first excited state. The Hamiltonian of the quantised EM field is [Miloni 1994]

$$\hat{H}_{\mathrm{EM}} = \int \mathrm{d}^3k \sum_{\sigma} \hbar\omega_{\mathbf{k}} \left(\hat{a}^{\dagger}_{\mathbf{k},\sigma} \hat{a}_{\mathbf{k},\sigma} + \frac{1}{2} \right) , \tag{1.1}$$

with σ the polarisation of the photon, $\mathbf{k}$ its wave vector, $\hbar\omega_{\mathbf{k}} = \hbar c|\mathbf{k}|$ its energy and $\hat{a}_{\mathbf{k},\sigma}$ the annihilation operator, such that $\left[\hat{a}_{\mathbf{k},\sigma}, \hat{a}^{\dagger}_{\mathbf{k}',\sigma'}\right] = \delta_{\mathbf{k},\mathbf{k}'}\delta_{\sigma,\sigma'}$. In its ground state the electromagnetic field has a finite energy associated with non-zero fluctuations in the electric and magnetic fields (even though no photons can be observed). This vacuum field interacts with the unique hydrogen electron leading to the radiative shift associated with the atom absorbing and re-emitting (or vice versa) random virtual photons on a time scale given by the Heisenberg uncertainty principle [Maclay 2020]. This can be seen as follows. The electron of the hydrogen atom interacting with the vacuum field can be modelled by the following Hamiltonian,

$$\hat{H} = \frac{(\mathbf{p} - e\mathbf{A})^2}{2m} + \hat{V}(\mathbf{r}) + \hat{H}_{\mathrm{EM}} \, , \tag{1.2}$$

where the first term on the right-hand side is the energy of an electron with kinetic momentum $\mathbf{p}$ in an electromagnetic field, $\hat{V}(\mathbf{r})$ is the nucleus Coulomb potential felt by the electron, and $\hat{H}_{\mathrm{EM}}$ is the bare electromagnetic field energy as given by equation (1.1). The minimal coupling canonical momentum $(\mathbf{p} - e\mathbf{A})$ is responsible for the interaction of the electron with the vacuum field through the interaction term $\hat{H}_{\mathrm{int}} = -e/m \times \mathbf{p} \cdot \mathbf{A}$. Since the potential vector associated with the quantised vacuum field is given by[2]

$$\hat{\mathbf{A}}(\mathbf{r}, t) = \int \mathrm{d}^3k \sum_{\sigma} \sqrt{\frac{\hbar}{16\pi^3 \epsilon_0 \omega_{\mathbf{k}}}} \left(\hat{a}_{\mathbf{k},\sigma} e^{i(\mathbf{kr} - i\omega_k t)} + \mathrm{h.c.} \right) \mathbf{e}_{\sigma} \, , \tag{1.3}$$

it can be seen that $\hat{H}_{\mathrm{int}}$ couples the state consisting of the atom being in its ith excited state and the EM field in its vacuum, $|i, 0\rangle$, to states of the form $|j, n_{\mathbf{k},\sigma} = 1\rangle$, where the atom is now in its jth excited state and the EM field is populated with one photon. Thus, the energy level of the $|i, 0\rangle$ state is shifted, as given by second-order perturbation theory, by the presence of any process involving the successive emission and absorption of a virtual photon of energy $\hbar\omega_{\mathbf{k}} = |E_i - E_j|$, where $E_{i(j)}$ is the energy of the ith (jth) state of the atom. The energy shift is given by

$$\Delta E_i = \sum_{j,\mathbf{k},\sigma} \frac{|\langle j, n_{\mathbf{k},\sigma} = 1 | \hat{H}_{\mathrm{int}} | i, 0 \rangle|^2}{E_i - E_j - \hbar\omega_{\mathbf{k}}} \, . \tag{1.4}$$

[2] h.c. stands for hermitian conjugate of the first term in the parenthesis.

Although relatively simple in appearance, a naive calculation of equation (1.4) leads to a divergent energy shift. This daunting problem led physicists to develop the renormalisation techniques [Bethe 1947] that are essential to quantum electrodynamics and are now extensively used to solve a wide range of physical situations. Other mechanisms are responsible for the Lamb shift of the hydrogen atom, but the interaction of the electron with the vacuum field accounts for most of this radiative shift and is a striking example of the interaction between the vacuum field and matter involving the exchange of a single quantum of light. This remains a very small effect, and much larger effects can be observed by increasing the coupling between the atom and the vacuum field, which is the aim of quantum optics and specifically cavity quantum electrodynamics.

1.1.2. Observing the quantum light in action

The archetypical and conceptually most simple cavity QED system consists of the coupling of a single atom to only one mode of the electromagnetic field confined in a high quality factor resonant cavity. It is formally described by the quantum Rabi Hamiltonian

$$\hat{H}_{\text{rabi}}/\hbar = \omega_a \hat{a}^\dagger \hat{a} + \frac{\omega_{\text{eg}}}{2}\hat{\sigma}_z + g\left(\hat{a}^\dagger + \hat{a}\right)\left(\hat{\sigma}_- + \hat{\sigma}_+\right), \tag{1.5}$$

where ω_a is the resonance frequency of the confined field mode, $\hbar\omega_{\text{eg}}$ is the transition energy between the ground state $|g\rangle$ and the first excited state $|e\rangle$ of the atom, and g is the coupling strength between the resonant mode and the atom. In this model, the atom is described as a two-level system while the EM field mode is modelled by a harmonic oscillator with a creation (annihilation) operator $\hat{a}^\dagger$ ($\hat{a}$) verifying the bosonic commutation relation $[\hat{a}, \hat{a}^\dagger] = 1$. The interaction term (the last term on the right-hand side of equation (1.5)) involves the exchange of a single atomic excitation, embodied by the transition operators $\hat{\sigma}_- = |g\rangle\langle e|$ and $\hat{\sigma}_+ = |e\rangle\langle g|$. The Pauli matrix $\hat{\sigma}_z$ is defined as $\hat{\sigma}_z = |e\rangle\langle e| - |g\rangle\langle g|$. In a realistic setting, both the cavity and the atom are prone to dissipation and decoherence, *i.e.* they can dissipate energy or lose phase coherence by interacting with the surrounding environment. Understanding this interaction between a quantum system and its environment, often reffered to as the study of open quantum systems, is at the heart of the work presented here and is a very fundamental question, as it is elusive to describe real physical phenomena based solely on the modelling of isolated quantum systems.

This dissipation is formally characterised by the decay rates κ for the cavity and γ for the atom[3]. The coupling strength g actually dictates the physics of the system, and the light-matter system behaves drastically differently depending on the magnitude of g with respect to the atomic transition frequency, ω_{eg}, or the resonance frequency of the cavity mode, ω_a. Whenever the coupling strength overcomes the dissipation rates but is still small compared to ω_a and ω_{eg}, the system is in what is called the ***strong***

[3]For the time being we only consider dissipation, the process by which a quantum system relax its energy in the surrounding environment. Interaction with the environment can also impinge on the system dynamics by supressing the phase coherence of the latter, a process known as dephasing and addressed further in this manuscript.

coupling regime. In this situation, the system undergoes a coherent exchange of a single quantum of energy between the atom and the EM field, the famous vacuum Rabi oscillations, first observed with Rydberg atoms [Brune et al. 1996] and latter reproduced in various experimental platforms [Johansson et al. 2006; Vasa et al. 2013; Zhang et al. 2016]. This ability to coherently control the light-matter interaction led to remarkable experimental tests of the quantum theory [Raimond et al. 2001]. The physics of the strong coupling regime is well captured by the Jaynes-Cummings Hamiltonian, which is obtained from equation (1.5) by retaining only the terms that conserve the total number of excitations $\hat{N} = \hat{a}^\dagger\hat{a} + \hat{\sigma}_+\hat{\sigma}_-$,

$$\hat{H}_{\mathrm{jc}}/\hbar = \omega_a\hat{a}^\dagger\hat{a} + \frac{\omega_{\mathrm{eg}}}{2}\hat{\sigma}_z + g\left(\hat{a}^\dagger\hat{\sigma}_- + \hat{a}\hat{\sigma}_+\right), \tag{1.6}$$

an approximation commonly referred to as the rotating wave approximation (RWA) because it artificially removes rapidly oscillating (also called counter-rotating) terms, $\hat{a}^\dagger\hat{\sigma}_+ + \hat{a}\hat{\sigma}_-$, from the system dynamics. If one pushes the coupling strength further to the point where it becomes a significant fraction of the bare energies, $g > 0.1 \times (\omega_a, \omega_{\mathrm{eg}})$, the system enters the ***ultrastrong coupling regime***. In this regime, the counter-rotating terms can no longer be neglected and one has to stick to the quantum Rabi model of equation (1.5), which does not conserve the number of excitations, $[\hat{H}_{\mathrm{rabi}}, \hat{N}] \neq 0$. These "non-conserving" processes affect the dynamics of the system by allowing effective interactions between states with different number of excitations via the exchange of virtual photons [Frisk Kockum et al. 2019; Forn-Díaz and Lamata 2019]. For example, considering the counter-rotating terms in equation (1.5) and assuming the resonance condition $\omega_{\mathrm{eg}} = 3\omega_a$ for the bare transitions, it is possible to observe an effective coupling between the $|0, e\rangle$ and $|3, g\rangle$ states[4] that do not have the same number of excitations, a process known as ***multiphoton Rabi oscillations*** [Garziano et al. 2015]. Such process is represented in Figure 1.2. To observe such multiphoton oscillations, one requires the

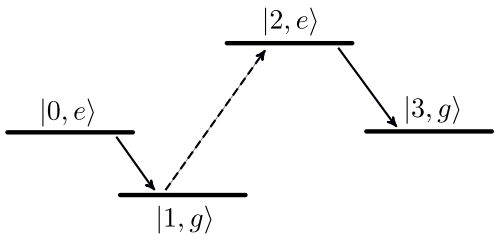

Figure 1.2.: Effective coupling between the $|0, e\rangle$ and $|3, g\rangle$ states of the quantum Rabi model. Plain arrows indicate RWA processes while the dashed arrow indicates a counter-rotating term : $\hat{a}^\dagger\hat{\sigma}_+$. Adapted from [Kockum et al. 2017].

[4] $|n, i\rangle = |n\rangle \otimes |i\rangle$ with $n \geq 0$ the number of photons in the resonant mode and $i \in \{e, g\}$ the state of the two level system.

effective photon-photon coupling strength, $g_{\gamma\gamma}$, to dominate over the dissipation rates, $g_{\gamma\gamma} \gg \{\kappa, \gamma\}$. In the ultrastrong coupling regime, the quantum Rabi model is also known to exhibit a complex light-matter ground state with a finite number of excitations (in contrast to the intuitive $|0, g\rangle$ ground state in the strong coupling regime, which contains no excitations), the detection of which remains an experimental challenge despite theoretical proposals [Andersen and Blais 2017; Ridolfo et al. 2021]. Reaching the ultrastrong coupling is not an easy task, and it has only recently been achieved with the first observation in intersubband polaritons by exploiting the increase in the interaction strength allowed by the collective coupling of a large number of dipoles to the same EM mode [Anappara et al. 2009]. On the other hand, the use of superconducting circuits allows to reach the ultrastrong coupling regime for a *single* artificial atom [Niemczyk et al. 2010; Forn-Dıaz et al. 2010] and is nowadays a favourable platform for the study of cavity QED in this extreme parameter regime.

1.1.3. Dissipation from the coupling to a harmonic bath

In the original QED problem, a single atom is coupled to a continuum of electromagnetic modes, while the quantum Rabi model limits the interaction to a single mode of the cavity field. By extending the quantum Rabi model to multiple modes of the field, a variety of physical problems can be implemented, including the spin-boson model, a canonical model for the dissipation of a two-level system,

$$\hat{H}_{\mathrm{sb}}/\hbar = \frac{\Delta}{2}\hat{\sigma}_x + \sum_k \omega_k \hat{a}_k^\dagger \hat{a}_k + \sum_k g_k \left(\hat{a}_k^\dagger + \hat{a}_k\right)\hat{\sigma}_z \,, \tag{1.7}$$

where the two-level system is now modelled by the two energy degenerate spin states $|\uparrow\rangle$ and $|\downarrow\rangle$ (eigenstates of $\hat{\sigma}_z$). Considering non-degenerate spin states would require the inclusion of an additional term in the Hamiltonian (1.7), namely $\epsilon\hat{\sigma}_z/2$, where ϵ is the energy difference between the two states. Nevertheless, the case $\epsilon = 0$ is the most interesting, since in this case the eigenstates of the isolated two-level system ($g_k = 0$) are maximally delocalised between the two spin states, $\left|\psi_{\mathrm{g(e)}}\right\rangle = (|\uparrow\rangle \mp |\downarrow\rangle)/\sqrt{2}$. The system under study does not necessarily have to be a "real" two-level system (such as an electron spin), but can be described by a general coordinate x subject to a double-well potential, as schematically shown in Figure 1.3. Assuming that $\hbar\omega_0 \gg k_B T$, where ω_0 is the frequency of classical oscillations in each well, and that the tunneling rate is much smaller than the barrier height, the dynamics of the system can be restricted to the two ground states of each individual well [Leggett et al. 1987], labelled $|\uparrow\rangle$ and $|\downarrow\rangle$.

In the usual spin-boson paradigm, the number of EM field modes is considered to be infinite. This is a consequence of the fact that the spin-boson model is a special case of the Caldeira-Legget model for the dissipation of a single-degree-of-freedom quantum system. Indeed, from the Caldeira-Legget theory, a dissipative environment can be modelled by an infinite set of harmonic oscillators weakly coupled to the system of interest [Caldeira and Leggett 1983; Weiss 2012]. The spin-boson model exhibits a localised-delocalised phase transition for the atomic degree of freedom, and as such is a favourable paradigm

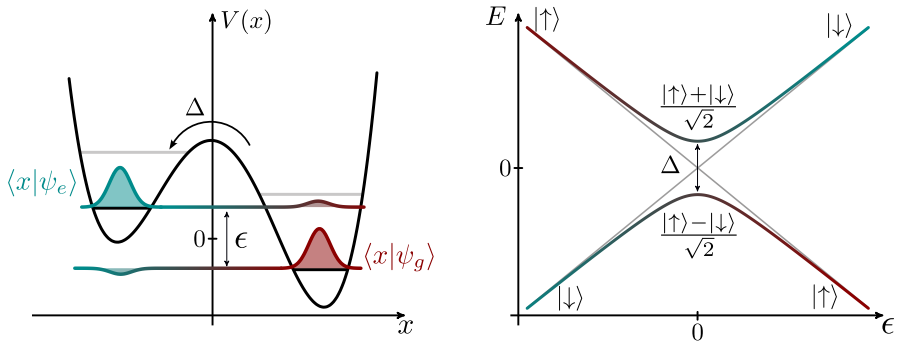

Figure 1.3.: Modelling of a two-level system. **Left.** Schematic of an asymmetric double-well potential $V(x)$. The system is described by its continuous general coordinate x and $V(x)$ admits two distinct minima. The ground states of each individual well, labelled $|\uparrow\rangle$ and $|\downarrow\rangle$, are detuned by a quantity ϵ, commonly called the bias, and the dynamics of the system is restricted to these two states. These two states can hybridise via quantum tunneling between the two wells at a rate Δ. The wavefunctions of the two-level system are shown in the case of large detuning compared to the tunneling rate. **Right.** Spectrum of the two-level system as a function of detuning ϵ for $\Delta \neq 0$ (coloured lines) and for $\Delta = 0$ (grey lines). The annotations indicate the eigenstates of the system in the limiting cases $\epsilon \gg \Delta$ and $\epsilon = 0$.

to study the problem of the quantum-to-classical transition [Schlosshauer 2007]. We can get an intuitive picture of this phase transition by looking at limiting cases. For $g_k = 0$, the two-level system is completely decoupled from the environment and the ground state of the spin-boson system is simply $|\mathrm{GS}\rangle = (|\uparrow\rangle - |\downarrow\rangle) \otimes |0\rangle / \sqrt{2}$ (where $|0\rangle$ corresponds to all harmonic oscillators being in their ground states of no excitations), *i.e* the atomic degree of freedom is maximally delocalised between its two states. On the other hand, if $\Delta = 0$, the coherent tunneling process between the two spin states is suppressed and the two-level system is localised either in the $|\uparrow\rangle$ state or in the $|\downarrow\rangle$ state. For a finite coupling g_k of the system to the environment, the latter still reads the spin state of the system, so that the ground state of the spin-boson system is now two fold degenerate. The corresponding degenerate ground states are $|\uparrow\rangle \otimes |f\rangle$ and $|\downarrow\rangle \otimes |-f\rangle$, where $|\pm f\rangle$ is the displaced vacuum of the environment (which depends on the atomic state) [Silbey and Harris 1984],

$$|\pm f\rangle = \exp\left[\pm \sum f_k (\hat{a}_k^\dagger - \hat{a}_k)\right] |0\rangle \ , \tag{1.8}$$

where $f_k = g_k / 2\omega_k$. For intermediate scenarios where $g_k \neq 0$ and $\Delta \neq 0$, there is a competition between delocalisation by quantum tunneling and localisation by the interaction

with the environment [Bera et al. 2014].

So far we have only considered the limiting case of a two-level system coupled to a bosonic environment, but the spin-boson model can be generalised to a multilevel atom [Kaur et al. 2021], which is of great interest since most experimental implementations are inded based on multilevel structures. The prediction for this quantum-to-classical phase transition has motivated experimental efforts towards the physical realisation of a multimode ultrastrong coupling system. The strong coupling of a single nonlinear boundary consisting of a multilevel atom (often called the impurity in this context) to many harmonic modes is nowadays within reach of superconducting circuits, allowing for the analogue simulation of quantum impurity models such as the spin-boson model. Within this experimental platform (called circuit-QED) the environment is implemented with high impedance multimode resonators or semi-infinite transmission lines. The environmental excitations are then nothing but microwave photons. In order to observe non-trivial many-body effects in such systems, the nonlinearity of the boundary and its coupling to the environment must be sufficiently large to achieve the simultaneous coupling of the impurity to many harmonic modes. This condition, defined as the ***superstrong coupling*** regime, is reached when the spectral width γ of the impurity is larger than ω_{fsr}, the free spectral range defined as the frequency difference between two successive harmonic modes of the environment [Meiser and Meystre 2006]. This regime has recently been reported in circuit-QED using very long distributed microwave resonators [Sundaresan et al. 2015] or slow light resonators made of Josephson junction arrays [Puertas Martínez et al. 2019; Kuzmin et al. 2019]. However, this condition alone is not sufficient to observe non-trivial many-body effects, as superstrong coupling can be obtained for a linear impurity – for example a harmonic oscillator coupled to many other harmonic oscillators. Strong nonlinearity is another necessary condition and can be achieved in circuit-QED, for example, by using strongly anharmonic qubits [Blais et al. 2004] or Josephson junctions with a small Josephson energy (E_{J}) to charging energy ratio (E_{C}) (details regarding this physical implementation are given in chapter 2). The first experiments combining these two necessary ingredients reported a non-perturbative renormalisation of the impurity tunneling rate, $\Delta \to \Delta^\star < \Delta$ (*i.e.* a giant Lamb shift) due to the zero point fluctuations of the environment [Forn-Díaz et al. 2017; Léger et al. 2019]. The experimental study of the dissipation of a highly anharmonic Josephson junction ($E_{\mathrm{J}}/E_{\mathrm{C}} \sim 1$) strongly coupled to an environment implemented with a Josephson junction array is essentially what led to the work presented in this manuscript. The latter builds on the work carried out at the Néel Institute in recent years [Puertas Martínez et al. 2019; Léger et al. 2019; Léger et al. 2023]

I.1.4. The environment point of view

Although quantum impurity models allow the study of the dissipation of a single-degree-of-freedom quantum system induced by its coupling to an environment, it can also be instructive to consider the dynamics of the environment itself when the coupling strength, g_k, goes beyond the weak coupling considered in the Caldeira and Legget paradigm. Indeed, due to the strong interaction with the nonlinear boundary, initially independent

modes of the environment begin to effectively interact with each other and develop correlations between them [Bera et al. 2014] such that the coupling of the system to the environment goes beyond the usual Born-Markov approximation. Non-conserving interactions between modes of the environment begin to develop and can play an important role in the impurity dynamics. It has recently been suggested in [Houzet and Glazman 2020] that the signature of a long predicted superconducting-to-insulating phase transition for a Josephson junction – playing the role of the nonlinear boundary, coupled to a dissipative environment [Schmid 1983; Bulgadaev 1984] can be found in the inelastic scattering of microwave photons off the impurity. Recent advances in circuit-QED allow to go beyond the study of the ground state of quantum impurity systems, and many theoretical proposals have predicted non-trivial dynamical or out-of-equilibrium effects in these systems [Goldstein et al. 2013; Peropadre et al. 2013; Sanchez-Burillo et al. 2014; Gheeraert et al. 2018]. More recently, extremely large nonlinear losses in a quantum impurity system consisting of a highly nonlinear Josephson junction coupled to a high impedance waveguide were first observed in [Kuzmin et al. 2021] and shortly after confirmed by [Léger et al. 2023]. These nonlinear losses were attributed to the quantum-impurity-mediated interactions between multiphoton states, leading to the decay of a single photon into several photons of lower energy, effectively creating a new loss channel.

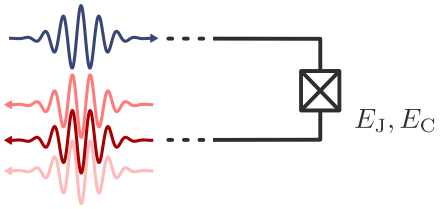

Figure 1.4.: Cartoon illustration of photon decay at the boundary impurity. Although it is only one of many possible conversion processes responsible for the nonlinear dissipation observed in the experiment of Léger and co-authors, this one-to-three conversion channel is actually the process studied in thesis.

The two aforementioned experiments were performed in a regime where the coupling between multiphotons states was large, but still smaller than the natural linewidth of the harmonic modes. This dissipative response of the environment was successfully described in the high-frequency regime ($\hbar\omega_k > \Delta^\star$ in the spin-boson language) by considering frequency conversion processes. The increase in losses for modes in the vicinity of the impurity's transition frequency is an indirect observation of the speculated spontaneous photon decay, and the direct measurement of the power emitted by such multiphoton conversion processes would provide an undeniable evidence that the dissipative response observed in previous experiments is indeed due to the inelastic scattering of microwave photons off the impurity. This direct observation of converted photons is the main objective of this thesis and is reported in chapter 4.

In addition, the observation of the multiphoton strong coupling regime [Mehta et

al. 2022], where the effective photon-photon interaction exceeds the linewidth of the modes has been reported by coupling a fluxonium qubit to a high impedance multimode resonator [Mehta et al. 2023]. The experimental signatures of this regime are avoided crossings between multi-photon states, which can be understood as a many-body version of the vacuum Rabi splitting, suggesting once again the importance of conversion processes in the many-body physics of these quantum impurity systems. They reported a photon-photon interaction strength $g_{\gamma\gamma}/2\pi \lesssim 3\,\mathrm{MHz}$. Although the experiment in reference [Mehta et al. 2023] provides clear evidence for the hybridisation of single photon states with multiphoton states, it does not provide a direct observation of the inelastic produced photons. In addition, Vrajitoarea and coauthors have recently integrated a fluxonium into a photonic crystal [Vrajitoarea et al. 2022], with circuit parameters deep in the quantum impurity regime, allowing for the observation of qualitative effects of non-conserving terms in the spectroscopy of the device as well as the detection of up-converted photons and the reconstruction of their strong correlations revealing the possibility for a driven-dissipative phase transition in such device.

1.1.5. Nonlinear microwave quantum optics

In addition to the above motivations, the direct observation of inelastically scattered microwave photons reported in this thesis is very much part of the field of quantum optics and, more specifically, microwave nonlinear optics in the few-excitation regime. Photon down-conversion, a process in which a photon at a given frequency is converted into several photons at lower frequencies, is at the heart of quantum optics and cavity QED. In quantum optics, shining a laser beam on a $\chi^{(2)}$ nonlinear medium allows the generation of entangled photon pairs by ***spontaneous parametric down-conversion*** (SPDC) where a "pump photon" is converted into two photons (usually called signal and idler photons) [Walls and Milburn 2008]. The same conversion process allows optical parametric amplification, where an additional incoming signal photon stimulates the decay of the pump photon into a signal and idler pair, thus effectively amplifying the signal. SPDC also enables the generation of non-classical states of light such as multiphoton Fock states or squeezed states. Higher order susceptibilities $\chi^{(n>2)}$ allow, in principle, to perform multiphoton SPDC (also known as generalized squeezing [Zelaya et al. 2018]) in which photons multiplets ($n > 2$ photons) are generated instead of a photon pair. However, due to the low nonlinearity of crystals, the efficiency of multiplet generation is very low and the experimental realisation of multiphoton SPDC remains a challenge. In fact, optical three-photon SPDC using a $\chi^{(3)}$ nonlinear crystal has only been observed once [Douady and Boulanger 2004] and relied on additional tricks such as seeding with an additional injection tone. The results of this pioneering experiment and additional informations are given in Figure 1.5.

The dawn of circuit-QED has seen a flourishing amount of experimental observations of nonlinear quantum optical phenomena in the microwave domain, such as the realization of near quantum-limited parametric amplification [Planat 2020], multimode squeezing [Esposito et al. 2022; Eichler et al. 2014], the generation of multiphoton Fock states [Hofheinz et al. 2008], the generation of Schrödinger cat states [Leghtas et al. 2015;

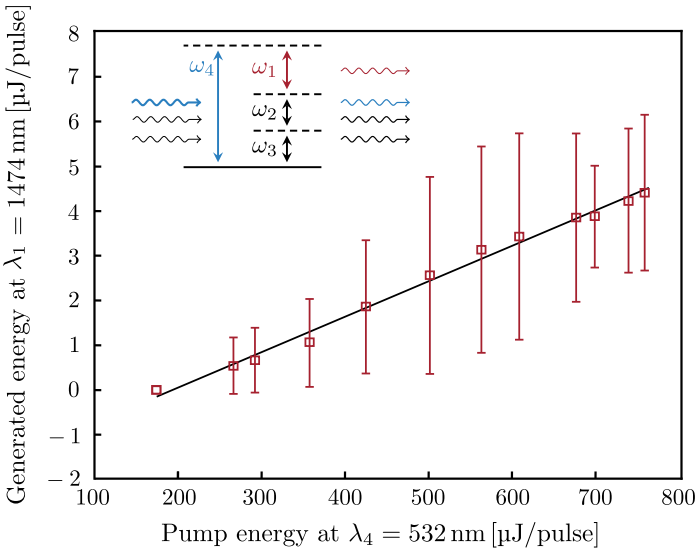

Figure 1.5.: Experimental observation of optical difference frequency generation with a $\chi^{(3)}$ nonlinear crystal. As shown in the energy diagram, a strong pump tone of wavelength $\lambda_4 = 2\pi c/\omega_4 = 532\,\mathrm{nm}$ together with an injection tone of wavelength $\lambda_2 = \lambda_3 = 1665\,\mathrm{nm}$ are sent to a $\chi^{(3)}$ nonlinear crystal, resulting in the generation of a third tone at frequency $\omega_1/2\pi = (\omega_4 - \omega_2 - \omega_3)/2\pi$. The energy of the injection tone is fixed at 100µJ/pulse. Adapted from [Douady and Boulanger 2004]

Grimm et al. 2020], *etc.* Three-photon SPDC has also been studied in the microwave domain and was recently observed in a flux-pumped superconducting parametric cavity [Chang et al. 2020], as well as classical subharmonic oscillations in similar devices [Svensson et al. 2018]. However, SPDC is a parametric process and relies on a strong undepleted pump tone, leading to the effective Hamiltonian under the parametric approximation $\hat{H} = \hbar g_0 \left(\lambda \hat{a}^{\dagger 3} + \lambda^* \hat{a}^3\right)$, where λ is the pump amplitude and $g^{1\leftrightarrow 3}$ is the interaction strength between the pump photons and mode $\hat{a}$ into which the photons are converted. In the present work, we demonstrate the realisation of the ***non-parametric*** counterpart of SPDC, which we call ***three-photon down-conversion fluorescence*** where the strong pump tone is replaced by a weak drive that transfers its energy to the system. The system then relaxes by emitting three-photons by cascaded spontaneous emission (fluorescence) thanks to the three-photon conversion process. The typical Hamiltonian term describing this conversion process is given by

$$\hat{H}^{1\leftrightarrow 3} = \hbar g^{1\leftrightarrow 3} \left(\hat{a}^{\dagger 3}\hat{b} \ + \hat{b}^{\dagger}\hat{a}^3\right) , \tag{1.9}$$

where $\hat{a}$ and $\hat{b}$ are two resonant modes of the system. Hamiltonian (1.9) is the main focus

of the work presented in this manuscript. The experimental realisation of Hamiltonian (1.9) is of great interest for several prospects such as continuous-variable quantum computing [Gottesman et al. 2001] or the generation of Greenberger-Horne-Zellinger states [Mermin 1990]. While in SPDC parametric pumping allows the interaction strength to be increased, $g^{1\leftrightarrow 3} \rightarrow g^{1\leftrightarrow 3}|\lambda|$ [Chang et al. 2020], three-photon down-conversion fluorescence must rely on other techniques to increase the effective multiphoton interaction strength. In this work, we present an experimental implementation of Hamiltonian (1.9) based on a multimode circuit QED setup. By strongly coupling a microwave resonator to an artificial atom, we are able to engineer an interaction strength $g^{1\leftrightarrow 3}$ similar to the natural decay of the resonator modes, thus allowing direct measurement of the photons emitted by this conversion process.

1.2. Organisation of the manuscript

In chapter 2 we present the building blocks used to design a multimode circuit-QED experiment that allows the experimental observation of interactions between modes of a bosonic environment. The latter is coupled to a single Josephson junction implementing a boundary impurity that provides the necessary nonlinearity. The discussion focuses on a specific interaction process, namely a three-photon conversion interaction term of the form of equation (1.9) between two modes of the environment. Two essential points are highlighted for the enhancement of the interaction strength $g^{1\leftrightarrow 3}$. The first point is the need to design a high impedance electromagnetic environment consisting of a Josephson junction array critically coupled (impedance matched) to the impurity junction. The second point describes how the circuit can be designed to limit the number of interacting modes to ideally only two in order to further enhance $g^{1\leftrightarrow 3}$. The rest of the chapter is devoted to the derivation of the spectrum of the emitted down-converted photons. First, a two-mode effective Hamiltonian is derived. From this Hamiltonian, a toy model for the photon conversion efficiency is presented, which gives indications of how to design the coupling of the system to the measurement line in order to maximise the flux of down-converted photons. A quantum model for the fluorescence spectrum is then presented. This model, developed by Denis M. Basko, has been extended based on calculations by Izak Snyman to incorporate the effects of dephasing on the modes. The resulting analytical formula gives some intuition of the underlying physical process and is compared with the experimental results in chapter 4.

Chapter 3 presents the experimental methods used to fabricate and measure the devices under study. The first part of this chapter presents the process used to fabricate the different samples of this manuscript. The second part focuses on the microwave measurement setup. Particular attention is paid to the calibration of the amplification chain, including the near quantum limited amplifier used to detect the very weak signal associated with the emission of the down-converted photons.

Chapter 4 reports the main results of this thesis. Based on the design criteria

outlined in chapter 2, we designed a device that allows the direct observation of down-conversion fluorescence. The experiment is summarised as follows. One mode of the system is populated with about one photon, which is converted into three excitations of another mode at a lower frequency thanks to the interaction term (1.9). The system then relaxes by emitting these three photons in the measurement line. Using state of the art near quantum-limited parametric amplification, we can directly measure the down-converted photons. We also show that the photon emission from the low-frequency mode is the counterpart of the nonlinear losses in the high-frequency mode, confirming the scenario envisioned in reference [Léger et al. 2023]. A detailed analysis of the spectroscopy of the device allows the system to be properly tuned to observe this three-photon down-conversion fluorescence.

Finally, chapter 5 presents the results associated with another device resulting from the weak coupling of the system to the measurement line. As discussed in chapter 2, this leads to a coherent energy exchange between a single-photon state and a three-photon state. These multiphoton Rabi oscillations are reflected in the presence of an avoided crossing in the measured spectrum of the device. This experiment was initially designed to verify the possibility of achieving nonlinear coupling between two modes of the system through three-photon conversion, and the corresponding sample was actually measured before the device presented in chapter 4. A by-product of this experiment is the observation of a doubling of the spectroscopic lines at the avoided crossing. This unexpected feature is associated with the presence of quasiparticles in the system, regardless of their location. A model developed by Tojosoa-Nantenaina Raveloarijaona allows a qualitative explanation of this phenomenon.

La lune nous accueillit quand nous atteignîmes l'arête. Nous remontâmes solennellement l'arête immaculée, un pied dans l'ombre, un pied dans la clarté. Nous arrivâmes au somment. Le gigantesque porte-à-faux du Doigt de Dieu se dressait contre le couchant où s'attardait encore une bande écarlate. Il semblait désigner dans le firmament une planète merveilleuse : Vénus peut-être.

— *Pierre Dalloz*, première hivernale de la Meije orientale, 1927

2 Theory

Contents

2.1. Multimode circuit quantum electrodynamics

As motivated in the previous chapter, the main objective of the work presented in this thesis is to experimentally study a quantum system with a single degree of freedom, characterised by its anharmonic potential $\hat{V}$, coupled to an ensemble of harmonic modes. The coupling of each individual mode to the anharmonic system is linear and characterised by the interaction strength g_k. The canonical Hamiltonian modelling this problem is given by the celebrated Caldeira-Legget model [Caldeira and Leggett 1983] for dissipation,

$$\hat{H} = \frac{\hat{p}^2}{2m} + \hat{V}(\hat{x}) + \hat{x}\sum_k g_k \hat{x}_k + \sum_k \frac{1}{2}\left(m_k\omega_k^2\hat{x}_k^2 + \frac{\hat{p}_k^2}{m_k}\right) + \hat{x}^2\sum_k \frac{g_k^2}{2m_k\omega_k^2}\,, \tag{2.1}$$

where $\hat{x}$ and $\hat{p}$ are the conjugate variables describing a quantum particle of mass m – often called quantum impurity in this manuscript because of the link between equation (2.1) and quantum impurity problems in condensed matter physics – and $\hat{x}_k$ and $\hat{p}_k$ model the set of harmonic modes to which it is coupled (each mode being characterised by its frequency ω_k and mass m_k). The last term on the right-hand side of equation (2.1) is a counter term to remove unphysical frequency shifts resulting from the linear coupling of the system to the bath [Caldeira and Leggett 1983].

The aim of this chapter is to introduce the building blocks of the experimental realisation of Hamiltonian (2.1) using the toolbox of circuit quantum electrodynamics, namely superconducting circuits. The main focus of this work is the study of the effective interactions between the initially independent harmonic modes owing to the ultrastrong coupling between the anharmonic system and the harmonic modes, $g_k/\omega_k \sim 0.1$. More specifically, we are interested in processes that do not conserve the number of excitations, namely photon conversion processes. To this end, we will present the design principles that allow the direct observation of such a process.

2.1.1. The Josephson junction

The Josephson junction (JJ) is a key component of circuit-QED [Blais et al. 2004] and of the work presented here. Since its discovery by B. D. Josephson [Josephson 1962] it has been used in a wide range of applications, from magnetometry [Deaver and Goree 1967], rapid single flux quantum (RSFQ) [Likharev and Semenov 1991] and metrology [Shapiro 1963; Hamilton 2000] to various designs of superconducting quantum bits [devoret and Martinis 2004]. In the present work, the Josephson junction allows both the implementation of the quantum impurity with anharmonic potential $\hat{V}$ as well as the realisation of a high impedance harmonic environment.

Although they have been extensively discussed in the literature, we will first recall some important properties of the Josephson junction that will allow us to understand the design principles of the experiment. The junctions used in this work are SIS (superconductor-insulator-superconductor) junctions made of aluminium and aluminium oxide [Lecocq et al. 2011]. Each of the superconducting lead hosts a Cooper pair condensate characterised by the macroscopic order parameter $\Psi_i = |\Psi_i|e^{i\varphi_i}$, where $|\Psi_i|^2$ corresponds to the Cooper pair density in each lead and φ_i is the Ginzburg-Landau superconducting phase of each lead [Tinkham 2004]. Due to proximity effects, Cooper pairs can tunnel from one lead to another. The tunneling of Cooper pairs through the SIS junction can be formally described by Hamiltonian (2.2), where the Josephson energy E_J is the energy associated to the tunneling of a single Cooper pair and n is the number of Cooper pairs transferred through the junction [Knight 2015], characterising the state of the tunnel junction $|n\rangle$[1]:

[1] Equivalently, n describes the number of excess charges in the case where a superconducting island can be defined, which is often the case.

$$\hat{H}_J = -\frac{1}{2}E_J \sum_{n=-\infty}^{\infty} |n\rangle \langle n+1| + |n+1\rangle \langle n| \ . \tag{2.2}$$

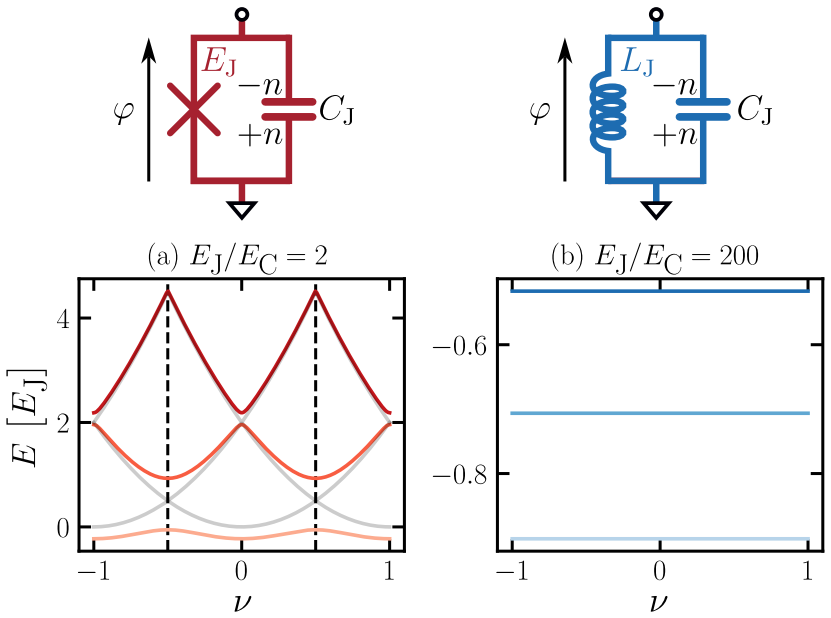

Figure 2.1.: Spectrum of the CPB Hamiltonian as a function of the quasi-momentum (sometimes called quasi-charge) ν for two different $E_\mathrm{J}/E_\mathrm{C}$ ratios. All the energies are given in units of E_J. **Left.** The different shades of red represent the band structure of a highly anharmonic junction ($E_\mathrm{C} = 0.5 \times E_\mathrm{J}$). The grey lines correspond to the spectrum of the same small junction without tunneling of Cooper pairs ($E_\mathrm{J} = 0$). The tunneling term allows to lift the degeneracy that appears for half integer values of the quasi-momentum (vertical dashed line). **Right.** Spectrum of a junction in the linear regime ($E_\mathrm{C} = E_\mathrm{J}/200$) with evenly spaced levels that are practically independent of the quasi-momentum value. This numerical diagonalisation of the CPB Hamiltonian confirms that a large junction can be considered as a harmonic oscillator. In this case, the tunnel junction is replaced by an inductor in the equivalent circuit schematics.

In addition, the insulating barrier between the two superconducting leads acts as a capacitor with a charging energy given by equation (2.3), where $E_C = 4e^2/2C_J$ is the charging energy associated with one cooper pair being transferred and C_J is the intrinsic capacitance of the junction. We have also introduced a charge offset, n_g, which can describe either a controlled bias of the junction, or uncontrolled sources of noise. The charging Hamiltonian reads:

$$\hat{H}_C = \frac{4e^2}{2C_J} \left(\hat{n} - n_\mathrm{g}\right)^2 , \tag{2.3}$$

where $\hat{n}$ is the operator associated with the number of Cooper pairs transferred, with eigenstates $|n\rangle$[2]. The variable conjugate to $\hat{n}$ is the superconducting phase difference $\hat{\varphi}$ such that $[\hat{n}, \hat{\varphi}] = i$. In the language of electrical engineering, n is related to the classical current I by $n(t) = \frac{1}{2e}\int_0^\tau \mathrm{d}\tau\, I(\tau)$ and φ to the classical voltage v by $\varphi(t) = \frac{1}{\Phi_0}\int_0^\tau \mathrm{d}\tau\, v(\tau)$, where $\Phi_0 = \hbar/2e \simeq 3.29 \times 10^{-16}\,\mathrm{V\,s}$ is the reduced flux quantum. Since $e^{i\hat{\varphi}}\,|n\rangle = |n+1\rangle$, the full Hamiltonian of the Josephson junction, known as the Cooper pair box (CPB) Hamiltonian, can be written as [Cottet 2002]:

$$\hat{H} = E_C \left(\hat{n} - n_\mathrm{g}\right)^2 - E_J \cos\hat{\varphi} = E_c \left(-i\frac{\mathrm{d}}{\mathrm{d}\varphi} - n_\mathrm{g}\right)^2 - E_J \cos\hat{\varphi}\,. \tag{2.4}$$

Hamiltonian (2.4) can be regarded as modelling the dynamics of a quantum particle moving in a 1D periodic potential along the φ axis. The variable φ plays the role of position and the Josephson energy E_J quantifies the height of the periodic potential barrier, while the charging energy E_C is equivalent to the kinetic energy of a particle of mass $C_J \times (\hbar/2e)^2$. This description holds if the phase φ is considered as an extended variable (*i.e.* φ lives on the whole real line)[3] [Sépulcre 2021], and in this case one can use the Bloch theorem to calculate the eigenstates of the system [Likharev and Zorin 1985], $\Psi_s(\nu) = e^{i\nu\varphi} u_\nu^s(\varphi)$, where s is the band-index, ν is the quasi-charge (analogous to the quasi-momentum of an electron in a crystal) and $u_\nu^s(\varphi)$ is a periodic function of φ. The eigenenergies of the junction display a band structure and these bands are continuous functions of the quasi-charge ν. Figure 2.1 shows the first three bands of a Josephson junction for two different $E_\mathrm{J}/E_\mathrm{C}$ ratios, calculated by solving the Schrödinger equation for Hamiltonian (2.4). The $E_\mathrm{J}/E_\mathrm{C}$ ratio plays an important role in the description of a Josephson junction. A hand waving argument allows one to understand the dynamics of the junction depending on this ratio. When $E_J \gg E_C$, *i.e.* when the potential barrier greatly overcomes the kinetic energy of the junction, the "particle" remains localised at the bottom of the cosine potential and remains close to its equilibrium position, $\varphi = 0$, with small phase fluctuations $\langle\hat{\varphi}^2\rangle \ll 1$. In this case, the cosine potential of equation (2.4) can legitimately be expanded to second order ($-E_J\cos\hat{\varphi} \to E_J\hat{\varphi}^2/2$), so that the tunnel barrier simply acts as a (kinetic) inductance $L_\mathrm{J} = \Phi_0^2/E_\mathrm{J}$ and the junction effectively behaves as a harmonic oscillator[4],

$$\hat{H}_\mathrm{lin} = E_C\hat{n}^2 + \frac{E_J}{2}\hat{\varphi}^2 = \hbar\omega_\mathrm{J}\left(\hat{a}^\dagger\hat{a} + \frac{1}{2}\right) . \tag{2.5}$$

[2] Formally, $\hat{n}\,|n\rangle = n\,|n\rangle$.

[3] In contrast to a compact phase living on a circle.

[4] Since the Hamiltonian is now quadratic, we remove the n_g dependence by applying the unitary transformation $\hat{U} = e^{-in_\mathrm{g}\hat{\varphi}}$. This explicitly shows that in the linear regime the spectrum of the isolated junction does not depend on the offset charge n_g, which is confirmed by the numerically calculated spectrum in Figure 2.1, right-hand panel. We have also dropped the constant $-E_J$ term.

The Hamiltonian (2.5) is diagonal in the basis of Fock states such that $\hat{a}^\dagger\hat{a}\,|N\rangle = N\,|N\rangle$ ($N = 0, 1, 2, \dots$), where $\hat{a}$ and $\hat{a}^\dagger$ are the usual annihilation and creation operators for the plasma oscillations of the linear Josephson junction. These plasma oscillations of the isolated junction consist of a sustained oscillation of Cooper pairs tunneling back and forth through the tunnel junction at the frequency $\omega_\mathrm{J} = \sqrt{2E_\mathrm{J}E_\mathrm{C}}/\hbar$ [Blais et al. 2004]. They are related to $\hat{n}$ and $\hat{\varphi}$ by the following relations,

$$\hat{\varphi} = \left(\frac{2E_\mathrm{C}}{E_\mathrm{J}}\right)^{1/4} \frac{\hat{a} + \hat{a}^\dagger}{\sqrt{2}}\,, \tag{2.6}$$

$$\hat{n} = \left(\frac{E_\mathrm{J}}{2E_\mathrm{C}}\right)^{1/4} \frac{\hat{a} - \hat{a}^\dagger}{\sqrt{2}i}\,. \tag{2.7}$$

Given the usual commutation relation for bosonic creation and annihilation operators $[\hat{a}, \hat{a}^\dagger]$, one can easily calculate the phase fluctuations across the junction,

$$\left\langle\hat{\varphi}^2\right\rangle = \varphi_\mathrm{zpf}^2\,(2n_\mathrm{th} + 1)\ , \tag{2.8}$$

where $n_\mathrm{th} = \left\langle\hat{a}^\dagger\hat{a}\right\rangle$ is the usual thermal filling factor describing the excitation of the system by thermal fluctuations,

$$n_\mathrm{th} = \frac{1}{\exp\left(\hbar\omega_\mathrm{J}/k_BT\right) - 1}\,. \tag{2.9}$$

In the work presented in this manuscript, the typical Josephson junctions used have a plasma frequency ω_J in the range of 2 GHz to 25 GHz, which is always at least one order of magnitude larger than the thermal energy $k_BT/h = k_B/h \times 10\,\mathrm{mK} \sim 0.2\,\mathrm{GHz}$, leading to a maximum thermal occupation $n_\mathrm{th} \leq 1 \times 10^{-4} \ll 1$. Thus, considering the experimental conditions, we will neglect the contribution of thermal fluctuations and assume that the phase fluctuations of a junction originate purely from the zero point fluctuations. These so-called zero point fluctuations of the superconducting phase φ_zpf^2 describe random phase fluctuations at zero temperature due to the quantum nature of the system. For a harmonic junction they take a simple form,

$$\varphi_\mathrm{zpf}^2 = \sqrt{\frac{E_\mathrm{C}}{2E_\mathrm{J}}}\,. \tag{2.10}$$

Finally, the simple relation between the phase fluctuations and the $E_\mathrm{J}/E_\mathrm{C}$ ratio in equation (2.10) confirms that when $E_J \gg E_C$ the former are indeed very small and the cosine potential can be approximated by a quadratic potential (*i.e.* the junction can be considered as an inductor with inductance $L_\mathrm{J} = \Phi_0^2/E_\mathrm{J}$).

2.1.2. The anharmonic junction

If $E_\mathrm{J}/E_\mathrm{C}$ is reduced for a fixed value of E_C, then the kinetic energy will allow the particle to explore a larger part of the cosine potential, leading to larger phase fluctuations $\langle\hat{\varphi}^2\rangle$. In this situation the cosine potential of the junction cannot be expanded to the lowest

order. However, we can obtain some information on the ground state properties of the junction by mapping the full Hamiltonian of equation (2.4) to the linear Hamiltonian known as the self-consistent harmonic approximation (SCHA) [Léger et al. 2019; Léger et al. 2023],

$$\hat{H}_{\text{scha}} = E_C \hat{n}^2 + \frac{E_J^\star}{2}\hat{\varphi}^2 \,, \tag{2.11}$$

where $E_\text{J}^\star$ is a variational parameter minimising the ground state energy of equation (2.11) and is given by the following self-consistent equation:

$$E_\text{J}^\star = E_\text{J} e^{-\langle \hat{\varphi}_0^2 \rangle / 2} = E_\text{J} \exp\left(-\sqrt{\frac{E_\text{C}}{8E_\text{J}^\star}} \right) . \tag{2.12}$$

From equation (2.12) we can see that the zero point fluctuation of a small[5] junction are given by $\varphi_\text{zpf}^2 = \sqrt{E_\text{C}/2E_\text{J}^\star}$.

Although equation (2.11) maps the Hamiltonian of a general Josephson junction (including junctions with a relatively small E_J/E_C ratio) to the Hamiltonian of a harmonic oscillator, it only allows to characterise the ground state of the junction and ignores the junction dynamics. In addition, the SCHA breaks down when $\langle \hat{\varphi}_0^2 \rangle$ becomes too large. Hence, to consider the full dynamics of a junction with a small E_J/E_C ratio ($\langle \hat{\varphi}_0^2 \rangle \gtrsim 1$), the full cosine potential must be considered.

The spectrum of a small junction is shown in Figure 2.1 (left panel) and shows a clearly defined band structure with respect to the quasi-charge ν and an anharmonic behaviour visible through the unevenly spaced energy levels.

2.1.3. High impedance electromagnetic environment

To design a multimode circuit-QED experiment, we need to implement a multimode resonator that will be coupled to the quantum impurity. Before describing the actual implementation of this multimode resonator, we need to understand how the coupling of the small junction to a generic electromagnetic environment affects its behaviour. This will allow guidelines to be defined for the design of the multimode resonator.

Any linear circuit coupled to the small junction can be modelled by its frequency dependent impedance $Z(\omega)$. For the time being, this impedance is assumed to be constant with frequency $Z(\omega) = Z_\text{env}$. The small junction itself is characterised by the impedance $Z_\text{J} = Z_\text{q}/2\pi \times \sqrt{2E_\text{C}/E_\text{J}}$, where $Z_\text{q} = h/(2e)^2 \simeq 6.5\,\text{k}\,\Omega$ is the superconducting quantum of impedance. Depending on the Z_J/Z_env ratio, the small junction enters into different regimes. If $Z_\text{J}/Z_\text{env} \gg 1$, the electromagnetic environment effectively shorts the small junction and the phase fluctuations are significantly reduced, $\langle \hat{\varphi}_0^2 \rangle \to 0$. In this situation, called the overdamped regime, the coupling of the small junction to the electromagnetic

[5] We use the term "small" for a junction with a small E_J/E_C ratio, as the latter is directly proportional to the square of the junction area.

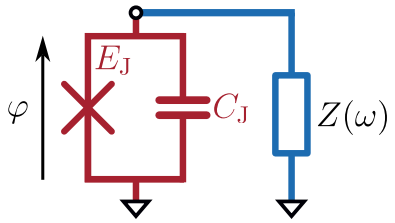

Figure 2.2.: Equivalent circuit representation of a small Josephson junction coupled to a general electromagnetic environment modelled by the frequency dependent impedance $Z(\omega)$.

environment leads to a reduction of the nonlinear behaviour of the junction ($\langle\hat{\varphi}_0^2\rangle \ll 1$) and it is not possible to observe a nonlinear process between the modes of the microwave resonator. On the other hand, if $Z_J/Z_{env} \ll 1$, the electromagnetic environment is seen as an open by the junction and there is no coupling between the modes of the resonator. From this simplified explanation we can see that in order to enhance the phase fluctuations of the small junction while maintaining a large coupling to the modes of the resonator, we need the impedances of both the resonator and the small junction to be equivalent, $Z_J/Z_{env} \sim 1$.

The previous discussion leads to the important design criterion of $Z_{env} \sim Z_J$. Therefore, we need to design a ***high impedance*** multimode resonator. A microwave resonator typically consists of a transmission line terminated with mismatched loads, $Z_{in}, Z_{out} \neq Z_{env}$. Now Z_{env} refers to the characteristic impedance of a standard transmission line $Z_{env} = \sqrt{L/C_g}$, where L is the inline inductance and C_g is the capacitance to ground. Due to the low geometric inductance of standard materials used to design stripline resonators, the characteristic impedance of such resonators will always be too small in comparison to Z_J. To circumvent this problem, we choose to design our microwave resonator with an array of large Josephson junctions [Chow et al. 1998; Corlevi et al. 2006; Puertas Martínez et al. 2019]. This allows to take advantage of the high kinetic inductance of Josephson junctions while still being in the linear regime. Therefore, the junctions of the array can effectively be considered as linear inductors with inductance $L = \Phi_0^2/E_{J,arr}$. Such an array is shown in Figure 2.3. For the moment we have left the boundary conditions Z_{in}, Z_{out} unspecified in order to concentrate on the bulk properties of the array, as if it were an infinite array. The main difference with a standard transmission line is that the intrinsic capacitances of the junctions shunt the inline (kinetic) inductances. This results in a bending of the dispersion relation compared to the usual linear relation $\omega_k = v_\varphi k$. As we will see below it also introduces a cut-off frequency ω_p, the plasma frequency, above which no mode is supported.

The exact dispersion relation of the JJ array shown in Figure 2.3 can be derived using Kirchoff's current law, leading to a result well known in the community [Puertas 2018]:

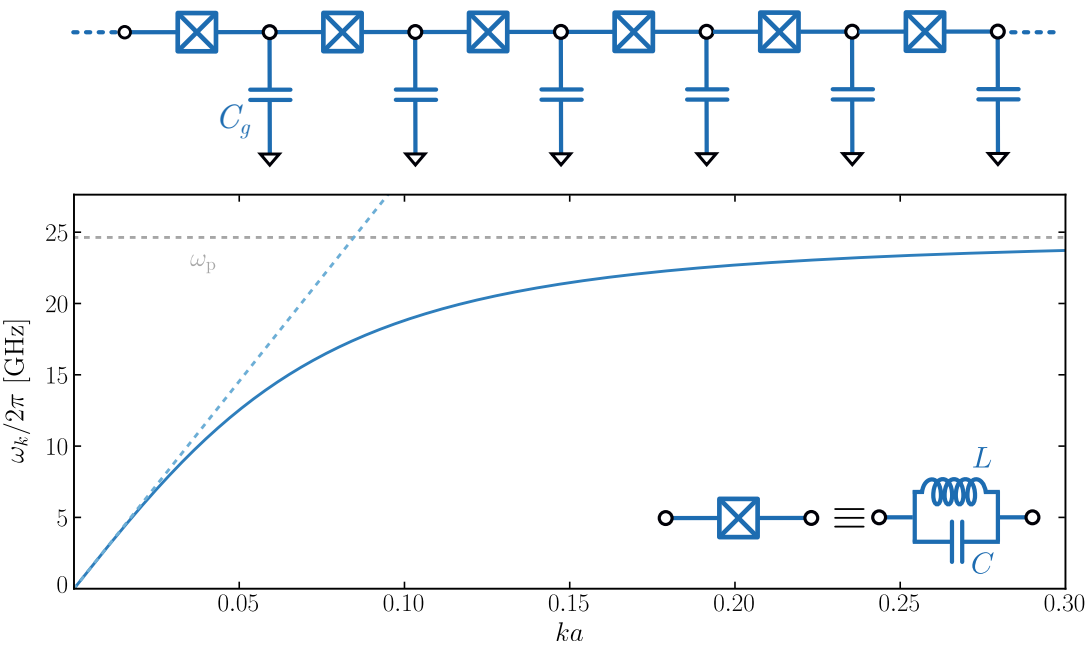

Figure 2.3.: **Top.** Equivalent circuit representation of an infinite array of linear Josephson junctions, characterised by their inline inductance $L = \Phi_0^2/E_{\mathrm{J,arr}}$, self-capacitance C and capacitance to ground C_{g}, implementing a high impedance transmission line. The inset of the lower panel explicitly shows the equivalence between the junctions of the array and LC oscillators. **Bottom.** Dispersion relation of the array calculated for realistic parameters, $E_{\mathrm{J}}/2\pi \simeq 413\,\mathrm{GHz}$, $E_{\mathrm{C}}/2\pi \simeq 0.75\,\mathrm{GHz}$ and $C_{\mathrm{g}} \simeq 0.75\,\mathrm{f\,F}$. The dark blue line is the full dispersion as given by equation (2.13). The light blue line is the linear limit valid when $ka \ll \sqrt{C_{\mathrm{g}}/C}$. The grey horizontal line represents the plasma frequency of the array ω_{p}

$$\omega_k = v_\varphi \sqrt{\frac{2\,(1-\cos ka)}{1+\frac{2C}{C_{\mathrm{g}}}(1-\cos ka)}}\,, \tag{2.13}$$

where we have introduced $v_\varphi = 1/\sqrt{LC_{\mathrm{g}}}$, the phase velocity in the small wavevector limit, $ka \ll \sqrt{C_{\mathrm{g}}/C}$, and a the size of the unit cell. Due to the discrete nature of the array, the maximum wavevector allowed is $ka = \pi$. This maximum wavevector results in a cutoff frequency $\omega_{\mathrm{p}} = 1/\sqrt{L\,(C + C_{\mathrm{g}}/4)}$ above which no modes are supported.

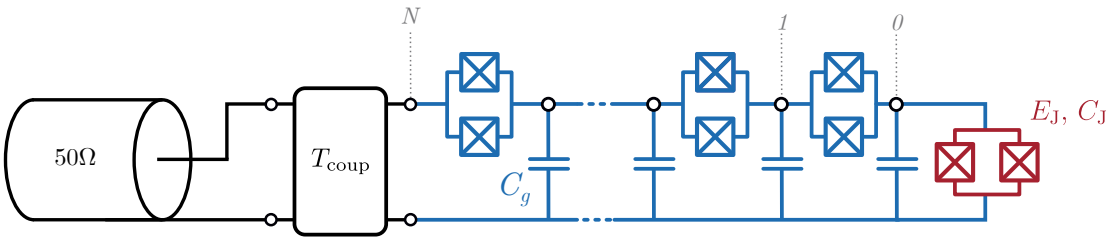

Figure 2.4.: Equivalent circuit representation of the multimode microwave cavity. A chain of N large Josephson junctions is coupled to a 50 Ω measurement line via a coupling network characterised by its transfer matrix T_{coup}. The chain is terminated at the other end by a small junction characterised by its characteristic impedance $Z_{\text{out}} = Z_{\text{J}}$. All the junctions in the system are actually implemented using superconducting quantum interference devices (SQUIDs), which act as tunable Josephson junctions whose Josephson energy can be tuned by means of an external magnetic field. The reason for this is highlighted in section 2.2.

2.1.4. Coupling the impurity to the array

Normal mode decomposition

To convert the high impedance transmission line described above into a multimode microwave resonator, we terminate it with unmatched loads, resulting in a non-zero reflection coefficient $r = \left(Z_{\text{env}} - Z_{\text{in (out)}}\right) / \left(Z_{\text{env}} + Z_{\text{in (out)}}\right)$ of the plane waves at the left (right) boundaries. The left boundary Z_{in} corresponds to the element coupling the system to a 50 Ω coaxial measurement line. Since two different coupling schemes (capacitive and galavanic) are to be studied, it is left unspecified for the time being. The right boundary is nothing more than the small junction introduced earlier. It will act as a nonlinear boundary condition on which incoming waves will eventually scatter inelastically. Interference between the left and right moving plane waves will result in the formation of standing waves, called the resonant modes of the array (sometimes referred to as plasma modes).

For the time being, we will ignore the nonlinear behaviour of the small junction and consider only its quadratic contribution. This is done by simply replacing the small junction with an inductance L_{J}. As explained in the previous section, since the junctions of the array are in the linear regime, they can legitimately be considered as linear inductances. This linearisation procedure leaves us with the linear system shown in Figure 2.5. Although considering the small junction as a linear element is not a correct approximation, it allows us to derive the so-called normal modes of the system. Later we will reintroduce the nonlinearity of the small junction and see the effect it has on these normal modes (renormalisation, interactions, etc...).

Assuming that the boundary conditions consist only of reactive elements (*i.e.* non dissipative elements), the Hamiltonian of the array is quadratic,

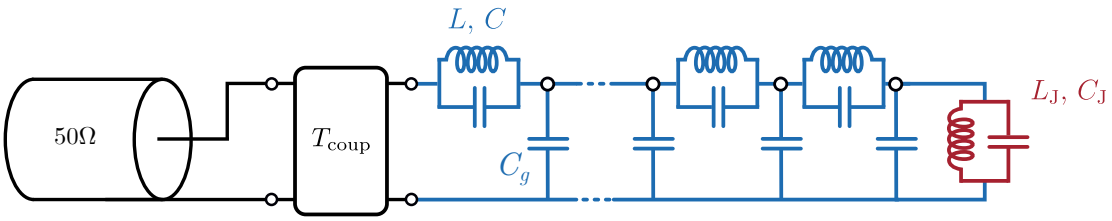

Figure 2.5.: Equivalent circuit representation of the linearised system. The junctions of the chain are considered as linear inductors with inductance $L = \Phi_0^2/E_{\text{J}}^{\text{arr}}$ and only the quadratic contribution of the right boundary impurity is considered.

$$\hat{H}_{\text{arr}} = \frac{(2e)^2}{2} \sum_{i,j=0}^{N} \hat{n}_i \left[C\right]^{-1}_{i,j} \hat{n}_j + \frac{\Phi_0^2}{2} \sum_{i,j=0}^{N} \hat{\varphi}_i \left[L^{-1}\right]_{i,j} \hat{\varphi}_j \,. \tag{2.14}$$

Modes of this system are solutions of the wave equation which consists in the generalised eigenvalue problem [Landau, L. D. and Lifshitz, E. M. 1976]

$$\left[L^{-1}\right] \overrightarrow{\varphi_k} = \omega_k^2 \left[C\right] \overrightarrow{\varphi_k} \,, \tag{2.15}$$

where $\overrightarrow{\varphi_k} = (\varphi_{0k}, \varphi_{1k}, \ldots, \varphi_{Nk})$ is the spatial profile of mode k and the ω_k are the positive square root of the eigenvalues of $\left[\Omega^2\right] = \left[C^{-1}\right]\left[L^{-1}\right]$. The allowed values of k are determined by the boundary conditions. Further details on the determination of the allowed values of wavevector k will be given when dealing with the actual system design. The Hamiltonian of the system can then be written in the following diagonal form,

$$\hat{H}_{\text{lin}} = \sum_k \hbar\omega_k \hat{a}_k^\dagger \hat{a}_k \,, \tag{2.16}$$

where $\hat{a}_k$ ($\hat{a}_k^\dagger$) is the annihilation (creation) operator for mode k bosonic excitations. They are related to the phase profile of the modes by[6]

$$\hat{\varphi}_i = \sum_k \varphi_{i,k} \left(\hat{a}_k + \hat{a}_k^\dagger\right) \,. \tag{2.17}$$

As a result, the phase fluctuations of the small junction can be expressed directly as a function of the mode amplitudes at the right boundary,

$$\langle \hat{\varphi}_0^2 \rangle = \sum_k \varphi_{0,k}^2 \,. \tag{2.18}$$

[6]Similarly for the charge profile of the modes : $\hat{n}_i = \sum_k n_{i,k} \left(\hat{a}_k - \hat{a}_k^\dagger\right)$.

Reintroducing the nonlinearity

To account for the anharmonic nature of the small junction, we reintroduce the nonlinear part of the cosine potential equation (2.4). Since the quadratic term of the cosine expansion has already been taken into account in the normal mode decomposition of the system, we subtract the $-\hat{\varphi}_0^2/2$ term from the cosine expansion. The complete Hamiltonian reads as

$$\hat{H} = \sum_k \hbar\omega_k \hat{a}_k^\dagger \hat{a}_k - E_\mathrm{J}\left(\cos\hat{\varphi}_0 + \frac{\hat{\varphi}_0^2}{2}\right) = \hat{H}_\mathrm{lin} + \hat{H}_\mathrm{nl}\,. \tag{2.19}$$

The second term on the right-hand side of equation (2.19), $\hat{H}_\mathrm{nl}$, is the purely nonlinear part of the system Hamiltonian. Considering $\hat{H}_\mathrm{nl}$ as a perturbation to the diagonal Hamiltonian $\hat{H}_0$, one can compute the decay probability of any initial state $|i\rangle = \bigotimes_k |n_k\rangle$[7] to any other eigenstate $|f\rangle = \bigotimes_k |m_k\rangle$ of $\hat{H}_0$ using first-order perturbation theory [Cohen-Tannoudji et al. 2018]

$$\mathcal{P}(t) = \frac{4}{\hbar^2}\sum_{f\neq i}\left|\langle f|\hat{H}_\mathrm{nl}|i\rangle\right|^2 \sin^2\left(\frac{\omega_\mathrm{if}t}{2}\right)\times\frac{1}{\omega_\mathrm{if}^2}\,, \tag{2.20}$$

where $\hbar\omega_\mathrm{if} = E_f - E_i$ is the energy difference between the initial and final states. From equation (2.20) it is clear that the decay rate is maximum when $\omega_\mathrm{if} = 0$. This is expected since the decay process should conserve energy (*i.e.* the final and initial states should have the same energy). Achieving this resonance condition is a critical part of the experiment. To experimentally observe conversion processes between the states $|i\rangle$ and $|f\rangle$, it is also of great interest to increase the matrix element $|\langle f|\hat{H}_\mathrm{nl}|i\rangle|$ as much as possible.

As emphasised earlier, the superconducting phase difference of the small junction can be written as a linear combination of the normal modes of the system. Replacing $\hat{\varphi}_0$ by its expression in equation (2.17) and writing the cosine as a Taylor series, one can see that the $\hat{H}_\mathrm{nl}$ potential contains all nonlinear processes at any order (see reference [Minev et al. 2021] for a general mathematical formulation). For the sake of illustration, we will first consider the $\hat{\varphi}_0^4$ expansion of $\hat{H}_\mathrm{nl}$, in order to explicitly demonstrate the emergence of the three-photon conversion terms we are interested in. This approximation is only valid if $\langle\hat{\varphi}_0^2\rangle$ is not too large. Although this condition is *a priori* not met for our system, the $\hat{\varphi}_0^4$ expansion gives some insight into the interactions induced by the nonlinear potential. For clarity, we will now omit the subscript 0 when writing the wave amplitude of the superconducting phase at the small junction site associated with mode k, *i.e.* $\varphi_{0,k} \equiv \varphi_k$.

[7] Here $|n_k\rangle$ is the Fock state associated to mode k.

$$\hat{H}_{\mathrm{nl},4} = -E_{\mathrm{J}}\frac{\hat{\varphi}_0^4}{24} = -\frac{E_{\mathrm{J}}}{24}\sum_{k,l,q,p}\varphi_k\varphi_l\varphi_q\varphi_p\left(\hat{a}_k+\hat{a}_k^\dagger\right)\left(\hat{a}_l+\hat{a}_l^\dagger\right)\left(\hat{a}_q+\hat{a}_q^\dagger\right)\left(\hat{a}_p+\hat{a}_p^\dagger\right)$$

$$= -\frac{E_{\mathrm{J}}}{4}\sum_{k,l,p,q}\varphi_k\varphi_l\varphi_p\varphi_q\hat{a}_k^\dagger\hat{a}_l^\dagger\hat{a}_p\hat{a}_q - \frac{E_{\mathrm{J}}}{2}\sum_{k,l}\varphi_k^2\varphi_l^2\hat{a}_k^\dagger\hat{a}_k$$

$$-\frac{E_{\mathrm{J}}}{6}\left(\sum_{k,l,p,q}\varphi_k\varphi_l\varphi_p\varphi_q\hat{a}_k^\dagger\hat{a}_l^\dagger\hat{a}_p^\dagger\hat{a}_q + \mathrm{h.c.}\right) + \dots . \tag{2.21}$$

$\hat{H}_{\mathrm{nl},4}$ includes two types of processes. The first kind are processes that conserve the number of excitations, as in the second line of equation (2.21)[8]. This includes $2 \leftrightarrow 2$ conversion processes where two photons (modes p and q) are converted into two other photons (modes k and l), as shown in the left panel of Figure 2.6. In the case where the frequencies of the initial and final photons are the same ($k = p$ and $l = q$), these processes are nothing more than the famous Kerr effect, a photon-photon interaction process where the resonance frequency of a mode is shifted by the populations in the system [Bourassa et al. 2012; Krupko et al. 2018]. An important consequence of the Kerr effect is the fact that successive Fock states of mode k[9] are not equally spaced in energy, since the mode k frequency depends on its own population (the so-called ***self-Kerr*** effect). Thus, the initially harmonic modes of the environment become anharmonic due to their coupling to the impurity. Similarly, the frequency of mode k also depends on the the population in all other modes of the system (this effect is usually referred to as the ***cross-Kerr*** effect). Another important consequence of the nonlinearity is the renormalisation of the normal mode frenquencies, as we can see in the second line of equation (2.21), due to the zero point fluctuations of each mode,

$$\omega_k \to \omega_k - \frac{E_{\mathrm{J}}}{2\hbar}\sum_l \varphi_k^2\varphi_l^2 \overset{\mathrm{def}}{=} \omega_k - \delta_k\,, \tag{2.22}$$

where δ_k is defined as the ***Lamb shift*** of mode k. The Kerr effect together with the Lamb shift will have a consequence on the resonance condition $\omega_{\mathrm{if}} = 0$, as we will see in section 2.2.

The second type of processes are those that do not conserve the number of excitations. In the case of the $\hat{\varphi}_0^4$ approximation they are given in the third line of equation (2.21) and correspond to the decay of a single photon into three photons, or the reverse process, namely the fusion of three photons to produce a single photon (see middle and right panels of Figure 2.6). The strength of this multiphoton interaction process is given by the prefactor $\hbar g^{q\leftrightarrow k,l,p} = E_{\mathrm{J}}/4 \times \varphi_k\varphi_l\varphi_p\varphi_q$. Higher order terms of the cosine potential will also contribute to this three-photon conversion process and their contribution will

[8] We have dropped the unphysical term $\hat{a}_k^\dagger\hat{a}_l$ for $k \neq l$, which does not conserve energy.
[9] Assuming other modes are in vacuum.

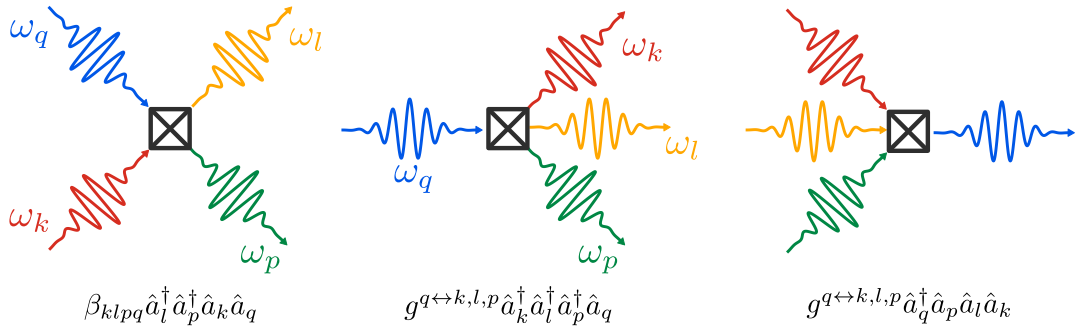

Figure 2.6.: Cartoon representation of the four-wave mixing processes in the $\hat{\varphi}_0^4$ approximation. **Left.** Four-wave mixing process conserving the number of excitations in the system and giving rise to the Kerr effect. To observe this process, the frequencies must satisfy the resonance condition $\omega_k + \omega_q = \omega_l + \omega_p$. **Middle&Right.** Three-photon conversion processes (down-conversion and up-conversion respectively) resulting from the $\hat{\varphi}_0^4$ expansion. To observe these processes, the frequencies must verify the resonance condition $\omega_k + \omega_l + \omega_p = \omega_q$.

renormalise the coupling strength $g^{q\leftrightarrow k,l,p}$ (see section 2.2 for an explicit formulation of this renormalisation in the case of two modes). In the case of the experiments presented in this thesis, we are interested in the processes given by the last line of equation (2.21), where a three-photon state of the system interacts with a single photon-state. If $|i\rangle$ is a single-photon state of mode q and $|f\rangle$ is a state composed of three photons in modes k, l and p, the matrix element introduced in equation (2.20) now explicitly writes

$$\left|\langle f|\hat{H}_{\mathrm{nl}}|i\rangle\right|^2 = \frac{E_{\mathrm{J}}^2}{16}\left|\langle f|\hat{\varphi}_0^4|i\rangle\right|^2 = \frac{E_{\mathrm{J}}^2}{16}\times\varphi_k^2\varphi_l^2\varphi_p^2\varphi_q^2 = \left|\hbar g^{q\leftrightarrow k,l,p}\right|^2 . \tag{2.23}$$

This expression shows the importance of enhancing the zero point fluctuations of the modes we want to couple together. The strategy for doing this is described in the next section.

2.2. Photon conversion between two modes of the environment

2.2.1. Limiting the interaction to a subset of environmental modes

In order to facilitate the experimental observation of the decay of a single photon into three photons, we will restrict ourselves to only two modes interacting together through a three-photon conversion process. The rationale behind this choice is as follows. When exciting the system in a single photon state, the nonlinearity of the small junction will allow this single photon state to decay into multiphoton states (as long as the energy conservation criterium $\omega_{\mathrm{if}} \simeq 0$ is satisfied). The input power is then distributed over the

bandwidth of the modes that make up the accessible multiphoton states. If many modes are at a frequency below the frequency of the excitation photon, the power emitted at individual mode frequencies will be a very small fraction of the input power (which is already small since we want to work in the single-photon regime) [Léger 2021].

The limit where only two modes are coupled via photon conversion provides a way to focus the input power on only one mode of lower frequency, thus facilitating the measurement of the outgoing converted photons. Since the typical measurement bandwidth of the experimental setup is between 3 GHz and 12 GHz, the two interacting modes must lie within this band with as few other modes as possible between them, ensuring that there is only one conversion channel associated with the probe mode. The frequency of the first mode of the system depends on the coupling scheme to the measurement line (left boundary of the array, Figure 2.4) and the number of junctions in the array. For a given left boundary condition, we want the lowest number of junctions in the array (ensuring that only a few modes interact, ideally two) while maintaining the first mode in the measurement bandwidth. A small number of junctions in the array results in the

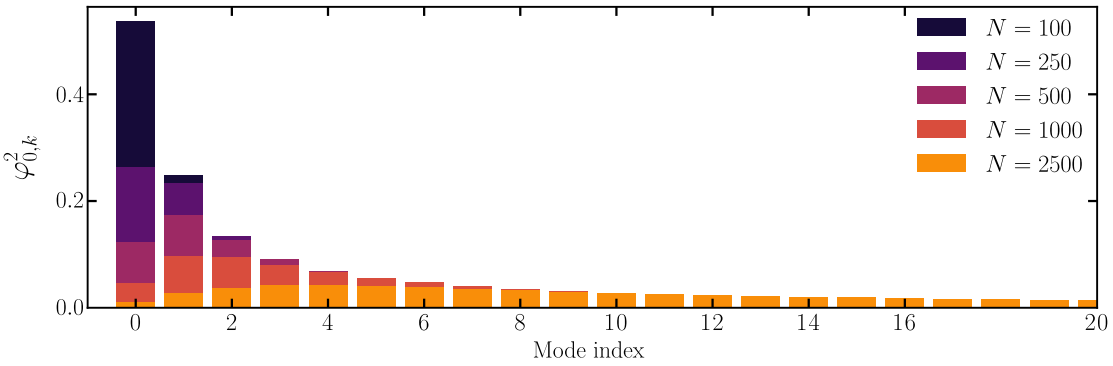

Figure 2.7.: Squared ampltitude of mode k at the small junction site, $\varphi^2_{0,k}$, showing the contribution of mode k to the zero point fluctuations, $\langle\hat{\varphi}^2_0\rangle = \sum_k \varphi^2_{0,k}$, for the first twenty modes and for different array length. Calculated in the case of galvanic coupling to the measurement line and for realistic system parameters. Shorter arrays concentrate the nonlinearity on the first few modes of the system, while longer arrays dilute the nonlinearity over a wide range of modes.

small junction sharing its nonlinearity with only the first few modes of the system. This results in an enhancement of $\varphi_{0,k}$ for the first few modes of the system. On the contrary, a longer chain tends to dilute the nonlinearity of the small junction in many modes of the system. This can be illustrated by calculating the eigenvector $\overrightarrow{\varphi_k}$ of the circuit shown in Figure 2.5 by solving the generalised eigenvalue problem equation (2.15). As given by equation (2.18), the relevant quantity to show the contribution of mode k to $\langle\hat{\varphi}^2_0\rangle$ is $\varphi^2_{0,k}$. In Figure 2.7 we show $\varphi^2_{0,k}$ for the first twenty modes of the system and for increasing

array length[10].

The conclusion of this numerical analysis is that in order to increase the conversion rate between a single-photon state and a multi-photon state, we need to work with a short chain and with the first few modes of the system. This justifies the lower limit of the array length to have the first mode of the system in the measurement bandwidth.

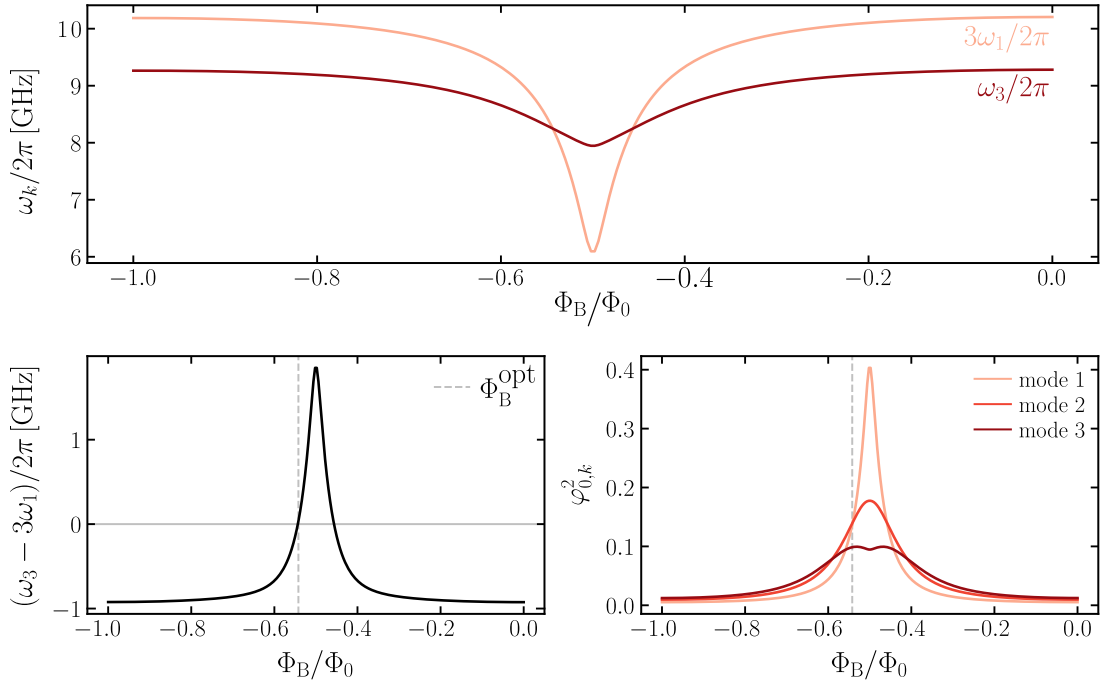

Figure 2.8.: Numerical simulation of the external flux tunability of the system showing the existence of an optimal external flux Φ_B^{opt} where the frequency of the third mode of the system is three times the frequency of the first mode. The parameters used for the simulation are the same as in Figure 2.7. **Top.** The light orange curve represents three times the frequency of the first mode, $3\omega_1/2\pi$ and the red curve represents the frequency of the third mode, $\omega_3/2\pi$. **Bottom left.** Detuning $\Delta^{1\leftrightarrow 3} = \omega_3 - 3\omega_1$ as a function of Φ_B. $\Delta^{1\leftrightarrow 3} = 0$ corresponds to the resonance condition required to observe three-photon conversion and is satisfied for $\Phi_B = \Phi_B^{opt}$, shown as a vertical dashed line. **Lower right.** Zero point fluctuations of mode 1 and 3 as a function of Φ_B.

In order to select the modes that interact together through the photon-conversion process, it is also necessary to fulfil the energy conservation requirement. In the present case of three-photon conversion, we want a three-photon state and a single-photon state

[10]The parameters used for this computation are the one of sample B, presented in Chapter 4.

to be energy degenerate. To achieve this resonance condition, the small junction at the end of the array is implemented by a Superconducting QUantum Interference Device (SQUID) acting as tunable Josephson junction. By passing an external flux Φ_B through the loop formed by the SQUID (see Figure 2.4 in red), the Josephson energy of the impurity can be tuned *in situ*. The flux dependence of E_J is given by

$$E_\mathrm{J}\left(\Phi_\mathrm{B}\right) = E_\mathrm{J}\left(\Phi_\mathrm{B}=0\right)\sqrt{\cos^2\left(\pi\frac{\Phi_\mathrm{B}}{\Phi_0}\right) + d^2\sin^2\left(\pi\frac{\Phi_\mathrm{B}}{\Phi_0}\right)}, \tag{2.24}$$

where d is the asymmetry of the SQUID. Although the SQUID is designed to be symmetric ($d=0$), the finite resolution imposed by electronic beam lithography necesserily leads to a finite asymmetry $d>0$, so that $0 < E_\mathrm{J}\left(\Phi_\mathrm{B}\right) < E_\mathrm{J}\left(\Phi_\mathrm{B}=0\right)$. Tuning E_J is equivalent to changing the right-hand boundary impedance, which results in a change in the mode frequencies. Given the characteristic impedance of the array, $Z_\mathrm{env}/Z_\mathrm{q} < 1$, we expect the small junction to exhibit an inductive (superconducting) behaviour, leading to a decrease in the resonant mode frequencies as E_J is reduced (*i.e* as the external flux Φ_B is swept from 0 to $\Phi_0/2$). The modulation of the eigenfrequencies of the system is a periodic function of Φ_B and the amplitude of the dispersion of mode k, $\Delta\omega_k = \left|\omega_k\left(\Phi_\mathrm{B}=0\right) - \omega_k\left(\Phi_\mathrm{B}=\pi/2\times\Phi_0\right)\right|$, increases with the mode index k. This dispersion of the mode frequencies with Φ_B can be used to satisfy the resonance condition $\omega_\mathrm{if}=0$ in equation (2.20). Figure 2.8 shows the results of the normal mode decomposition as a function of the external magnetic flux Φ_B in the case of a galvanic coupling between the measurement line and the array. In this case, there is a sweet spot in the external flux, $\Phi_\mathrm{B}^\mathrm{opt}$, such that the resonance condition is verified between the first and third mode of the system, $\omega_3 = 3\omega_1$.

2.2.2. Effective two mode Hamiltonian

As emphasised in the previous section, we deliberately design the system so that only two modes interact through three-photon conversion processes. It is therefore convenient to derive an effective Hamiltonian that describes the dynamics of only these two modes. The full system Hamiltonian is written as $\hat{H} = \hat{H}_0 + \hat{H}_\mathrm{nl}$ and the perturbation $\hat{H}_\mathrm{nl}$ couples the eigenstates $|\Psi\rangle = \bigotimes_k |n_k\rangle$ of $\hat{H}_0$. It is convenient to divide the Hilbert space of the system into two subspaces. Given two modes a and b[11] that we are interested in, the subspace under study, $\mathcal{H}_\mathrm{ab}$, is defined as the subspace spanned by all states of the two modes of interest, while all other modes are in vacuum. A basis of this subspace can be formally written as $\{|n_a, n_b\rangle = 1/\sqrt{n_a! n_b!}\hat{a}^{\dagger n_a}\hat{b}^{\dagger n_b}|0\rangle\}$, with $n = n_a + n_b > 0$. The other subspace is the orthogonal complement of $\mathcal{H}_\mathrm{ab}$, denoted $\mathcal{H}_\mathrm{ab}^\perp$, whose basis can be formally written as $\{\bigotimes_k |n_k\rangle \,|\forall(n_1, n_2, ..., n_N) \in \mathbb{N}^N, \sum_{k\neq k_a,k_b} n_k \neq 0\}$.

The effective Hamiltonian $\hat{H}_\mathrm{SW}$ that decouples $\mathcal{H}_\mathrm{ab}$ and $\mathcal{H}_\mathrm{ab}^\perp$ (block diagonal, see equation (2.25)) and reproduces the low energy spectrum of $\hat{H}$ is given by the Schrieffer-Wolff

[11] Since we are now interested in only two modes, we will use the notations $\hat{a} = \hat{a}_{k_a}$ and $\hat{b} = \hat{a}_{k_b}$, where the two modes are indexed k_a and k_b such that $k_b > k_a$.

transformation [Schrieffer and Wolff 1966].

$$\hat{H}_{\rm SW} = \hat{U}_{\rm SW}\hat{H}\hat{U}_{\rm SW}^{\dagger} = \begin{bmatrix} \hat{H}_{\rm ab} & 0 \\ 0 & \hat{H}_{\rm ab}^{\perp} \end{bmatrix} . \tag{2.25}$$

The effective two mode Hamiltonian will be nothing but $\hat{H}_{\rm eff} = \hat{H}_{\rm ab}$ and is given by (at first order) [Bravyi et al. 2011],

$$\hat{H}_{\rm eff} = \hat{P}_{\rm ab}\hat{H}_0 + \hat{P}_{\rm ab}\hat{H}_{\rm nl}\hat{P}_{\rm ab} , \tag{2.26}$$

where we defined the projector on the interesting energy subspace,

$$\hat{P}_{\rm ab} = \sum_i |i\rangle \otimes |0\rangle \langle i| \otimes \langle 0| \quad . \tag{2.27}$$

The details of the calculation of $\hat{H}_{\rm eff}$ are given in appendix A. The final expression for the effective two mode Hamiltonian is given by

$$\hat{H}_{\rm eff} = \hbar\omega_a \hat{a}^{\dagger}\hat{a} + \hbar\omega_b \hat{b}^{\dagger}\hat{b} - E_J^{\rm S}\cos\left(\hat{\varphi}_a + \hat{\varphi}_b\right) - \frac{E_J}{2}\left(\hat{\varphi}_a + \hat{\varphi}_b\right)^2 , \tag{2.28}$$

where we defined the renormalised Josephson energy[12],

$$E_J^{\rm S} = E_{\rm J}\exp\left(-\frac{1}{2}\sum_{k\neq k_a,k_b}\varphi_{0,k}^2\right) , \tag{2.29}$$

and the operators

$$\hat{\varphi}_a = \varphi_{0,a}\left(\hat{a}^{\dagger} + \hat{a}\right) \ , \ \hat{\varphi}_b = \varphi_{0,b}\left(\hat{b}^{\dagger} + \hat{b}\right) . \tag{2.30}$$

Within this model, it is possible to derive the exact decay rate from state $|0_a, 1_b\rangle$ to state $|3_a, 0_b\rangle$ including the full cosine potential. The matrix element coupling the single-photon state of mode b to the three-photon state of mode a is given by (see appendix B for a detailed derivation)

$$-E_{\rm J}^{\rm S}\langle 3_a, 0_b|\cos\left(\hat{\varphi}_a + \hat{\varphi}_b\right)|0_a, 1_b\rangle = E_{\rm J}^{\rm S}e^{-\frac{1}{2}\left(\varphi_{0,a}^2+\varphi_{0,b}^2\right)} \times \frac{\varphi_{0,a}^3\varphi_{0,b}}{\sqrt{6}} , \tag{2.31}$$

where we actually recover $E_{\rm J}^{\star} = E_{\rm J}^{\rm S}e^{-\frac{1}{2}\left(\varphi_{0,a}^2+\varphi_{0,b}^2\right)}$. Equation (2.31) shows that the conversion rate is slightly renormalised with respect to the conversion derived for the $\hat{\varphi}_0^4$ approximation in equation (2.23).

Since we are interested in the coupling between a single-photon state of mode b and a three-photon state of mode a, we further simplify the model by considering only the

[12]Note the difference with the renormalised Josephson energy $E_{\rm J}^{\star}$ given in equation (2.12).

Kerr effect and a three-photon conversion term. The final model Hamiltonian is then given by

$$\begin{aligned}\hat{H}_{\text{eff}} = \omega_a'\hat{a}^\dagger\hat{a} \; &+ \frac{K_a}{2}\hat{a}^\dagger\hat{a}^\dagger\hat{a}\;\hat{a} \; + \omega_b'\hat{b}^\dagger\hat{b} \; + \frac{K_b}{2}\hat{b}^\dagger\hat{b}^\dagger\hat{b}\;\hat{b} \\ &+ K_{ab}\hat{a}^\dagger\hat{a}\;\hat{b}^\dagger\hat{b} \; + g^{1\leftrightarrow 3}\left(\hat{a}^{\dagger 3}\hat{b} + \hat{b}^\dagger\hat{a}^3\right),\end{aligned} \tag{2.32}$$

where $K_{a(b)}$ is the self-Kerr coefficient of mode $a(b)$, K_{ab} is the cross-Kerr interaction between the two modes and $g^{1\leftrightarrow 3}$ is the three-photon coupling strength. All four of these coefficients come from the full cosine term of equation (2.28). ω_a' and ω_b' are the Lamb-shifted frequencies of mode a and b. More specifically, $g^{1\leftrightarrow 3}$ is given by equation (2.31) and $\sqrt{6}g^{1\leftrightarrow 3} = -E_{\text{J}}^{\text{S}}\,\langle 3_a, 0_b|\cos\left(\hat{\varphi}_a + \hat{\varphi}_b\right)|0_a, 1_b\rangle$.

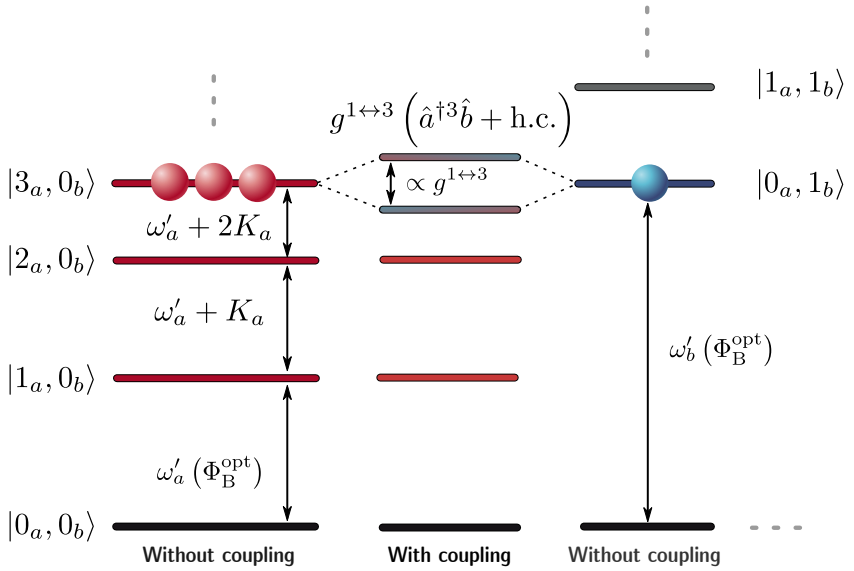

Figure 2.9.: Cartoon representation of the energy landscape of the two-mode effective Hamiltonian (2.32). In the absence of multiphoton coupling ($g^{1\leftrightarrow 3} = 0$), the first three Fock states of mode a are shown in red while the single-photon state of mode b is shown in blue. At $\Phi_{\text{B}} = \Phi_{\text{B}}^{\text{opt}}$, the three-photon state $|3_a, 0_b\rangle$ and the single photon-state $|0_a, 1_b\rangle$ are energy degenerate. The multiphoton coupling $\hat{H}^{1\leftrightarrow 3} = g^{1\leftrightarrow 3}(\hat{a}^{\dagger 3}\hat{b} + \text{h.c.})$ lifts this degeneracy and a splitting appears in the spectrum.

From Hamiltonian (2.32), the resonance condition to be verified in order to observe the three-photon down-conversion between modes a and b is given by

$$\Delta^{1\leftrightarrow 3} = 3\left(\omega_a' + K_a\right) - \omega_b' = 0\,. \tag{2.33}$$

2.3. Detecting the photons: an open quantum system approach

So far we have only considered the isolated system. In reality, each mode of our system is coupled to the outside world via different dissipation channels. Of course, in order to be probed (in reflection), our system is connected to a measurement line at the left boundary of the array, as shown in Figure 2.4. This coupling to the measurement line, characterised by the ***radiative decay rate*** Γ_i^{r} (where i is the mode index) is a controlled decay channel that will be used to probe the physics associated with the three-photon down-conversion process. However, the modes of the system are also coupled to uncontrolled decay channels through which the energy of the system dissipates in unmonitored baths. Examples of uncontrolled decay channels include dielectric losses in the substrate, dielectric losses in the junctions oxide barrier or quasiparticle losses. These losses are collected and characterised by the ***non-radiative decay rate*** Γ_i^{nr}.

2.3.1. Input-output formalism

In this section, we describe the usual input-output formalism [Gardiner and Zoller 2004] used to model driven dissipative quantum circuits [Roy and Devoret 2018]. In this paradigm, a given dissipation channel is modelled by a one-dimensional semi-infinite transmission line. This choice of model is very natural for the coaxial measurement line used to probe the system, since it directly implements a transmission line through which transverse electro-magnetic modes can propagate. However, non-radiative dissipation channels are also modelled by fictitious semi-infinite transmission lines coupled to the system. For the sake of simplicity, only the coupling of mode a to the measurement line is described below. Extension to other modes of the system and to non-radiative decay channels easily follows by adding other baths coupled to the system. The bath α to which mode a is coupled is described by the Hamiltonian of the semi-infinite transmission line with the system localised at $x = 0$ [Leppäkangas et al. 2018],

$$\hat{H}_\alpha = \int_0^\infty \mathrm{d}x \left[\frac{\hat{q}^2}{2c} + \frac{1}{2l}\left(\frac{\partial\hat{\Phi}}{\partial x}\right)^2\right], \tag{2.34}$$

where $\hat{q}(x,t)$ is the charge density field and $\hat{\Phi}(x,t)$ is the flux field in the transmission line. The Heisenberg's equation of motion for $\hat{q}(x,t)$ and $\hat{\Phi}(x,t)$ result in the standard massless Klein-Gordon field equation,

$$\frac{\partial^2\hat{\Phi}}{\partial t^2} = \frac{1}{v_\alpha^2}\frac{\partial^2\hat{\Phi}}{\partial^2 x}\,, \tag{2.35}$$

where $v_\alpha = 1/\sqrt{lc}$ is the velocity of the propagating field. General solutions to this equation are left and right propagating waves,

$$\hat{\Phi}(x,t) = \hat{\Phi}_{\text{in}}(x - v_\alpha t) + \hat{\Phi}_{\text{out}}(x + v_\alpha t)\,, \tag{2.36}$$

where $\hat{\Phi}_{\text{in}}$ is the incident left propagating field and $\hat{\Phi}_{\text{out}}$ is the reflected (or radiated) right propagating field. They can be written formally as follows:

$$\hat{\Phi}_{\text{in}}(x - v_\alpha t) = \sqrt{\frac{Z_\alpha}{2\pi}} \int_0^\infty \mathrm{d}\omega \sqrt{\frac{\hbar}{2\omega}} \left[\hat{\alpha}(\omega) e^{-i\omega(t - x/v_\alpha)} + \text{h.c.}\right]\,, \tag{2.37}$$

$$\hat{\Phi}_{\text{out}}(x + v_\alpha t) = \sqrt{\frac{Z_\alpha}{2\pi}} \int_0^\infty \mathrm{d}\omega \sqrt{\frac{\hbar}{2\omega}} \left[\hat{\alpha}(-\omega) e^{-i\omega(t + x/v_\alpha)} + \text{h.c.}\right]\,, \tag{2.38}$$

where $\alpha(\omega)$ ($\alpha^\dagger(\omega)$) are the bosonic annihilation (creation) operators for photons propagating in the bath[13], and Hamiltonian (2.34) is directly diagonalised [Roy and Devoret 2018],

$$\hat{H}_\alpha = \int_{-\infty}^{+\infty} \mathrm{d}\omega\, \hbar|\omega| \hat{\alpha}^\dagger(\omega)\hat{\alpha}(\omega)\,. \tag{2.39}$$

The coupling between mode a and bath α is modelled by the linear interaction [Gardiner and Zoller 2004]

$$\hat{H}_{\text{int},\alpha} = i\hbar \int_{-\infty}^{+\infty} \mathrm{d}\omega \sqrt{\frac{\Gamma_a^{\text{r}}}{2\pi}} \left(\hat{\alpha}^\dagger(\omega)\hat{a} + \hat{a}^\dagger\hat{\alpha}(\omega)\right)\,, \tag{2.40}$$

where Γ_a^{r} is the Fermi-Golden rule radiative decay rate. Thus, the dissipation of mode a through its coupling to the measurement line is modelled by the total Hamiltonian

$$\hat{H}_\Sigma = \hat{H}_{\text{sys}} + \hat{H}_\alpha + \hat{H}_{\text{int},\alpha}\,. \tag{2.41}$$

The dynamics of mode a is given by the quantum Langevin equation (QLE) [Roy and Devoret 2018],

$$\frac{\mathrm{d}\hat{a}(t)}{\mathrm{d}t} = -\frac{i}{\hbar}\left[\hat{a}(t), \hat{H}_{\text{sys}}\right] - \frac{\Gamma_a^{\text{r}}}{2}\hat{a}(t) + \sqrt{\Gamma_a^{\text{r}}}\hat{\alpha}_{\text{in}}(t)\,, \tag{2.42}$$

where we have defined the input field at $x = 0$ as

$$\hat{\alpha}_{\text{in}}(t) = \int_0^\infty \mathrm{d}\omega \hat{\alpha}(\omega) e^{-i\omega t}\,. \tag{2.43}$$

The output field is defined in the same way, just by replacing $\hat{\alpha}(\omega)$ by $\hat{\alpha}(-\omega)$ and is linked to the input field by the famous input-output relation,

$$\hat{\alpha}_{\text{in}}(t) + \hat{\alpha}_{\text{out}}(t) = \sqrt{\Gamma_a^{\text{r}}}\hat{a}(t)\,. \tag{2.44}$$

[13] The sign in $\hat{\alpha}(\pm\omega)$ in (2.38) refers to the direction of propagation of the considered photon, since $k = \omega/v_\alpha$.

In practice, we will consider different baths to describe the dissipation of individual modes of the system (*i.e.* mode a will be coupled to a given bath α, while mode b will be coupled to another bath β, independent of bath α). Additional baths are also used to model the non-radiative losses of modes a and b.

2.3.2. Toy model of the conversion efficiency

Since the aim of the experiment presented in this thesis is to measure the outgoing flux of the converted photons generated by the multi-photon coupling in equation (2.32), it would be useful to obtain an estimate of the order of magnitude of this outgoing photon flux in order to design the experiment correctly so as to be able to resolve the emitted power.

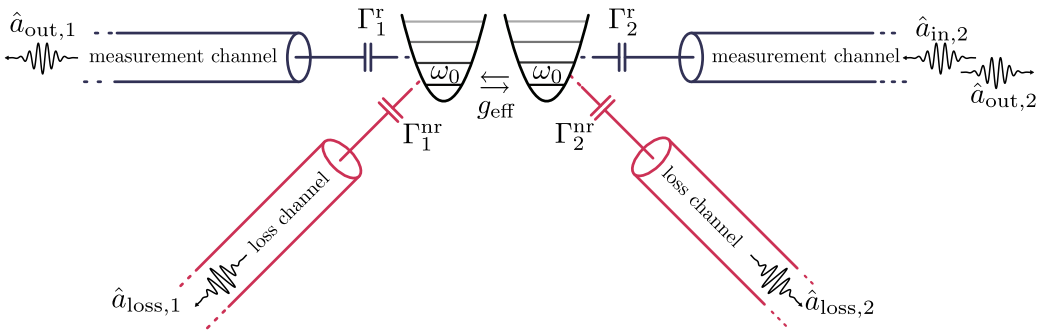

Figure 2.10.: Toy model of the conversion efficiency. Two linearly coupled harmonic oscillators model the two nonlinearly coupled states $|0_a, 1_b\rangle$ and $|3_a, 0_b\rangle$.

To estimate the conversion efficiency, we will use a toy model in which the two coupled states $|0_a, 1_b\rangle$ and $|3_a, 0_b\rangle$ are modelled by two degenerate harmonic oscillators (see Figure 2.10 for a cartoon representation of the toy model) interacting via an effective linear coupling term [Koshino et al. 2022].

$$\frac{\hat{H}_{\text{sys}}}{\hbar} = (\omega_0 + \epsilon)\,\hat{a}_1^\dagger \hat{a}_1 + \omega_0 \hat{a}_2^\dagger \hat{a}_2 + g_{\text{eff}}\left(\hat{a}_1^\dagger \hat{a}_2 + \hat{a}_2^\dagger \hat{a}_1\right), \tag{2.45}$$

where $\omega_0 = \omega_b' = 3\,(\omega_a' + K_a)$ is the frequency of mode b at $\Phi_{\text{B}} = \Phi_{\text{B}}^{\text{opt}}$ (*i.e.* when the states $|0_a, 1_b\rangle$ and $|3_a, 0_b\rangle$ are frequency degenerate), ϵ is the detuning between the modes and $g_{\text{eff}} = g^{1\leftrightarrow 3}\,\langle 3_a, 0_b|\hat{a}^{\dagger 3}\hat{b}|0_a, 1_b\rangle = \sqrt{6}g^{1\leftrightarrow 3}$ is the effective coupling strength. As emphasised earlier, both oscillators are assumed to be coupled to a single measuring channel with which they can exchange energy at a rate Γ_i^{r}, as well as to a loss channel characterised by a decay rate Γ_i^{nr} and modelling the internal losses of the oscillators. To account for the multiphoton nature of the state $|3_a, 0_b\rangle$, the radiative decay rate (non-radiative decay rate) of the oscillator $\hat{a}_1$ is set to $\Gamma_1^{\text{r}} = 3\Gamma_a^{\text{r}}$ ($\Gamma_1^{\text{nr}} = 3\Gamma_a^{\text{nr}}$) [Leppäkangas

et al. 2018][14]. On the other hand, the oscillator $\hat{a}_2$, which models the single-photon state $|0_a, 1_b\rangle$ is directly characterised by the rates $\Gamma_2^{\mathrm{r}} = \Gamma_b^{\mathrm{r}}$ and $\Gamma_2^{\mathrm{nr}} = \Gamma_b^{\mathrm{nr}}$.

We want to estimate the outgoing field $\hat{\alpha}_{\mathrm{out},1}$ when driving mode $\hat{a}_2$ with an incoming field $\hat{\alpha}_{\mathrm{in},2}$. This is done using the input-output formalism introduced earlier. To account for the non-radiative losses of the modes, we have to add an additional unmonitored bath (*i.e.* no incident coherent tone is sent in the corresponding bath and its input field is zero upon averaging). This gives the following equation (2.46) for both oscillators, together with the input-output relation equation (2.44),

$$\frac{\mathrm{d}\hat{a}_i(t)}{\mathrm{d}t} = -\frac{i}{\hbar}\left[\hat{a}_i, \hat{H}_{\mathrm{sys}}\right] - \frac{\Gamma_i^{\mathrm{tot}}}{2}\hat{a}_i(t) + \sqrt{\Gamma_i^{\mathrm{r}}}\hat{\alpha}_{\mathrm{in},i}(t)\,. \tag{2.46}$$

Substituting the expression of $\hat{H}_{\mathrm{sys}}$, equation (2.45), into equation (2.46) and considering the steady-state response, the following system of equations is obtained,

$$0 = \left[i\left(\Delta\omega + \epsilon\right) + \frac{\Gamma_1^{\mathrm{tot}}}{2}\right]\hat{a}_1 + ig_{\mathrm{eff}}\hat{a}_2\,, \tag{2.47}$$

$$\sqrt{\Gamma_2^{\mathrm{r}}}\hat{\alpha}_{\mathrm{in},2} = \left[i\Delta\omega + \frac{\Gamma_2^{\mathrm{tot}}}{2}\right]\hat{a}_2 + ig_{\mathrm{eff}}\hat{a}_1\,, \tag{2.48}$$

$$\hat{\alpha}_{\mathrm{out},1} = \sqrt{\Gamma_1^{\mathrm{r}}}\hat{a}_1\,, \tag{2.49}$$

$$\hat{\alpha}_{\mathrm{out},2} + \hat{\alpha}_{\mathrm{in},2} = \sqrt{\Gamma_2^{\mathrm{r}}}\hat{a}_2\,, \tag{2.50}$$

where we have introduced $\Gamma_i^{\mathrm{tot}} = \Gamma_i^{\mathrm{nr}} + \Gamma_i^{\mathrm{r}}$, the total decay rate of oscillator i. In practice, the input field is a driving coherent tone at frequency ω_{d}, $\hat{\alpha}_{\mathrm{in}}(t) = \alpha_d e^{-i\omega_{\mathrm{d}}t}$, and $\Delta\omega = \omega_0 - \omega_{\mathrm{d}}$ is the detuning of the driving frequency to the transition frequency ω_0. In equation (2.49) we explicitly impose $\langle\hat{\alpha}_{\mathrm{in},1}\rangle = 0$ because in the situation described here the system is only driven around the mode b frequency. The reflection coefficient r_{22} is defined as the ratio of the coherently reflected signal $\hat{\alpha}_{\mathrm{out},2}$ to the input signal $\hat{\alpha}_{\mathrm{in},2}$. It is given by equation (2.51). Figure 2.11 shows colour maps of r_{22} as a function of the drive detuning $\Delta\omega$ and mode detuning ϵ, for a constant value of g_{eff}.

$$r_{22} = \frac{\langle\hat{\alpha}_{\mathrm{out},2}\rangle}{\langle\hat{\alpha}_{\mathrm{in},2}\rangle} = \frac{\Gamma_2^{\mathrm{r}}\left(\frac{\Gamma_1^{\mathrm{tot}}}{2} + i(\Delta\omega + \epsilon)\right)}{\left(\frac{\Gamma_2^{\mathrm{tot}}}{2} + i\Delta\omega\right)\left(\frac{\Gamma_1^{\mathrm{tot}}}{2} + i(\Delta\omega + \epsilon)\right) + g_{\mathrm{eff}}^2} - 1\,. \tag{2.51}$$

To get the conversion rate, we want to compare $\langle\hat{\alpha}_{\mathrm{out},1}^\dagger\hat{\alpha}_{\mathrm{out},1}\rangle$ with $\langle\hat{\alpha}_{\mathrm{in},2}^\dagger\hat{\alpha}_{\mathrm{in},2}\rangle$. Solving for $\hat{\alpha}_{\mathrm{out},1}$ in equation (2.47) to (2.50) readily gives

[14] Since the system is linearly coupled to the measurement line, the decay rate of a Fock state $|n_i\rangle$, as given by the Fermi-Golden rule, is simply $n_i\Gamma_i$, where Γ_i is the decay rate of mode i.

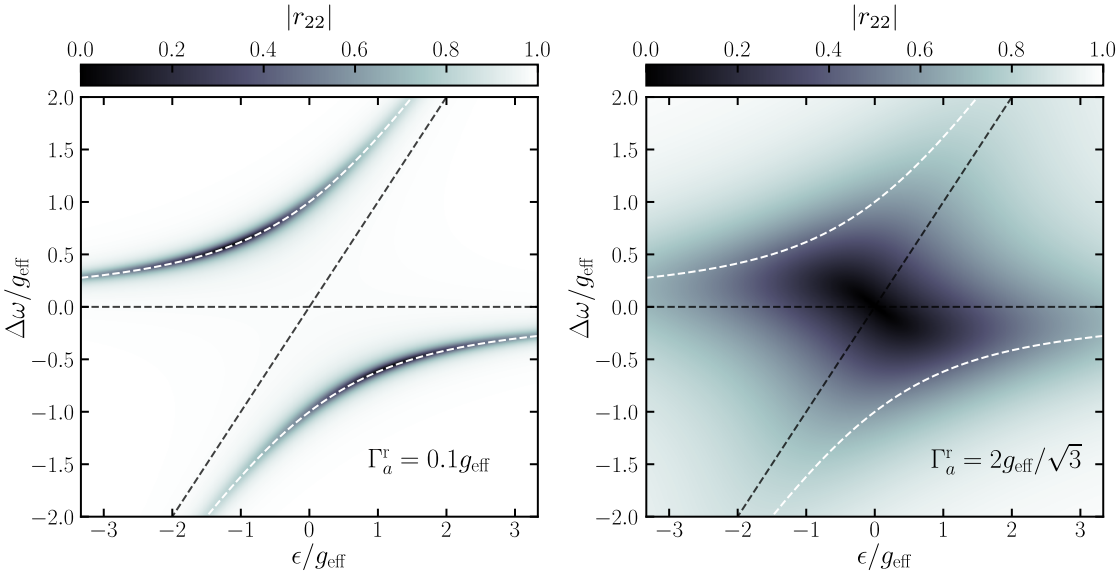

Figure 2.11.: Colour maps of the reflection coefficient r_{22}, given by equation (2.51), as a function of the drive detuning, $\Delta\omega$, and of the mode detuning, ϵ, for a constant value of $g_{\text{eff}}/2\pi = 60\,\text{MHz}$. **Left.** When the radiative decay rate is small compared to the effective coupling strength. **Right.** When the radiative decay rate is optimised to obtain the maximum conversion coefficient T_{21}. In both cases the internal losses are set to zero. The white dashed lines show the eigenvalues of the Hamiltonian (2.45), while the black dashed lines show the eigenvalues of the uncoupled system ($g_{\text{eff}} = 0$) for reference.

$$\left[\left(\frac{\Gamma_1^{\text{tot}}}{2} + i\left(\Delta\omega + \epsilon\right)\right)\left(\frac{\Gamma_2^{\text{tot}}}{2} + i\Delta\omega\right) + g_{\text{eff}}^2\right]\hat{\alpha}_{\text{out},2} = -ig_{\text{eff}}\sqrt{\Gamma_1^{\text{r}}\Gamma_2^{\text{r}}}\hat{\alpha}_{\text{in},2}\,. \tag{2.52}$$

Finally, multiplying the complex conjugate of equation (2.52) allows us to express the output photon flux normalised to the input photon flux. We call this quantity the conversion coefficient, T_{12}, and it is given by

$$T_{12} = \frac{\left\langle \hat{\alpha}_{\text{out},1}^\dagger \hat{\alpha}_{\text{out},1}\right\rangle}{\left\langle \hat{\alpha}_{\text{in},2}^\dagger \hat{\alpha}_{\text{in},2}\right\rangle} = \frac{\Gamma_1^{\text{r}}\Gamma_2^{\text{r}}|g_{\text{eff}}|^2}{\left|\left(\frac{\Gamma_1^{\text{tot}}}{2} + i\Delta\omega\right)\left(\frac{\Gamma_2^{\text{tot}}}{2} + i\left(\Delta\omega + \epsilon\right)\right) + g_{\text{eff}}^2\right|^2}\,. \tag{2.53}$$

For simplicity, let's assume that the two modes have the same radiative decay rates $\Gamma_a^{\text{r}} = \Gamma_b^{\text{r}}$ and no internal losses $\Gamma_a^{\text{nr}} = \Gamma_b^{\text{nr}} = 0$. In this situation, we can distinguish two

limiting scenarios. The first scenario corresponds to the situation where the radiative decay rate is much weaker than the coupling g_{eff}. In this case, the two modes hybridise and one can observe a splitting in the spectrum at $\epsilon = 0$, as shown in the left panel of Figure 2.11. In this situation, the conversion coefficient is maximised for $\Delta\omega = \pm g_{\text{eff}}$, as most of the driving energy is absorbed when the driving tone hits the frequency of one of the two new eigenstates of the system (see the white dashed lines in Figure 2.11). The second scenario corresponds to increasing the radiative decay rate, Γ_a^{r}, to the point where it is of the same order of magnitude as g_{eff}. In this situation, the coherent energy exchange between the two modes is damped by the dissipation coming from the non-negligible coupling to the measurement line and, as observed in the right panel of Figure 2.11, the system absorbs most of the driving energy for $\Delta\omega = 0$. Therefore, in this case, the conversion coefficient is maximised for $\Delta\omega = 0$ and is given by

$$|T_{12}| = \frac{\sqrt{3}\Gamma_a^{\text{r}} g_{\text{eff}}}{3\Gamma_a^{\text{r}2}/4 + g_{\text{eff}}^2}\,, \tag{2.54}$$

giving the criterion $\Gamma_a^{\text{r}} = 2g_{\text{eff}}/\sqrt{3}$ for optimal power transfer between the two modes. Figure 2.12 shows T_{21} as a function of $\Gamma_a^{\text{r}} = \Gamma_b^{\text{r}}$, respectively without ($\Gamma_a^{\text{nr}} = \Gamma_b^{\text{nr}} = 0$, left panel) and with internal losses ($\Gamma_a^{\text{nr}} = \Gamma_b^{\text{nr}} = 0.1 g_{\text{eff}}$). It can be seen that for $\Gamma_a^{\text{r}} \ll g_{\text{eff}}$ (horizontal grey line), the radiated power $P_{\text{out},1} = T_{21} P_{\text{in},2}$ is maximised when the system is driven at $\omega_0 \pm g_{\text{eff}}$, which is the frequency of the hybrid states, and is a significant fraction of the input power. However, when non-radiative decay is included in the model, the situation is slightly different. In the right panel of Figure 2.12 we plot the conversion coefficient again, but this time with a finite value of the non-radiative decay rate, $\Gamma_a^{\text{nr}} = \Gamma_b^{\text{nr}} = 0.1 g_{\text{eff}}$. This value is chosen to match typical internal losses observed in high-impedance waveguides based on Josephson junction arrays. We observe a dramatic decrease in the conversion coefficient at $\Delta\omega = \pm g_{\text{eff}}$ for low coupling to the measurement line. The difference in the conversion coefficient with and without internal losses is essentially the energy lost in the unmonitored dissipation channels that model the non-radiative losses. As can be seen in the right panel of Figure 2.12, the addition of internal losses does not change the condition given by equation (2.54). When $\Gamma_a^{\text{r}} \gg g_{\text{eff}}$, the population of the driven oscillator decays rapidly before any conversion takes place, resulting in a low conversion efficiency. As confirmed by equation (2.54) and Figure 2.12, the optimum conversion efficiency occurs for a coupling to the measurement line of the same order of magnitude as the coupling constant g_{eff}. Therefore, to maximise the power emitted by the three-photon down-conversion process, the system should be designed so that the radiative decay rates of modes a and b are equivalent to the effective coupling strength $\sqrt{6} g^{1\leftrightarrow 3}$.

2.3.3. Quantum model for the fluorescence spectrum

The previous study allowed only a rough estimate of the conversion efficiency between modes a and b. We will now move to a more complete description that allows a quantitative description of the spectrum of converted photons. Given the total Hamiltonian

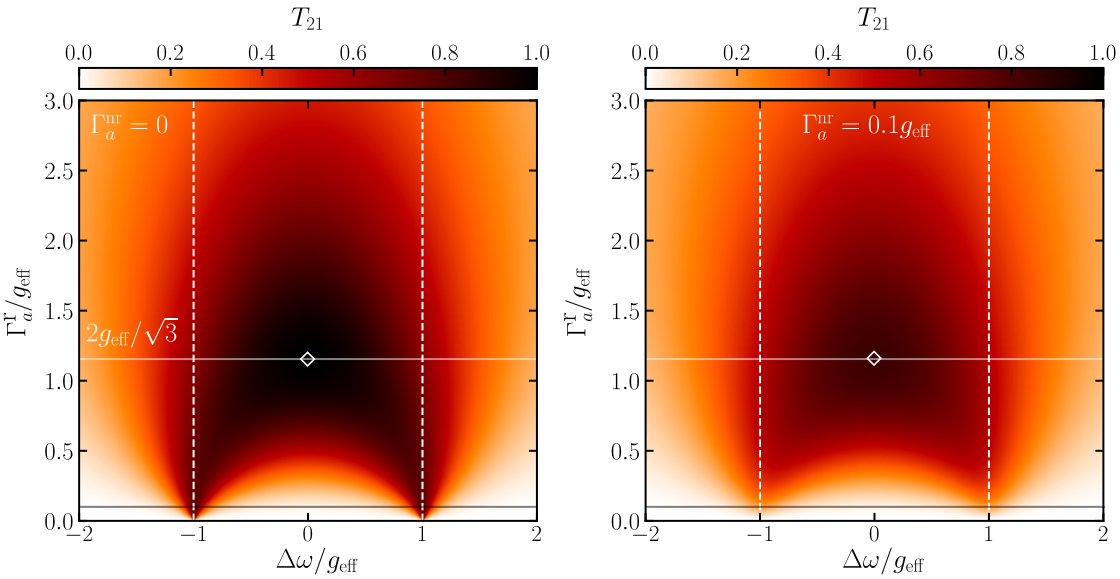

Figure 2.12.: Colour maps of the conversion efficiency, given by equation (2.53), as a function of the drive detuning, $\Delta\omega$, and the radiative losses, $\Gamma_a^{\rm r}$, for a constant value of $g_{\rm eff}/2\pi = 60\,\text{MHz}$. The mode detuning ϵ is set to zero. **Left.** Without internal losses ($\Gamma_a^{\rm nr} = 0$). **Right.** With internal losses ($\Gamma_a^{\rm nr} = 0.1g_{\rm eff}$). In both cases, the conversion coefficient is maximum for $\Delta = 0$ and $\Gamma_a^{\rm r} = 2g_{\rm eff}/\sqrt{3}$ (white diamonds).

$$\hat{H}_\Sigma = \hat{H}_{\rm eff} + \hat{H}_\alpha + \hat{H}_\beta + \hat{H}_{{\rm int},\alpha} + \hat{H}_{{\rm int},\beta}\,, \tag{2.55}$$

where α and β are the radiative baths coupled to modes a and b respectively. For simplicity, we will ignore non-radiative baths for now as it is straightforward to adjust the result to account for these additional loss channels. Modes a and b follow the QLE in equation (2.42), which can be recast into a Lindblad master equation [Gely et al. 2019] such that an operator of the system, $\hat{\mathcal{O}}$, follows the following master equation in the Heisenberg picture,

$$\frac{{\rm d}\hat{\mathcal{O}}}{{\rm d}t} = +\frac{i}{\hbar}\left[\hat{H}_{\rm eff} + \hat{H}_{\rm drive}, \hat{\mathcal{O}}\right] + \Gamma_a^{\rm r}\mathcal{D}[\hat{a}](\hat{\mathcal{O}}) + \Gamma_b^{\rm r}\mathcal{D}[\hat{b}](\hat{\mathcal{O}})\,, \tag{2.56}$$

where $\hat{H}_{\rm drive} = \epsilon_d(e^{-i\omega_{\rm d}t}\hat{b}^\dagger - e^{i\omega_{\rm d}t}\hat{b})$ is an additional term to the Hamiltonian describing the driving of mode b by a coherent tone with frequency $\omega_{\rm d} \sim \omega_b'$, and $\mathcal{D}[\hat{X}](\hat{\mathcal{O}}) = \frac{1}{2}(2\hat{X}^\dagger\hat{\mathcal{O}}\hat{X} - \hat{\mathcal{O}}\hat{X}^\dagger\hat{X} - \hat{X}^\dagger\hat{X}\hat{\mathcal{O}})$ is the usual Lindblad superoperator modelling the dissipation in the baths [Gorini et al. 1978].

To remove the explicit time dependence of the driving term, we move to the rotating frame via the unitary transformation $\hat{U} = e^{i\hat{\mathcal{N}}\omega_{\rm d}t}$, where $\hat{\mathcal{N}}$ is the conserved number of

excitations, defined as

$$\hat{\mathcal{N}} = \frac{1}{3}\hat{a}^\dagger\hat{a} + \hat{b}^\dagger\hat{b} + \int \mathrm{d}\omega \left[\frac{1}{3}\hat{\alpha}^\dagger(\omega)\hat{\alpha}(\omega) + \hat{\beta}^\dagger(\omega)\hat{\beta}(\omega)\right] . \tag{2.57}$$

The wave function $\hat{U}^\dagger |\Psi\rangle$ is the solution of the Schrödinger equation with the transformed Hamiltonian $\hat{\tilde{H}}_\Sigma = \hat{U}^\dagger \hat{H}_\Sigma \hat{U} - i\hat{U}^\dagger(\mathrm{d}\hat{U}/\mathrm{d}t)$. In this framework, the Hamiltonian is then obtained by redefining the two frequencies $\tilde{\omega}_a = \omega'_a - \omega_\mathrm{d}/3$ and $\tilde{\omega}_b = \omega'_b - \omega_\mathrm{d}$ and removing $e^{\pm i\omega_\mathrm{d} t}$ in the driving terms.

The aim of the experiment is to observe three-photon down-conversion in the low power regime. More precisely, we want to excite only the single-photon state of mode b without exciting higher levels. It is therefore legitimate to restrict the Hilbert space to the first two states of mode b, namely $|0_b\rangle$ and $|1_b\rangle$. The three-photon conversion process will then allow the mode a to be populated up to the three-photon state, so that we retain only the first four states of mode a, $|0_a\rangle$, $|1_a\rangle$, $|2_a\rangle$ and $|3_a\rangle$. Given this truncation of the Hilbert space, it is convenient to introduce the operator basis $\hat{\rho}_{n,n'} = |n_a\rangle\langle n'_a|$, which are the transition operators between the different levels of mode a and are such that the average $\langle\hat{\rho}_{n,n'}\rangle = \rho_{n',n}$ is the corresponding element of the Schrödinger picture density matrix. The mode a annihilation operator is then given by

$$\hat{a} = \hat{\rho}_{01} + \sqrt{2}\hat{\rho}_{12} + \sqrt{3}\hat{\rho}_{23} , \tag{2.58}$$

and the Hamiltonian associated with mode a can be written as

$$\hat{H}_a = \tilde{\omega}_a\hat{\rho}_{11} + (2\tilde{\omega}_a + K_a)\,\hat{\rho}_{22} + 3\,(\tilde{\omega}_a + K_a)\,\hat{\rho}_{33} + \sqrt{6}g^{1\leftrightarrow 3}\left(\hat{\rho}_{30}\hat{b} + \hat{b}^\dagger\hat{\rho}_{03}\right) . \tag{2.59}$$

The system of coupled equations corresponding to the Heisenberg master equations (equation (2.56)) for the operators $\hat{\rho}_{n,n'}$ can be written in the matrix form,

$$\frac{\mathrm{d}\,\langle\hat{\rho}_\mu\rangle}{\mathrm{d}t} = \sum_\nu \mathcal{L}_{\mu\nu}\,\langle\hat{\rho}_\nu\rangle \ , \tag{2.60}$$

where $\mu, \nu \in \{01, 12, 23, 20, 31, 30, 00, 11, 22, 33\}$ and $\mathcal{L}$ is a block diagonal matrix:

$$\mathcal{L} = \begin{bmatrix} \mathcal{L}_1 & 0 \\ 0 & \mathcal{L}_2 \end{bmatrix} . \tag{2.61}$$

Since $\mathcal{L}_1$ acts on the sector containing $\hat{\rho}_{01}$, $\hat{\rho}_{12}$ and $\hat{\rho}_{23}$, it is the block that we must consider in order to solve the dynamics of $\hat{a}(t)$. It is given by

$$\mathcal{L}_1 = \begin{bmatrix} -i\tilde{\omega}_{10} - \frac{\Gamma^\mathrm{r}_a}{2} & \sqrt{2}\Gamma^\mathrm{r}_a & 0 & 0 & ig_\mathrm{eff}\langle\hat{b}\rangle \\ 0 & -i\tilde{\omega}_{21} - \frac{3}{2}\Gamma^\mathrm{r}_a & \sqrt{6}\Gamma^\mathrm{r}_a & 0 & 0 \\ 0 & 0 & -i\tilde{\omega}_{32} - \frac{5}{2}\Gamma^\mathrm{r}_a & -i\sqrt{6}g_\mathrm{eff}\langle\hat{b}\rangle & 0 \\ 0 & 0 & -ig_\mathrm{eff}\langle\hat{b}^\dagger\rangle & i\tilde{\omega}_{20} - \Gamma^\mathrm{r}_a & \sqrt{3}\Gamma^\mathrm{r}_a \\ ig_\mathrm{eff}\langle\hat{b}^\dagger\rangle & 0 & 0 & 0 & i\tilde{\omega}_{31} - 2\Gamma^\mathrm{r}_a \end{bmatrix} , \tag{2.62}$$

where $\tilde{\omega}_{10} = \tilde{\omega}_a$, $\tilde{\omega}_{21} = \tilde{\omega}_a + K_a$, $\tilde{\omega}_{32} = \tilde{\omega}_a + 2K_b$, $\tilde{\omega}_{20} = \tilde{\omega}_{21} + \tilde{\omega}_{10}$ and $\tilde{\omega}_{31} = \tilde{\omega}_{32} + \tilde{\omega}_{21}$ are the transition frequencies between the different levels of mode a (as depicted in Figure 2.9) in the rotating frame. We have also used the definition of $g_{\text{eff}} = \sqrt{6} g^{1\leftrightarrow 3}$ given in section 2.3.2. As can be seen from the expression of $\mathcal{L}_1$, the time evolution of $\langle \hat{\rho}_{01} \rangle$, $\langle \hat{\rho}_{12} \rangle$ and $\langle \hat{\rho}_{23} \rangle$ explicitly depends on the time evolution of $\langle \hat{b} \rangle$. Therefore, one must also consider the dynamics of $\langle \hat{b} \rangle$ through

$$\frac{\mathrm{d}\langle \hat{b} \rangle}{\mathrm{d}t} = -i \left(\tilde{\omega}_b + \frac{\Gamma_b^{\mathrm{r}}}{2} \right) \langle \hat{b} \rangle - i g_{\text{eff}} \langle \hat{\rho}_{03} \rangle - i \epsilon_{\mathrm{d}} \,, \tag{2.63}$$

where we have neglected the nonlinearity of mode b as it is assumed to be weakly driven.

The quantity we want to compute is the spectrum of the emitted photons, which is directly proportional to the Fourier transform of the first-order coherence function of the radiated field [Carmichael 1999]. In the rotating frame we have

$$I(\tilde{\omega}) = \int_{-\infty}^{+\infty} \mathrm{d}\tau e^{-i\tilde{\omega}\tau} \left\langle \hat{\alpha}_{\text{out}}^{\dagger}(0) \hat{\alpha}_{\text{out}}(\tau) \right\rangle = \Gamma_a^{\mathrm{r}} \int_{-\infty}^{+\infty} \mathrm{d}\tau e^{-i\tilde{\omega}\tau} \left\langle \hat{a}^{\dagger}(0) \hat{a}(\tau) \right\rangle \,, \tag{2.64}$$

where $\tilde{\omega} = \omega - \omega_{\mathrm{d}}/3$. Using equation (2.58), we can write the first-order coherence function of mode a as

$$\left\langle \hat{a}^{\dagger}(0) \hat{a}(\tau) \right\rangle = \sum_{\mu} a_{\mu} \left\langle \hat{a}^{\dagger} \hat{\rho}_{\mu}(\tau) \right\rangle \,, \tag{2.65}$$

where $\mu \in \{01, 12, 23, 20, 31\}$ and $a_{\mu} = (1, \sqrt{2}, \sqrt{3}, 0, 0)$. The quantum regression formula [Gardiner and Zoller 2004] allows the time-dependent mean $\langle \hat{a}^{\dagger} \hat{\rho}_{\mu}(\tau) \rangle$ to be caluclated. Indeed, $\langle \hat{a}^{\dagger} \hat{\rho}_{\mu}(\tau) \rangle$ follows the same evolution as $\langle \hat{\rho}_{\mu}(\tau) \rangle$ given by equation (2.60) with $\langle \hat{a}^{\dagger} \hat{\rho}_{\mu}(0) \rangle$ as initial condition. The spectrum can then be calculated as follows:

$$\begin{aligned} I(\tilde{\omega}) = \Gamma_a^{\mathrm{r}} \int_0^{\infty} \mathrm{d}\tau e^{-i\tilde{\omega}\tau} \sum_{\mu\nu} a_{\mu} \left(e^{\mathcal{L}_1 \tau} \right)_{\mu\nu} \left\langle \hat{a}^{\dagger} \hat{\rho}_{\mu}(0) \right\rangle \\ = \Gamma_a^{\mathrm{r}} \sum_{\mu\nu} a_{\mu} \left(-i\tilde{\omega} \mathbb{1} - \mathcal{L}_1 \right)^{-1}_{\mu\nu} \left\langle \hat{a}^{\dagger} \hat{\rho}_{\mu}(0) \right\rangle + \text{c.c.} \,, \end{aligned} \tag{2.66}$$

where we used the PT symmetry of the first-order coherence function $G^{(1)}(-\tau) = G^{(1)}(\tau)^*$ and the fact that the Laplace transform of the exponential of the matrix $\mathcal{L}_1$ is given by the resolvent of $\mathcal{L}_1$ at $s = i\omega$. The final step in the calculation of the emission spectrum is the determination of the initial condition $\langle \hat{a}^{\dagger} \hat{\rho}_{\mu}(0) \rangle$, which amounts to determining the stationary solution for $\langle \hat{\rho}_{30} \rangle$, $\langle \hat{\rho}_{11} \rangle$,$\langle \hat{\rho}_{22} \rangle$ and $\langle \hat{\rho}_{33} \rangle$[15]. Details of this calculation are given in appendix C. We obtain the following expression for the spectrum of down-converted photons:

[15] We used the obvious relation $\hat{a}^{\dagger} |n\rangle \langle n'| = \sqrt{n+1} |n+1\rangle \langle n'| = \sqrt{n+1} \hat{\rho}_{n+1,n'}$.

$$I(\tilde{\omega}) = \Gamma_a^{\mathrm{r}} 3|\Xi|^2 \frac{3\left(\frac{3}{2}\Gamma_a - i\tilde{\omega}\right)^2 + i\frac{3}{2}\Gamma_a\left(\tilde{\omega}_{10} - \tilde{\omega}_{21}\right) + \tilde{\omega}_{10}^2 + \tilde{\omega}_{10}\tilde{\omega}_{21} + \tilde{\omega}_{21}^2}{\left[\frac{3}{2}\Gamma_a + i\left(\tilde{\omega}_{21} - \tilde{\omega}\right)\right]\left[\frac{\Gamma_a}{2} + i\left(\tilde{\omega}_{10} - \tilde{\omega}\right)\right]\left[\Gamma_a - i\left(\tilde{\omega}_{20} + \tilde{\omega}\right)\right]} + \text{c.c.}\,, \quad (2.67)$$

where $\Gamma_a = \Gamma_a^{\mathrm{r}} + \Gamma_a^{\mathrm{nr}}$ is the total decay rate, taking into account both radiative and internal losses. We have also introduced

$$\Xi = \frac{i g_{\mathrm{eff}} \epsilon_{\mathrm{d}}}{g_{\mathrm{eff}}^2 + \left(\frac{3}{2}\Gamma_a + i\tilde{\omega}_{30}\right)\left(\frac{\Gamma_b}{2} + i\tilde{\omega}_b\right)}\,, \quad (2.68)$$

which describes the population of the state $|3_a, 0_b\rangle$ by driving mode b and via the conversion process. Here Γ_b is the total decay rate of mode b.

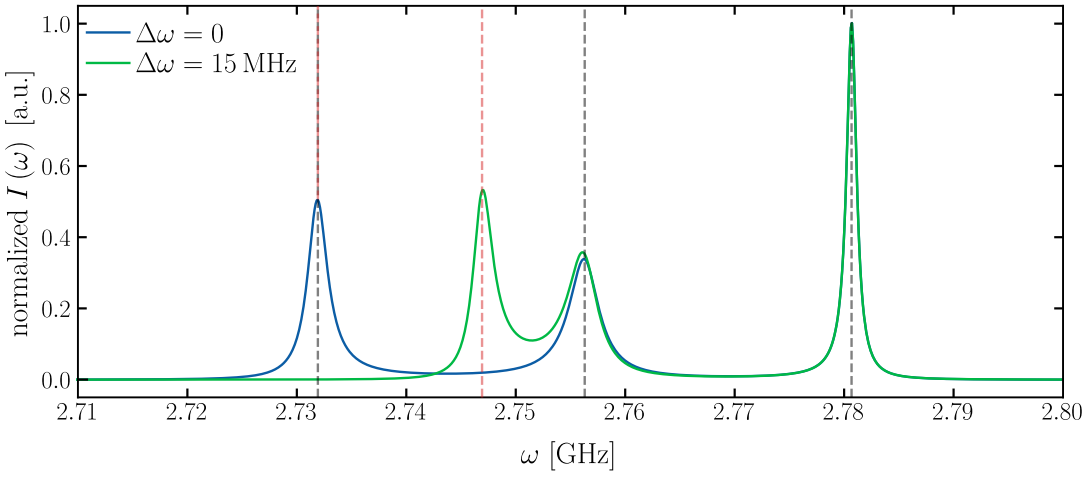

Figure 2.13.: Computed down-conversion spectrum in the laboratory frame for two different values of the detuning of the drive frequency to the transition frequency of mode b, $\Delta\omega = \omega_b - \omega_{\mathrm{d}}$ (corresponding to the two different curves). The grey dashed lines represent the three successive transition frequencies of the mode a energy ladder (shown in Figure 2.9), $\omega_{10} = \omega_a$, $\omega_{21} = \omega_a + K_a$ and $\omega_{32} = \omega_a + 2K_a$. The red dashed line represents the drive frequency dependent emission peak, $\omega = \omega_{\mathrm{d}} - 2\omega_a + K_a$. The parameters used to compute the spectra are: $\Gamma_a^{\mathrm{r}} = \Gamma_b^{\mathrm{r}} = 2\pi \times 1\,\mathrm{MHz}$, $\Gamma_a^{\mathrm{nr}} = \Gamma_b^{\mathrm{nr}} = 2\pi \times 0.1\,\mathrm{MHz}$ and $K_a/2\pi = -25\,\mathrm{MHz}$.

In order to get an understanding of equation (2.67), let's analyse the spectral structure of $I(\tilde{\omega})$. There are three emission peaks, one of which depends on the driving frequency. In the laboratory frame, the frequencies of these peaks are $\omega = \omega_{\mathrm{d}} - 2\omega_a + K_a$, $\omega = \omega_{21} = \omega_a + K_a$ and $\omega = \omega_{10} = \omega_a$. Figure 2.13 shows normalised conversion spectra

in the case where the two states $|3_a, 0_b\rangle$ and $|0_a, 1_b\rangle$ are degenerate (*i.e.* $\Delta^{1\leftrightarrow 3} = 0$) and for different detuning of the drive frequency with respect to ω_b. As can be seen, there is a clear dependence of one of the three emission peaks on the drive frequency. The computation is intentionally done with narrow modes to clearly see the structure of the emission spectrum. Although, as argued in section 2.3.2, such a weak coupling to the measurement line would result in a very low photon flux, it allows to understand the mechanism of three-photon down-conversion fluorescence.

As it is an important feature of the spectrum given by equation (2.67), we will now explain the reason for the presence of a drive frequency dependent emission peak. Sending an incoming tone at a frequency ω_d that is slightly detuned from mode b frequency, ω_b, will drive the $|0_a, 0_b\rangle \to |0_a, 1_b\rangle$ transition to the first excited state of mode b. This transition is a virtual process in the sense that it results from the Hamiltonian dynamics of the wave function, but the system plus measurement line ensemble cannot remain in the final state $|0_a, 1_b\rangle$ of this transition since energy is not conserved $\omega_\mathrm{d} \neq \omega_b$. The single photon in mode b is then converted into three photons in mode a by the three-photon conversion interaction. This transition is again virtual, since the energy of the three photons in mode a still does not match the energy of the incoming photon (it is degenerate to the single photon level of mode b). The $|3_a, 0_b\rangle$ state can then relax to the $|2_a, 0_b\rangle$ state by emitting a photon in the measurement line, which can be detected. Since the detected photon is a real photon, it must obey energy conservation. The incoming photon has an energy ω_d and the latter transition, $|3_a, 0_b\rangle \to |2_a, 0_b\rangle$, gives in the final state energy $\omega_\mathrm{detect} + \omega_{20}$, so that the detected photon must have the energy $\omega_\mathrm{detect} = \omega_\mathrm{d} - \omega_{20}$. This is the drive frequency dependent peak that we recover in equation (2.67). The system then undergoes the two subsequent real transitions, $|2_a, 0_b\rangle \to |1_a, 0_b\rangle$ and $|1_a, 0_b\rangle \to |0_a, 0_b\rangle$, by emitting two photons in the measurement line at frequencies ω_{21} and ω_{10} respectively. This cascaded fluorescence process is summarised in Figure 2.14.

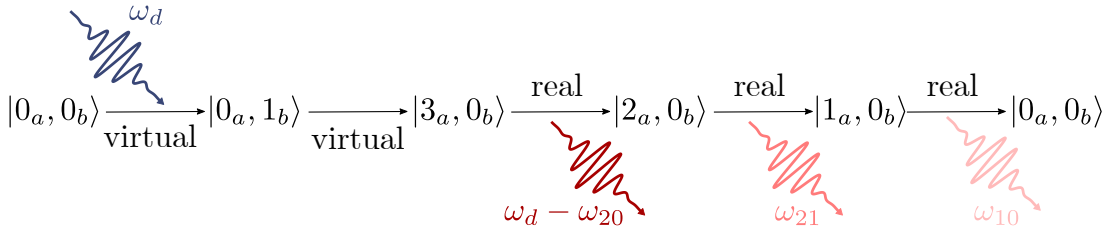

Figure 2.14.: Diagram representing the cascaded fluorescence process converting a single drive photon into three photons. The first two transitions are virtual transitions.

In the next section we will see that taking into account the dephasing of mode a can produce an additional peak in the emission spectrum at a constant frequency of ω_{32}.

2.3.4. Effect of pure dephasing

So far we have only discussed the decoherence of the modes arising from energy relaxation (dissipation) in baths that are linearly coupled to the system. Another source of decoherence is the pure dephasing. In contrast to relaxation, pure dephasing does not involve any energy exchange between the system and the surrounding baths and can be described as the result of the modulation of a system parameter induced by classical noise in a variable coupled to the system [Groszkowski et al. 2018; Ithier et al. 2005; Koch et al. 2007]. Namely, if the transition energy E_{if} depends on the classical variable λ, the dephasing is characterised by the energy susceptibilty $\partial E_{if}/\partial\lambda$.

Since the system studied here is flux tunable thanks to the use of a SQUID, it is highly prone to flux noise, namely classical noise in the applied external flux Φ_B. Figure 2.15 illustrates the effect of flux noise on mode a. Since the derivative of the resonant frequency with respect to Φ_B, $\partial\omega_1/\partial\Phi_\mathrm{B}$, is much larger in the vicinity of $|\Phi_\mathrm{B}| = 0.5\Phi_0$, the system will be much more prone to dephasing for these values of external flux than for lower flux values. Since the optimal point for observing photon conversion, Φ_B^{opt}, lies in this range (see Figure 2.8), this motivates us to take dephasing into account when modelling the three-photon down-conversion fluorescence process. In section 4.2.4 we show experimental evidence for this flux-noise-induced dephasing.

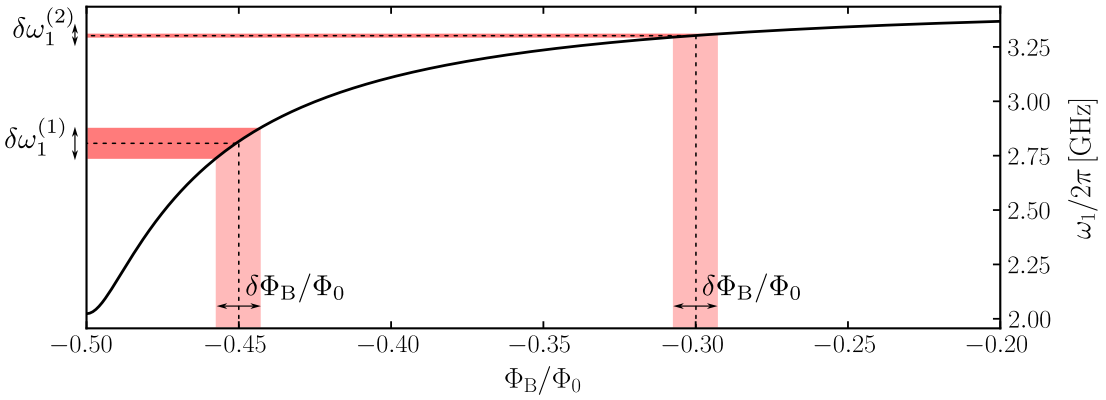

Figure 2.15.: Illustration of flux-noise-induced dephasing on mode a. The system is much more prone to flux noise for external fluxes close to, but not equal to $-0.5\Phi_0$.

Another source of dephasing can actually come from the Kerr nonlinearity of the modes. In fact, the frequency of mode a is modulated by the population of both the mode a (through the self-Kerr effect) and mode b (through the cross-Kerr effect). By rewriting equation (2.32) in normal order, we can easily find that the resonant frequency of mode a becomes

$$\omega_a\left(n_a, n_b\right) = \omega_a' + \frac{K_a}{2}\left(n_a - 1\right) + K_{ab} n_b\,, \tag{2.69}$$

where n_a and n_b are the mean number of photons in mode a and b respectively. Any noise in n_b due to classical noise in the driving field leads to dephasing of mode a by cross-Kerr coupling [Bertet et al. 2005].

Physically, the effect of dephasing on mode a is to allow, through random fluctuations of ω_a, the three-photon state $|3_a, 0_b\rangle$ to have the same energy as the incoming photon (even though, as described in the previous section, the drive frequency is detuned from $\omega_b = \omega_{30}$), so that the second transition shown in Figure 2.14 is now a real transition and not a virtual one. This creates an additional peak whose position is no longer dependent on the drive frequency.

To quantitatively account for this in the derivation of the spectrum of emitted photons, we introduce random fluctuations in the frequency of mode a by adding a term $\xi(t)\hat{a}^\dagger\hat{a}$ to Hamiltonian (2.32), where $\xi(t)$ follows a Gaussian distribution with standard deviation Γ_a^ϕ, the pure dephasing rate. After noise averaging, the master equation (2.60) now reads

$$\frac{\mathrm{d}\langle\hat{\rho}_\mu\rangle}{\mathrm{d}t} = \sum_\nu \left(\mathcal{L} - \frac{\Gamma_a^\phi}{2}\mathcal{D}^{\phi 2}\right)_{\mu\nu} \langle\hat{\rho}_\nu\rangle \ , \tag{2.70}$$

where $\mathcal{D}^\phi_{\mu\nu} = \delta_{\mu\nu}(m-n)$ is the Lindblad superoperator modelling pure dephasing (see derivation in appendix C). The emission spectrum is then calculated using equation (2.66), replacing $\mathcal{L}_1$ by $\mathcal{L}_1 - \Gamma_a^\phi/2\,\mathcal{D}^{\phi 2}$. The final expression is rather tedious and is given in appendix C. Figure 2.16 compares the emission spectrum with and without dephasing for finite detuning of the drive to mode b, confirming the appearance of an extra peak at frequency ω_{32}.

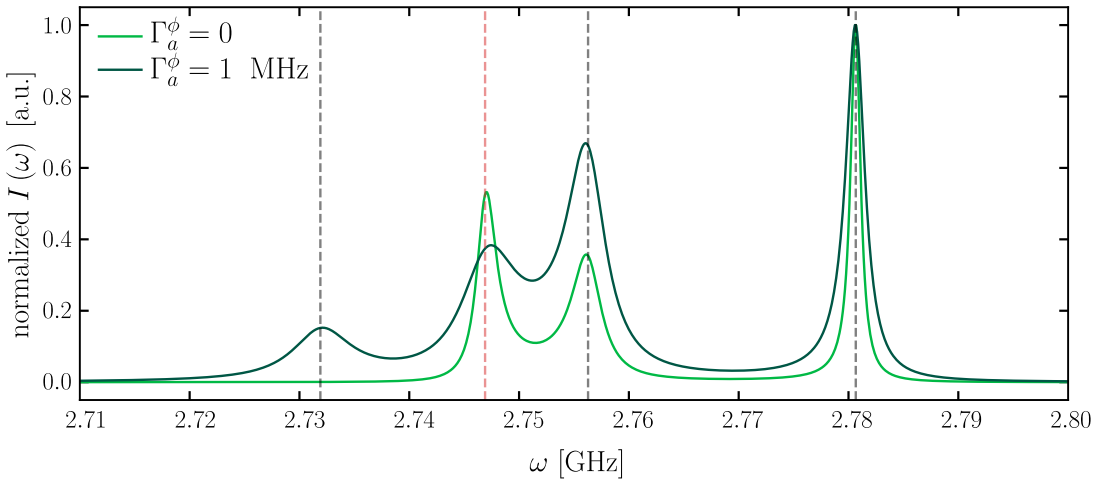

Figure 2.16.: Emission spectrum including mode a dephasing compared to the emission spectrum calculated without dephasing. Both spectra are normalised to the maximum intensity. The pure dephasing rate is set to $\Gamma_a^\phi/2\pi = 1\,\mathrm{MHz}$. The detuning of the drive is set to $\Delta\omega/2\pi = 15\,\mathrm{MHz}$. Dephasing allows an extra emission peak at frequency ω_{32} and the intensity of the drive dependent peak is reduced.

Dans l'attente, au contraire, on ne pense pas seulement à ce qui est actuellement, mais à ce qui pourrait être, à ce qui va peut-être arriver. Nous devenons la proie de nos sentiments, de nos craintes et de nos aspirations. Notre vie actuelle n'est plus seule. Il s'y superpose une vie refusée, une vie possible. Et nous nous demandons si nous avons bien conduit notre vie.

— *Lucien Devies*, récit de la première de la muraille Nord-Ouest de l'Ailefroide Occidentale, 1936

3

Experimental methods

Contents

This chapter is dedicated to the techniques used to fabricate the different samples studied in this work, and to the cryogenic and microwave setup used to perform the measurement presented in the following chapters. In particular, we focus on the state of the art microwave detection hardware essential for the measurement of the spectrum of down-converted photons.

3.1. Nanofabrication

The samples measured in this work were fabricated in the Néel Institute's own clean room, benefiting from the expertise developed over the years by the Superconducting Quantum Circuits group in the fabrication of long and dense arrays of Josephson junctions. While the fabrication techniques used here are described in great detail in the references [Puertas 2018] and [Planat 2020], here we will simply summarise the main fabrication principles and present the detailed fabrication recipe.

3.1.1. Fabrication process

The process used to fabricate the samples studied in this work is based on electron beam lithography and the so-called Bridge Free Fabrication (BFF) technique for the fabrication of Josephson junctions. The BFF technique, first introduced by F. Lecocq as the Controlled Undercut Technique (CUT) [Lecocq et al. 2011], allows the fabrication of Josephson junctions in a single lithography step using two layers of electron-sensitive resists and a double-angle evaporation of aluminuum. Other techniques also allow Josephson junctions to be fabricated in a single lithography step and are known as the Dolan bridge technique [Dolan 2008] and the "Manhattan" technique [Kreikebaum et al. 2020]. In contrast to the BFF technique, the Dolan bridge technique relies on the use of suspended resist bridges, which makes it difficult to clean the surface prior to metal deposition and thus reducing the fabricated junction's quality (see reference [Lecocq 2011] for a detailed comparison between the Dolan and the BFF techniques). On the other hand, the Manhattan technique is not very suitable for the design of complex circuits such as the one considered here.

Bilayer of resist

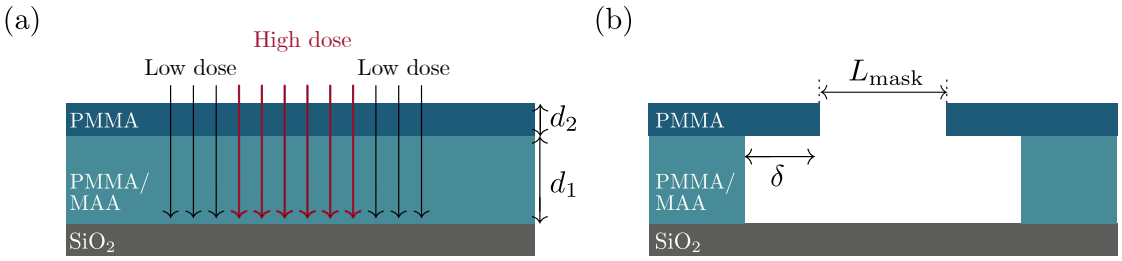

Figure 3.1.: Schematic representation of the mask realisation process. **(a)** Two stacked layers of positive electronic resists are exposed to an electron beam. Two different doses are used to create the desired mask. The top resist layer (thickness d_2) is only sensitive to high doses, while the bottom resist layer (thickness d_1) is sensitive to low doses. **(b)** After development, the exposed parts of the resist stack are removed. Areas exposed at a low dose remove only the bottom layer, while areas exposed at a high dose remove both layers, allowing the formation of the desired undercut δ used in the BFF technique.

Two layers of electronic resist are used to create the mask required to produce the desired structures. After exposure to an electron beam, the resist becomes soluble and can be removed with the appropriate solvent. The first layer of resist is more sensitive to the electron beam than the second, meaning that it will dissolve in the solvent at a lower dose (the dose quantifies the density of charges received by the target and is given by $D = IT/A$, where I is the beam current, T is the exposure time and A is the exposed area). Therefore, by using two different doses during the electronic lithography process,

it is possible to create an undercut in a controlled manner. Note that a native undercut will always be present due to proximity effects caused by electron scattering. Figure 3.1 illustrates the lithography process used to create the desired mask for Josephson junction fabrication and the resulting mask after development (*i.e.* after dissolving the exposed resist in the solvent). The electronic resists used in this work are PMMA/MAA (copolymer) for the first layer and PMMA (polymer) for the second layer with typical thicknesses of $d_1 \sim 750\,\text{nm}$ and $d_2 \sim 200\,\text{nm}$ respectively.

Double angle evaporation

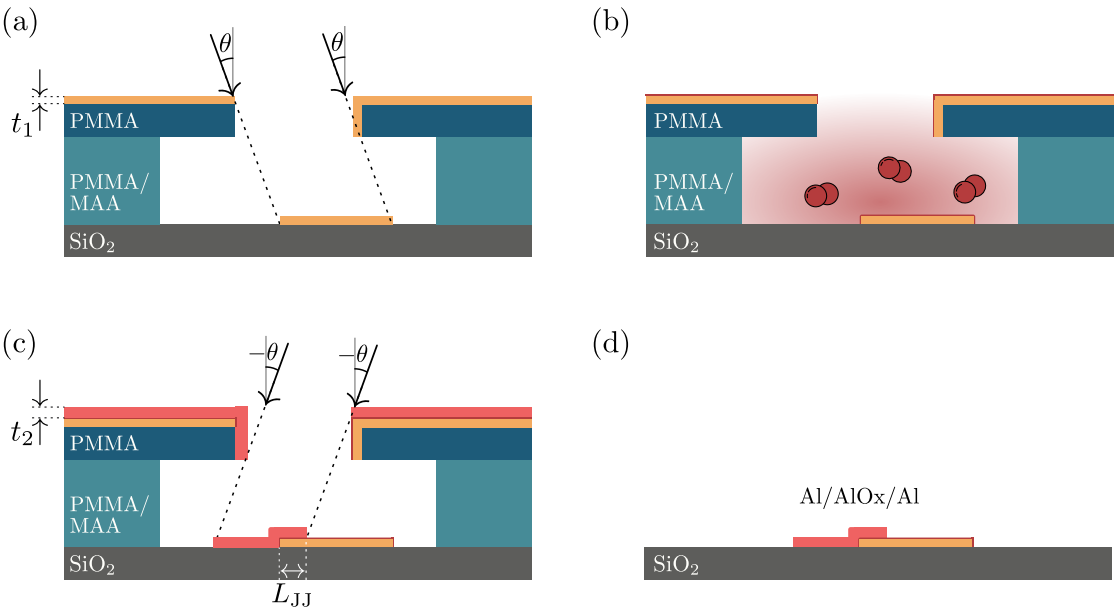

Figure 3.2.: Double angle evaporation process for a Josephson junction. **(a)** A first layer of thickness t_1 of aluminium is evaporated at an angle θ. **(b)** Static oxidation allows the formation of the AlOx barrier. **(c)** A second Al layer of thickness t_2 is evaporated at an angle $-\theta$. **(d)** Lifting off the resist and the metal deposited on it, leaving only the desired structures on the silicon oxide.

By exploiting the ability to create undercuts in the bilayer mask, Josephson junctions can be fabricated in a single lithography step. After developing the mask, the sample is placed in an evaporator and a first layer of aluminium is deposited at an angle θ. Once the desired thickness t_1 is deposited, *in situ* static oxidation is performed in a controlled atmosphere to create the desired aluminium oxide (AlOx) barrier. A second layer of aluminium is then deposited at an angle $-\theta$ to complete the fabrication of the junctions. The remainder of the resist forming the mask and the metal deposited on it are then removed by dissolving the unexposed resist in a strong solvent, leaving only the desired structures. Figure 3.2 shows the double angle evaporation process using the

bridge free mask. The mask shown in Figures 3.1 and 3.2 can be easily adapted to produce the simple wires needed to connect the different junctions (see for example Figure 3.4). The size of the fabricated junction depends on the size of the mask and the various parameters defined in Figure 3.1 and 3.2,

$$L_{\mathrm{JJ}} = L_{\mathrm{mask}} - t_1(1 + \tan\theta) - 2(d_1 + d_2)\tan\theta\,, \tag{3.1}$$

where L_{mask} is the size of the hole in the top resist layer. To properly design the mask for the desired junction size, the thickness of the deposited resist is systematically determined by interferometric measurement. The design of the mask is then directly adapted using equation (3.1).

Different structures

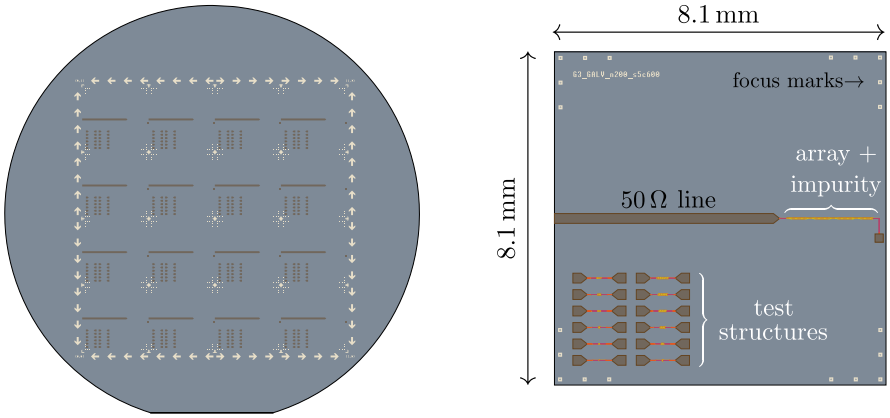

Figure 3.3.: Cartoon representation of the fabricated devices. **Left.** The complete wafer consisting of sixteen samples. The arrows (not to scale) are used to help locate the focusing marks used for the e-beam lithography. **Right.** Detailed patterning of a single chip. The size of the focusing marks is exaggerated for clarity.

During a fabrication run, sixteen samples are fabricated on a two-inch silicon wafer with a 200 nm gold layer deposited on the underside[1] as a back ground plane. Each of the sixteen samples consists of an 8.1 mm × 8.1 mm chip on which the desired structures are written. Figure 3.3 shows the overall structure of a wafer and the detailed structure of a single chip. As a first step in the fabrication process, markers are created on the wafer to enable the correct focusing of the electron beam for the subsequent mask creation. Each chip contains a 50 Ω measurement line, which provides the link between the coaxial cables of the measurement setup and the on-chip system under study. Test structures are also included to characterise the fabricated junctions.

[1]The Au layer is actually preceded with a 15 nm Ti layer for the gold to properly stick.

The most important structure constituting the devices studied here is obviously the Josephson junction. Two different junction designs are used and are presented in Figure 3.4. The first (left panel of Figure 3.4) is suitable for the large junctions forming the array, while the second (right panel of Figure 3.4) is suitable for the small junction of the impurity. Figure 3.4 shows the layout of the doses used to fabricate the junctions as well as SEM images of the resulting structures after evaporation and lift-off.

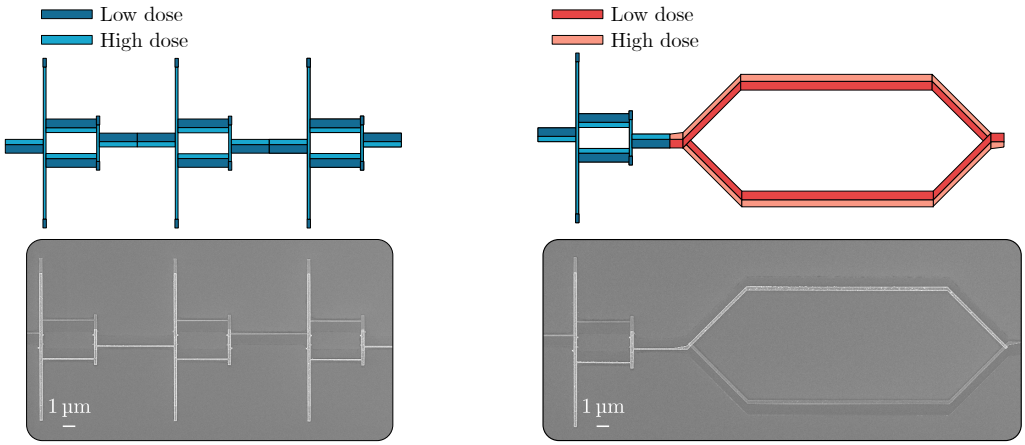

Figure 3.4.: The two different SQUID geometries used in this work. In blue the square SQUIDs used for the array and in red the hexagonal SQUID used for the impurity. The upper raw shows the layout of the different doses used for electron beam lithography. Dark blue (red) corresponds to the low dose layer of the array (small junction) SQUIDs, while light blue (red) corresponds to the high dose layer. The bottom row shows scanning electron microscope images of the fabricated structures after double angle evaporation and lift-off.

3.1.2. Characterisation of the samples

After fabrication of the samples, room temperature DC tests are performed to estimate the parameters of the fabricated junctions. The critical current of a Josephson junction, I_c, is given by the Ambegaokar-Baratoff formula [Ambegaokar and Baratoff 1963]

$$I_c R_n = \frac{\pi \Delta}{2|e|}, \tag{3.2}$$

where R_n is the normal state resistance near the critical temperature, Δ is the gap of the superconductor making up the leads and e is the electron charge. For aluminium, $\Delta/|e| = 210\,\mu V$. Since we only have access to the room temperature resistance, R_n is estimated via $R_n \simeq \alpha_B R_{rt}$ [Claudon 2005]. The room temperature resistance, R_{rt}, is

obtained by performing four probe resistance measurements on test structures. These test structures consist of short chains with a varying number of the element to characterise (typically from three to nine). The resistance of the test chain as a function of the number of elements is fitted and allows the room temperature resistance of a single element, here an array SQUID or the impurity SQUID, to be extracted. Figure 3.5 shows the results of the DC test for the two different types of junctions of the sample studied in chapter 4.

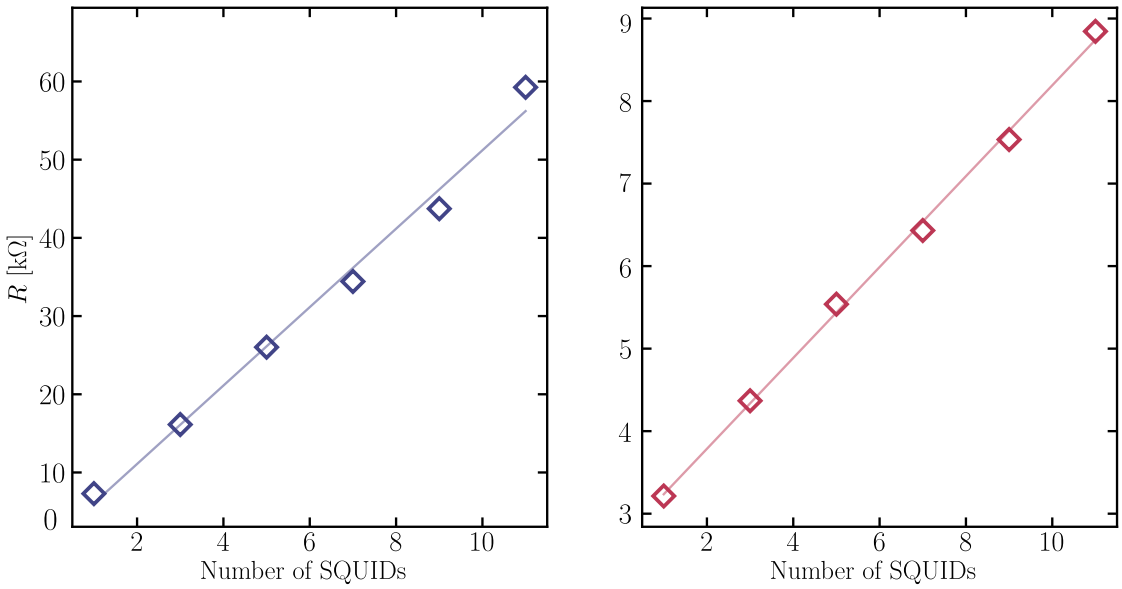

Figure 3.5.: Room temperature resistance measurements on test structures allowing the estimation of the fabricated junctions parameters. **Left.** Characterisation of the small JJ. **Right.** Characterization of the array.

To complete the characterisation of the samples, SEM images are taken in order to estimate the size of the junctions fabricated and the size of the loops forming the SQUIDs. Figure 3.4 shows examples of such images. The self-capacitance of the junctions is estimated via the size of the junctions by the relation

$$C_J = 45\,\mathrm{fF}/\mu\mathrm{m}^2 \times A\,, \tag{3.3}$$

where A is the sum of the sizes of the two junctions that make up the SQUID.

3.2. Experimental setup

Carrying out the experiments presented in this thesis requires a considerable amount of hardware resources, which we would like to present in this section. Given the frequencies of the transitions involved in the system under study (typically between 1 and 20 GHz), the success of the experiment relies heavily on cryogenic techniques and on advanced microwave engineering. While the former makes it possible to reduce the number of thermal excitations in the system to a minimum, the latter is crucial to properly excite and measure the system.

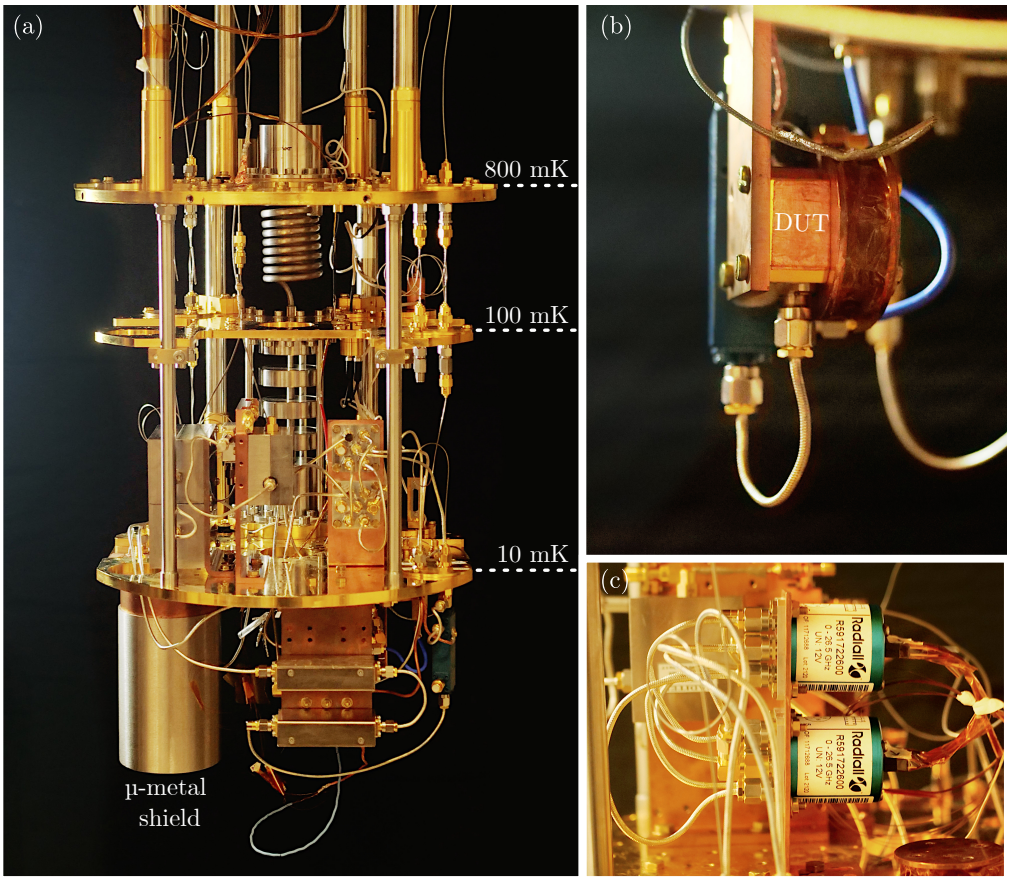

Figure 3.6.: Photographs of the cryogenic experimental set-up. **(a)** General view of the coldest stages of the dilution refrigerator. The sample is placed in the 10 m K stage and is protected from static magnetic fields by a μ-metal shield. **(b)** View inside the μ-metal shield with the sample placed in a copper sample holder and the superconducting coil that allows the biasing of the SQUIDs. The directional coupler used to couple the sample to the input and output lines is also placed inside the shield. **(c)** Zoom on the microwave switches.

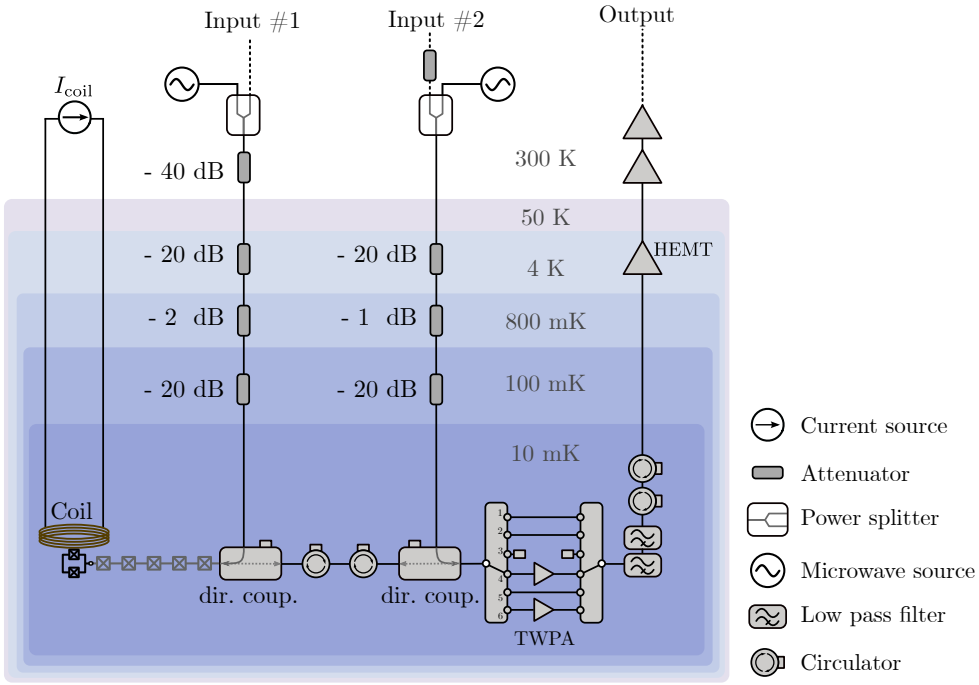

Figure 3.7.: Schematic of the experimental set-up. The sample is put at the lowest temperature stage of a dilution refrigirator. It is probed in reflection via a directional coupler and the input tone can be generated either by a VNA or by a microwave source depending on the nature of the measurement to be performed. The RF tone used to pump the TWPA is generated by a microwave source at room temperature. A DC source sends current to a superconducting coil mounted on top of the sample holder. This coil then generates a magnetic flux through the impurity loop.

The experimental set-up is summarised in Figure 3.7. It consists essentially of three different radio frequency (RF) lines: an input line that drives the sample, a pumping line that triggers parametric processes that allow the amplification of the signal with a travelling wave parametric amplifier (TWPA; see section 3.2.1), and an output line that collects and amplifies the signal to be measured. The sample itself is anchored at the lowest temperature stage of a dilution refrigerator[2] (see Figure 3.6). The main reason for placing the device under test inside a dilution refrigerator is that such equipment allows very low temperatures to be reached, $T \simeq 10\,\mathrm{mK}$, which allows the thermal excitations of the system to be neglected (*i.e.* in the absence of a driving tone, the

[2]All the measurements presented in this manuscript were performed in a BlueFors LD250 cryogen-free dilution refrigeration system.

system can be considered in its ground state). Indeed, the number of thermal excitations at $\omega_0\left(\Phi_\mathrm{B}=0.5\Phi_0\right)/2\pi \gtrsim 1.5\,\mathrm{GHz}$ (which is the lowest resonance frequency we can find in our devices[3]) as given by the Bose-Einstein distribution in equation (2.9), remains much smaller than half a photon, the vacuum fluctuations. The input line allows the system to be excited with a coherent tone. This tone is generated either by a vector network analyser (VNA)[4] in the context of single-tone spectroscopy, or by a microwave source[5] in the context of two-tone spectroscopy and fluorescence measurements. Such instruments operate at room temperature and therefore radiate a considerable amount of noise power towards the sample. This broadband thermal noise can undesirably excite modes of the system. To avoid this problem, we use attenuators along the input line. These attenuators are anchored at different stages of the dilution refrigerator (see Figure 3.7). The role of an attenuator is to dissipate some of the energy of the incoming signal into a bath whose temperature is lower than the equivalent noise temperature of the incoming signal. In turn, part of the incoming signal is transmitted and the effective noise temperature of the transmitted signal is reduced compared to the noise temperature of the incoming signal. The effect of the attenuator is usually described using a beam splitter model [Dassonneville 2019]:

$$\left\langle |a_\mathrm{out}(\omega)|^2 \right\rangle = t\left\langle |a_\mathrm{in}(\omega)|^2 \right\rangle + (1-t)\left\langle |b_\mathrm{in}(\omega)|^2 \right\rangle \tag{3.4}$$

$$\left\langle |b_\mathrm{out}(\omega)|^2 \right\rangle = t\left\langle |b_\mathrm{in}(\omega)|^2 \right\rangle + (1-t)\left\langle |a_\mathrm{in}(\omega)|^2 \right\rangle\,, \tag{3.5}$$

where t is the attenuator transparency. $\left\langle |a_\mathrm{in}(\omega)|^2 \right\rangle/4Z_0 = S_{a,\mathrm{in}}(\omega, T_\mathrm{in})$ is the power spectral density associated with the input noise and is given by the celebrated Johnson-Nyquist formula [Nyquist 1928],

$$S_{a,\mathrm{in}}(\omega, T_\mathrm{in}) = \frac{\hbar\omega}{e^{\hbar\omega/k_\mathrm{B}T_\mathrm{in}}-1} = \hbar\omega n_\mathrm{th}(\omega, T_\mathrm{in})\,, \tag{3.6}$$

where T_in is the equivalent input noise temperature. The power spectral density of the outgoing signal is defined in the same way for a_out with an equivalent output noise temperature T_out. In addition, $\left\langle |b_\mathrm{in}(\omega)|^2 \right\rangle/4Z_0$ represents the noise power spectral density associated with the radiation generated by the thermal bath to which the attenuator is anchored, at a temperature T_att. Finally, $\left\langle |b_\mathrm{out}(\omega)|^2 \right\rangle/4Z_0$ is the power spectral density associated with the noise absorbed by the thermal bath. As the device under test is probed in reflection, the input line is connected at the 10 mK stage to a directional coupler, a four port device that allows the outgoing signal to be separated from the input signal. The input signal is directed to the sample and any reflected or radiated signal is directed to the detection chain. This directional coupler also acts as a (non-reciprocal) attenuator at 10 mK, as only a small part of the signal is transmitted from the input line to the device.

[3] This is considering the worst case scenario of working at $\Phi_\mathrm{B}=0.5\Phi_0$. Most of the measurements were performed for lower external fluxes, then further increasing the transition frequency and reducing the number thermal excitations.

[4] Rohde&Schwarz-ZNB20.

[5] Agilent E8257D PSG Microwave Analog Signal Generator.

3.2.1. The detection chain

The detection chain is at the heart of the experiments carried out in this thesis. Before being recorded, the signal of interest undergoes a series of operations such as amplification, mixing and filtering (both analogue and digital) in order to be recorded by classical electronics. Although essential, these operations are associated with distortions of the signal of interest and a good understanding of the detection chain is necessary to properly analyse the recorded classical signal.

General description

In order for the signal of interest to be measured by the room temperature electronics, it must be amplified. This is done by connecting several amplifiers in series. The first amplifier in the amplification chain can be either a TWPA or a cryogenic amplifier based on a high-electron-mobility transistor (HEMT), depending on the measurements to be made. As shown in Figures 3.6 and 3.7, the experimental setup is equipped with six-way microwave switches[6]. The main use of these switches is to select whether or not to use a TWPA as the first stage of amplification of the signal. This is useful for two reasons. Firstly, it allows the true gain of the TWPA to be measured, taking into account the frequency-dependent dielectric losses. The second reason is also related to the intrinsic losses of the TWPA: due to the values of the resonance frequencies of the a and b modes, the measurements we want to perform cover almost the entire bandwidth of the setup (2.5-12 GHz). However, the performance of the TWPA are greatly reduced in the high frequency range of this band due to the frequency-increasing dielectric losses (see Figure 3.9). Therefore, using the TWPA to perform the mode b single-tone spectroscopy presented in section 4.2 does not significantly improve the measurement time, while adding distortions to the signal that would need to be taken into account to properly characterise the system. For this reason, we decided to bypass the TWPA when performing the mode b spectroscopy (thanks to the through positions of the microwave switches). However, when it comes to measuring the emitted down-converted photons around 3 GHz, the TWPA is an essential component without which the measurements would be much more laborious (see for example the comparison of the measurement of the emitted power with and without TWPA in Figure 4.11). As shown in Figure 3.7, two additional room temperature amplifiers are added. The characteristics of the amplification chain (total gain and equivalent noise temperature) are given by [Friis 1944] (considering the TWPA as the first amplifier)

$$G_{\text{tot}} = G_{\text{twpa}} \times G_{\text{hemt}} \times G_{\text{rt}} \,, \tag{3.7}$$

$$T_{\text{N}} = T_{\text{twpa}} + \frac{T_{\text{hemt}}}{G_{\text{twpa}}} + \frac{T_{\text{rt}}}{G_{\text{twpa}} \times G_{\text{hemt}}} \,. \tag{3.8}$$

Of course, equation (3.8) still holds if the TWPA is bypassed by setting $G_{\text{twpa}} = 1$ and $T_{\text{twpa}} = 0\,\text{K}$. If the gain of the first amplifier in the chain is high enough, the equivalent

[6] Radiall R591722600 coaxial subminiature switches.

noise temperature is dominated by the noise temperature of the first amplifier.

3.2.2. Travelling wave parametric amplification in a nutshell

Because of the drastic impact it had on the ability to obtain the results presented in this manuscript, we will briefly review the working principles of the parametric amplifier used in this work. There is, of course, a flourishing literature on this subject, and we refer the reader to the very complete collection of academic papers on Josephson parametric amplifiers, such as review articles [Aumentado 2020; Fasolo et al. 2020; Esposito et al. 2021], Ph.D thesis [Planat 2020; Ranadive 2022] or many of the journal articles cited in these references.

According to the rules of quantum mechanics, an ideal amplifier adds half a quantum[7] of noise (at a given frequency) to the input of the amplifier. This added noise comes from an additional idler mode, an internal mode of the amplifier, which allows the bosonic commutation relation for the output field to be statisfied. Using the Haus-Caves model of a phase-preserving amplifier,

$$\hat{a}_{\text{out}} = \sqrt{G}\hat{a}_{\text{in}} + \sqrt{G-1}\hat{h}^{\dagger}_{\text{amp}}\,, \tag{3.9}$$

with G the power gain, $\hat{a}_{\text{in}}$ the input field such that $[\hat{a}_{\text{in}}, \hat{a}^{\dagger}_{\text{in}}] = 1$, $\hat{h}_{\text{amp}}$ the idler mode such that $[\hat{h}_{\text{amp}}, \hat{h}^{\dagger}_{\text{amp}}] = 1$, and $\hat{a}_{\text{out}}$ the amplified output, indeed veryfying $[\hat{a}_{\text{out}}, \hat{a}^{\dagger}_{\text{out}}] = 1$. Together with the half photon vacuum noise of the input field (we neglect the input thermal fluctuations since the amplifier is anchored at the 10 mK stage of the refrigerator), the total noise referred to the input of the amplifier is at least one photon. This lower bound is defined as the standard quantum limit (SQL). The aim of using a travelling wave parametric amplifier is to get as close as possible to this SQL of noise added by the amplification chain. An amplifier operating at the SQL is called a quantum limited parametric amplifier, and much effort is being put into building broadband quantum limited amplifiers with high dynamic range[8]. Resonant structures such as Josephson parametric amplifiers (JPAs) are very close to the standard quantum limit, but have a limited amplification bandwidth (typically tenths of MHz [Planat et al. 2019]). Although suitable for single-shot qubit measurements at a single frequency, their lack of bandwidth is detrimental to a microwave quantum optics experiment such as the one performed in this work.

Instead of using resonant structures, the use of 50 Ω matched nonlinear transmission lines (here implemented by a Josephson metamaterial) provides a travelling wave amplification process that allows broadband amplification near the quantum limit. The TWPA used here implements a four-wave mixing process where the signal to be amplified, at frequency ω_s, propagates along the metamaterial and is mixed with a strong pump tone at frequency ω_p. The mixing between the pump tone and the signal amplifies

[7] This holds for phase preserving amplifiers, which is the case of the amplifier used here.

[8] The dynamic range of an amplifier is defined as the range of signal power within which the gain of the amplifier is constant.

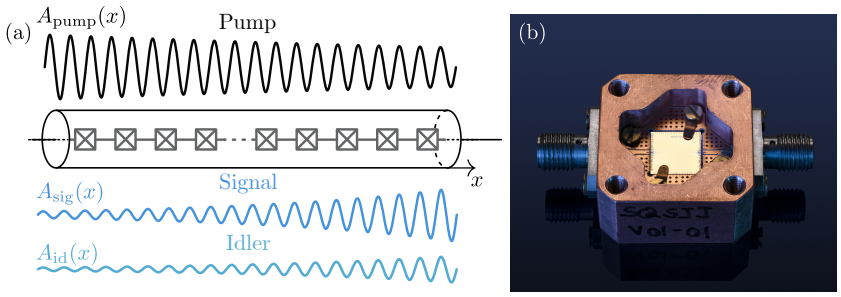

Figure 3.8.: **(a)** Cartoon representation of traveling wave parametric amplification implemented with Josephson metamaterials. The weak signal travels in the metamaterial alongside a strong pump tone. The pump tone provides the necessary energy to amplify the signal through a four-wave mixing process together with the generation of an idler tone. Adapted from [Esposito et al. 2021]. **(b)** Photograph of a typical TWPA enclosed in a copper sample holder.

the signal and produces an additional idler tone at frequency ω_i (see Figure 3.8). The three tones are related by the energy conservation relation $2\omega_p = \omega_s + \omega_i$. Interestingly, the four-wave mixing process that allows the signal to be amplified is similar to the type of photon conversion process introduced in section 2.1.4. The main difference is that in a TWPA this process is a parametric process and requires a strong pump tone to occur. It is a purely classical process where the strong pump tone modulates the inductance of the nonlinear elements composing the metamaterial, providing the energy for the mixing process. The parametric amplifier used in this work was designed and fabricated in-house by Arpit Ranadive as part of his Ph.D work in the Superconducting Quantum Circuits group [Ranadive 2022], using the clean room facilities of the Néel Institute. It is a specific type of TWPA, called reversed-Kerr TWPA (RK-TWPA), based on an array of superconducting nonlinear asymmetric inductive elements (SNAILs). The use of such nonlinear elements makes it possible to suppress the three-wave mixing processes that occurs naturally and that would otherwise spoil the amplifier's performance. This is achieved by threading half a quantum of flux through the loop that forms the SNAILs. This also allows the phase matching condition for the amplification process to take place. The band of amplification can be easily tuned by changing the pump frequency. In fact, in RK-TWPAs, the signal is amplified over a wide band (typically 3 GHz) centred around the pump frequency.

To provide amplification, the TWPA is pumped with an intense monochromatic tone

sent through the dedicated pump line[9]. The pump line is coupled to the TWPA by using a directional coupler. In addition, any back-propagation of the pump tone towards the sample is strongly attenuated by using two isolators placed between the output of the sample's directional coupler and the input of the TWPA's directional coupler. A power combiner at room temperature provides the ability to probe the TWPA transmission with a VNA and is used to calibrate G_{twpa} as explained in section 3.2.4.

3.2.3. Performance and calibration of the TWPA

There are several metrics to consider when using a parametric amplifier. The first metric to look at is obviously the gain of the amplifier. It must be high enough to be able to neglect the added noise of the subsequent amplifiers (see equation (3.8)). For this purpose, it is generally assumed that, given the typical noise temperature of transistor-based cryogenic amplifiers, $T_{\text{hemt}} \simeq 4\,\text{K}$, and assuming that the TWPA operates at the SQL (*i.e* it adds half a photon of noise), G_{twpa} should be greater than 20 dB. However, this cirterion is somewhat strict in the sense that the presence of losses between the radiation source and the TWPA will inevitably increase the system noise referred to the input of the TWPA [Aumentado 2020], thus relaxing slightly the requirement to have G_{twpa} greater than 20 dB. In our setup, these losses are mainly due to the use of directional couplers and isolators between the device and the TWPA (see the Figure 3.12 for an estimate of these losses). Furthermore, considering the TWPA to add half a photon of noise is an idealisation and in reality the amplifier we use operates above the SQL while still dramatically reducing the system noise compared to the sole use of a HEMT amplifier – such a class of amplifiers is usually referred to as *near* quantum limited amplifiers. In practice, the TWPA is tuned to find a comprimise between maximising the gain level in the frequency band of interest and minimising the gain variations within that band. Indeed, to that day, the presence of strong variations in the gain profile of a TWPA (see Figure 3.9, bottom panel) still remains a limitation in the use of such amplifiers, and their reduction is an extensive subject of research. To calibrate the gain of the TWPA, we take advantage of the microwave switches installed in the refrigerator and measure the transmission through the TWPA while the pump tone is sent and compare it to the transmission through the same line when the TWPA is bypassed. In both cases, a VNA is used to measure the transmission between the input of the pump line ("Input #2" in Figure 3.7) and the output of the setup ("Output" in Figure 3.7). A typical gain profile is shown in Figure 3.9 for the same TWPA settings used to measure the spectrum of down-converted photons. The TWPA is pumped at a frequency $\omega_p/2\pi = 4.998\,\text{GHz}$ in order to have maximum gain on a wide band around 3 GHz, which is the frequency range of interest. The upper panel of Figure 3.9 shows the transmission through the TWPA measured with a VNA for different configurations that allow the pure gain of the TWPA to be extracted. The different configurations are as follows:

- TWPA bypassed : the microwave switches are in position 1 and no pump tone is

[9]The pump signal is generated at room temperature using a Rohde&Schwarz SGS100A SGMA RF source.

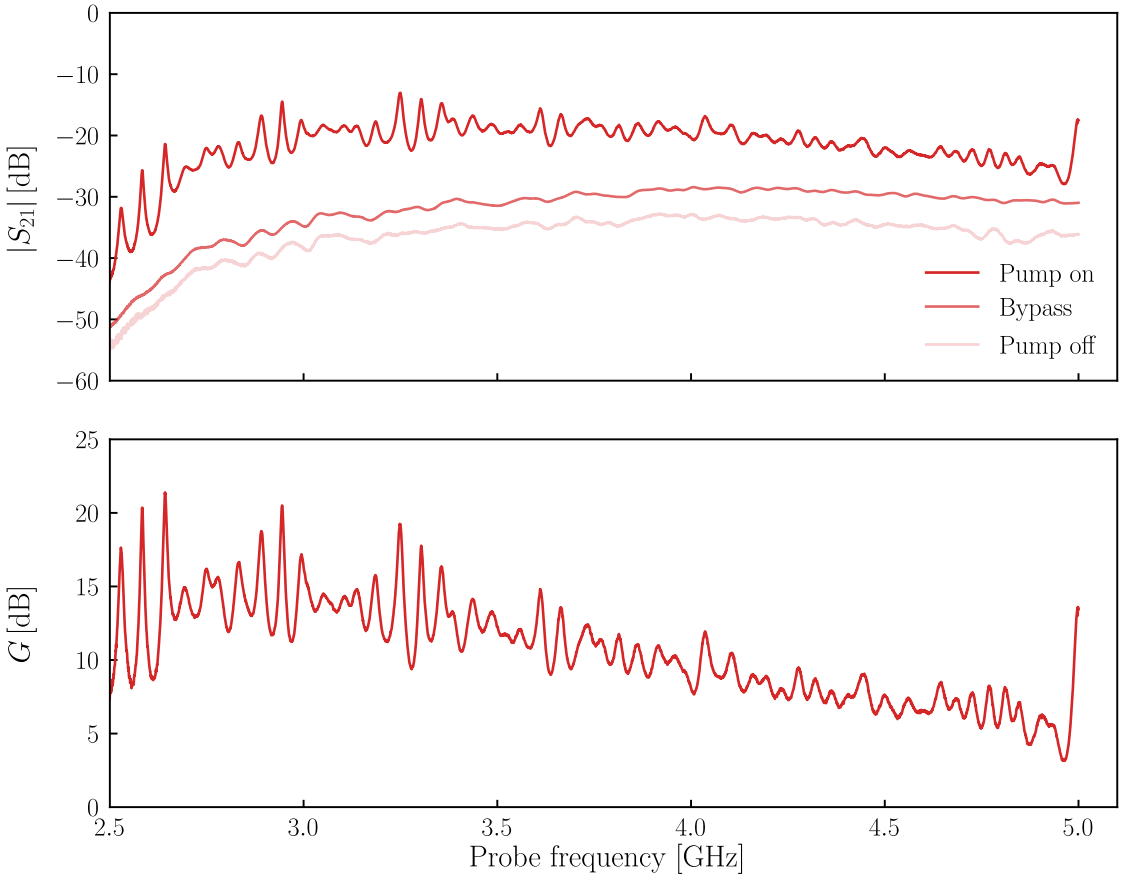

Figure 3.9.: Example of TWPA pure gain measurement. **Top.** Transmission through the setup (between "Input#2" and "Output" of Figure 3.7) for the three different configurations of the amplification chain. In medium red, the TWPA is bypassed. In light red, the TWPA is included as the first amplifier of the output line but no pump is sent to trigger the parametric amplification process (*i.e.* the signal only gets attenuated by the intrinsic losses of the TWPA). In dark red, the TWPA is pumped to trigger the parametric amplification process. The difference between the medium red and the light red curves gives the frequency dependent losses of the TWPA. **Bottom.** Pure gain of the TWPA (*i.e.* the dark red curve minus the medium red curve of the top panel).

sent through the pump line (red curve in Figure 3.9).

- TWPA off : the microwave switches are in position 4 and no pump tone is sent through the pump line (light blue curve in Figure 3.9).

- TWPA on : the microwave switches are in position 4 and the pump tone is sent

through the pump line (dark blue curve in Figure 3.9).

The difference in transmission between the TWPA bypassed position and the TWPA off position readily gives access to the intrinsic losses of the TWPA and it is clear that they increase with frequency. Extending this study to higher frequencies in the measurement setup band reveals losses of almost 11 dB at 9 GHz (not shown here), confirming the limitation of using the TWPA to probe mode b of the system.

Another good proxy for evaluating the performance of the TWPA is the improvement in the signal-to-noise ratio (SNR). The SNR is a commonly used quantity in microwave engineering to assess the ease with which a signal can be detected. It is defined as the ratio of signal power, P_{sig}, to the level of background noise, P_{noise}, and is usually expressed in decibels,

$$\text{SNR} = 10 \log \left(\frac{P_{\text{sig}}}{P_{\text{noise}}} \right) , \tag{3.10}$$

where the background noise level is derived using the Johnson–Nyquist formula (3.6), $P_{\text{noise}} = S_{\text{in}}(\omega, T_{\text{N}})\Delta\omega$, where $\Delta\omega/2\pi$ is the measurement bandwidth. The use of a near quantum limited amplifier allows the system noise T_{N} to be reduced while amplifying both the signal and the noise:

$$\begin{aligned} P_{\text{sig}} &\rightarrow G_{\text{twpa}} \times P_{\text{sig}} , \\ P_{\text{noise}} &\rightarrow G_{\text{twpa}} \times P_{\text{noise}} , \\ T_{\text{N}} &\rightarrow T'_{N} , \end{aligned} \tag{3.11}$$

where $T_{\text{N}} \sim 4\,\text{K}$ is the system noise without TWPA and $T'_{\text{N}} < T_{\text{N}}$ is the system noise when using the TWPA. From equations (3.6), (3.10) and (3.11) one readily sees that the use of a TWPA increases the SNR compared to the use of a HEMT amplfier alone. We characterise the SNR improvement directly by measuring the power transmitted at the output of the measurement setup when sending a signal tone at a given frequency, ω_s, in the pump line. The transmitted power is measured with a spectrum analyser over a given frequency range around the signal frequency. It allows to extract both the signal power P_{sig} and the background noise level P_{noise}. This spectrum is measured for the three different configurations of the amplification chain– TWPA bypassed, on and off. For each of these configurations, the measured power is referred to the input of the amplification chain (*i.e.* the data are normalised by the total gain of the chain, which depends on the configuration). These measurements are performed for both $\omega_s/2\pi = 3\,\text{GHz}$ and $\omega_s/2\pi = 9\,\text{GHz}$ in order to compare the performance of the TWPA at both low and high frequencies. The results of this characterisation are shown in Figure 3.10. The amplification of a signal at 3 GHz (left panel) shows an SNR improvement of approximately 14 dB, clearly demonstrating the benefits of using a TWPA to measure the spectrum of emitted photons around $\omega_a/2\pi \sim 3\,\text{GHz}$. The relatively small SNR improvement at 9 GHz confirms the degradation of the TWPA performance at high frequencies.

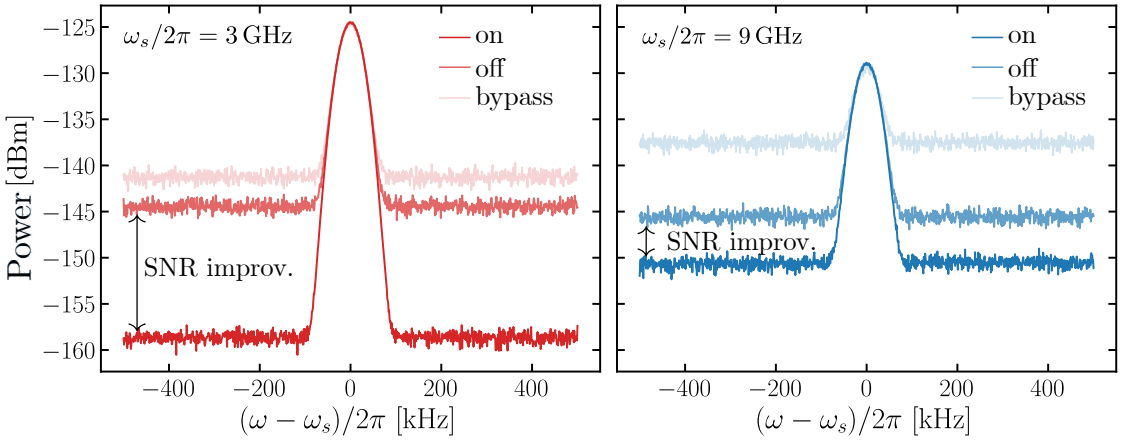

Figure 3.10.: Power spectrum measurement on a band of 1 MHz around a known signal at frequency $\omega_s/2\pi = 3\,\mathrm{GHz}$ (left panel) and $\omega_s/2\pi = 9\,\mathrm{GHz}$ (right panel) The data is taken when the TWPA is bypassed (the HEMT is the first amplification stage), when the signal is amplified by the TWPA (pump on) and when the signal is transmitted through the TWPA without being amplified (pump off). The settings of the TWPA are different when performing the characterisation at 3 GHz and at 9 GHz. Every curve is normalised to the total gain of the amplification chain.

3.2.4. Calibration of the output line

In order to properly quantify the power emitted by the photon conversion process, it is very important to calibrate the gain of the amplification chain. We have already seen how to properly calibrate the gain of the TWPA. The rest of the detection chain (starting from the output of the microwave switches) must also be calibrated. To do this, we install a 50 Ω load on one of the microwave switches (position 3, see Figure 3.7). Since the switches are anchored to the 10 mK stage of the dilution refrigerator, this load will emit thermal radiation whose power spectral density is given by [Clerk et al. 2010]

$$S_{\mathrm{load}}\left(\omega, T_{\mathrm{load}}\right) = \frac{\hbar\omega}{2} \coth\left(\frac{\hbar\omega}{2k_{\mathrm{B}}T_{\mathrm{load}}}\right), \tag{3.12}$$

where T_{load} is the temperature of the load (which in this case is assumed to be the temperature of the mixing chamber of our refrigerator). This broadband thermal noise is amplified by the HEMT and subsequent amplifiers so that the measured power at room temperature is given by

$$P = G(\omega)\left[S_{\mathrm{load}}\left(\omega, T_{\mathrm{load}}\right) + k_{\mathrm{B}}T_{\mathrm{N}}(\omega)\right]\Delta\omega\,, \tag{3.13}$$

where $G(\omega)$ is the gain of the amplification chain starting from the HEMT and $T_{\mathrm{N}}(\omega)$ is the associated noise temperature. Both quantities are frequency dependent, which is the reason why it is important to calibrate the gain of the amplification chain when

analysing the broadband power spectra reported in this work. The spectrum of the

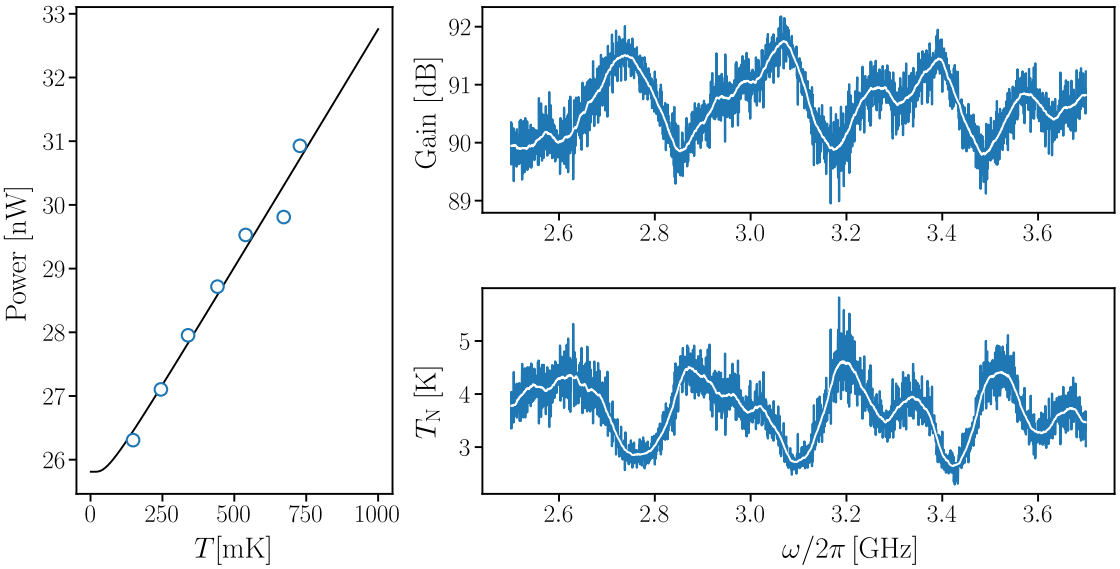

Figure 3.11.: Calibration of the output line with a 50 Ω load. **Left.** Power emitted by the load on a 500 kHz bandwidth around 3.15 GHz as a function of the temperature of the mixing chamber. The black line is a fit of equation (3.13) to the data, which allows the extraction of the gain and noise temperature of the amplification chain at $\omega/2\pi = 3.15$ GHz. **Upper right.** Gain of the amplification chain as a function of frequency. **Lower right.** Noise temperature of the amplification chain as a function of frequency. The white curves correspond to the digital filtering of the corresponding blue data and are used for the calibration of the emission data.

power emitted by the load is measured using a spectrum analyser, and $\Delta\omega/2\pi$ is the bandwidth over which the power is measured around the frequency $\omega/2\pi$. As shown in equations (3.12) and (3.13), heating the load sufficiently (so that the thermal radiation overcomes the noise added by the amplification) will induce noticeable variations in the measured power spectrum. At a given frequency, the gain and the noise temperature can be obtained by measuring the output power for different load temperatures. The mixing chamber of the dilution refrigerator used in this work is equipped with a heater which makes it possible to control the temperature of the coldest stage and thus the temperature of the load anchored to this stage. The power spectrum emitted by the load is recorded with a resolution bandwidth $\Delta\omega/2\pi = 500$ kHz for different temperatures of the mixing chamber and then analysed to extract the spectrally resolved calibration of the gain G and of T_N. The results of this calibration are shown in Figure 3.11 for frequencies ranging between 2.5 GHz and 3.7 GHz, which is the band of interest when measuring the spectrum of down-converted photons.

3.2.5. Losses between the sample and the TWPA

Due to the finite insertion losses of the microwave components used to perform the necessary isolation between the device and the TWPA, the signal of interest is slightly attenuated before it is actually amplified. To properly quantify the radiated power at the output of the sample, this attenuation must be taken into account. This is done by leveraging the presence of two different input lines in the measurement setup, namely the drive line of the sample and the pump line of the TWPA. Since they essentially have the same characteristics (attenuation), it is possible to compare the transmission through the measurement setup when the input tone is sent through the sample line and when it is sent through the pump line. For this calibration, the TWPA is bypassed and the input tone is set out of resonance with any mode of the system by selecting the appropriate external flux Φ_B. The results of this calibration are shown in Figure 3.12

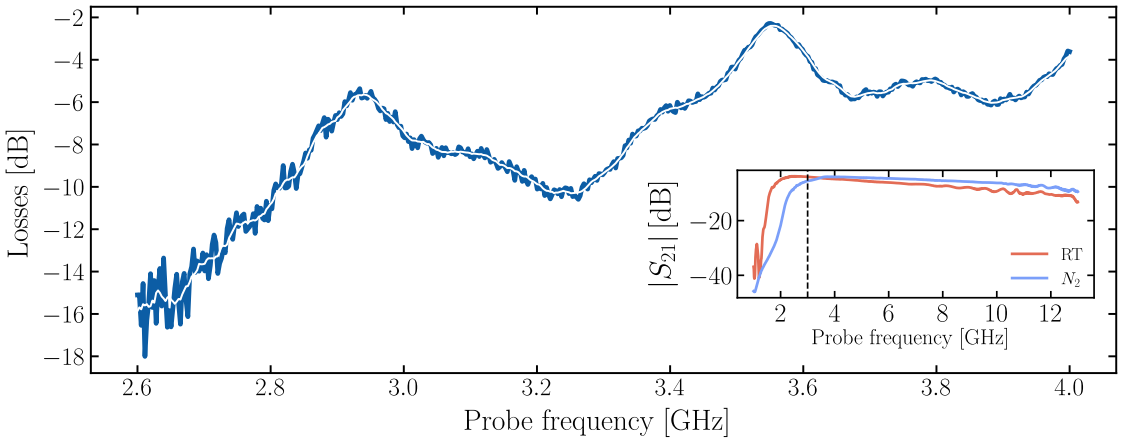

Figure 3.12.: Calibration of the losses occurring between the output of the device under test and the input of the micowave switches. The white line is a smoothed version of the raw data (blue) used to calibrate the fluorescence measurement of section 4.3. The inset shows an example of the characterisation of the isolators used in the measurement setup, showing non-negligible insertion losses at the frequency of interest.

and reveal a drastic attenuation of the output signal before the first amplification stage in the frequency range of interest. This is typically due to the insertion losses in both isolators and directional couplers. Additionally, since the frequency range of interest is at the edge of the bandwidth of the isolators, the insertions losses may be significantly higher than the nominal values given in the data sheets (see the inset of Figure 3.12 for an exemple of the characterisation of an isolator both at room temperature and at the liquid nitrogen temperature of 77 K).

Cette face était si bien préservée des regards indiscrets qu'elle n'avait pas subi l'examen des foules. Telle est bien la raison de notre amour pour ces dernières "terres inconnues" de nos Alpes dauphinoises, où le jugement du touriste n'a pas précédé la conquête du grimpeur.

— *Henry Le Breton*, première de la face Nord de la Pointe du Vallon des Etages, 1935

4

Down-conversion fluorescence

Contents

In this chapter we present the experimental results related to the strong down-conversion regime. Motivated by the arguments presented in chapter 2, section 2.3.2, we have designed a sample strongly coupled to the measurement line, $\Gamma_i^{\mathrm{r}} \gtrsim g_{\mathrm{eff}}$ which provides an optimal conversion efficiency. In this situation, dissipation of the modes of the system is dominated by the coupling to the measurement line, so that the three-photon down-conversion process appears as a dissipation channel for mode b and where the converted photons escape to the measurement line, making it possible to measure the spectrum of the emitted photons.

4.1. Sample presentation and characterisation

4.1.1. Sample characteristics

The sample consists of an array of $N = 200$ junctions galvanically coupled to the measurement line and terminated by a small junction. The junctions of the array are designed to be in the linear regime and the room temperature resistance measurements on test structures (see chapter 3, section 3.1.2) provide the estimation of $E_{\mathrm{J}}^{\mathrm{arr}}/E_{\mathrm{C}}^{\mathrm{arr}} \simeq 284$. The array is actually implemented by asymmetric SQUIDs (see Figure 4.1, light blue) with a large asymmetry d estimated at 0.75, which allows a slow modulation of the array characteristic impedance Z_{env} by means of an external magnetic flux Φ_{B}. At the right boundary, the array is galvanically coupled to the small JJ. The latter is implemented by a nearly symmetric SQUID ($d \sim 0.025$) with bare Josephson energy $E_{\mathrm{J}}(\Phi_{\mathrm{B}} = 0)/h = 27\,\mathrm{GHz}$ together with an intrinsic capacitance $C_{\mathrm{J}} \sim 8.5\,\mathrm{fF}$ leading to $E_{\mathrm{J}}/E_{\mathrm{C}} \sim 3$. Figure 4.1 shows an equivalent circuit diagram of the device and scanning electron microscope (SEM) images of the measured sample. Table 4.2 summarises the estimated circuit parameters of the device under investigation.

	Small JJ	**Chain**
C_j[fF]	8.5	88
C_g[fF]		0.7
E_{J}/h[GHz]	27.2	247.0
E_{C}/h[GHz]	9.1	0.9
$E_{\mathrm{J}}/E_{\mathrm{C}}$	3.0	284.0
Z/Z_{Q}	0.1	0.1
$\omega_{\mathrm{J(P)}}/2\pi$[GHz]	22.3	20.8

Table 4.2.: Characteristics of the junction array and the impurity for the device under investigation.

Due to the impedance mismatch between the measurement line and the array, there is always a finite coupling between the measurement line and the system due to the non-zero reflection at the left-boundary $r = (Z_0 - Z_{\mathrm{env}})/(Z_0 + Z_{\mathrm{env}})$. Using the ABCD matrix technique [Pozar 2011], it can be determined that, given the characteristic impedance of the array Z_{env}, the galvanic coupling to the measurement line is sufficient to satisfy the condition $\Gamma^{\mathrm{nr}} \gtrsim g_{\mathrm{eff}}$. Given the boundary conditions, and approximating the $50\,\Omega$ measurement line by a short to ground[1], wave vectors of the normal modes of the system are given by

[1] This is justified because the impedance of the measurement line, $Z_0 = 50\,\Omega$, is small compared to the characteristic impedance of the array, $Z_c \sim 910\,\Omega$.

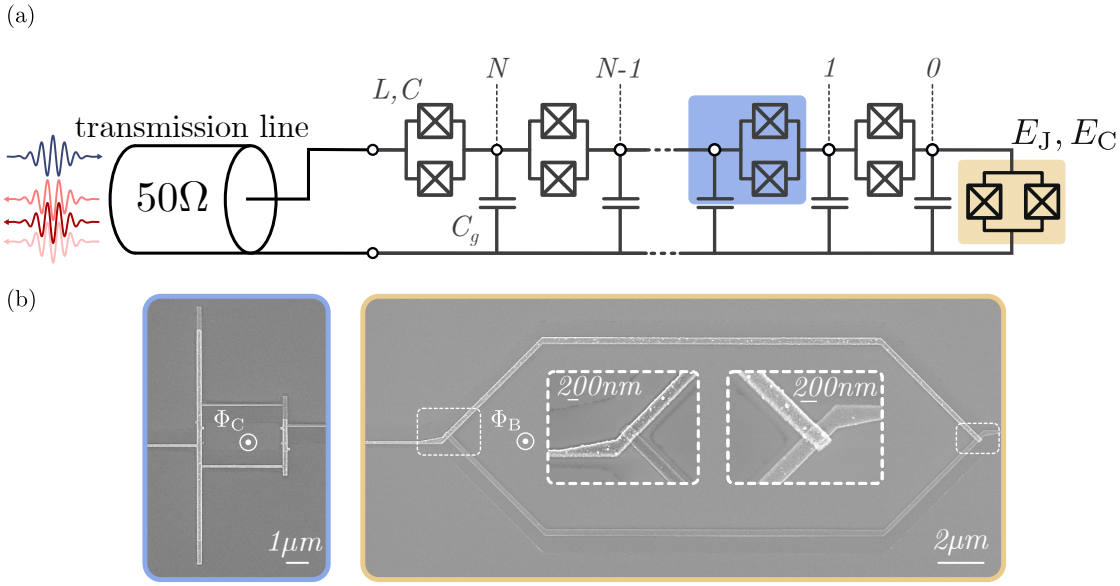

Figure 4.1.: **Top.** Schematic of the measured circuit. The SQUID array, shown in light grey, is characterised by its flux-tunable lumped element inductance $L(\Phi_B)$, capacitance C and ground capacitance C_g. The chain contains $N = 200$ SQUIDs in the linear regime ($E_J/E_C = 284$ at $\Phi_C = \Phi_B/14 = 0$) and is terminated by a nonlinear SQUID ($E_J/E_C \sim 3$ at $\Phi_B = 0$), shown in black and characterised by its flux-tunable Josephson energy $E_J(\Phi_B)$ and capacitance C_J. **Bottom.** SEM images. In the blue outline, image of a single SQUID of the array corresponding to the blue shaded area of the upper panel. In gold contour, image of the nonlinear SQUID corresponding to the gold shaded area of the upper panel.

$$k_n = \frac{(n+1/2)\,\pi}{N-1/2} + \frac{\theta_k}{N-1/2}\,, \tag{4.1}$$

where N is the number of junctions in the array. The first term on the right-hand side of Equation (4.1) is the unperturbed wave vector of a $\lambda/2$ lumped transmission line (ground-ground boundaries), while the second term is the impurity induced phase shift, self-consistently determined by [Léger 2021]

$$\theta_k = \arctan\frac{\lambda_k - 1}{\lambda_k + 1}\sqrt{\left(\frac{4C}{C_g}+1\right)\left(\frac{\omega_p^2}{\omega_k^2}-1\right)}\,, \tag{4.2}$$

$$\lambda_k = 1 + \frac{L}{L_J}\frac{1-\omega_k^2 L_J\,(C_J J + C_g)}{1-\omega_k^2 LC}\,. \tag{4.3}$$

4.1.2. Two-tone spectroscopy

In order to characterise the sample under study, we measure the dispersion relation of the system at $\Phi_B = 0$ using a technique known as two-tone spectroscopy [Weißl et al. 2015]. This technique makes it possible to measure the resonance frequency of modes outside of the measurement bandwidth of the experimental setup by exploiting the cross-Kerr effect. The idea is to probe the system in reflection at a single frequency corresponding to the resonance frequency of a given mode and to drive the system with a second tone of varying frequency. Each time the second tone drives a resonant mode of the system, the resonant frequency of the probe mode gets shifted, resulting in a significant variation in the amplitude and phase of the reflection coefficient. It is the changes in the reflection of the probe tone correlated with the frequency of the second tone that allow the dispersion relation of the system to be extracted. Figure 4.2 shows the result of the two-tone spectroscopy of the sample at $\Phi_B = 0$. The analytical dispersion relation (2.13) (light blue line) is fitted to the data by self-consistently solving for the wave vectors as given by equations (4.1) and (4.3). The array ground capacitance $C_g = 0.73\,\mathrm{fF}$ is estimated from this fitting procedure.

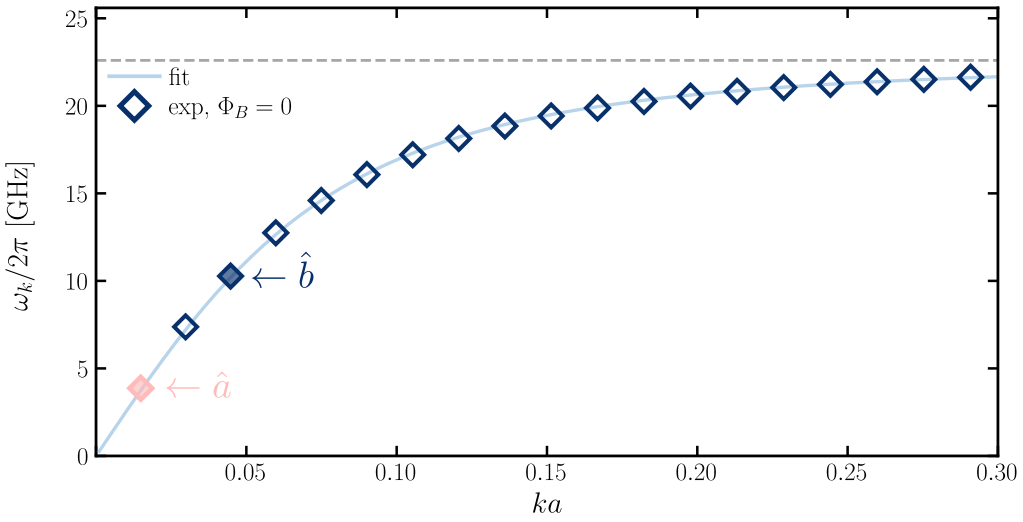

Figure 4.2.: Extraction of the dispersion relation of the sample based on a two-tone spectroscopy measurement at $\Phi_B = 0$. The blue diamonds represent the extracted mode frequencies. The plain blue line is the fitted analytical dispersion relation. The two modes coupled together through the photon conversion process are coloured in red and blue for mode a and b, respectively.

The two modes a and b, which are coupled by the photon conversion term in this sample are the first and third modes of the system, respectively (in red and blue in Figure 4.2).

4.2. Single tone spectroscopy of the conversion process

In order to explore the three-photon conversion process, the system must be tuned by means of the external magnetic flux Φ_B to bring the three-photon state of mode a and the single-photon state of mode b into resonance. This section describes how the resonance condition $\Delta^{1\leftrightarrow 3} = 0$ can be found by performing single-tone spectroscopy of mode b. The results of mode b single-tone spectroscopy will also allow us to discuss qualitatively the effect of the photon conversion process on mode b dissipation.

4.2.1. Single tone spectroscopy in reflection

The system is probed in reflection and the single-tone spectroscopy measurements performed here consist of continuously sending a low power monochromatic microwave tone, $\hat{a}_{\text{in}}$, at a frequency ω_d close to mode b resonance frequency. The coherently reflected signal, $\hat{a}_{\text{out}}$, which carries information about the system, is amplified and recorded for comparison with the input signal. The resulting reflection coefficient is defined by

$$S_{11}(\omega_d) = \frac{\langle \hat{a}_{\text{out}} \rangle}{\langle \hat{a}_{\text{in}} \rangle} \,. \tag{4.4}$$

If mode b is considered as a harmonic mode, the reflection coefficient can easily be calculated via the input-output theory equations (2.42) and (2.44), leading to the well-known formula

$$S_{11}(\omega_d) = \frac{\Gamma_b^{\text{nr}} - \Gamma_b^{\text{r}} + 2i\Delta\omega}{\Gamma_b^{\text{nr}} + \Gamma_b^{\text{r}} - 2i\Delta\omega} \,, \tag{4.5}$$

where $\Delta\omega = \omega_d - \omega_b$. The qualitative behaviour of the reflection coefficient depends on the ratio between the radiative and non-radiative losses of mode b.

- **Overcoupling regime :** when the coupling to the measurement line is the dominant dissipation channel, $\Gamma_b^{\text{r}} \gg \Gamma_b^{\text{nr}}$, most of the signal is reflected on the sample, $|S_{11}(\omega_b)| \leq 1$ and the reflected signal is phase-shifted by 2π with respect to the input signal.
- **Critical coupling regime :** when the non-radiative losses are equal to the coupling to the measurement line, $\Gamma_b^{\text{r}} = \Gamma_b^{\text{nr}}$, the amplitude of the reflected signal vanishes, $|S_{11}(\omega_b)| = 0$ and the reflected signal is phase-shifted by π with respect to the input signal.
- **Undercoupling regime :** when the non-radiative losses are the dominant dissipation channel, the amplitude of the reflection coefficient remains finite and the reflected signal is phase-shifted by a quantity lower than π with respect to the input signal.

These three regimes are illustrated in Figure 4.3 and will be used in the following to qualitatively understand the single-tone spectroscopy data of mode b.

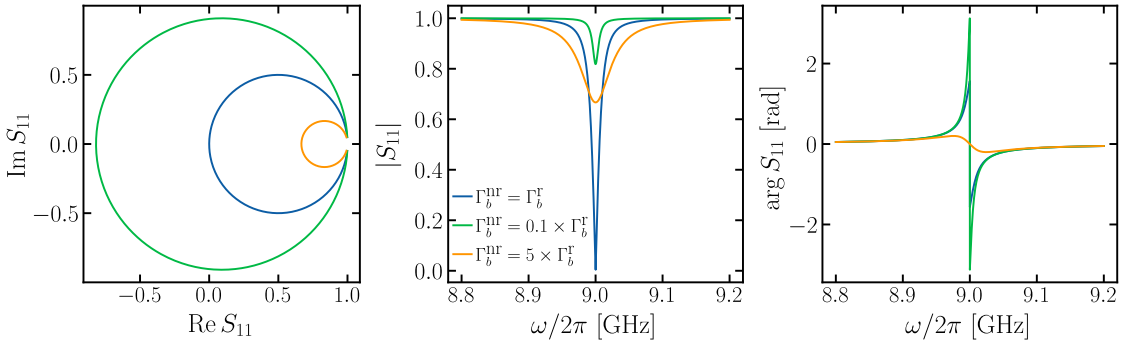

Figure 4.3.: Reflection coefficient for the three coupling regimes of an harmonic mode. **Left.** The reflection coefficient $S_{11}(\omega_d)$ describes a circle in the complex plane, where the $(1, 0)$ point corresponds to the off-resonance points $|\Delta\omega|/\omega_b \gg 1$. **Middle.** Amplitude of the reflection coefficient. **Right.** Phase of the reflection coefficient.

4.2.2. Photon conversion as a loss channel

By performing single-tone spectroscopy in the vicinity of mode b resonant frequency, we can quantitatively extract the internal losses $\Gamma_b^{\rm nr}$ as given by equation (4.5). Figure 4.4 shows an example of a single-tone spectroscopy measurement for $\Phi_{\rm B}$ comprised between $-0.52 \times \Phi_0$ and $-0.23 \times \Phi_0$ where mode b is probed in reflection as its frequency is tuned over a wide frequency range by the magnetic flux $\Phi_{\rm B}$ applied through the small junction SQUID. The left panel shows the two-dimensional map of the magnitude of the reflection coefficient $|S_{11}(\omega_d)|$ as a function of the probe frequency $\omega_{\rm d}$ and magnetic flux $\Phi_{\rm B}$. From this measurement it is clear that $|S_{11}(\omega_d)|$ vanishes for a given range of Φ_B around $-0.44 \times \Phi_0$. The lower right panel of Figure 4.4 shows the trace of $|S_{11}(\omega_d)|$ which presents the maximum absorption at resonance (dark pink, $\Phi_{\rm B} = -0.44 \times \Phi_0$), and another trace arbitrarily far from the latter (light pink, $\Phi_{\rm B} = -0.31 \times \Phi_0$), showing a drastic $\sim -20\,$dB attenuation of the reflected signal at resonance. The observed behaviour can be understood by the following discussion of the different coupling regimes of a resonator introduced in the previous section. To maximise the flux of outgoing converted photons in the measurement line, the sample is designed so that $g^{1\leftrightarrow 3} \sim \Gamma_b^{\rm r} \gg \Gamma_b^{\rm nr}$. In this case, mode b is in the overcoupling regime and at resonance, the driving tone is expected to be almost completely reflected at the input port of the device $|S_{11}(\omega_d = \omega_b)| \lesssim 1$ while experiencing a 2π phase shift. As $\Gamma_b^{\rm nr}$ increases to the point where mode b reaches critical coupling $\Gamma_b^{\rm r} = \Gamma_b^{\rm nr}$, almost all of the input signal is absorbed, resulting in the disappearance of the reflected signal amplitude, $|S_{11}(\omega_d = \omega_b)| \sim 0$. Thus, the decrease in the reflected signal amplitude near $\Phi_B = -0.44 \times \Phi_0$ observed in Figure 4.6 suggests an increase of the internal losses $\Gamma_b^{\rm nr}$ caused by an additional decay channel, which we attribute to the photon conversion process

$$\Gamma_b^{\rm nr} = \Gamma_b^{\rm nr,0} + \Gamma^{1\to 3}\,, \tag{4.6}$$

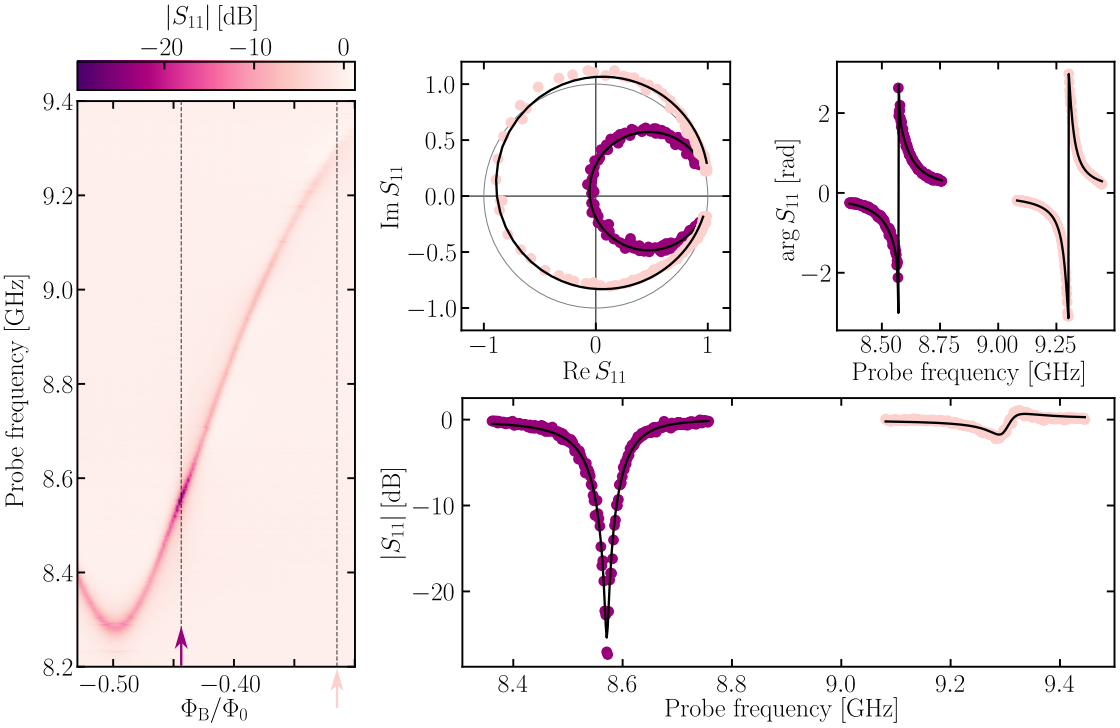

Figure 4.4.: Single tone spectroscopy of mode b. **Left.** Colour map of the amplitude of the reflection coefficient $|S_{11}(\omega_d)|$ as ω_b is tuned with Φ_B. The dark spot around $\Phi_B = -0.44 \times \Phi_0$ indicates a drastic reduction in the amplitude of the reflected signal, suggesting the presence of an additional loss channel associated with photon conversion at $\Phi_B = -0.44\Phi_0$. **Right.** Reflection coefficient for the two vertical cuts displayed in the left panel. Dark pink where the internal losses are maximal, light pink arbitrarily away from this point. Black curves correspond to a fit of the data.

where $\Gamma_b^{\mathrm{nr},0}$ is the non-radiative decay rate when mode b is not subject to any conversion process and $\Gamma^{1\to3}$ is the non-radiative losses associated with the photon conversion process. Although looking at the amplitude of the reflection coefficient gives a first idea of the trend of the internal losses as a function of Φ_B, one must also consider the amplitude of the phase shift at resonance to draw a conclusion. Indeed, a further increase of the non-radiative losses $\Gamma_b^{\mathrm{nr}} > \Gamma_b^{\mathrm{r}}$ leads to an undercoupling of mode b such that $|S_{11}(\omega_d)| \sim 1$ and the signature of the increased losses is no longer visible in the amplitude but in the phase of the reflection coefficient (see Figure 4.3).

To be precise in the determination of the optimal flux Φ_B that results in the highest conversion rate, we proceed to the quantitative extraction of the internal losses of mode b, Γ_b^{nr}, as a function of Φ_B by fitting the one-tone spectroscopy data of Figure 4.4.

The following discussion is based on the method presented in [Rieger et al. 2023], and we refer the reader to this reference for further details and derivations of the method summarised here. To extract Γ_b^{nr}, we employ the circle-fit method [Probst et al. 2015] and account for distortions in the line shape caused by spurious interference processes. Indeed, due to the finite directivity of the directional couplers used in the microwave setup[2], the outgoing reflected signal can interfere with the directly transmitted input signal, leading to Fano interference [Rieger et al. 2023]. The effect of such an interference process is to tilt the circle of normalised data in the complex plane, *i.e.* the center point is no longer on the real axis anymore (*e.g.* compare the left panel of Figure 4.3, where there is no interference, and the right panel of Figure 4.4 where we can clearly see a tilt in the light pink circle, consistent with the asymmetric line shape of the corresponding reflection amplitude). In the absence of interference associated with a background path, the radius of the circle in the complex plane gives direct access to the ratio between the total losses and the radiative losses $\Gamma_b^{\mathrm{tot}}/\Gamma_b^{\mathrm{nr}}$. However, the presence of interference leads to an uncertainty in the extracted decay rates. We take this uncertainty into account in the analysis of the spectroscopy data.

Figure 4.5 shows the extracted non-radiative losses of mode b as a function of Φ_{B} associated with the spectroscopy data of Figure 4.4. The shaded area corresponds to the uncertainty in the extraction of Γ_b^{nr} calculated by taking the minimum value of the isolation $|b| = 16\,\mathrm{dB}$. From this measurement we can clearly see a sharp increase in the internal losses of mode b with a maximum value for $\Phi_{\mathrm{B}} = -0.44 \times \Phi_0$ and an increase of about 30 MHz associated to the down-conversion process.

The above is the main results of the single-tone spectroscopy of mode b. We now discuss other subtle effects that can be observed in Figure 4.5. In addition to the sharp increase in the internal losses, a slow modulation of the non-radiative decay rates can be observed as the external flux is swept. This observation is compatible with the flux noise introduced in section 2.3.4. In the following, we exploit the tunability of the array junctions to give an estimate of the pure dephasing rate of mode b. Since we expect no dephasing at $\Phi_{\mathrm{B}} = 0.5\Phi_0$, the increase in Γ_b^{nr} cannot be explained by pure dephasing alone. At this point, one can invoke the reduced Josephson energy of the small junction, which causes it to enter a highly nonlinear regime, $E_{\mathrm{J}}/E_{\mathrm{C}} \ll 1$, inducing other nonlinear processes such as quantum or thermal phase slips. Since for $\Phi_{\mathrm{B}}/\Phi_0 = 0.5$, the Josephson energy E_{J} is of the same order of magnitude than the thermal fluctuations, $k_{\mathrm{B}}T/h \sim 0.5\,\mathrm{GHz}$, finite temperature effects must be considered in this regime. In addition, a finite temperature can lead to thermally assisted photon conversion processes, where a driving photon can mix with a thermal photon to produce two photons of different frequencies. Using the numerical tools developed in [Sépulcre 2021] for small E_{J}, we can qualitatively reproduce the observed behaviour of the internal losses as a function of Φ_{B} for a finite temperature T.

[2]The directional coupler used in this experiment (Krytar 2-18 GHz) has a directivity greater than $-16\,\mathrm{dB}$, as specified in the specification sheet of the component.

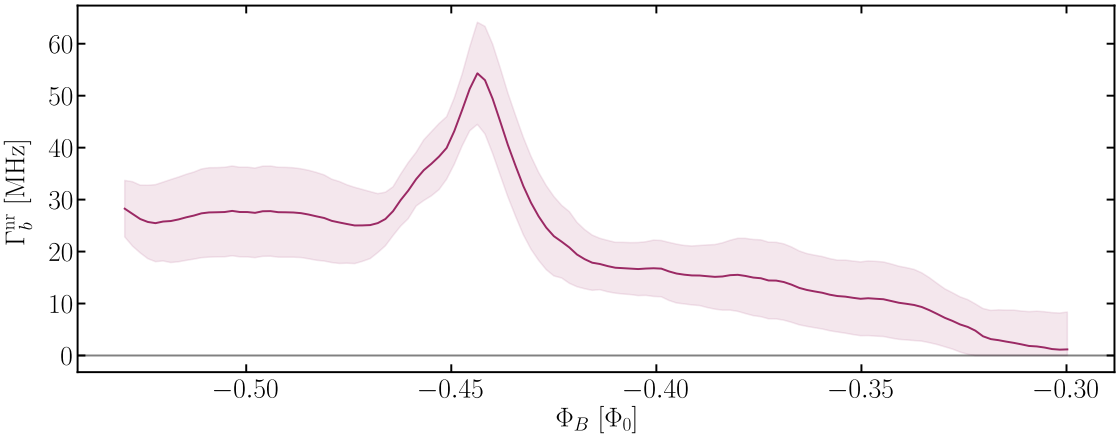

Figure 4.5.: Internal losses of mode b as a function of the external magnetic flux Φ_{B}. The shaded area corresponds to the uncertainty in the extraction of Φ_{B} due to interferences between the outgoing reflected signal and spurious background paths.

4.2.3. Different impedances of the array

So far we have only used the tunability of the small junction for a fixed value of chain impedance. The system can also be tuned using another control, namely changing the inductance of the array by applying an external magnetic flux through the SQUIDs that make up the array. The external magnetic flux used to tune the junctions of the array is actually the same as that used to tune E_{J} of the small junction. The tuning of the two types of junctions is made essentially independant by choosing a small junction loop that is about fourteen times larger than the loop of the junctions of the array (see Figure 4.1), so that the flux threading the SQUIDs of the array is $\Phi_{\mathrm{C}} = \Phi_{\mathrm{B}}/14$. Figure 4.6 shows the single-tone spectroscopy of mode b for a large span of magnetic flux applied through the small junction, revealing two distinct modulation periods associated with the modulation of both the impurity junction (short periodicity) and the junctions of the array (long periodicity). Tuning the inline inductance of the array makes it possible to change its characteristic impedance $Z_{\mathrm{env}}(\Phi_{\mathrm{C}}) = \sqrt{L(\Phi_{\mathrm{C}})/C_{\mathrm{g}}}$. It also changes the speed at which waves travel back and forth in the array, resulting in a change in the resonant frequencies of the standing waves. Thus, tuning Φ_{C} changes the optimal flux that must be passed through the small junction, $\Phi_{\mathrm{B}}^{\mathrm{opt}}$, to achieve the resonance condition $\Delta^{1\leftrightarrow 3} = 0$. As a result, the mode b frequency at which conversion is observed is also changed (see right panel of Figure 4.7), and the same applies to the mode a frequency at which photons are emitted.

Figure 4.7 shows the extracted internal losses of mode b for different periods of the

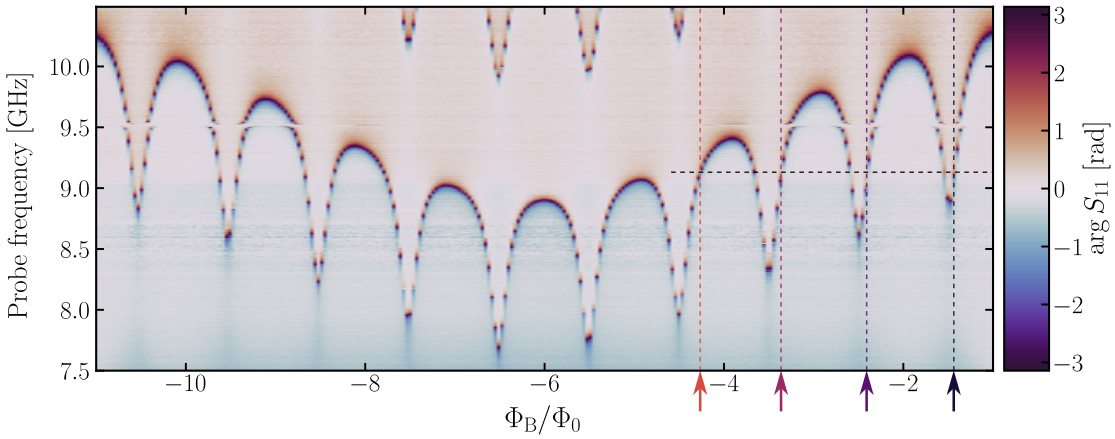

Figure 4.6.: Single-tone spectroscopy of mode b for Φ_B varying between $-11 \times \Phi_0$ and $-\Phi_0$ clearly revealing two periods of modulation corresponding to the two type of SQUIDs, those of the array and the one of the small junction. The coupling of mode b to a parasitic mode around 9.5 GHz can be observed. The vertical dashed line represents the flux point used to study the internal losses as a function of Φ_B at a fixed value of $\omega_b/2\pi$ (see section 2.3.4). The dark blue arrow corresponds to the external flux point for which the converted photons are measured in 4.3.

Φ_B modulation[3] (corresponding to a given array impedance[4]). For better visibility of the data, Φ_B is reduced to the $[-\Phi_0, 0]$ interval and the data associated with different arches are offset.

For each arch we observe a sharp increase in the non-radiative losses up to 70 MHz above the base level (second curve from the top). The losses induced by down-conversion thus greatly exceed other sources of non-radiative decay, $\Gamma^{1\leftrightarrow 3} \gtrsim \Gamma_b^{\mathrm{nr},0}$, so that the system can be considered to be in a **strong down-conversion regime**.

Due to the modulation of the array impedance, the frequencies involved in the conversion process vary over a wide range, depending on the arch chosen. For example, the frequency of mode b which allows photon conversion spans more than 1 GHz, from $\omega_b/2\pi = 9.13$ GHz (dark blue curve) to $\omega_b/2\pi = 7.95$ GHz (yellow curve).

[3] In the following, we use the term "arch" to refer to different periods of the Φ_B modulation, such that the nth arch corresponds to the data taken between $\Phi_B = -n \times \Phi_0$ and $\Phi_B = -(n+1) \times \Phi_0$.

[4] As can be seen in Figure 4.6, the in-line inductance of the array cannot strictly speaking be considered as a constant within a given period of the Φ_B modulation, but the variations in the chain impedance remain small compared to the bare value.

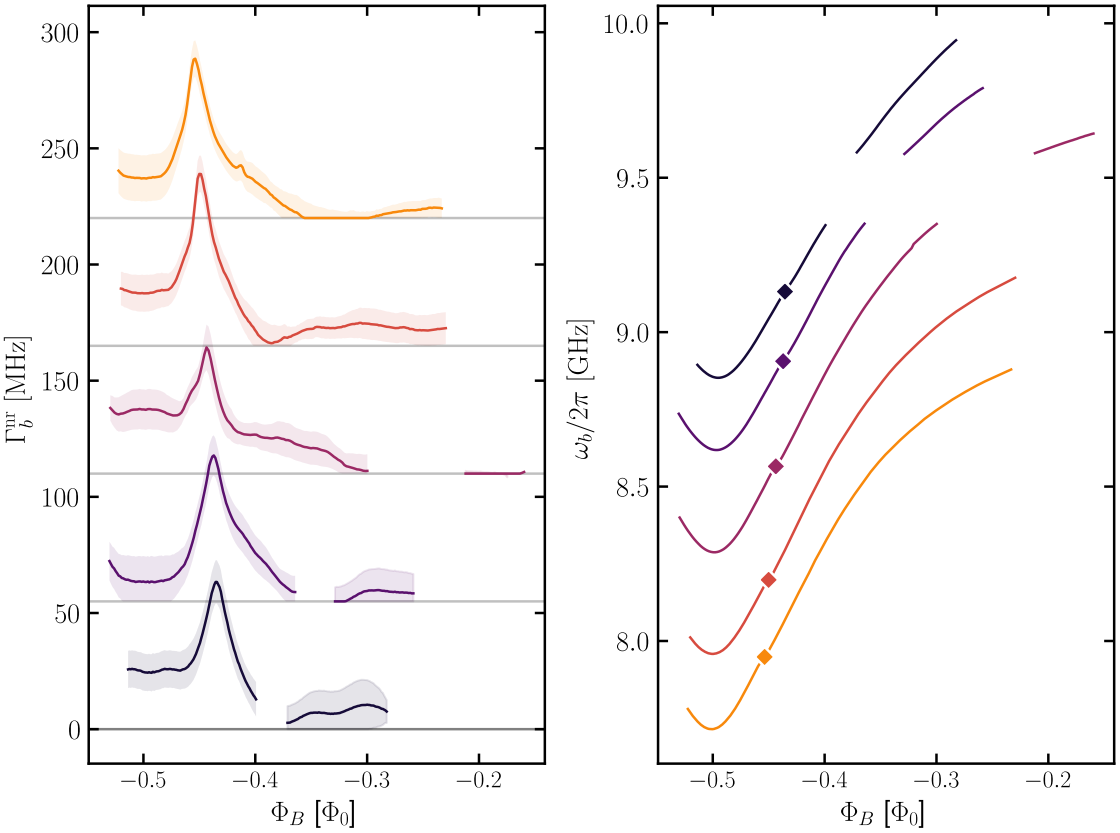

Figure 4.7.: **Left.** Mode b internal losses as a function of the external magnetic flux Φ_{B}. Different colours correspond to different array impedances Z_{env}. The curves are offset vertically for clarity. The shaded area around the data shows the uncertainty in the extracted internal losses due to the imperfect isolation of the microwave components used in the output line. For all values of the array impedance, Z_{env}, Γ_b^{b} shows a sharp increase which is attributed to the three-photon down-conversion process. **Right.** Resonant frequency of mode b as a function of Φ_{B} for different values of Z_{env} (same colour code as left panel). The diamond markers show the mode b frequency at the points where the internal losses are maximised.

4.2.4. Pure dephasing

Thanks to the tunability of the array impedance, it is possible to perform the spectroscopy of mode b for different values of the flux applied through the small junction, while keeping the frequency of mode b constant. Indeed, as it can be seen in Figure 4.6, mode b crosses the same frequency (horizontal dashed line) several times for different values of Φ_{B} (vertical dashed line). We can leverage this feature of the sample to further characterise the properties of the system in order to properly model the photon conversion process.

More specifically, we will estimate the pure dephasing rate of modes a and b as this can play an important role in the fluorescence spectrum, as discussed in section 2.3.4.

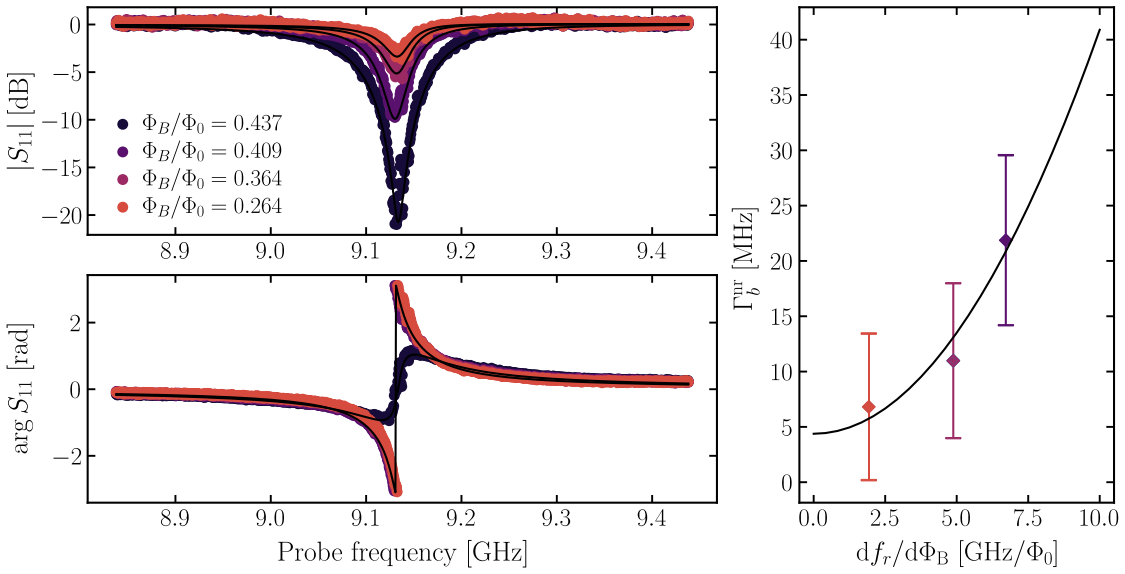

Figure 4.8.: **Left.** Single-tone spectroscopy of mode b for different magnetic flux Φ_B while keeping the mode resonance frequency constant (thanks to the array tunability). The colour code corresponds to the arrows in Figure 4.6. The red trace corresponds to the flux point where photon conversion is measured while for the blue traces there is no photon conversion process. The black lines correpond to individual fits to the data performed in order to extract the non-radiative losses. **Right.** Non-radiative losses of mode b at a fixed frequency $\omega_b/2\pi = 9.13\,\mathrm{GHz}$ as a function of the slope $\partial f_b/\partial\Phi_B$. The black line shows a parabolic fit and the error bars are calculated in the same way as described in section 4.2.2.

Figure 4.8 shows the single tone spectroscopy of mode b for different values of the magnetic flux Φ_B while keeping the resonance frequency $\omega_b/2\pi = 9.13\,\mathrm{GHz}$ constant. This constant value of the resonant frequency is chosen as the value at which we actually observe the photon conversion process (dark blue curve). Keeping the resonant frequency constant by moving to successive arches allows the spectroscopy of mode b to be performed for different slopes $\partial f_b/\partial\Phi_B$. The non-radiative losses of mode b, Γ_b^{nr}, are then extracted. The right panel of Figure 4.8 shows Γ_b^{nr} as a function of the slope of the flux modulation and shows a quadratic dependence of the internal losses as a function of $\partial f_b/\partial\Phi_B$. This is a clear signature of the presence of pure dephasing in the system. The flux point at which the photon conversion is measured (dark blue curve) actually falls at the maximum of the slope, $\partial f_b/\partial\Phi_B \sim 7\,\mathrm{GHz}/\Phi_0$. For the other three traces of the left panel of Figure 4.8, no down-conversion takes places and the non-radiative losses are

modelled by[5]

$$\Gamma_b^{\mathrm{nr}} = \Gamma_b^{\mathrm{nr},0} + A_\phi \left(\frac{\partial f_b}{\partial \Phi_{\mathrm{B}}} \right)^2 . \tag{4.7}$$

At this point it is quite clear that the non-radiative losses of mode b are dominated by pure dephasing, and the pure dephasing rate of mode b is $\Gamma_b^{\phi}/2\pi \simeq 17\,\mathrm{MHz}$. Unfortunately, the exact same analysis cannot be easily performed for mode a. In fact, this mode is at the edge of the measurement bandwidth (around 3 GHz), so the line shape of the measured reflection coefficient gets significantly distored and it is not possible to reliably extract the non-radiative losses of mode a, Γ_a^{nr}. However, we can still extract the slope of the flux modulation, $\partial f_a/\partial \Phi_{\mathrm{B}} \simeq 12.5\,\mathrm{GHz}/\Phi_0$, which also indicates that mode a is strongly subject to pure dephasing at the flux point where we measure the converted photons. The conclusion of this qualitative study is that pure dephasing is indeed a dominant source of decoherence in the system under study and that it must be properly accounted for in the modelling of the spectrum of converted photons (see section 2.3.4).

4.3. Direct observation of the converted photons

In the previous section, we studied the effect of the photon conversion process on the single-tone spectroscopy of mode b and concluded that the observed sharp increase in non-radiative losses was due to the decay of probe photons into triplets of photons emitted at mode a frequency. However, at this stage, it can be argued that this observation of the down-conversion process remains indirect. To confirm that the observed increase in Γ_b^{nr} is indeed due to the three-photon down-conversion process, we now turn to the direct measurement of these down-converted photons and show that we can indeed recover the lost photons.

4.3.1. Measurement principle

The system is tuned by applying an external magnetic flux $\Phi_{\mathrm{B}} = -1.44\Phi_0$ corresponding to the maximum of the internal losses of mode b on the second arch (maximum of the dark blue curve in Figure 4.7). At this point the three-photon state of mode a, $|3_a, 0_b\rangle$, and the single-photon state of mode b, $|0_a, 1_b\rangle$, are in resonance, $\Delta^{1\leftrightarrow 3} = 0$.

A continuous low power drive tone at a frequency ω_d close to mode b resonance frequency is sent on the device to drive mode b's first transition, $|0_a, 0_b\rangle \leftrightarrow |0_a, 1_b\rangle$. This signal is generated at room temperature by a microwave source[6] and is attenuated as described in chapter 3. According to the model presented in section 2.3.3, multiphoton coupling then allows the energy to be transferred from the $|0_a, 1_b\rangle$ state to the $|3_a, 0_b\rangle$ state and for the subsequent cascaded decay from $|3_a, 0_b\rangle$ to $|0_a, 0_b\rangle$ by sequentially emiting three-photons at ω_{32} (or $\omega_d - \omega_{20}$, see the discussion in section 2.3.4), ω_{21} and ω_{10}. The signal associated with the emission of these three-photons is then amplified by the TWPA. The frequency of the tone used to pump the TWPA is detuned from any

[5] Assuming an exponential decay of the off-diagonal elements of the density matrix.
[6] Agilent E8257D PSG Microwave Analog Signal Generator.

resonant mode of the system and we have checked that it does not affect the emitted signal. The signal is then further amplified by a cryogenic amplifier[7] at the 4 K stage of the dilution refrigerator, and then by two further amplifiers at room temperature (see Figure 3.7), and finally sent to a spectrum analyser. The itinerant output of the measurement setup is characterised by its complex amplitude $S(t) = I(t) + iQ(t)$ [Lang 2014] and its power spectral density is composed of several Lorentzian peaks (see section 2.3.3). This signal is then down-converted to an intermediate frequency $\omega_{\text{if}}/2\pi$ by mixing it with the monochromatic signal generated by a local oscillator at frequency $\omega_{\text{LO}}/2\pi$ (*i.e.* the spectrum of the signal is shifted by $\omega_{\text{LO}}/2\pi$)[8]. The down-converted signal is then filtered using a bandpass filter with a given bandwidth. This bandwidth, called the resolution bandwidth, determines the resolution of the measured spectrum as well as the noise level of the measurement. The filtered down-converted signal is then digitised and digitally down-converted to DC to extract the quadratures I and Q. Further digital signal processing is performed to return the measured power.

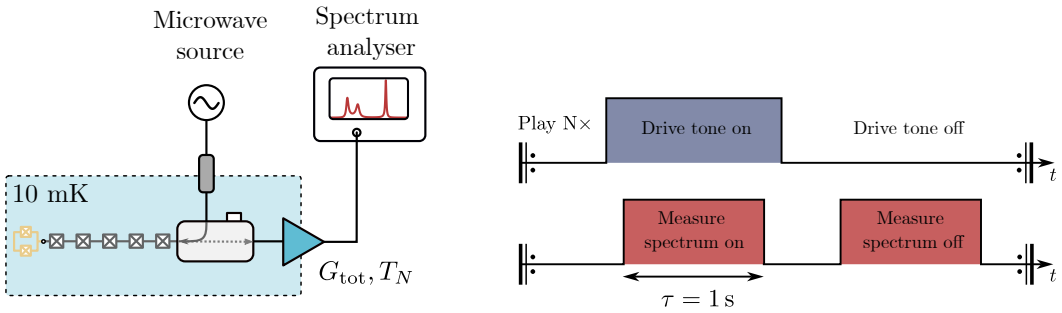

Figure 4.9.: **Left.** Simplified schematic of the measurement setup. **Right.** Schematic of the on-off measurement scheme.

The main challenge associated with such a measurement is the fact that the signal to be measured is a very weak signal (fraction of a photon) and spreads over a relatively large bandwidth (a few hundred of MHz). Each point of a single acquired spectrum is the result of the integrated RMS power over a frequency range given by the resolution bandwidth (RBW) around the frequency ν of interest. Since each spectrum consists of N points and is measured during time τ, each point of the spectrum is integrated during time $t_s = \tau/N$. In order to measure N statistically independent samples, the acquisition time must satisfy $\tau > N/\Delta\nu$, where $\Delta\nu$ is the resolution bandwidth. Then the standard deviation of the background thermal noise power measured by the spectrum analyser is

[7] Low Noise Factory - LNC0314A - 0.4-14GHz Cryogenic Low Noise Amplifier.

[8] Note that in modern spectrum analysers, such as the one used to perform the measurement presented in this work, several stages of down-conversion are cascaded to arrive at the intermediate frequency, effectively implementing what is usually called a superheterodyne detection scheme. This is done to remove spurious sidebands.

given by (assuming white noise)

$$P_\sigma = \sqrt{\frac{2N\Delta\nu}{\tau}} k_B T_N G_{\text{tot}} \,, \tag{4.8}$$

where T_N is the equivalent noise temperature of the amplification chain and G_{tot} is the total gain of the amplification chain, including the TWPA, the HEMT, the two room temperature amplifiers and any losses induced by imperfections in the microwave components of the output line (*e.g.* insertion losses of the isolators, microwave switches and losses in the coaxial cables)[9].

To to be able to measure the signal associated with the emission of the down-converted photons, $P_{\text{sig}} = I(\nu)h\nu\Delta\nu$, we need a signal-to-noise ratio (SNR) greater than one. In other words, the amplified signal must overcome the amplified noise, $G_{\text{tot}}P_{\text{sig}} > P_\sigma$. In this context of very low power measurements, we adopt a different definition of SNR to that introduced in section 3.2.3. Instead of comparing the signal power with the noise floor, we compare it with the standard deviation of the background noise P_σ,

$$\text{SNR} = \frac{G_{\text{tot}}P_{\text{sig}}}{P_\sigma} = \sqrt{\frac{\tau\Delta\nu}{2N}} \times \frac{I(\nu)h\nu}{k_B T_N} \,. \tag{4.9}$$

By reducing the noise temperature of the amplification chain, T_N, the TWPA allows the standard deviation of the noise to be reduced (see equation (4.8)), resulting in a large improvement in SNR compared to using a standard HEMT as the first stage of amplification (see section 3.2.3 for a quantitative measurement of the SNR improvement at 3 GHz). To further increase the SNR, the acquisition of the emission spectrum is repeated N_{avg} times, adding a factor $1/\sqrt{N_{\text{avg}}}$ in the standard deviation of the noise in equation (4.8), $P_\sigma \to P_\sigma/\sqrt{N_{\text{avg}}}$. Due to the very low intensity of the signal to be measured, the measurement is very sensitive to low frequency noise that can arise from slow time drifts in the amplification chain. To avoid this problem, we use an "ON-OFF" measurement scheme. In this scheme, the emission spectrum is first measured when a drive tone is sent at frequency $\omega_d/2\pi$ (the drive tone is said to be "ON"), triggering the emission of down-converted photons, the signal of interest. Following this measurement, another spectrum is acquired without the drive tone being sent (in this case the drive tone is said to be "OFF"), resulting in a measurement of the background thermal radiation only. This measurement sequence, shown in Figure 4.9, is repeated N_{avg} times. The purpose of the "OFF" measurement is to remove any background drift that could lead to artefacts in the averaged spectrum. In addition, due to the presence of variations in the gain of the amplification chain as a function of frequency, it is important to normalise the data by the gain extracted from the calibration presented in section 3.2.

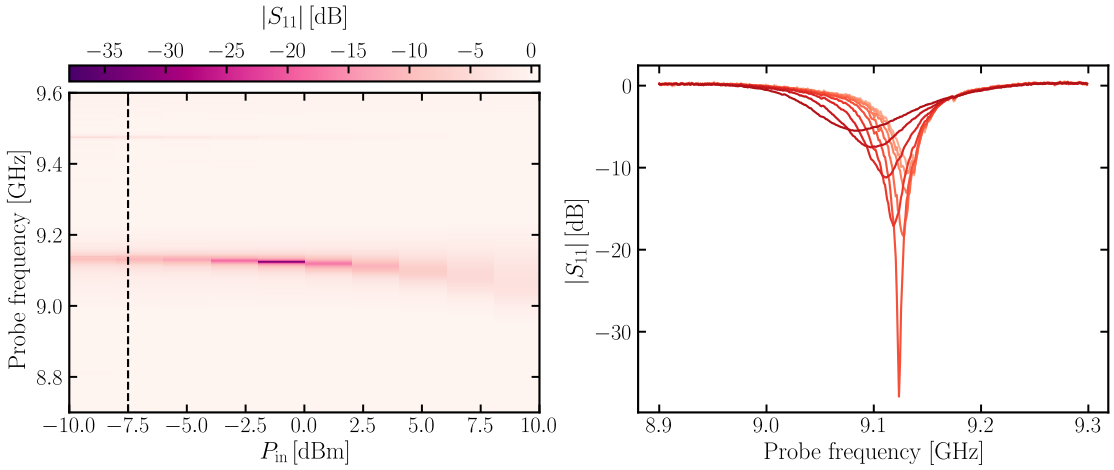

Figure 4.10.: Power dependence of $S_{11}(\omega_d)$. **Left.** Colour map of the magnitude of the reflection coefficient $|S_{11}(\omega_d)|$ in the vicinity of mode b resonance frequency and as a function of the input power at room temperature. The vertical dashed line shows the power used to perform the multimode fluorescence measurement. **Right.** Single-tone traces (corresponding to the data in the left panel) for increasing input power (from light red to dark red).

4.3.2. Chosing the drive power

Choosing the appropriate input power is an important part of measuring the signal coming from the down-converted photons. On the one hand, it is desirable to maximise the flux of outgoing photons in order to ease the measurement (the SNR is obviously improved by increasing the signal power, P_{sig}). On the other hand, one wants to populate mode b ideally whith one excitation that will eventually be converted into three excitations of mode a by the photon conversion process. More precisely, the experiment aims at the single-photon regime, defined by an average number of photons in mode b of order one. The anharmonicity of the modes of the system allows an intuitive visualisation of the maximum power that can be input before triggering the nonlinearity of mode b. Looking at the power dependence of the reflection coefficient S_{11} plotted in Figure 4.10, one can clearly see the nonlinearity of mode b as the input power is increased. In fact, the resonance frequency shows a clear downward shift as the input power is increased. Since the expected nonlinearity of the modes is comparable to their linewidth, any significant shift in the reflection data suggests an average number of photons in mode b significantly

[9]The factor $\sqrt{2}$ in equation (4.8) comes from the properties of a Gaussian distribution. In fact, $P_\sigma^2 = 1/4Z_0^2 \times \mathbb{E}\left[(V_{\text{noise}}^2 - \mathbb{E}(V_{\text{noise}}^2))^2\right]$, where V_{noise} is the noisy voltage coming from the finite noise temperature of the amplification chain, following a Gaussian distribution with standard deviation given by $\mathbb{E}(V_{\text{noise}}^2) = 4Z_0 k_{\text{B}} T_N \Delta\nu$. Using the König-Huygens theorem and the 4th central moment of V_{noise}, $P_\sigma^2 = 1/4Z_0^2 \times \left(\mathbb{E}(V_{\text{noise}}^4) - \mathbb{E}(V_{\text{noise}}^2)^2\right) = 2/4Z_0^2 \times \mathbb{E}(V_{\text{noise}}^2)^2 = 2(k_B T \Delta\nu)^2$.

greater than one. We therefore chose to drive mode b with an input power such that no significant shift in the resonance frequency can be resolved, ensuring that the system is in the single photon regime. Unless otherwise stated, the fluorescence spectra presented in the following were measured with an input power of $-7.5\,\mathrm{dBm}$ at room temperature, shown as a vertical dashed line in Figure 4.10. The generated signal is attenuated by $-121.6\,\mathrm{dB}$ before the sample input, resulting in a $-129\,\mathrm{dBm}$ input power referred to the input of the sample.

4.3.3. Experimental results

We now present the results corresponding to the measurements of the spectrum of emitted photons, $I(\omega)$. The spectra are acquired on a 1 GHz span around 3.125 GHz with a resolution bandwidth of 5 MHz. Each spectrum contains 200 points and is acquires with a sweep time of 1 s. Each ON-OFF sequence is repeated 22500 times. Figure 4.11 panel (b) shows the spectrum measured with (dark red curve) and without (light red curve) TWPA for otherwise identical experimental parameters. Considering the total measurement time of about 20 h required to obtain a signal with very low SNR using only a HEMT amplifier as the first stage of amplification, this measurement clearly demonstrates the advantages of using a TWPA in such a low power microwave quantum optics experiment. Using the TWPA, the emission line shape corresponding to the down-converted photons becomes much clearer.

Panel (a) of Figure 4.11 shows a colour map of the outgoing flux of converted photons per unit bandwidth, $I(\omega)$, as a function of the drive frequency $\omega_d/2\pi$ for a fixed external magnetic flux $\Phi_\mathrm{B} = -1.44\Phi_0$. Compared to the data presented in panels (b) and (c), each spectrum is averaged only 2000 times, which explains the low SNR compared to the spectra presented below. One can clearly identify a distinct emission spot around the $(\nu_b', \nu_a') = (9.13, 3.16)\,\mathrm{GHz}$ point (diamond marker). As expected, when the driving tone is significantly detuned from the mode b resonance frequency, the converted photon signal disappears. This is best seen in panel (c), where we measure the number of photons emitted over a 5 MHz bandwidth around 3.125 GHz (this corresponds to the horizontal dashed line in panel (a)), which shows a distinctive Lorentzian line shape (see black line) with a full width at half maximum of about 110 MHz around ν_b. Note that the SNR of the measurement in panel (c) appears to be much better than in panel (b) because the former is performed at a single frequency. In this case, the number of samples is reduced to $N = 1$ for the same measurement time, thus improving the signal-to-noise ratio (see equation (4.9)). In panel (b), the spectrum is measured when the drive is in resonance with mode b (vertical dashed line in panel (c)) and clearly shows that the signal from the down-converted photons is strongest at $\omega/2\pi = \nu_a$. In addition, the spectrum is not symmetric around this maximum, which we attribute to the anharmonicity of mode a (see next section).

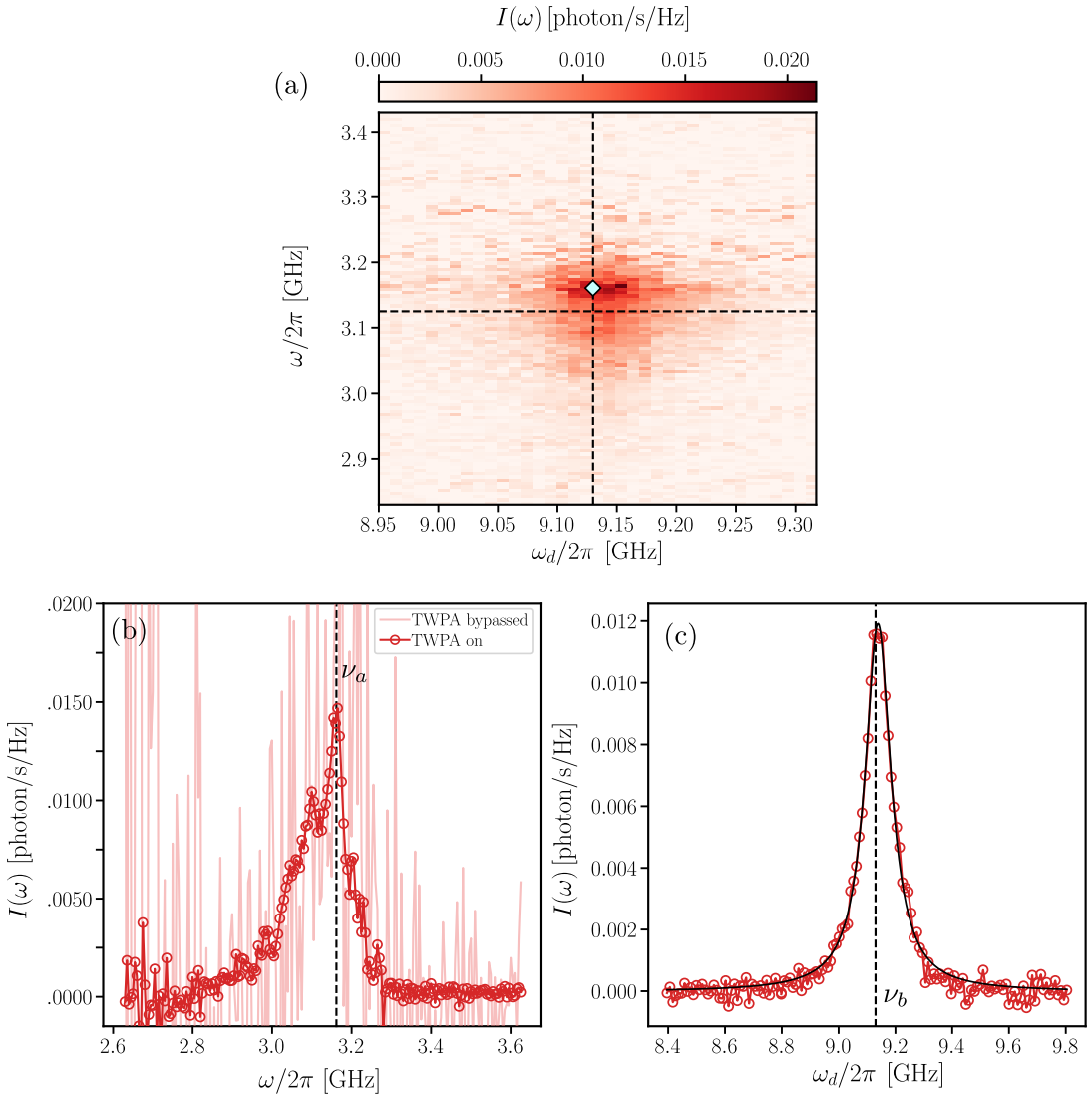

Figure 4.11.: Measurement of the down-converted photons. **(a)** Colour map of the emission spectrum $I(\omega)$ as a function of the drive frequency $\omega_d/2\pi$ for a constant drive power estimated at -129 dBm. For visibility, the scale is limited to the minimum value of $I(\omega) = 0$. **(b)** Emission spectrum at a fixed drive frequency $\omega_d/2\pi = \omega_b/2\pi = 9.13\,\mathrm{GHz}$ with (dark red) and without (light red) TWPA. The data shown in panels (a), (b) and (c) are acquired at $\Phi_\mathrm{B} = -1.44\Phi_0$. **(c)** Number of converted photons measured over a 5 MHz bandwidth around $\omega/2\pi = 3.125\,\mathrm{GHz}$ (horizontal dashed line in panel (a)) as a function of the drive frequency $\omega_d/2\pi$. The black line represents a Lorentzian fit to the data.

4.3.4. Data vs theory

We now turn to the comparison between the experimental data presented above and the theoretical model developed in section 2.3.3. For this purpose, we will compare the emission spectra measured for three different values of the detuning of the driving tone to the resonance frequency of mode b, $\tilde{\omega}_b = \omega_d - \omega'_b = 2\pi \times \{-50, 0, 50\}$ MHz. In addition, the system is again tuned at the flux point that maximises the internal losses of mode b in order to fulfil the resonance condition $\Delta^{1\leftrightarrow 3} = 0$. Most of the parameters that go into the analytical expression of the emission spectrum equation (2.67) can actually be estimated thanks to the single-tone spectroscopy of the device. From the $S_{11}(\omega_d)$ data at $\Phi_\mathrm{B} = -1.44\Phi_0$, we estimate the radiative decay rates of modes a and b to be $\Gamma^\mathrm{r}_a/2\pi \simeq 84$ MHz and $\Gamma^\mathrm{r}_b/2\pi \simeq 53$ MHz, respectively. From the pure dephasing analysis presented in section 4.2.4, the non-radiative losses of mode b are estimated to be $\Gamma^\mathrm{nr}_b/2\pi \simeq 4$ MHz. Finally the non-radiative losses of mode a are $\Gamma^\mathrm{nr}_a/2\pi \simeq 3$ MHz. The first transitions of mode a and b are estimated to be $\nu'_a = 3.16$ GHz and $\nu'_b = 9.13$ GHz, respectively.

From the design of the sample, it is expected that the modes of the chain hybridise with the impurity and thus inherit a nonlinear behaviour from this coupling. However, we have seen in section 2.3.3 that including the nonlinearity in the model leads to a peculiar shape of the emission spectrum with multiple emission peaks. The experimentally measured spectra show a single, slightly asymmetric emission peak. On the other hand, if modes a and b were to be linear (*i.e.* with equally spaced energy levels), the resonance condition to observe photon conversion would be $3\omega'_a - \omega'_b = 0$. However, given the above-mentioned parameters of the system, it directly follows that $3\omega'_a - \omega'_b = 2\pi \times 350$ MHz. This suggests that mode a has a large nonlinearity and further supports the choice of modelling modes a and b with anharmonic oscillators. The resonance condition given by the model consisting of two nonlinearly coupled Kerr oscillators introduced in section (2.32) imposes the value of the self-Kerr coefficient of mode a based on the known values of ω'_a and ω'_b, $K_a = \omega'_b/3 - \omega'_a$. The only remaining parameter is the nonlinear coupling strength, $g^{1\leftrightarrow 3}$. This parameter is used as the only fitting parameter. The model is fitted simultaneously to the three data sets corresponding to the three different values of detuning $\tilde{\omega}_b$. The results of this procedure are shown in the left panel of Figure 4.12. One can readily see that at this stage the agreement between the fitted theoretical model and the experimental data is hardly qualitative. In fact, the spectral structure of the experimentally measured emission spectrum is not correctly reproduced. However, the model does gives the correct order of magnitude for the flux of outgoing photon per unit bandwidth, with a reasonable fitted value of $g^{1\leftrightarrow 3}/2\pi = 11$ MHz, which is of the same order of magnitude as the estimate that can be made on the basis of equation (2.31). The model on which equation (2.67) is based is built on the hypothesis that modes a and b can be described by anharmonic Kerr oscillators, and the resonance condition $\Delta^{1\leftrightarrow 3}$ would give a self-Kerr coefficient for mode a of -117 MHz. On the other hand, a crude φ_0^4 expansion of the cosine in Hamiltonian (2.32) would give about $K_a/2\pi = 30$ MHz. In fact, there is no reason for the anhamornicity of the system modes to be governed solely by the Kerr effect, and higher orders of the cosine potential can in principle contribute to

level repulsion [Hriscu and Nazarov 2011]. All in all, this motivates a different approach to comparing the data with model.

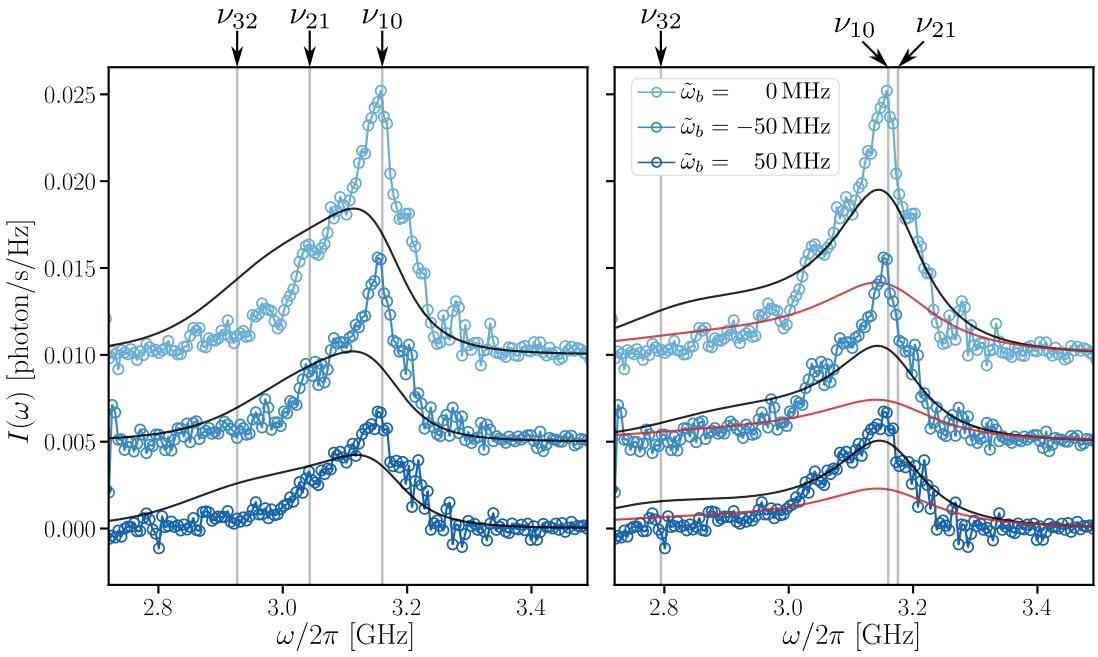

Figure 4.12.: Comparison between experimental data and theoretical model. The blue data points represent the emission spectra measured for three different values of the detuning $\tilde{\omega}_b = \omega_b - \omega_d$ and for $\Delta^{1\leftrightarrow 3} = 0$. The data corresponding to different detunings of the drive are vertically shifted for clarity. **Left.** Fitting of the theoretical model of equation (2.67) to the data (black lines) with only $g^{1\leftrightarrow 3}$ as a free parameter. All other parameters are estimated from single-tone spectroscopy. The vertical lines represent the successive transitions of mode a, ω_{10}, ω_{21} and ω_{32}. **Right.** Fitting of the theoretical model of equation (2.67) to the data (black lines) with $g^{1\leftrightarrow 3}$ and ω_{21} as free parameters. The red lines show the expected emission spectrum including the dephasing of mode a. The rationale behind this procedure is explained in the main text.

In this second approach, the anharmonicity of mode a is left unspecified. In this case, instead of explicitly writing the different transitions as a function of an *ad hoc* coefficient, K_a, the ν_{21} transition is left as a fitting parameter. Although the Hamiltonian used to derive equation (2.67) assumes Kerr oscillators, the calculation can be straightforwardly adapted to generic level spacings and equation (2.67) remains valid. The resonance condition constraint now appears as $\nu_{30} = \omega_b'/2\pi$, *i.e.* the third excited

state of mode a must coincide with the first excited state of mode b. The first transition of mode a is again given by $\nu_{10} = \omega'_a/2\pi$. The ν_{32} transition is then derived by *via* $\nu_{32} = \nu_{30} - \nu_{21} - \nu_{10}$. All other parameters are set to the same values as above. The results of this fitting procedure are shown in the right panel of Figure 4.12. Both the position and the structure of the emission spectrum are better captured by this second procedure, but the agreement is still not quantitative. It can also be seen that the fitted value of ν_{21} is very close to ν_{10}. This is because the experimental data essentially features a single, clearly defined emission peak. If it were otherwise, the model would predict an additional peak of significant intensity that cannot be resolved experimentally. Finally, the energy conservation criterion puts the final transition, ν_{32} at about 2.79 GHz, where the experimental data also show no emission. Note also that the model predicts that the leftmost peak should be drive dependent, with a frequency $\nu_d - \nu_{20}$ (which coincides with ν_{32} at zero detuning). Experimentally, we do not resolve any significant dependence of the positions of the emission peaks on the drive detuning. The right panel of Figure 4.12 shows in red lines the effect of including dephasing to mode a ($\Gamma_a^\phi/2\pi = 50$ MHz) on the modelled spectrum (see section 2.3.4). Taking dephasing into account results in an overall reduction of the photon flux as well as the suppression of the drive dependent peak.

In the end, the theoretical model of section 2.3.3 gives a fairly good account of the magnitude of the outgoing flux of converted photons and of the fact that the predominant contribution to this emission comes from the first transition of mode a, namely ν_{10}. On the other hand, the model lacks quantitative agreement and should therefore be taken with a grain of salt. Further development of the theoretical model will be necessary in order to achieve, if at all possible, a quantitative agreement between theory and experiment. Such refinements to the theoretical model could include finite temperature effects, which could lead to thermally assisted photon conversion processes, as well as the inclusion of other modes of the system (rather than the two-mode effective model). Such additions will greatly increase the complexity of the model, and it is worth mentioning that the two-mode model described in this work, although it has clear limitations, gives a simple yet convincing picture of the ingredients necessary to observe two-mode fluorescence.

4.3.5. Power dependence of the emission spectrum

The theoretical model in equation (2.67) predicts a linear dependence of the total output power on the input power P_{in}. The total output power is given by

$$P_{\text{out}} = \int \mathrm{d}\omega I(\omega)\hbar\omega \tag{4.10}$$

where $I(\omega)\hbar\omega$ corresponds to the power spectral density associated with the emission of the converted photons. Integrating this quantity thus gives the total output power. This is estimated experimentally using

$$P = \hbar\Delta\omega \sum_i I_i\omega_i \tag{4.11}$$

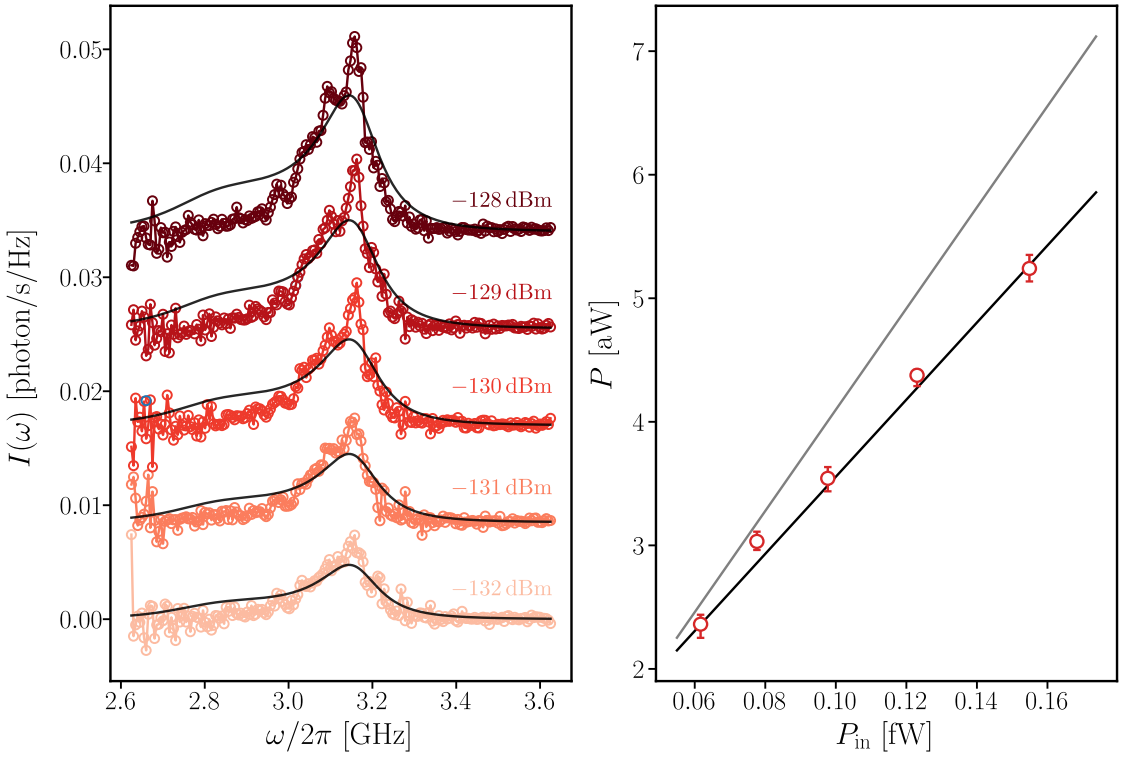

Figure 4.13.: Power dependence of the emission spectrum. **Left.** Emission spectra for increasing driving tone power P_{in} (from light red to dark red). Data corresponding to different powers are vertically shifted for clarity. Black solid lines correspond to the emission spectra as calculated by the theoretical model using the same parameters as the black solid lines in the right panel of Figure 4.12. **Right.** Integrated output power as a function of P_{in}. The grey line is the expected integrated power given by the theoretical model. The black line is an *ad hoc* linear fit to the data.

where the sum is realised over the number of samples that make up the experimentally measured spectrum, $\omega_i/2\pi$ is the frequency at which sample i is measured and $P_i = \hbar I_i \Delta\omega = \hbar I(\omega_i)\Delta\omega$ is the corresponding measured output power. To check the linear dependence of the measured total output power with respect to the input power, we measure several emission spectra for different values of P_{in} while still remaining in the single-photon regime. The resulting spectra are shown in the left panel of Figure 4.13 together with the prediction from the theoretical model. The total output power as a function of the input power calculated from these data, using equation (4.11), is shown in the right panel of Figure 4.13. The grey line represents the theoretically calculated total output power while the black line is a simple linear fit. Although the experimental data deviate from the theoretical predictions, the orders of magnitude agree and the measured total power still depends linearly on the input power.

Nous tâchons de comprendre cette tragédie du monde inerte qui se joue sous nos yeux et pour nous seuls. Cependant j'aurais tort de laisser croire qu'aucune inquiétude, même légère, ne vient troubler notre sérénité.

— *Jean Vernet*, première de l'Arête Rouge, face Sud de la Barre des Écrins, 1926

5 Multiphoton strong coupling

Contents

In this chapter, we present the findings related to the measurement of another sample. Compared with the preceding chapter, the device being discussed in this case is weakly coupled to the measurement line, which makes it possible to observe an avoided crossing between two states with a distinct number of excitations. This avoided crossing in the device spectrum is the result of what is usually referred to in the literature as multiphoton Rabi oscillations [Garziano et al. 2015], a process that has attracted much theoretical interest [Duan et al. 2015; Duan et al. 2016; Felicetti 2018]. However, to our knowledge, very few direct observations of a fundamental multiphoton coupling have been reported.

In a remarkable circuit-QED experiment, such multiphoton coupling was observed in the case of a two-degree-of-freedom circuit consisting of a large-inductance loop dcSQUID [Lecocq et al. 2012]. Furthermore, F. Lecocq and collaborators not only observed an avoided crossing in the spectrum of the circuit, but also detected a coherent energy exchange between the $|0_s, 1_a\rangle$ and $|2_s, 0_a\rangle$[1] states of the circuit by means of time-resolved measurements. They reported a rate of energy exchange as large as 815 MHz between these two states. An other spectral signature of photon down-conversion processes has recently been reported in a device akin to the one showcased in this thesis [Mehta et al. 2023]. However, the present work differs from the aforementioned study in terms

[1] The indices s and a stand for the symmetric and the anti-symmetric modes of the circuit studied in [Lecocq et al. 2012].

of both the number of junctions in the array and the type of impurity utilized at the boundary of the array. Mehta and colleagues connected a fluxonium qubit to a heavily dense array of Josephson junctions, thus creating a quasi-continuous electromagnetic environment, resulting in a fine structure of the circuit spectrum. On the other hand and as explained in details in Chapter 2, the devices studied in this work are designed to select only two modes of the environment interacting together. The objective of this chapter's experiment was to take the first step towards the direct observation of the down-converted photons. Indeed, the observation of an avoided crossing in the spectrum is a clear signature of the presence of a non-conserving term in the dynamics of the system and allows us to confirm that we can indeed select two modes of the system to interact with each other. The presented sample was specifically designed to achieve this objective. Since it is unrealistic to witness an anti-crossing in the spectrum and a substantial flow of emitted photons within the same sample, each observation required a separate sample, and this is why the multi-mode fluorescence measurement presented in the previous chapter required the fabrication of a new device. In addition, the present experiment allows the direct measurement of the nonlinear coupling strength $g^{1\leftrightarrow 3}$.

Surprisingly, the observation of an avoided crossing also allows us to highlight charging effects caused by the presence of quasiparticles in the system, which were not expected in the design of the experiment. As we will demonstrate, the nonlinear interaction term which causes photon down-conversion represents a distinctive approach for investigating higher excited states of the system. By "higher excited states" we refer to states comprising multiple excitations of the system that are typically indistinguishable through single-tone spectroscopy. These higher excited states are significantly more subject to charge noise than single-photon states, resulting in noticeable charging effects in the avoided crossing between a single-photon and a three-photon state. One can get an intuition of this effect by recalling the simple case of the isolated junction. Indeed, the energy spectrum for a highly nonlinear junction (*i.e.* with a small $E_\mathrm{J}/E_\mathrm{C}$) depends strongly on the number of offset charges n_g on the associated superconducting island. As shown in Figure 5.1, higher excited states show a greater charge dispersion. The observation of such charging effects in a strongly multimode system shines new light on potential decoherence effects in superconducting circuits. Indeed, promising circuits for quantum computing often consist of arrays of linear junctions (implementing large inductances) galvanically coupled to a small junction [Dassonneville et al. 2020; Manucharyan et al. 2009]. Nonlinear coupling between modes of the array together with qualitative charging effects on excited states of these modes could affect the coherence of the resulting qubit. Hence, the observation of such effects is a first step torwards their understanding and their mitigation.

5.1. Sample presentation

For this chapter, the sample being investigated is designed so that its spectrum shows an avoided crossing between a single-photon state and a multiphoton state, resulting from the coherent exchange of energy between these two states. As as result,

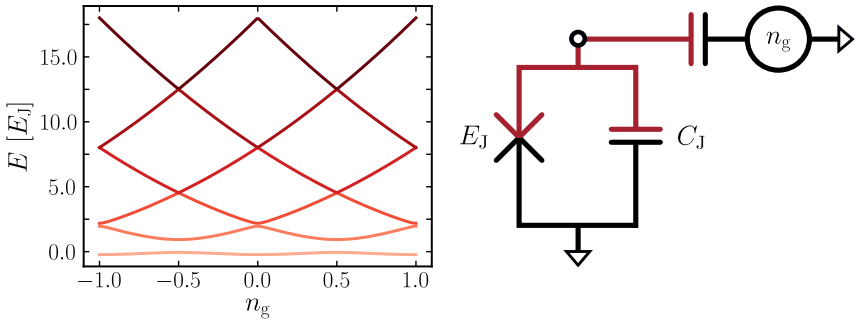

Figure 5.1.: **Left.** Energy spectrum of the isolated Josephson junction with $E_J/E_C = 2$ as a function of the offset charge n_g. The different shades of red indicate the different energy levels. **Right.** Circuit model of the isolated junction subjected to charge noise. The red region represents the superconducting island and the charge offset is generated by a voltage source.

this sample will often be referred to as the "coherent conversion sample". It remains an array of large junctions galvanically coupled to a small junction, which acts as the sole source of non-linearity in the circuit. In this case, the system is capacitively coupled to the measurement line, resulting in the system modes being in the undercoupled regime. This is the main difference from the strong conversion sample discussed in chapter 4 and it is necessary to enable the observation of a detailed structure in the spectrum of the device. Indeed, if the spectral broadening of the modes is excessively high, the possibility of observing an avoided crossing through single tone spectroscopy disappears. Due to the small level of internal losses in this circuit ($\Gamma^{nr}/2\pi \sim 1\,\mathrm{MHz}$) compared to the anticipated lift of degeneracy, the visibility of the fine structure of the system spectrum is controlled by the coupling to the measurement line (*i.e.* the radiative decay rate Γ_b^r). The array has been designed to exhibit a one to three photon-conversion interaction between its first and second modes, as highlighted in blue and red in Figure 5.3. It now consists of $N = 100$ junctions, with a small non-linearity due to $E_J^{arr}/E_C^{arr} \simeq 560$. The small junction located at the array's right boundary has a bare Josephson energy $E_J(\Phi_B = 0)/h$ of approximately 40 GHz and charging energy E_C/h of approximately 9.2 GHz, providing a large non-linearity due to $E_J/E_C = 4.3$. The capacitance network shown in the equivalent circuit representation in Figure 5.2 models the capacitive coupling to the measurement line. The corresponding transmission (ABCD) matrix is given by

$$T_{coup} = \begin{bmatrix} 1 + C_{c,i}/C_c & 1/i\omega C_c \\ i\omega(C_{c,o} + C_{c,i} + C_{c,i}C_{c,o}/C_c) & 1 + C_{c,i}/C_c \end{bmatrix} . \tag{5.1}$$

The values of the coupling capacitors C_c, $C_{c,i}$ and $C_{c,o}$ are estimated from the device geometry using electromagnetic simulations. Using the same method as for the previous device, the dispersion relation of the present device is measured at $\Phi_B = 0$ by two-tone spectroscopy. The outcomes, with a fit of the analytical dispersion relation (2.13), are

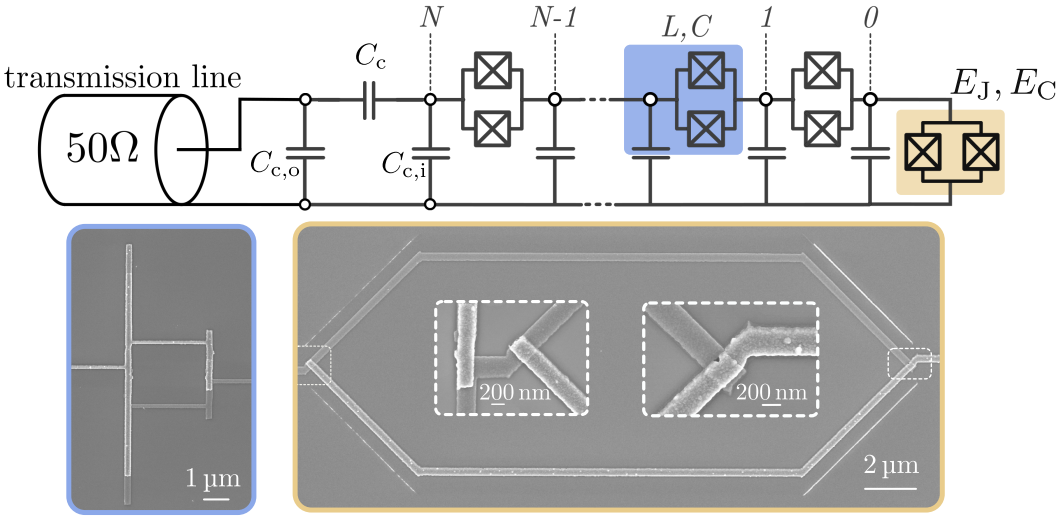

Figure 5.2.: **Top.** Schematic of the measured circuit. The SQUID array, shown in light grey, is characterised by its flux-tunable lumped element inductance $L(\Phi_B)$, capacitance C and ground capacitance C_g. The chain contains $N = 100$ SQUIDs in the linear regime ($E_J/E_C = 560$ at $\Phi_B = 0$) and is terminated by a nonlinear SQUID ($E_J/E_C \sim 4.3$ at $\Phi_B = 0$), shown in gold, characterised by its flux-tunable Josephson energy $E_J(\Phi_B)$ and capacitance C_J. **Bottom.** SEM images. In the blue contour, the image of a single SQUID of the array corresponding to the blue shaded area of the upper panel. In gold contour, image of the nonlinear SQUID corresponding to the gold shaded area of the upper panel.

featured in Figure 5.3 and provide an estimate for C_g. Compared to the prior galvanic coupling, the unperturbed wavevector is no longer determined by that of a $\lambda/2$ lumped transmission line. Given the smallness of the coupling capacitance, it is appropriate to approximate it by replacing the left boudary by an open one. Therefore, the wave vector of the system's normal modes is given by

$$k_n = \frac{n\pi}{N - 1/2} + \frac{\theta_k}{N - 1/2}\,, \tag{5.2}$$

with θ_k given by equation (4.3). Note that for this sample we could only measure the frequency of the first four modes of the system, even using two-tone spectroscopy. Table 5.2 summarises the parameters of the coherent conversion sample.

	Small JJ	**Chain**
C_j[fF]	8.4	105.2
C_g[fF]		0.8
E_J/h[GHz]	40.0	412.7
E_C/h[GHz]	9.2	0.7
$E_\mathrm{J}/E_\mathrm{C}$	4.3	560.5
Z/Z_Q	0.1	0.1
$\omega_{\mathrm{J(P)}}/2\pi$[GHz]	27.2	24.6
C_c[fF]		2.0
$C_{c,i}$[fF]		2.1
$C_{c,o}$[fF]		85.5

Table 5.2.: Coherent conversion sample parameters.

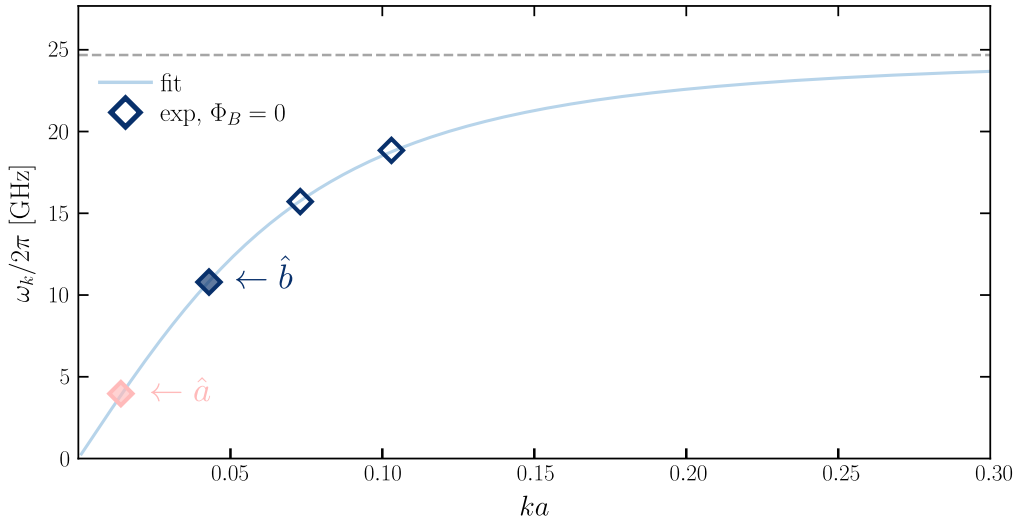

Figure 5.3.: Dispersion relation of the coherent conversion sample based on a two-tone spectroscopy measurement of the first four modes of the device at $\Phi_\mathrm{B} = 0$. The diamonds represent the extracted mode frequencies. The plain blue line is the fitted analytical dispersion relation. The two modes coupled by the photon conversion interaction are coloured in red and blue for mode a and b respectively.

5.2. Multiphoton avoided crossing

We recall that the minimal effective Hamiltonian modeling the system we want to study is given by equation (2.32),

$$\begin{aligned}\hat{H}_{\text{eff}} = \omega_a'\hat{a}^\dagger\hat{a} \;&+ \frac{K_a}{2}\hat{a}^\dagger\hat{a}^\dagger\hat{a}\;\hat{a} \;+ \omega_b'\hat{b}^\dagger\hat{b} \;+ \frac{K_b}{2}\hat{b}^\dagger\hat{b}^\dagger\hat{b}\;\hat{b} \\ &+ K_{ab}\hat{a}^\dagger\hat{a}\;\hat{b}^\dagger\hat{b} \;+ g^{1\leftrightarrow 3}\left(\hat{a}^{\dagger 3}\hat{b} + \hat{b}^\dagger\hat{a}^3\right).\end{aligned}$$

The only non-zero off-diagonal matrix elements $\langle n_a', n_b'|\hat{H}_{\text{eff}}|n_a, n_b\rangle$ are those verifying $|n_a' - n_a| = 3$ and $|n_b' - n_b| = 1$ for $(n_a, n_b, n_a', n_b') \in \mathbb{N}$. As such, the subspace formed by the basis states $|0,1\rangle$ and $|3,0\rangle$ is completely decoupled from any other subspaces and it is sufficient to consider the projection of the effective Hamiltonian on this subspace. The resulting Hamiltonian matrix on this subspace is

$$\begin{array}{c} \\ |3,0\rangle \to \\ |0,1\rangle \to \end{array} \begin{array}{c} \begin{array}{cc} |3,0\rangle & |0,1\rangle \end{array} \\ \begin{bmatrix} 3\left(\omega_a' + K_a\right) & \sqrt{6}g^{1\leftrightarrow 3} \\ \sqrt{6}g^{1\leftrightarrow 3} & \omega_b' \end{bmatrix} \end{array}, \tag{5.3}$$

with its eigenvalues

$$E_\pm = \frac{3\omega_a' + \omega_b'}{2} \pm \sqrt{\left(\frac{\Delta^{1\leftrightarrow 3}}{2}\right)^2 + \left(\sqrt{6}g^{1\leftrightarrow 3}\right)^2}, \tag{5.4}$$

where $\Delta^{1\leftrightarrow 3} = 3\left(\omega_a' + K_a\right) - \omega_b'$ is the detuning between the states. At $\Delta^{1\leftrightarrow 3} = 0$, the corresponding eigenstates are symmetric and anti-symmetric superpositions of the $|0,1\rangle$ and $|3,0\rangle$ states,

$$|\psi_+\rangle = \left(|0,1\rangle + |3,0\rangle\right)/\sqrt{2}, \tag{5.5}$$

$$|\psi_-\rangle = \left(|0,1\rangle - |3,0\rangle\right)/\sqrt{2}. \tag{5.6}$$

As the detuning $\Delta^{1\leftrightarrow 3}$ between the levels is adjusted through the use of the external magnetic flux Φ_{B}, it is expected that an avoided crossing will be observed in the system's spectrum, resulting in a $2\sqrt{6}g^{1\leftrightarrow 3}$ splitting at zero detuning. To investigate the coupling between the $|3_{\text{a}}, 0_{\text{b}}\rangle$ and $|0_{\text{a}}, 1_{\text{b}}\rangle$ states, we perform the single-tone spectroscopy of mode b as we vary the external magnetic flux Φ_{B}. The resulting measurement is shown in Figure 5.4. Only single-photon states can be resolved in single-tone spectroscopy due to the linear coupling of the system to the measurement line. Hence, only the doubling of the spectroscopic lines near $\Phi_{\text{B}} = -0.42\Phi_0$ reveals the presence of the three-photon state through its hybridisation with the single-photon state. Near and at the anticrossing, the states $|3_{\text{a}}, 0_{\text{b}}\rangle$ and $|0_{\text{a}}, 1_{\text{b}}\rangle$ are no longer eigenstates of the system. The new eigenstates

are a linear combination of these two states, and only the single-photon part of these new eigenstates can be probed thanks to the linear coupling of the system to the measurement line.

We observe a splitting of 175 MHz resulting from the three photon down-conversion process with strength

$$g^{1\leftrightarrow 3}/2\pi \simeq 36\,\mathrm{MHz}\,.$$

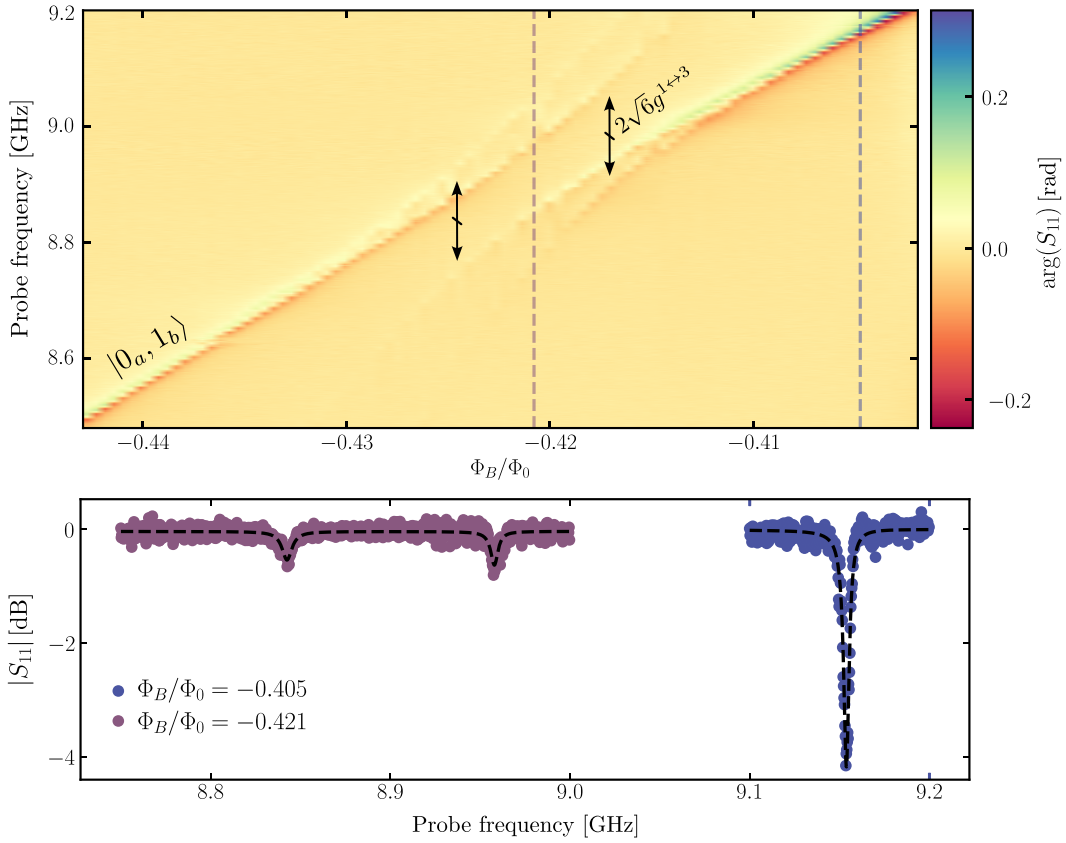

Figure 5.4.: Multiphoton avoided crossing. **Top.** Phase of the reflection coefficient measured in single-tone spectroscopy as a function of the external flux Φ_B showing an avoided crossing between the $|0_a, 1_b\rangle$ and the $|3_a, 0_b\rangle$ states. Surprisingly we observe an additional doubling of the spectroscopic lines at the avoided crossing. This observation is discussed in the main text. The observed splitting is around 175 MHz. **Bottom.** Amplitude of the reflection coefficient $|S_{11}|$ far from the avoided crossing (blue curve corresponding to the blue dashed line in the top panel) and close to the avoided crossing (purple curve corresponding to the purple dashed line in the top panel).

The radiative decay rates of mode a and b are estimated to be 120 kHz and 770 kHz respectively. On the other hand, the non-radiative decay rates are estimated to be $\Gamma_a^{\mathrm{nr}}/2\pi = 3.5\,\mathrm{MHz}$ and $\Gamma_b^{\mathrm{nr}}/2\pi = 6.3\,\mathrm{MHz}$. The value of $g^{1\leftrightarrow 3}$ then overcomes both the radiative and non-radiative decay rates of the modes and the system is indeed found to be in the multiphoton strong coupling regime. From equation (2.31) and the diagonalisation of the linearised system, we can estimate the expected nonlinear coupling strength to be approximately 14 MHz. Although giving the good order of magnitude, the experimentally measured coupling strength surpasses the expectations.

5.3. Discussion on charge dispersion

As can be seen in the top panel of Figure 5.4, an additional, unexpected doubling of the spectroscopic lines can be resolved at the avoided crossing point. Figure 5.5 shows a well resolved reflection trace near the avoided crossing and one can clearly see four resonance dips instead of the expected two. This is attributed to the dispersion of the $|3_a, 0_b\rangle$ state due to charge noise. Due to this charge dispersion in the system spectrum, the resonance condition does not occur for the same magnetic flux Φ_{B}, depending on the parity of the number of quasiparticles in the system. In the example of Figure 5.5 we have $0 < |\Delta^{1\leftrightarrow 3}(n_{\mathrm{g}} = 0.5)| < |\Delta^{1\leftrightarrow 3}(n_{\mathrm{g}} = 0)|$. Indeed, for $n_{\mathrm{g}} = 0$, the resonance dip associated with the $|\psi_-\rangle$ state is much more pronounced than that associated with the $|\psi_+\rangle$ state. This is expected if the detuning is comparable to the effective coupling strength, $\Delta^{1\leftrightarrow 3} \sim g_{\mathrm{eff}}$ (see Figure 2.11). On the other hand, for $n_{\mathrm{g}} = 0.5$, both $|\psi_+\rangle$ and $|\psi_-\rangle$ can be well resolved, which allows us to conclude that $|\Delta^{1\leftrightarrow 3}(n_{\mathrm{g}} = 0.5)| < |\Delta^{1\leftrightarrow 3}(n_{\mathrm{g}} = 0)|$. However, at $\Delta^{1\leftrightarrow 3} = 0$ one would expect both resonances to have the same dip amplitude, which allows us to state that $\Delta^{1\leftrightarrow 3}(n_{\mathrm{g}} = 0.5)$ is finite.

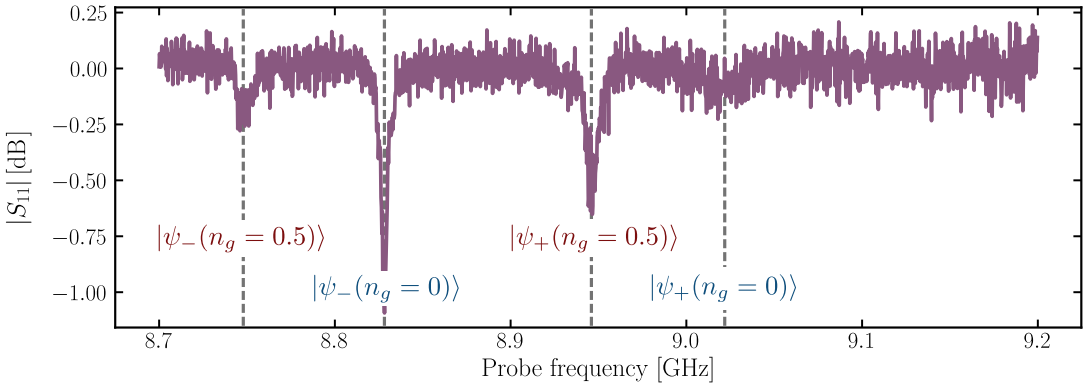

Figure 5.5.: Magnitude of the reflection coefficient as a function of probe frequency near the avoided crossing. Four resonances can be distinguished. We label the resonance dips with the corresponding eigenstates.

5.3.I. Symmetries of the microscopic Hamiltonian

In the microscopic description presented in Chapter 2, we deliberately excluded background charges to simplify the discussion. However, as the system comprises a series of superconducting islands, it is necessary to consider the presence of background charges, the origin of which is not specified here. The microscopic Hamiltonian is then given by

$$\hat{H} = \frac{(2e)^2}{2} \sum_{i,j} (\hat{n}_i - n_{\mathrm{g},i}) \, [C]^{-1}_{i,j} \, (\hat{n}_j - n_{\mathrm{g},j}) + \frac{\Phi_0^2}{2L} \sum_k (\hat{\varphi}_{k+1} - \hat{\varphi}_k)^2 - E_\mathrm{J} \cos \hat{\varphi}_0 \,, \quad (5.7)$$

with $n_{\mathrm{g},i}$ a classical variable that models the charge offset at site i. The symmetry of this Hamiltonian is nothing but the simultaneous 2π-translation of each phase φ_k. In order to gauge out the offset charges, $n_{\mathrm{g,i}}$, one can apply the following unitary transform

$$\hat{U} = \underbrace{\exp\left(i \sum_i n_{\mathrm{g},i} \hat{\varphi}_i \right)}_{\hat{U}_1} \times \underbrace{\exp\left(-\frac{i}{N} \sum_j n_{\mathrm{g},j} \sum_i \hat{\varphi}_i \right)}_{\hat{U}_2} . \quad (5.8)$$

The first term in the right hand side of equation (5.8), $\hat{U}_1$, translates all the island charges according to $\hat{n}_i \to \hat{n}_i + n_{\mathrm{g,i}}$, hence gauging out the offset charges. However this simple unitary transform does not maintain the invariance of the transformed wavefunction, $\psi' = \hat{U}_1 \psi$, under the the simultaneous 2π-translation of each phase,

$$\psi'(\overrightarrow{\varphi} + 2\pi \overrightarrow{u}) = e^{i 2\pi n_\mathrm{g}^\mathrm{tot}} \psi'(\overrightarrow{\varphi}) \,,$$

with $n_\mathrm{g}^\mathrm{tot} = \sum n_{\mathrm{g,i}}$ the total number of background charges in the system and $\overrightarrow{u} = (1, \ldots, 1)$ is the vector containing N ones. The second term in the right hand side of equation (5.8), $\hat{U}_2$, translates all the charges by the same amount, $\hat{n}_i \to \hat{n}_i - n_\mathrm{g}^\mathrm{tot}/N$ and allows to restore the invariance of the wavefunction under the simultaneous 2π-translation of each phase,

$$\psi''(\overrightarrow{\varphi} + 2\pi \overrightarrow{u}) = \exp\left(i 2\pi n_\mathrm{g}^\mathrm{tot} - \frac{i}{N} 2N\pi n_\mathrm{g}^\mathrm{tot} \right) \psi''(\overrightarrow{\varphi}) = \psi''(\overrightarrow{\varphi}) \,. \quad (5.9)$$

The transformed Hamiltonian, $\hat{H}'' = \hat{U} \hat{H} \hat{U}^\dagger$ is given by

$$\hat{H}'' = \frac{(2e)^2}{2} \sum_{i,j} \left(\hat{n}_i - \frac{n_\mathrm{g}^\mathrm{tot}}{N} \right) [C]^{-1}_{i,j} \left(\hat{n}_j - \frac{n_\mathrm{g}^\mathrm{tot}}{N} \right) + \frac{\Phi_0^2}{2L} \sum_i (\hat{\varphi}_{i+1} - \hat{\varphi}_i)^2 - E_\mathrm{J} \cos \hat{\varphi}_0 \quad (5.10)$$

and shows explicitely the dependance of the spectrum on the total background charge $n_\mathrm{g}^\mathrm{tot}$. Hence, the system is able to respond sensitively to the presence of quasiparticles, regardless of their position in the chain. Due to the large number of degrees of freedom present in the system, it is illusory to perform an exact diagonalisation of Hamiltonian (5.10).

5.3.2. Two-junction chain toy model

The simplest scenario involving a two-junction chain reduces the degrees of freedom to two, providing a qualitative description of the phenomenon we are observing. Figure 5.6 depicts the corresponding circuit for this simplified model.

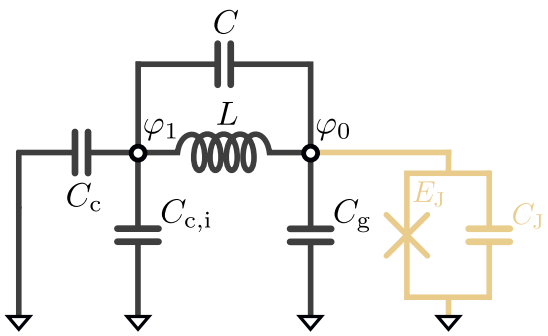

Figure 5.6.: Equivalent circuit of the minimal two mode toy model consisting of a single array junction coupled to the impurity junction. The array junction is modelled by a linear inductor and is capacitively coupled to the measurement line to its left. The input impedance seen by the circuit is approximated by a short circuit to ground.

The gauge transformed Hamiltonian of this circuit is expressed by equation (5.10) with i and j being elements of $\{0, 1\}$. It explicitly writes

$$\begin{aligned}\hat{H}'' = &\frac{4e^2}{2} C_{00}^{-1} \left(\hat{n}_0 - \frac{n_\mathrm{g}^\mathrm{tot}}{2}\right)^2 + \frac{4e^2}{2} C_{11}^{-1} \left(\hat{n}_1 - \frac{n_\mathrm{g}^\mathrm{tot}}{2}\right)^2 \\ &+ 4e^2 C_{01}^{-1} \left(\hat{n}_0 - \frac{n_\mathrm{g}^\mathrm{tot}}{2}\right)\left(\hat{n}_1 - \frac{n_\mathrm{g}^\mathrm{tot}}{2}\right) + \frac{\Phi_0^2}{2L} (\hat{\varphi}_0 - \hat{\varphi}_1)^2 \\ &- E_\mathrm{J} \cos \hat{\varphi}_0 \,, \end{aligned} \tag{5.11}$$

with

$$C = \begin{bmatrix} C_\mathrm{J} + C_\mathrm{g} + C & -C \\ -C & C_\mathrm{c,i} + C + C_\mathrm{c} \end{bmatrix} \tag{5.12}$$

the capacitance matrix associated to the two-junction chain circuit represented in Figure 5.6. As highlighted in section 5.3.1, Hamiltonian (5.11) remains unchanged by the simultaneous 2π-translation of φ_0 and φ_1. Applying the unitary transformation $\hat{V} = \exp(\hat{n}_1 \hat{\varphi}_0)$ to $\hat{H}''$ simplifies the computation of the spectrum of (5.11). The trans-

formed Hamiltonian can be written as follows,

$$\begin{aligned}\hat{V}\hat{H}''\hat{V}^\dagger = &\frac{4e^2}{2}C_1^{-1}\hat{n}_1^2 + \frac{\Phi_0^2}{2L}\hat{\varphi_1}^2 \\ &+ \left(g_{01}\hat{n}_0 + g_{g1}n_\mathrm{g}^\mathrm{tot}\right)\hat{n}_1 \\ &+ \frac{4e^2}{2}C_{00}^{-1}\left(\hat{n}_0 - \frac{n_\mathrm{g}^\mathrm{tot}}{2}\right)^2 - \frac{4e^2 n_\mathrm{g} C_{01}^{-1}}{2}\left(\hat{n}_0 - \frac{n_\mathrm{g}^\mathrm{tot}}{2}\right) - E_\mathrm{J}\cos\hat{\varphi}_0\,, \end{aligned} \tag{5.13}$$

where $C_1^{-1} = C_{00}^{-1} + C_{11}^{-1} + 2C_{01}^{-1}$, $g_{01} = C_{01}^{-1} - C_{00}^{-1}$ and $g_{g1} = C_{00}^{-1} - C_{11}^{-1}$. The first two terms on the right-hand side of Equation (5.13) are in the form of a harmonic LC oscillator with general coordinate φ_1, while the last term corresponds to the impurity contribution to the energy. The second line is the coupling between the harmonic oscillator and the small junction via the charge operators. When the total offset charge is set to $n_\mathrm{g}^\mathrm{tot} = 0$, the Hamiltonian of a harmonic oscillator coupled to a charge qubit can be retrieved. The transformed Hamiltonian remains invariant when φ_0 is translated by 2π, but not when φ_1 undergoes a 2π-translation. φ_0 can be regarded as a compact variable, with $\varphi_0 \in (-\pi, \pi]$, and the number of Cooper pairs at the impurity site is discrete, $n_0 \in \mathbb{Z}$. Conversely, the phase φ_1 is an extended variable with $\varphi_1 \in \mathbb{R}$. The Hamiltonian matrix is typically written using a basis consisting of the tensor product of the Fock states of the harmonic oscillator and the charge states of the small junction, $|n_0\rangle \otimes |N_1\rangle$. Here, $\hat{n}_0\,|n_0\rangle = n_0\,|n_0\rangle$ and $\hat{a}_1^\dagger\hat{a}_1\,|N_1\rangle = N_1\,|N_1\rangle$. The annihilation operator $\hat{a}_1$ for the harmonic oscillator is defined as usual by

$$\begin{aligned}\hat{\varphi}_1 &= \sqrt{\frac{1}{2y_1}}\left(\hat{a}_1 + \hat{a}_1^\dagger\right)\,, \\ \hat{n}_1 &= i\sqrt{\frac{y_1}{2}}\left(\hat{a}_1 - \hat{a}_1^\dagger\right)\,, \end{aligned} \tag{5.14}$$

with $y_1 = \sqrt{E_\mathrm{L}/2E_{\mathrm{C},1}}$, $E_\mathrm{L} = \Phi_0^2/2L$ and $E_{\mathrm{C},1} = 2e^2C_1^{-1}$. Using equation (2.2), the matrix element of the transformed Hamiltonian can be expressed as

$$\begin{aligned}\langle n_0, N_1|\,\hat{V}\hat{H}''\hat{V}^\dagger\,\left|n_0', N_1'\right\rangle = &\quad \hbar\omega_0 N_1 \delta_{N_1,N_1'}\delta_{n_0,n_0'} \\ &+ i\sqrt{\frac{y_1}{2}}\left(g_{01}n_0 + g_{g1}n_\mathrm{g}\right)\sqrt{N_1+1}\left(\delta_{N_1,N_1'+1} - \delta_{N_1+1,N_1'}\right)\delta_{n_0,n_0'} \\ &+ \left[\frac{1}{2}C_{00}^{-1}\left(n_0 - \frac{n_\mathrm{g}}{2}\right)^2 - \frac{n_\mathrm{g}}{2}C_{01}^{-1}\left(n_0 - \frac{n_\mathrm{g}}{2}\right)\right]\delta_{N_1,N_1'}\delta_{n_0,n_0'} \\ &- \frac{E_\mathrm{J}}{2}\delta_{N_1,N_1'}\left(\delta_{n_0,n_0'+1} + \delta_{n_0+1,n_0'}\right) \end{aligned} \tag{5.15}$$

The matrix elements provided above enable us to numerically diagonalise $\hat{V}\hat{H}''\hat{V}^\dagger$ and compute the spectrum of $\hat{H}''$. The toy model is designed to explain the charge dispersion observed in Figure 5.4, so the parameters are adjusted to accurately replicate this behavior. In order to achieve this, it is necessary for the spectrum of $\hat{H}''$ to show an avoided-crossing between two excited-states. Additionally, for the charging effect to be noticeable at the avoided crossing, it is necessary for the latter to occur for a sufficiently small value of the impurity Josephson energy E_J. Otherwise, the non-linearity of the small junction will not be sufficient to observe significant charge dispersion (see the single-junction example in Figure 2.1). Figure 5.7 illustrates the outcomes of the numerical diagonalisation, showcasing the energy of the first three states in the circuit. It displays their dependence on the impurity Josephson energy, with one ($n_\mathrm{g}^\mathrm{tot} = 0.5$, dashed lines) and zero ($n_\mathrm{g}^\mathrm{tot} = 0$, solid lines) quasiparticles in the chain. The parameters employed are the same as those given in table 5.2, excluding the inductance $L = \Phi_0^2/E_\mathrm{J}^\mathrm{ch}$ which is set to 1.8 nH and has been adjusted in line with the previously described criteria. To perform the numerical diagonalisation, a total of 31 charge states, $n_0 \in \{-15, \ldots, 15\}$ and 15 Fock states, $N_1 \in \{0, 1, \ldots, 14\}$, were used. As speculated, the charge dispersion, as given by the difference between the solid and dashed lines, increases as the non-linearity of the impurity increases (*i.e.* as E_J decreases). Although the eigen-frequencies produced by this toy model do not correspond to the experimental results, the simulated spectrum shows an avoided crossing for a finite value of the external flux Φ_B, thus reproducing the doubling of the spectral lines observed in the experiment. The right panel of Figure 5.7 provides an enlarged image of the simulated avoided crossing.

5.3.3. Variational approach

The two-junction toy model can replicate the observed doubling of the spectroscopic line at the avoided crossing qualitatively, but it fails to achieve quantitative agreement. To establish a microscopic correspondence between the experimental findings and the theoretical model, we employ a variational method that accounts for all the degrees of freedom of the circuit. The following is only a brief introduction to the calculation principle, and the actual calculation of the spectrum relies on technical details that are beyond the scope of this manuscript. The complete method to compute the excited states of the system based on the compactifiaction of the variational ansatz was developed by Tojosoa Nantenaina Raveloarijaona as part of his PhD work.

We aim to find a linear Hamiltonian that best reproduces the low energy spectrum of (5.7),

$$\hat{H}_\mathrm{var} = \frac{(2e)^2}{2} \sum_{i,j} (\hat{n}_i - n_{\mathrm{g},i}) \, [C]^{-1}_{i,j} \, (\hat{n}_j - n_{\mathrm{g},j}) + \frac{\Phi_0^2}{2L} \sum_k (\hat{\varphi}_{k+1} - \hat{\varphi}_k)^2 + \frac{x}{2}\hat{\varphi}_0^2 \,, \qquad (5.16)$$

where we simply replaced the cosine term of equation (5.7) by a quadratic term whose corresponding energy scale, x, is a varitional parameter to be optimized. The trial Hamiltonian is quadratic in φ_0 such that $\hat{H}_\mathrm{var}$ is not invariant under the global 2π-

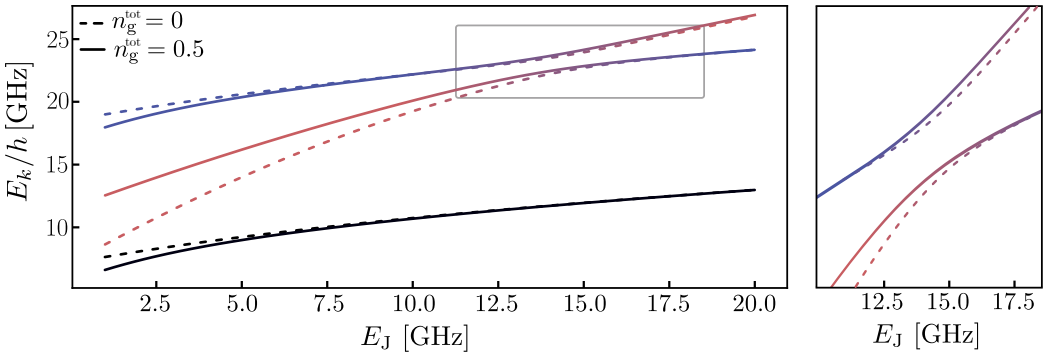

Figure 5.7.: Energy of the first three odd excited states of the two-junction chain as a function of the impurity Josephson energy E_J. The energy range on the x-axis corresponds to the variations of the Josephson energy of the small junction with the external magnetic flux. **Left.** Energy of the first three states for an even number of quasiparticles ($n_g^{tot} = 0$, solid lines) or an odd number of quasiparticles ($n_g^{tot} = 0.5$, dashed lines) in the system. The smallest E_J value corresponds to $|\Phi_B| = 0.5\Phi_0$. The spectrum shows an avoided crossing, which we highlight with a colour gradient. **Right.** Zoom in on the grey rectangle in the left panel, which clearly shows the doubling of the energy levels caused by the parity of the number of background charges.

translation anymore. This symmetry is restored by using the compactification operator $\hat{\circlearrowleft}$ on the eigenstates of $\hat{H}_{\text{var}}$. The trial states for the variational procedure are then

$$\left|\psi^{\circlearrowleft}(x, n_g)\right\rangle = \hat{\circlearrowleft} \left|\psi(x, n_g)\right\rangle \,, \tag{5.17}$$

where the compactification operator is defined as [Kaur et al. 2021]

$$\hat{\circlearrowleft} = \sum_{w \in \mathbb{Z}} e^{i2\pi w \sum_k \hat{n}_k} \,. \tag{5.18}$$

The effect of this operator is simply to sum the wavefunctions obtained by the $2\pi w$ displacement of the state $|\psi\rangle$ to be compactified, for all integer values of w,

$$\psi^{\circlearrowleft}(\overrightarrow{\varphi}) = \sum_{w \in \mathbb{Z}} \psi(\overrightarrow{\varphi} - 2\pi w \overrightarrow{u}) \,, \tag{5.19}$$

where $\overrightarrow{\varphi} = (\hat{\varphi}_0, \hat{\varphi}_1, \ldots, \hat{\varphi}_N)$. Hence, the wavefunction's symmetry is restored,

$$\psi^{\circlearrowleft}(\overrightarrow{\varphi} + 2\pi\overrightarrow{u}) = \sum_{w\in\mathbb{Z}} \langle \overrightarrow{\varphi} - 2\pi(w-1)\overrightarrow{u}|\psi\rangle = \sum_{w\in\mathbb{Z}} \psi(\overrightarrow{\varphi} - 2\pi w\overrightarrow{u}) = \psi^{\circlearrowleft}(\overrightarrow{\varphi})\,. \quad (5.20)$$

The quantity that needs to be minimized for $\hat{H}_{\text{var}}$ to accurately reproduce the low energy spectrum of $\hat{H}$ is

$$E_k = \frac{\langle \psi_k^{\circlearrowleft}(x_k, n_{\text{g}})|\hat{H}(n_{\text{g}})|\psi_k^{\circlearrowleft}(x_k, n_{\text{g}})\rangle}{\langle \psi_k^{\circlearrowleft}(x, n_{\text{g}})|\psi_k^{\circlearrowleft}(x_k, n_{\text{g}})\rangle}\,, \quad (5.21)$$

with $|\psi_k^{\circlearrowleft}(x_k, n_{\text{g}})\rangle$ the compactified k-th eigenstate of Hamiltonian (5.16). Since we want to reproduce the low energy spectrum of $\hat{H}$ up to a few excited states, the optimisation procedure is repeated for all desired states, with a different variational parameter x_k for each state. In practice, the first three odd excited states are computed. The first and third excited states of mode $k = 0$, $|\psi_0^1\rangle$ and $|\psi_0^3\rangle$, and the first excited state of mode $k = 1$, $|\psi_1^1\rangle$, are approximated by the variational method and the Hamiltonian $\hat{H}$ is projected onto the subspace formed by these three states. The resulting three by three matrix is then numerically diagonalised to obtain the spectrum of the system. Figure 5.8 shows the computed spectrum as a function of the external magnetic flux. As can be seen in the top panel, the charge dispersion of the energy levels increases as $|\Phi_{\text{B}}|$ approaches $0.5\Phi_0$, which we expect from the increase in the small junction non-linearity as $|\Phi_{\text{B}}|$ approaches $0.5\Phi_0$. At $|\Phi_{\text{B}}| = 0.5\Phi_0$, the charge dispersion of the state $|\psi_1^1\rangle \equiv |n_a = 0, n_b = 1\rangle$ (blue line) remains small and within the linewidth of the mode, $|\langle\psi_1^1|\hat{H}(n_{\text{g}} = 0)|\psi_1^1\rangle - \langle\psi_1^1|\hat{H}(n_{\text{g}} = 0.5)|\psi_1^1\rangle| < \Gamma_{\text{b}}^{\text{r}} + \Gamma_{\text{b}}^{\text{nr}}$, which explains why we never observed charging effects in the single-tone spectroscopy of mode b away from the avoided crossing. On the contrary, for the state $|\psi_0^1\rangle$ the charge dispersion near $|\Phi_{\text{B}}| = 0.5\Phi_0$ is much more significant and could in principle be observed in the single-tone spectroscopy of mode a. However, since the mode a frequency drops out of the measurement band near $|\Phi_{\text{B}}| = 0.5\Phi_0$, we could only resolve the $0 \to 1$ transition of mode a when it is not significantly affected by charge noise. The above explains why we could not observe any charging effects in the single-tone spectroscopy of the device. In addition, we can see that the coupling between states $|\psi_1^1\rangle$ and $|\psi_0^3\rangle$ occurs at a flux point where the third excited state of mode b, $|\psi_0^3\rangle$, starts to develop a significant charge dispersion. A zoom in on the avoided crossing is shown in the bottom panel of Figure 5.8. The results of the variational approach are in excellent agreement with the experimental data of Figure 5.4, both for the position and the magnitude of the level splitting.

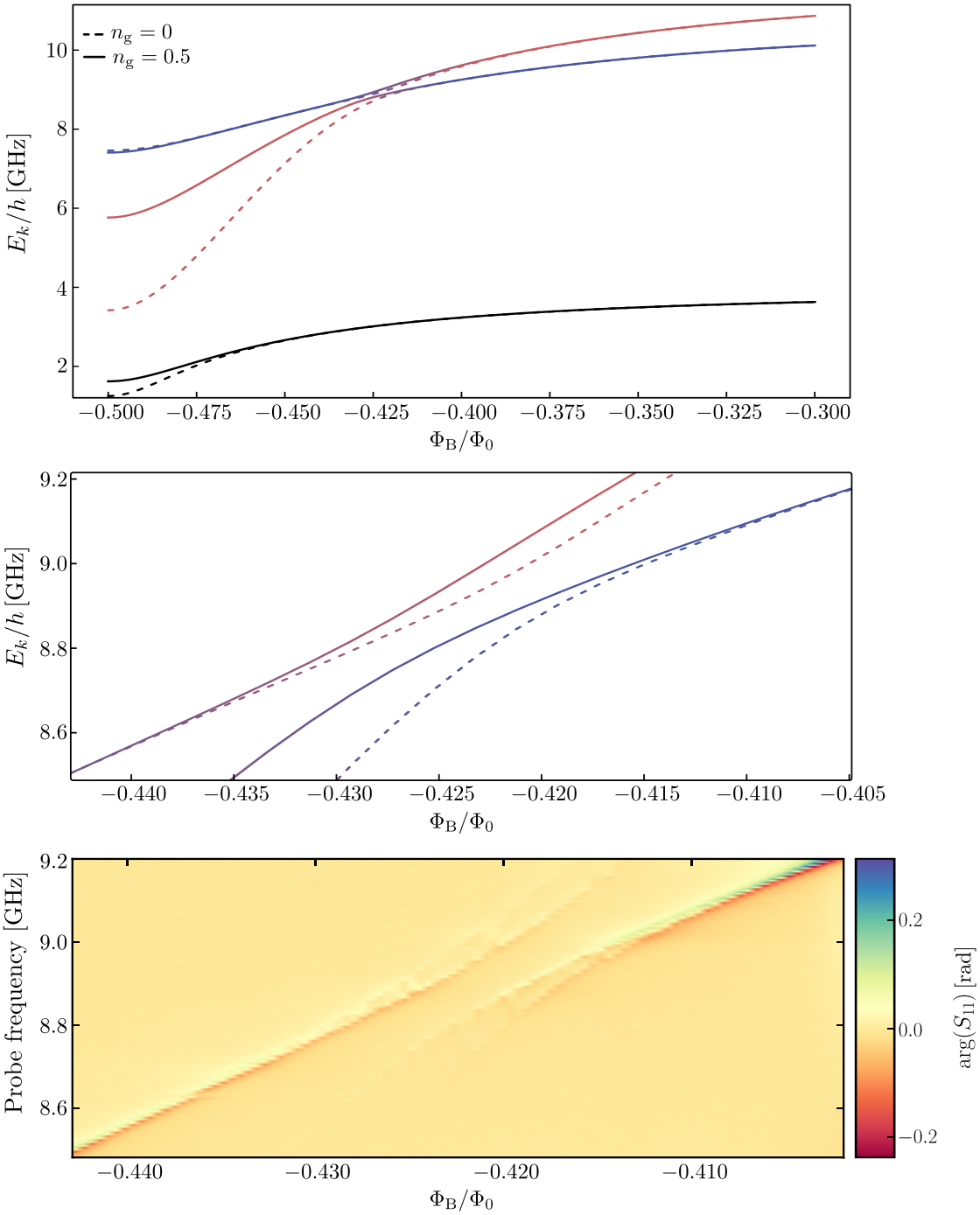

Figure 5.8.: **Top&Middle.** Spectrum computed with the variational approach with (solid lines) and without (dashed lines) quasiparticles in the system as a function of the external magnetic flux Φ_B. **Middle.** Zoom on the avoided crossing. **Bottom.** Experimental data for comparison with the middle panel.

6

Conclusion and perspectives

6.1. Conclusion

In this thesis work, we have investigated the effective photon-photon interactions resulting from the ultrastrong coupling of a multimode microwave resonator to a single quantum impurity. The system was deliberately designed to tailor a specific photon-photon interaction, namely three-photon conversion, in the low power regime. This nonlinear process couples a single-photon state of a given resonant mode of the system, called mode b, to a three-photon state of another mode, called a. The strength of this nonlinear coupling, characterised by the coupling constant $g^{1\leftrightarrow 3}$, greatly overcomes the intrinsic losses of the two modes involved, $g^{1\leftrightarrow 3} \gg \Gamma^{\mathrm{nr}}_{a(b)}$. Two different regimes have been studied.

The first regime, called the ***strong down-conversion regime***, consists of a strong coupling of the system to the measurement line. In this regime we observed a drastic increase in the non-radiative losses of the high-frequency mode (mode b) as the single-photon state and the three-photon state are brought into resonance. This increase in Γ^{nr}_{b} is directly related to the three-photon conversion process by measuring the multimode fluorescence of the system. In this experiment, we measured the power radiated around the resonant frequency of mode a when the system is driven with a coherent tone in resonance with mode b. To our knowledge, this result constitutes the first ***direct observation*** of the spontaneous decay of microwave photons in the low power regime. The systematic analysis of the linear spectroscopy of the device allowed the extraction of the system parameters, so that the measured spectrum of down-converted photons could be compared with the predictions of a two-mode effective model. Although having clear limitations, the theoretical predictions explain the observed multimode fluorescence of the system remarkably well.

In the second regime, called the ***multiphoton strong coupling***, the system is weakly coupled to the measurement line so that the nonlinear coupling strength, $g^{1\leftrightarrow 3}$, overcomes both the intrinsic losses and the radiative decay rates of the system, $g^{1\leftrightarrow 3} \gg \{\Gamma^{\mathrm{nr}}_{a(b)}, \Gamma^{\mathrm{r}}_{a(b)}\}$. In this situation, an avoided crossing could be resolved in the linear spectroscopy of the device, the observation of which is reminiscent of three-photon Rabi oscillation at a rate of 175 MHz between modes a and b. The quantum superposition of the single-photon state with the three-photon states allowed the observation of significant charging effects on the higher excited state of the system.

6.2. Perspectives

Measuring the power emitted by the spontaneous down-conversion of microwave photons is only a first step towards very exciting quantum optics experiments in the microwave domain. In this section we present immediate prospects for the work presented in this thesis.

6.2.1. Correlations measurements

A direct perspective of the multimode fluorescence experiment presented in chapter 4 would be to measure the second-order correlations of the itinerant radiation produced by the down-conversion process, which are directly related to the second-order coherence function of $\hat{a}$,

$$G^{(2)}(\tau) = \left\langle \hat{\alpha}^{\dagger}_{\mathrm{out}}(0)\hat{\alpha}^{\dagger}_{\mathrm{out}}(\tau)\hat{\alpha}_{\mathrm{out}}(\tau)\hat{\alpha}_{\mathrm{out}}(0) \right\rangle = {\Gamma^{\mathrm{r}}_a}^4 \left\langle \hat{a}^{\dagger}(0)\hat{a}^{\dagger}(\tau)\hat{a}(\tau)\hat{a}(0) \right\rangle . \tag{6.1}$$

The measurement of this quantity provides information about the nature of the emitted photons. Coherent radiation, such as that used to drive the system, is characterised by a constant value of $G^{(2)}(\tau)$. On the other hand, $G^{(2)}(0) > G^{(2)}(\tau > 0)$ indicates ***photon bunching***, which refers to photons that tend to be emitted in bunches. Since the observed down-conversion is associated with the cascaded decay of the $|3_a, 0_b\rangle$ state with the successive emission of three photons in the measuremernt line, we expect the photons to be emitted in packets of three. Using similar methods to those used to calculate the power spectrum in section 2.3.3, it can be shown that [Vakhtel 2023]

$$G^{(2)}(\tau) = {\Gamma^{\mathrm{r}}_a}^4 9|\Xi|^2 e^{-2\Gamma^{\mathrm{tot}}_a \tau} , \tag{6.2}$$

which clearly predicts photon bunching, since $G^{(2)}(0) > G^{(2)}(\tau > 0)$.

Recent cicuit-QED experiments have demonstrated the possibility of measuring such second-order correlations of itinerant microwave photons using linear detectors as those commonly used in experiments involving microwave radiations[1] [Bozyigit et al. 2011; Lang et al. 2011]. However, to achieve the same signal-to-noise ratio as for power measurements, the number of repetitions used for averaging must be squared. Given the already large number of repetitions needed to measure the emitted power, improving the amplification chain appears to be a crucial step towards the measurement of the down-converted photon statistics. A direct improvement to the current measurement setup would be to reduce the insertion losses that occur between the radiation source and the TWPA, allowing both a stronger signal and a lower noise temperature of the amplification chain.

6.2.2. Resolving the indivudual photons

From the theoretical model developed in section 2.3.3, we expect the down-conversion process to produce three photons of different frequencies due to the anharmonicity of

[1] Single-photon counters do not yet exist at microwave frequencies.

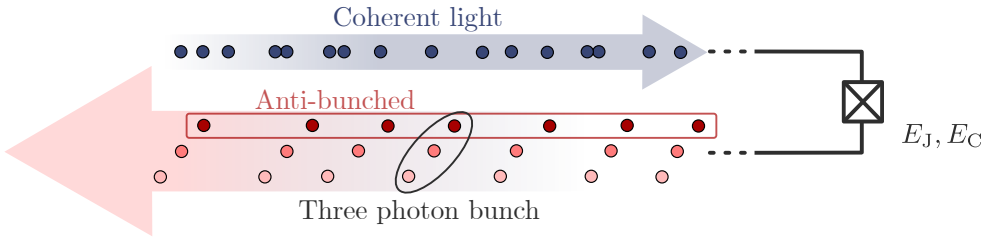

Figure 6.1.: Cartoon of the expected photon statistics. The down-conversion process produces bunches of three photons, while these photons are emitted individually in an anti-bunched manner.

mode a. In the work presented here, we could not clearly distinguish several emission peaks in the measured spectrum due to the strong coupling to the measurement line. The designing of a new device with reduced coupling to the measurement might allow the spectral structure of the emission spectrum to be resolved. Several emission peaks could be distinguished in the power spectrum and the statistics of the photons associated with the different peaks together with their cross-correlations could be investigated. Although the radiation produced by the down-conversion consists of bunches of photons, the single transitions resulting from the cascaded decay can be expected to produce ***anti-bunched photons*** (see Figure 6.1) since the $|3_a, 0_b\rangle$ state must be repopulated before any of the three photons can be produced again. This anti-bunching could in principle be observed in the measurement of the "filtered" second-order correlations,

$$\tilde{G}^2(\tau) = \left\langle \hat{\tilde{\alpha}}^\dagger_{\text{out}}(0)\hat{\tilde{\alpha}}^\dagger_{\text{out}}(\tau)\hat{\tilde{\alpha}}_{\text{out}}(\tau)\hat{\tilde{\alpha}}_{\text{out}}(0)\right\rangle , \tag{6.3}$$

where, $\hat{\tilde{\alpha}}_{\text{out}}$ is the filtered output field, defined as

$$\hat{\tilde{\alpha}}_{\text{out}} = \int_0^\infty \mathrm{d}\omega g(\omega)\hat{\alpha}(-\omega)e^{-i\omega t} , \tag{6.4}$$

and $g(\omega)$ is a window function centered around the frequency of interest.

Appendices

A

Two mode effective Hamiltonian

In this appendix, the detailed derivation of the two mode effective Hamiltonian equation (2.28) is presented.

The Hamiltonian of the system in the normal mode basis is given by equation (2.19),

$$\hat{H} = \hbar\omega_k \hat{a}_k^\dagger \hat{a}_k - E_\mathrm{J}\left[\cos\hat{\varphi}_{0,k} + \frac{1}{2}\hat{\varphi}_{0,k}^2\right] \tag{A.1}$$

and we want to compute the projection in equation (2.26). With the definition of the projector given in equation (2.27),

$$\begin{aligned}\hat{H}_\mathrm{eff} = & \sum_{k=a,b} \hbar\omega_k \hat{a}_k^\dagger \hat{a}_k \\ & - E_\mathrm{j} \sum_{i,j} |i\rangle \otimes |0\rangle \langle i| \otimes \langle 0| \cos\hat{\varphi}_{0,k} |j\rangle \otimes |0\rangle \langle j| \otimes \langle 0| \\ & - E_\mathrm{j} \sum_{i,j} |i\rangle \otimes |0\rangle \langle i| \otimes \langle 0| \frac{1}{2}\hat{\varphi}_{0,k}^2 |j\rangle \otimes |0\rangle \langle j| \otimes \langle 0| \ .\end{aligned} \tag{A.2}$$

Let's calculate the cosine term in $\hat{H}_\mathrm{eff}$ first:

$$\begin{aligned}\cos\left(\varphi_{0,k}\left(\hat{a}_k^\dagger + \hat{a}_k\right)\right) &= \frac{1}{2}\sum_{\pm}\left(\prod_{k=0}^{N} e^{\pm i\varphi_{0,k}\hat{a}_k^\dagger}\right)\left(\prod_{k=0}^{N} e^{\pm i\varphi_{0,k}\hat{a}_k}\right)\left(\prod_{k=0}^{N} e^{-\frac{1}{2}\varphi_{0,k}^2}\right) \\ &= \frac{1}{2}\left(\prod_{k=0}^{N} e^{-\frac{1}{2}\varphi_{0,k}^2}\right)\sum_{\pm}\left(\prod_{k\neq k_a,k_b} e^{\pm i\varphi_{0,k}\hat{a}_k^\dagger}\right)\left(\prod_{k=k_a,k_b} e^{\pm i\varphi_{0,k}\hat{a}_k^\dagger}\right) \\ &\quad \times \left(\prod_{k=k_a,k_b} e^{\pm i\varphi_{0,k}\hat{a}_k}\right)\left(\prod_{k\neq a,b} e^{\pm i\varphi_{0,k}\hat{a}_k}\right)\end{aligned} \tag{A.3}$$

Since $e^{\pm i\varphi_{0,k}\hat{a}_k}\,|i\rangle\otimes|0\rangle = \mathbb{1}\,|i\rangle\otimes|0\rangle$ for $k \neq k_a, k_b$,

$$\langle i|\otimes\langle 0|\cos\hat{\varphi}_{0,k}\,|i\rangle\otimes|0\rangle = \exp\left(-\frac{1}{2}\sum_{k\neq k_a,k_b}\varphi_{0,k}^2\right)\langle i|\otimes\langle 0|\cos\left(\sum_{k=k_a,k_b}\hat{\varphi}_{0,k}\right)|i\rangle\otimes|0\rangle\ . \tag{A.4}$$

Calculating the last term of $\hat{H}_{\text{eff}}$ is straightforward:

$$\begin{aligned}\langle i|\otimes\langle 0|\,\frac{1}{2}\hat{\varphi}_{0,k}^2\,|j\rangle\otimes|0\rangle = \langle i|\otimes\langle 0|\left[\frac{1}{2}\sum_{k=k_a,k_b}\hat{\varphi}_{0,k}\right]^2|j\rangle\otimes|0\rangle \\ + \langle i|\otimes\langle 0|\,\frac{1}{2}\sum_{k\neq k_a,k_b}\varphi_{0,k}^2\,|j\rangle\otimes|0\rangle\ .\end{aligned} \tag{A.5}$$

Finally, the effective Hamiltonian is given by

$$\begin{aligned}\hat{H}_{\text{eff}} = \sum_{k=k_a,k_b}\hbar\omega_k\hat{a}_k^\dagger\hat{a}_k - E_{\text{J}}^{\text{S}}\cos\left(\sum_{k=k_a,k_b}\hat{\varphi}_{0,k}\right) - \frac{E_{\text{J}}}{2}\left(\sum_{k=k_a,k_b}\hat{\varphi}_{0,k}\right)^2 \\ -\frac{E_{\text{J}}}{2}\sum_{k\neq k_a,k_b}\varphi_{0,k}^2\,,\end{aligned} \tag{A.6}$$

where we defined the renormalised Josephson energy:

$$E_{\text{J}}^{\text{S}} = E_{\text{J}}\exp\left(-\frac{1}{2}\sum_{k\neq k_a,k_b}\phi_{0,k}^2\right)\ . \tag{A.7}$$

B

Cosine matrix elements in the two modes model

In this appendix, we present a derivation of the cosine matrix elements of the two mode effective Hamiltonian, which allows us to derive equation (2.31). We write the matrix element as

$$\left\langle n'm' \right| \cos\hat{\varphi}_0 \left| nm \right\rangle = c^{(a)}_{n'n} c^{(b)}_{m'm} + s^{(a)}_{n'n} s^{(b)}_{m'm} \,, \tag{B.1}$$

where the sine and cosine matrix elements for mode a are defined as

$$c^{(i)}_{kl} = \left\langle k \middle| \cos\left(\varphi_{0,a}\left(\hat{a}^\dagger + \hat{a}\right)\right) \middle| l \right\rangle \,, \tag{B.2}$$

$$s^{(i)}_{kl} = \left\langle k \middle| \sin\left(\varphi_{0,a}\left(\hat{a}^\dagger + \hat{a}\right)\right) \middle| l \right\rangle \,. \tag{B.3}$$

The same applies to mode b by simply replacing $\hat{a}$ with $\hat{b}$ in the above. Using $e^{\lambda(\hat{A}+\hat{B})} = e^{\lambda\hat{A}} e^{\lambda\hat{B}} e^{\lambda^2/2[\hat{B},\hat{A}]}$ for two operators such that $[[\hat{B},\hat{A}],\hat{A}] = [[\hat{B},\hat{A}],\hat{B}] = 0$, we can write

$$\begin{aligned} \cos\left(\varphi_{0a}\left(\hat{a}^\dagger + \hat{a}\right)\right) &= \frac{1}{2}\left[e^{i\varphi_{0a}\left(\hat{a}^\dagger+\hat{a}\right)} + e^{-i\varphi_{0a}\left(\hat{a}^\dagger+\hat{a}\right)}\right] \\ &= \frac{e^{-\varphi_{0a}^2/2}}{2}\left[e^{i\varphi_{0a}\hat{a}^\dagger} e^{i\varphi_{0a}\hat{a}} + e^{-i\varphi_{0a}\hat{a}^\dagger} e^{-i\varphi_{0a}\hat{a}}\right] \,, \end{aligned} \tag{B.4}$$

such that

$$\begin{aligned} e^{i\varphi_{0a}\hat{a}^\dagger} e^{i\varphi_{0a}\hat{a}} \left| l \right\rangle &= e^{i\varphi_{0a}\hat{a}^\dagger} \sum_{j=0}^{\infty} \frac{(i\varphi_{0a})^j}{j!} \hat{a}^j \left| l \right\rangle \\ &= e^{i\varphi_{0a}\hat{a}^\dagger} \sum_{j=0}^{l} \frac{(i\phi_{0a})^j}{j!} \sqrt{\frac{l!}{(l-j)!}} \left| l-j \right\rangle \\ &= \sum_{j'=0}^{\infty} \frac{(i\varphi_{0a})^{j'}}{j'!} \hat{a}^{\dagger j'} \sum_{j=0}^{l} \frac{(i\varphi_{0a})^j}{j!} \sqrt{\frac{l!}{(l-j)!}} \left| l-j \right\rangle \\ &= \sum_{j=0}^{l} \frac{(i\varphi_{0a})^j}{j!} \sqrt{\frac{l!}{(l-j)!}} \sum_{j'=0}^{\infty} \frac{(i\varphi_{0a})^{j'}}{j'!} \sqrt{\frac{(l-j+j')!}{(l-j)!}} \left| l-j+j' \right\rangle \,. \end{aligned} \tag{B.5}$$

Using $\langle k|l-j+j'\rangle = \delta_{k,l-j+j'}$ we end up with

$$\langle k|\, e^{i\varphi_{0a}\hat{a}^\dagger} e^{i\varphi_{0a}\hat{a}}\, |l\rangle = \sum_{j=0}^{l} (i\varphi_{0a})^{2j+k-l}\, \frac{k!}{j!(k-l+j)!(l-j)!} \sqrt{\frac{l!}{k!}}\,. \tag{B.6}$$

We distinguish the two cases with $k-l$ odd and even. If $k-l$ is even,

$$(i\varphi_{0a})^{2j+k-l} = (-1)^{j+\frac{k-l}{2}} \left(\varphi_{0a}^2\right)^j \varphi_{0a}^{k-l}\,.$$

On the other hand, if $k-l$ is odd,

$$(i\varphi_{0a})^{2j+k-l} = i \times (-1)^{j+\frac{k-l-1}{2}} \left(\varphi_{0a}^2\right)^j \varphi_{0a}^{k-l}\,.$$

In then comes that

$$\langle k|\, e^{i\varphi_{0a}\hat{a}^\dagger} e^{i\varphi_{0a}\hat{a}}\, |l\rangle = \begin{cases} (-1)^{\frac{k-l}{2}} \varphi_{0a}^{k-l} \sqrt{\frac{l!}{k!}} \mathcal{L}_l^{k-l}(\varphi_{0a}^2) & \text{if } k+l \text{ even,} \\ \\ i \times (-1)^{\frac{k-l-1}{2}} \varphi_{0a}^{k-l} \sqrt{\frac{l!}{k!}} \mathcal{L}_l^{k-l}(\varphi_{0a}^2) & \text{otherwise,} \end{cases} \tag{B.7}$$

where we introduced the expression of the associated Laguerre polynomial defined, for $k \geq 0$, by

$$\mathcal{L}_n^k(x) = \sum_{j=0}^{n} (-1)^j \frac{(n+k)!}{(n-j)!(k+j)!j!} x^j\,. \tag{B.8}$$

It directly comes that

$$\langle k|\, e^{-i\varphi_{0a}\hat{a}^\dagger} e^{-i\varphi_{0a}\hat{a}}\, |l\rangle = \begin{cases} (-1)^{\frac{k-l}{2}} \varphi_{0a}^{k-l} \sqrt{\frac{l!}{k!}} \mathcal{L}_l^{k-l}(\varphi_{0a}^2) & \text{if } k+l \text{ even,} \\ \\ -i \times (-1)^{\frac{k-l-1}{2}} \varphi_{0a}^{k-l} \sqrt{\frac{l!}{k!}} \mathcal{L}_l^{k-l}(\varphi_{0a}^2) & \text{otherwise.} \end{cases} \tag{B.9}$$

Finally we find an expression for $c_{kl}^{(a)}$,

$$c_{kl}^{(a)} = \begin{cases} (-1)^{\frac{k-l}{2}} \varphi_{0a}^{k-l} e^{-\frac{\varphi_{0a}^2}{2}} \sqrt{\frac{l!}{k!}} \mathcal{L}_l^{k-l}(\varphi_{0a}^2) & \text{if } k+l \text{ even,} \\ \\ 0 & \text{otherwise.} \end{cases} \tag{B.10}$$

We proceed to the same type of calculation for $s_{kl}^{(i)}$,

$$\begin{aligned}\sin\hat{\varphi}_a &= \frac{1}{2i}\left(e^{i\varphi_{0a}\left(\hat{a}^\dagger+\hat{a}\right)} - e^{-i\varphi_{0a}\left(\hat{a}^\dagger+\hat{a}\right)}\right) \\ &= \frac{e^{-\varphi_{0a}^2}}{2i}\left[e^{i\varphi_{0a}\hat{a}^\dagger}e^{i\varphi_{0a}\hat{a}} - e^{-i\varphi_{0a}\hat{a}^\dagger}e^{-i\varphi_{0a}\hat{a}}\right], \end{aligned} \tag{B.11}$$

such that we find:

$$s_{kl}^{(a)} = \begin{cases} 0 & \text{if } k+l \text{ even}, \\ (-1)^{\frac{k-l-1}{2}}\phi_{0a}^{k-l}e^{-\frac{\varphi_{0a}^2}{2}}\sqrt{\frac{l!}{k!}}\mathcal{L}_l^{k-l}(\varphi_{0a}^2) & \text{otherwise.} \end{cases} \tag{B.12}$$

We can then directly apply equations (B.10) and (B.12) to derive equation (2.31),

$$\langle 3_a, 0_b|\cos\left(\hat{\varphi}_a+\hat{\varphi}_b\right)|0_a, 1_b\rangle = c_{03}^{(a)}c_{10}^{(b)} + s_{03}^{(a)}s_{10}^{(b)} = s_{03}^{(a)}s_{10}^{(b)}\,, \tag{B.13}$$

where we used the fact that $c_{03}^{(a)} = c_{10}^{(b)} = 0$. The above expression is easily evaluated and we get

$$\langle 3_a, 0_b|\cos\left(\hat{\varphi}_a+\hat{\varphi}_b\right)|0_a, 1_b\rangle = -\frac{1}{\sqrt{6}}e^{-\frac{1}{2}\left(\varphi_{0a}^2+\varphi_{0b}^2\right)}\varphi_{0a}^3\varphi_{0b}\,. \tag{B.14}$$

C

Calculation of the emitted spectrum

C.1. Details for the calculation of equation 2.67

In chapter 2 we came up with the following formula for the spectrum of down-converted photons,

$$I(\tilde{\omega}) = \Gamma_a^{\mathrm{r}} \sum_{\mu\nu} a_\mu \left(-i\tilde{\omega}\mathbb{1} - \mathcal{L}\right)^{-1}_{\mu\nu} \left\langle \hat{a}^\dagger \hat{\rho}_\mu(0) \right\rangle + \text{c.c.}\,. \tag{C.1}$$

In order to evaluate the above expression, it is necessary to write the initial conditions $\left\langle \hat{a}^\dagger \hat{\rho}_\mu(0) \right\rangle$ explicitly. The sum in equation (C.1) spans the ensemble $\{01, 12, 23, 20, 31\}$ and these initial conditions are formally written as

$$\begin{gathered} \langle \hat{a}^\dagger \hat{\rho}_{01} \rangle = \langle \hat{\rho}_{11} \rangle,\ \langle \hat{a}^\dagger \hat{\rho}_{12} \rangle = \sqrt{2}\, \langle \hat{\rho}_{22} \rangle\,,\ \langle \hat{a}^\dagger \hat{\rho}_{23} \rangle = \sqrt{3}\, \langle \hat{\rho}_{33} \rangle\,, \\ \langle \hat{a}^\dagger \hat{\rho}_{20} \rangle = \sqrt{3}\, \langle \hat{\rho}_{30} \rangle\,,\ \langle \hat{a}^\dagger \hat{\rho}_{31} \rangle = 0, \end{gathered} \tag{C.2}$$

where we used the fact that $\hat{a}^\dagger \hat{\rho}_{\mathrm{n,m}} = \sqrt{n+1}\hat{\rho}_{\mathrm{n+1,m}}$ for $n < 3$, and $\hat{a}^\dagger \hat{\rho}_{\mathrm{n,m}} = 0$ for $n \geq 3$ (because of the truncation of the Hilbert space). Looking at the equations in (C.2), we see that we have to find the stationary solutions for $\langle \hat{\rho}_{\mu\nu} \rangle$ with $\mu, \nu \in \{30, 00, 11, 22, 33, 03\}$. This is done by solving

$$\sum_\nu (\mathcal{L}_2)_{\mu\nu} \langle \hat{\rho}_\nu \rangle = 0\,, \tag{C.3}$$

where $\mathcal{L}_2$ was introduced in 2.3.3 and is formally given by

$$\mathcal{L}_2 = \begin{pmatrix} i\tilde{\omega}_{30} - \frac{3}{2}\Gamma_a^{\mathrm{r}} & ig_{\mathrm{eff}}\langle \hat{b}^\dagger \rangle & 0 & 0 & -ig_{\mathrm{eff}}\langle \hat{b} \rangle & 0 \\ ig_{\mathrm{eff}}\langle \hat{b} \rangle & 0 & \Gamma_a^{\mathrm{r}} & 0 & 0 & -ig_{\mathrm{eff}}\langle \hat{b}^\dagger \rangle \\ 0 & 0 & -\Gamma_b^{\mathrm{r}} & 2\Gamma_b^{\mathrm{r}} & 0 & 0 \\ 0 & 0 & 0 & -2\Gamma_a^{\mathrm{r}} & 3\Gamma_a^{\mathrm{r}} & 0 \\ -ig_{\mathrm{eff}}\langle \hat{b} \rangle & 0 & 0 & 0 & -3\Gamma_a^{\mathrm{r}} & ig_{\mathrm{eff}}\langle \hat{b}^\dagger \rangle \\ 0 & -ig_{\mathrm{eff}}\langle \hat{b} \rangle & 0 & 0 & ig_{\mathrm{eff}}\langle \hat{a} \rangle & -i\tilde{\omega}_{30} - \frac{3}{2}\Gamma_a^{\mathrm{r}} \end{pmatrix}. \tag{C.4}$$

Applying equation (C.3) to $\mu = 30$ gives

$$\langle\hat{\rho}_{30}\rangle = i\Xi\left(\langle\hat{\rho}_{00}\rangle - \langle\hat{\rho}_{33}\rangle\right) , \tag{C.5}$$

where we defined

$$\Xi = \frac{g_{\text{eff}}\langle\hat{b}^\dagger\rangle}{\frac{3}{2}\Gamma_a^{\text{r}} - i\tilde{\omega}_{30}} . \tag{C.6}$$

Similarly, applying equation (C.3) to $\mu = 11$ gives

$$\begin{aligned}\Gamma_a^{\text{r}}\langle\hat{\rho}_{11}\rangle &= ig_{\text{eff}}\langle\hat{b}^\dagger\rangle\langle\hat{\rho}_{03}\rangle - ig_{\text{eff}}\langle\hat{b}\rangle\langle\hat{\rho}_{30}\rangle \\ &= i\Xi\left(\frac{3}{2}\Gamma_a^{\text{r}} - i\tilde{\omega}_{30}\right)\langle\hat{\rho}_{30}\rangle^* - i\Xi^*\left(\frac{3}{2}\Gamma_a^{\text{r}} + i\tilde{\omega}_{30}\right)\langle\hat{\rho}_{30}\rangle ,\end{aligned} \tag{C.7}$$

where we have used the fact that $\langle\hat{\rho}_{03}\rangle = \langle\hat{\rho}_{30}\rangle^*$. Substituting $\langle\hat{\rho}_{30}\rangle$ for its expression given in equation (C.5), we find

$$\langle\hat{\rho}_{11}\rangle = 3|\Xi|^2\left(\langle\hat{\rho}_{00}\rangle - \langle\hat{\rho}_{33}\rangle\right) . \tag{C.8}$$

For $\mu = 33$ and following the same procedure as before, we obtain

$$\langle\hat{\rho}_{33}\rangle = |\Xi|^2\left(\langle\hat{\rho}_{00}\rangle - \langle\hat{\rho}_{33}\rangle\right) \tag{C.9}$$

Finally, for $\mu = 22$, equation (C.3) readily gives

$$\langle\hat{\rho}_{22}\rangle = \frac{3}{2}\langle\hat{\rho}_{33}\rangle = \frac{3}{2}|\Xi|^2\left(\langle\hat{\rho}_{00}\rangle - \langle\hat{\rho}_{33}\rangle\right) . \tag{C.10}$$

Using the fact that $\mathbb{1} = \hat{\rho}_{00} + \hat{\rho}_{11} + \hat{\rho}_{22} + \hat{\rho}_{33}$ (*i.e.* the completeness relation of the truncated basis of mode a) to eliminate $\hat{\rho}_{00}$, we obtain the following result for the useful initial conditions:

$$\begin{pmatrix}\langle\hat{\rho}_{11}\rangle\\ \langle\hat{\rho}_{22}\rangle\\ \langle\hat{\rho}_{33}\rangle\\ \langle\hat{\rho}_{30}\rangle\end{pmatrix} = \begin{pmatrix}3|\Xi|^2\\ \frac{3}{2}|\Xi|^2\\ |\Xi|^2\\ i\Xi\end{pmatrix} \times \left(1 - \langle\hat{\rho}_{11}\rangle - \langle\hat{\rho}_{22}\rangle - \langle\hat{\rho}_{33}\rangle\right) . \tag{C.11}$$

For a weak drive, the excited states populations can be neglected so that $(1 - \langle\hat{\rho}_{11}\rangle - \langle\hat{\rho}_{22}\rangle - \langle\hat{\rho}_{33}\rangle) = 1$. Ξ actually depends on $\langle\hat{b}^\dagger\rangle$. In this weak coulping regime, we can express the latter by taking the steady-state solution of equation (2.63). Together with equation (C.3) for $\mu = 03$ they form the following system of equations:

$$0 = -\left(i\tilde{\omega}_b + \frac{\Gamma_b^{\text{r}}}{2}\right)\langle\hat{b}\rangle - ig_{\text{eff}}\langle\hat{\rho}_{03}\rangle - i\epsilon_{\text{d}} , \tag{C.12}$$

$$0 = -\left(i\tilde{\omega}_{30} + \frac{3}{2}\Gamma_a^{\text{r}}\right)\langle\hat{\rho}_{03}\rangle - ig_{\text{eff}}\langle\hat{b}\rangle\underbrace{\left(1 - \langle\hat{\rho}_{11}\rangle - \langle\hat{\rho}_{22}\rangle - \langle\hat{\rho}_{33}\rangle\right)}_{=1\text{(weak drive)}} . \tag{C.13}$$

Solving for $\langle\hat{\rho}_{03}\rangle$, Ξ now explicitly writes

$$\Xi = \frac{ig_{\text{eff}}\epsilon_{\text{d}}^{*}}{g_{\text{eff}}^{2} + \left(\frac{3\Gamma_a^{\text{r}}}{2} - i\tilde{\omega}_{30}\right)\left(\frac{\Gamma_b^{\text{r}}}{2} + i\tilde{\omega}_{b}\right)}\,. \tag{C.14}$$

The spectrum is caluclated as

$$\begin{aligned} I(\tilde{\omega}) =& \Gamma_a^{\text{r}}\left(a_{01}z_{01} + a_{12}z_{12} + a_{23}z_{23} + a_{20}z_{20} + a_{31}z_{31}\right) + \text{c.c.} \\ =& \Gamma_a^{\text{r}}\left(z_{01} + \sqrt{2}z_{12} + \sqrt{3}z_{23}\right) + \text{c.c.}\,, \end{aligned} \tag{C.15}$$

where we have used the definition of $a_{20} = a_{31} = 0$ and z_{01}, z_{12}, z_{23}, z_{20} and z_{31} are the solutions of

$$(-i\tilde{\omega}\mathbb{1} - \mathcal{L}_1)\begin{pmatrix} z_{01} \\ z_{12} \\ z_{23} \\ z_{20} \\ z_{31} \end{pmatrix} = \begin{pmatrix} |\Xi|^2 \\ |\Xi|^2/2 \\ |\Xi|^2/3 \\ i\Xi \\ 0 \end{pmatrix}\,. \tag{C.16}$$

The last line of equation (C.16) explicitly writes

$$-ig_{\text{eff}}\langle\hat{b}^{\dagger}\rangle z_{01} + \left[-i\left(\tilde{\omega}_{31} + \tilde{\omega}\right) + 2\Gamma_a^{\text{r}}\right] z_{31} = 0\,. \tag{C.17}$$

Since we expect the emission spectra to be of order $|\Xi|^2$, and given that $g_{\text{eff}}\langle\hat{b}\rangle \propto \Xi$ (see equation (C.6)), we neglect the first term on the left-hand side of equation (C.17). This leads to $z_{31} = 0$. The penultimate line then reads

$$ig_{\text{eff}}\langle\hat{b}^{\dagger}\rangle z_{23} + \left[-i\left(\tilde{\omega}_{20} + \tilde{\omega}\right) + \Gamma_a^{\text{r}}\right] z_{20} - \sqrt{3}\Gamma_a^{\text{r}} = 0\,, \tag{C.18}$$

and since the first term in the left-hand side is again negligeable for the same reasons as in the above, this leads to

$$z_{20} = \frac{i\Xi}{\Gamma_a^{\text{r}} - i(\tilde{\omega}_{20} + \tilde{\omega})} \tag{C.19}$$

All in all, the $20 - 31$ sector is eliminated and equation (C.16) is reduced to

$$\begin{pmatrix} i\left(\tilde{\omega}_{10}-\tilde{\omega}\right)+\frac{\Gamma_a^{\mathrm{r}}}{2} & -\sqrt{2}\Gamma_a^{\mathrm{r}} & 0 \\ 0 & i\left(\tilde{\omega}_{21}-\tilde{\omega}\right)+\frac{3}{2}\Gamma_a^{\mathrm{r}} & -\sqrt{6}\Gamma_a^{\mathrm{r}} \\ 0 & 0 & i\left(\tilde{\omega}_{32}+\tilde{\omega}\right)+\frac{5}{2}\Gamma_a^{\mathrm{r}} \end{pmatrix} \begin{pmatrix} z_{01} \\ z_{12} \\ z_{23} \end{pmatrix}$$

$$= 3|\Xi|^2 \begin{pmatrix} 1 \\ 1/2 \\ 1/3\left[1+\frac{\frac{3}{2}\Gamma_a^{\mathrm{r}}+i\tilde{\omega}_{30}}{\Gamma_a^{\mathrm{r}}-i(\tilde{\omega}_{20}+\tilde{\omega})}\right] \end{pmatrix} . \tag{C.20}$$

Solving this system of equations and using equation (C.1), the spectrum of emitted photons is expressed as follows:

$$I(\tilde{\omega}) = \Gamma_a^{\mathrm{r}} 3|\Xi|^2 \frac{3\left(\frac{3}{2}\Gamma_a - i\tilde{\omega}\right)^2 + i\frac{3}{2}\Gamma_a\left(\tilde{\omega}_{10}-\tilde{\omega}_{21}\right) + \tilde{\omega}_{10}^2 + \tilde{\omega}_{10}\tilde{\omega}_{21} + \tilde{\omega}_{21}^2}{\left[\frac{3}{2}\Gamma_a + i\left(\tilde{\omega}_{21}-\tilde{\omega}\right)\right]\left[\frac{\Gamma_a}{2} + i\left(\tilde{\omega}_{10}-\tilde{\omega}\right)\right]\left[\Gamma_a - i\left(\tilde{\omega}_{20}+\tilde{\omega}\right)\right]} + \text{c.c.}\,, \tag{C.21}$$

C.2. Inclusion of dephasing on mode a

To include the effect of mode a dephasing on the spectrum of emitted photons, we add an additional term to the effective Hamiltonian, namely

$$\hat{H}_a^{\phi} = \xi(t)\hat{a}^{\dagger}\hat{a}\,, \tag{C.22}$$

where $\xi(t)$ is a random variable that model the fluctuations in time of the resonance frequency of mode a. These random fluctuations in ω_a' are assumed to be Gaussian and are characterised by the dephasing rate Γ_a^{ϕ}, such that

$$\overline{\xi(t)\xi(t')} = \Gamma_a^{\phi}\delta(t-t')\,, \tag{C.23}$$

where the overbar denotes noise averaging. Given that $[\xi(t)\hat{a}^{\dagger}\hat{a}, \hat{\rho}_{mn}] = \xi(t)(m-n)\hat{\rho}_{mn}$, the inclusion of this term adds a contribution to the diagonal elements of $\mathcal{L}$ and equation (2.60) becomes

$$\frac{\mathrm{d}\left\langle\hat{\rho}_{\mu}\right\rangle}{\mathrm{d}t} = \sum_{\nu}\left(\mathcal{L}_{\mu\nu} + i\xi(t)\mathcal{D}_{\mu\nu}^{\phi}\right)\left\langle\hat{\rho}_{\nu}\right\rangle\,, \tag{C.24}$$

where $\mathcal{D}_{\mu\nu}^{\phi} = \delta_{\mu\nu}(m-n)$[1]. Since the right-hand side of equation (C.24) is now explicitly time-dependant, the quantum regression theorem now writes

[1] $\mu \equiv (m,n)$.

$$\left\langle \hat{a}^\dagger(0)\hat{a}(\tau)\right\rangle = \sum_{\mu\nu} a_\mu \left[T\exp\int_0^\tau \mathrm{d}t\left(\mathcal{L}+i\xi(t)\mathcal{D}^\phi\right)\right]_{\mu\nu}\left\langle \hat{a}^\dagger\hat{\rho}_\mu(0)\right\rangle . \tag{C.25}$$

Noise averaging the above expression leads to (we do not present the details of this calculation here)

$$\overline{\langle \hat{a}^\dagger(0)\hat{a}(\tau)\rangle} = \sum_{\mu\nu} a_\mu \left[e^{(\mathcal{L}+\Gamma_a^\phi \mathcal{D}^{\phi 2}/2)\tau}\right]_{\mu\nu}\overline{\langle \hat{a}^\dagger\hat{\rho}_\mu(0)\rangle}\,, \tag{C.26}$$

such that the emission spectrum is now expressed as

$$I(\tilde{\omega}) = \Gamma_a^{\mathrm{r}} \sum_{\mu\nu} a_\mu \left(-i\tilde{\omega}\mathbb{1}-\mathcal{L}-\Gamma_a^\phi\mathcal{D}^{\phi 2}/2\right)^{-1}_{\mu\nu}\overline{\langle \hat{a}^\dagger\hat{\rho}_\mu(0)\rangle} + \text{c.c.}\,. \tag{C.27}$$

From this point the calculation principle is similar to the case without dephasing, although with a redefined matrix $\left(-i\tilde{\omega}\mathbb{1}-\mathcal{L}-\Gamma_a^\phi\mathcal{D}^{\phi 2}/2\right)$. The result is given in the next page.

$$
\begin{aligned}
I(\omega) = \Gamma_a & \frac{3|\Xi|^2}{1+\frac{13}{2}\left(1+\frac{3\Gamma_a^\phi}{\Gamma_a}\right)|\Xi|^2} \times \\
& \left[\left(1+\frac{3\Gamma_a^\phi}{\Gamma_a}\right) \times \frac{3\left(\frac{3}{2}\Gamma_a+\Gamma_a^\phi-i\tilde{\omega}\right)^2+\frac{3i}{2}\Gamma_a\left(\tilde{\omega}_{10}-\tilde{\omega}_{21}\right)+\left(\tilde{\omega}_{10}+i\frac{\Gamma_a^\phi}{2}\right)^2+\left(\tilde{\omega}_{10}+i\frac{\Gamma_a^\phi}{2}\right)\left(\tilde{\omega}_{21}+i\frac{\Gamma_a^\phi}{2}\right)+\left(\tilde{\omega}_{21}+i\frac{\Gamma_a^\phi}{2}\right)^2}{\left[\frac{\Gamma_a}{2}+\frac{\Gamma_a^\phi}{2}+i\left(\tilde{\omega}_{10}-\tilde{\omega}\right)\right]\left[\frac{3}{2}\Gamma_a+\frac{\Gamma_a^\phi}{2}+i\left(\tilde{\omega}_{21}-\tilde{\omega}\right)\right]\left[2\frac{\Gamma_a}{2}+2\Gamma_a^\phi-i\left(\tilde{\omega}_{20}+\tilde{\omega}\right)\right]}\right. \\
& \left. + \frac{3\Gamma_a^\phi}{\Gamma_a} \times \frac{\left(\frac{\Gamma_a}{2}-i\tilde{\omega}_{30}\right)\left(4\Gamma_a^2+\left[\frac{\Gamma_a}{2}+\frac{\Gamma_a^\phi}{2}+i\left(\tilde{\omega}_{10}-\tilde{\omega}\right)\right]\left[\frac{7}{2}\Gamma_a+\frac{\Gamma_a^\phi}{2}+i\left(\tilde{\omega}_{21}-\tilde{\omega}\right)\right]\right)}{\left[\frac{\Gamma_a}{2}+\frac{\Gamma_a^\phi}{2}+i\left(\tilde{\omega}_{10}-\tilde{\omega}\right)\right]\left[\frac{3}{2}\Gamma_a+\frac{\Gamma_a^\phi}{2}+i\left(\tilde{\omega}_{21}-\tilde{\omega}\right)\right]\left[\frac{5}{2}\Gamma_a+\frac{\Gamma_a^\phi}{2}+i\left(\tilde{\omega}_{32}-\tilde{\omega}\right)\right]\left[\Gamma_a+2\Gamma_a^\phi-i\left(\tilde{\omega}_{20}+\tilde{\omega}\right)\right]}\right] \\
& + \text{ c.c.}
\end{aligned}
\tag{C.28}
$$

D
Nanofabrication recipe

In this appendix, we present the detailed recipe used to fabricate the samples studied in this thesis. More specifically, the recipe presented here is the one used to fabricate the sample measured to report the results of chapter 4. Most of the steps are identical for all the fabrication rounds performed during this project, however the development step for the bilayer mask was changed from using the standard MIBK:IPA solvent to the cold development technique using an IPA:DI mixture cooled to 1 °C. The doses used for the e-beam lithography were changed to adapt to this new solvent. Table D.1 presents the fabrication steps for the realisation of the focus marks and the back ground, plane while Table D.2 describes the different steps for the fabrication of the devices using the double angle evaporation. The sixteen chips of the wafer are then diced to be measured individually.

Step	Details
Spin coating	Pre-bake at 180 °C for 2 min Spin coating: PMMA 3% 4000rpm at 4000rpm/s for 30s Bake 5 min at 180 °C Measure thickness at ellipsometer (typically 100 nm to 150 nm)
E-beam lithography	Beam current: $I = 15\,\mathrm{nA}$ Dose: $D = 10\,\mathrm{C/cm^2}$
Resist development	Plunge in MIBK:IPA (1:3) for 60 s Plunge in IPA for 30 s Dry with N_2
Markers evaporation	5 nm of Ti at $0.1\,\mathrm{nm\,s^{-1}}$ 50 nm of Au at $0.1\,\mathrm{nm\,s^{-1}}$
Back ground evaporation	15 nm of Ti at $0.1\,\mathrm{nm\,s^{-1}}$ 200 nm of Au at $0.1\,\mathrm{nm\,s^{-1}}$
Lift-off	Plunge in NMP at 80 °C for 5h Rinse with acetone, ethanol, IPA Dry with N_2

Table D.1.: Recipe used for creating the focus marks and the back ground plane.

Step	Details
Surface cleaning	Reactive ion etching Plasma O_2 at 20 W for 2min
Spin coating	Pre-bake at 200 °C for 2 min Spin coating: PMMA/MAA 9% 3000rpm at 3000rpm/s for 30s Bake 10min at 200 °C Measure thickness at ellipsometer (typically 700 nm to 800 nm) Spin coating: PMMA 4% 5000rpm at 5000rpm/s for 30s Bake 5min at 180 °C Measure thickness at ellipsometer (typically 200 nm)
E-beam lithography	**Large structures** Beam current: $I = 15$ nA Dose: $D = 15$ C/cm^2 **Small structures** Beam current: $I = 1.2$ nA low dose layer: $D = 4.5$ C/cm^2 high dose layer: $D = 23$ C/cm^2
Resist development	Plunge in MIBK:DI (3:1) at 1.5 °C for 60s Plunge in DI for 30s Dry with N_2
Surface cleaning Double angle evaporation	Reactive ion etching Plasma O_2 at 10 W for 15s 20 nm of Al with an angle $\theta = 35$ Static oxidation : 5 min at 5 mbar of O_2 50 nm of Al with an angle $-\theta = -35$
Lift-off	Plunge in NMP at 80 °C for 5h Ultrasonic bath for 60s in a new beaker of NMP Rinse with acetone, ethanol and IPA Dry with N_2

Table D.2.: Fabrication recipe for the main structures.

Bibliography

Ambegaokar, Vinay and Alexis Baratoff (June 1963). "Tunneling Between Superconductors". In: *Physical Review Letters* 10.11. Publisher: American Physical Society, pp. 486–489. DOI: 10.1103/PhysRevLett.10.486 (cit. on p. 51).

Anappara, Aji A., Simone De Liberato, Alessandro Tredicucci, Cristiano Ciuti, Giorgio Biasiol, Lucia Sorba, and Fabio Beltram (May 2009). "Signatures of the ultrastrong light-matter coupling regime". en. In: *Physical Review B* 79.20, p. 201303. ISSN: 1098-0121, 1550-235X. DOI: 10.1103/PhysRevB.79.201303 (cit. on p. 6).

Andersen, Christian Kraglund and Alexandre Blais (Feb. 2017). "Ultrastrong coupling dynamics with a transmon qubit". en. In: *New Journal of Physics* 19.2, p. 023022. ISSN: 1367-2630. DOI: 10.1088/1367-2630/aa5941 (cit. on p. 6).

Aumentado, Jose (Aug. 2020). "Superconducting Parametric Amplifiers: The State of the Art in Josephson Parametric Amplifiers". In: *IEEE Microwave Magazine* 21.8. Conference Name: IEEE Microwave Magazine, pp. 45–59. ISSN: 1557-9581. DOI: 10.1109/MMM.2020.2993476 (cit. on pp. 57, 59).

Bera, Soumya, Serge Florens, Harold U. Baranger, Nicolas Roch, Ahsan Nazir, and Alex W. Chin (Mar. 2014). "Stabilizing spin coherence through environmental entanglement in strongly dissipative quantum systems". In: *Physical Review B* 89.12. Publisher: American Physical Society, p. 121108. DOI: 10.1103/PhysRevB.89.121108 (cit. on pp. 8, 9).

Bertet, P., I. Chiorescu, G. Burkard, K. Semba, C. J. P. M. Harmans, D. P. DiVincenzo, and J. E. Mooij (Dec. 2005). "Dephasing of a Superconducting Qubit Induced by Photon Noise". en. In: *Physical Review Letters* 95.25, p. 257002. ISSN: 0031-9007, 1079-7114. DOI: 10.1103/PhysRevLett.95.257002 (cit. on p. 45).

Bethe, H. A. (Aug. 1947). "The Electromagnetic Shift of Energy Levels". In: *Physical Review* 72.4. Publisher: American Physical Society, pp. 339–341. DOI: 10.1103/PhysRev.72.339 (cit. on p. 4).

Blais, Alexandre, Ren-Shou Huang, Andreas Wallraff, S. M. Girvin, and R. J. Schoelkopf (June 2004). "Cavity quantum electrodynamics for superconducting electrical circuits: An architecture for quantum computation". en. In: *Physical Review A* 69.6, p. 062320. ISSN: 1050-2947, 1094-1622. DOI: 10.1103/PhysRevA.69.062320 (cit. on pp. 8, 16, 19).

Bourassa, J., F. Beaudoin, Jay M. Gambetta, and A. Blais (July 2012). "Josephson junction-embedded transmission-line resonators: from Kerr medium to in-line transmon". en. In: *Physical Review A* 86.1, p. 013814. ISSN: 1050-2947, 1094-1622. DOI: 10.1103/PhysRevA.86.013814 (cit. on p. 26).

Bozyigit, D., C. Lang, L. Steffen, J. M. Fink, C. Eichler, M. Baur, R. Bianchetti, P. J. Leek, S. Filipp, M. P. da Silva, A. Blais, and A. Wallraff (Feb. 2011). "Antibunching of microwave-frequency photons observed in correlation measurements using linear detectors". en. In: *Nature Physics* 7.2. Number: 2 Publisher: Nature Publishing Group, pp. 154–158. ISSN: 1745-2481. DOI: 10.1038/nphys1845 (cit. on p. 104).

Bravyi, Sergey, David DiVincenzo, and Daniel Loss (Oct. 2011). "Schrieffer-Wolff transformation for quantum many-body systems". en. In: *Annals of Physics* 326.10, pp. 2793–2826. ISSN: 00034916. DOI: 10.1016/j.aop.2011.06.004 (cit. on p. 31).

Brune, M., F. Schmidt-Kaler, A. Maali, J. Dreyer, E. Hagley, J. M. Raimond, and S. Haroche (Mar. 1996). "Quantum Rabi Oscillation: A Direct Test of Field Quantization in a Cavity". en. In: *Physical Review Letters* 76.11, pp. 1800–1803. ISSN: 0031-9007, 1079-7114. DOI: 10.1103/PhysRevLett.76.1800 (cit. on p. 5).

Bulgadaev, S.A (1984). "Phase diagram of a dissipative quantum system". In: (cit. on p. 9).

Caldeira, A. O. and A. J. Leggett (1983). "Quantum tunnelling in a dissipative system". In: *Annals of Physics* 149.2, pp. 374–456. ISSN: 0003-4916. DOI: https://doi.org/10.1016/0003-4916(83)90202-6 (cit. on pp. 6, 15, 16).

Carmichael, Howard J. (1999). *Statistical Methods in Quantum Optics 1*. en. Berlin, Heidelberg: Springer Berlin Heidelberg. ISBN: 978-3-642-08133-0 978-3-662-03875-8. DOI: 10.1007/978-3-662-03875-8 (cit. on p. 41).

Chang, C. W. Sandbo, Carlos Sabín, P. Forn-Díaz, Fernando Quijandría, A. M. Vadiraj, I. Nsanzineza, G. Johansson, and C. M. Wilson (Jan. 2020). "Observation of Three-Photon Spontaneous Parametric Down-Conversion in a Superconducting Parametric Cavity". en. In: *Physical Review X* 10.1, p. 011011. ISSN: 2160-3308. DOI: 10.1103/PhysRevX.10.011011 (cit. on pp. 11, 12).

Chow, Edmond, Per Delsing, and David B. Haviland (July 1998). "Length-Scale Dependence of the Superconductor-to-Insulator Quantum Phase Transition in One Dimension". en. In: *Physical Review Letters* 81.1, pp. 204–207. ISSN: 0031-9007, 1079-7114. DOI: 10.1103/PhysRevLett.81.204 (cit. on p. 21).

Claudon, Julien (2005). "Oscillations cohérentes dans un circuit quantique supraconducteur : le SQUID dc". PhD thesis. Université Joseph Fourier - Grenoble I (cit. on p. 51).

Clerk, A. A., M. H. Devoret, S. M. Girvin, F. Marquardt, and R. J. Schoelkopf (Apr. 2010). "Introduction to Quantum Noise, Measurement and Amplification". en. In: *Reviews of Modern Physics* 82.2, pp. 1155–1208. ISSN: 0034-6861, 1539-0756. DOI: 10.1103/RevModPhys.82.1155 (cit. on p. 62).

Cohen-Tannoudji, Claude, Bernard Diu, and Franck Laloë (2018). *Mécanique quantique - Tome II*. fr (cit. on p. 25).

Corlevi, S., W. Guichard, F. W. J. Hekking, and D. B. Haviland (Aug. 2006). "Phase-Charge Duality of a Josephson Junction in a Fluctuating Electromagnetic Environment". en. In: *Physical Review Letters* 97.9, p. 096802. ISSN: 0031-9007, 1079-7114. DOI: 10.1103/PhysRevLett.97.096802 (cit. on p. 21).

Cottet, Audrey (2002). "Implémentation d'un bit quantique dans un circuit supraconducteur / Implementation of a quantum bit in a superconducting circuit". Theses. Université Pierre et Marie Curie - Paris VI (cit. on p. 18).

Dassonneville, R., T. Ramos, V. Milchakov, L. Planat, É. Dumur, F. Foroughi, J. Puertas, S. Leger, K. Bharadwaj, J. Delaforce, C. Naud, W. Hasch-Guichard, J. J. García-Ripoll, N. Roch, and O. Buisson (Feb. 2020). "Fast High-Fidelity Quantum Nondemolition Qubit Readout via a Nonperturbative Cross-Kerr Coupling". en. In: *Physical Review X* 10.1, p. 011045. ISSN: 2160-3308. DOI: 10.1103/PhysRevX.10.011045 (cit. on p. 88).

Dassonneville, Remy (2019). "Qubit readouts using a transmon molecule in a 3D circuit quantum electrodynamics architecture". en. PhD thesis. Université Grenoble Alpes (cit. on p. 55).

Deaver, Bascom S. and William S. Goree (Mar. 1967). "Some Techniques for Sensitive Magnetic Measurements Using Superconducting Circuits and Magnetic Shields". en. In: *Review of Scientific Instruments* 38.3, pp. 311–318. ISSN: 0034-6748, 1089-7623. DOI: 10.1063/1.1720694 (cit. on p. 16).

devoret, Michel H. and John M. Martinis (Oct. 2004). "Implementing Qubits with Superconducting Integrated Circuits". en. In: *Quantum Information Processing* 3.1, pp. 163–203. ISSN: 1573-1332. DOI: 10.1007/s11128-004-3101-5 (cit. on p. 16).

Dolan, G. J. (Aug. 2008). "Offset masks for lift-off photoprocessing". In: *Applied Physics Letters* 31.5, pp. 337–339. ISSN: 0003-6951. DOI: 10.1063/1.89690 (cit. on p. 48).

Douady, J. and B. Boulanger (Dec. 2004). "Experimental demonstration of a pure third-order optical parametric downconversion process". en. In: *Optics Letters* 29.23, p. 2794. ISSN: 0146-9592, 1539-4794. DOI: 10.1364/OL.29.002794 (cit. on pp. 10, 11).

Duan, Liwei, Shu He, Daniel Braak, and Qing-Hu Chen (Nov. 2015). "Solution of the two-mode quantum Rabi model using extended squeezed states". en. In: *Europhysics Letters* 112.3. Publisher: EDP Sciences, IOP Publishing and Società Italiana di Fisica, p. 34003. ISSN: 0295-5075. DOI: 10.1209/0295-5075/112/34003 (cit. on p. 87).

Duan, Liwei, You-Fei Xie, Daniel Braak, and Qing-Hu Chen (Oct. 2016). "Two-photon Rabi model: analytic solutions and spectral collapse". en. In: *Journal of Physics A: Mathematical and Theoretical* 49.46. Publisher: IOP Publishing, p. 464002. ISSN: 1751-8121. DOI: 10.1088/1751-8113/49/46/464002 (cit. on p. 87).

Eichler, C., Y. Salathe, J. Mlynek, S. Schmidt, and A. Wallraff (Sept. 2014). "Quantum-Limited Amplification and Entanglement in Coupled Nonlinear Resonators". In: *Phys-*

ical Review Letters 113.11. Publisher: American Physical Society, p. 110502. DOI: 10.1103/PhysRevLett.113.110502 (cit. on p. 10).

Esposito, Martina, Arpit Ranadive, Luca Planat, Sebastian Leger, Dorian Fraudet, Vincent Jouanny, Olivier Buisson, Wiebke Guichard, Cécile Naud, José Aumentado, Florent Lecocq, and Nicolas Roch (Apr. 2022). "Observation of two-mode squeezing in a traveling wave parametric amplifier". en. In: *Physical Review Letters* 128.15, p. 153603. ISSN: 0031-9007, 1079-7114. DOI: 10.1103/PhysRevLett.128.153603 (cit. on p. 10).

Esposito, Martina, Arpit Ranadive, Luca Planat, and Nicolas Roch (Sept. 2021). "Perspective on traveling wave microwave parametric amplifiers". In: *Applied Physics Letters* 119.12, p. 120501. ISSN: 0003-6951. DOI: 10.1063/5.0064892 (cit. on pp. 57, 58).

Fasolo, Luca, Angelo Greco, Emanuele Enrico, J Thirumalai, and SI Pokutnyi (2020). "Superconducting josephson-based metamaterials for quantum-limited parametric amplification: A review". In: *Advances in Condensed-Matter and Materials Physics-Rudimentary Research to Topical Technology*. Publisher: IntechOpen (cit. on p. 57).

Felicetti, S (2018). "Two-photon quantum Rabi model with superconducting circuits". en. In: *PHYSICAL REVIEW A* (cit. on p. 87).

Forn-Díaz, P and L Lamata (2019). "Ultrastrong coupling regimes of light-matter interaction". en. In: *Rev. Mod. Phys.* 91.2 (cit. on p. 5).

Forn-Díaz, P., J. J. García-Ripoll, B. Peropadre, J.-L. Orgiazzi, M. A. Yurtalan, R. Belyansky, C. M. Wilson, and A. Lupascu (Jan. 2017). "Ultrastrong coupling of a single artificial atom to an electromagnetic continuum in the nonperturbative regime". en. In: *Nature Physics* 13.1, pp. 39–43. ISSN: 1745-2481. DOI: 10.1038/nphys3905 (cit. on p. 8).

Forn-Dıaz, P, J Lisenfeld, D Marcos, J J Garcıa-Ripoll, and E Solano (2010). "Observation of the Bloch-Siegert Shift in a Qubit-Oscillator System in the Ultrastrong Coupling Regime". en. In: *PHYSICAL REVIEW LETTERS* (cit. on p. 6).

Friis, H.T. (July 1944). "Noise Figures of Radio Receivers". In: *Proceedings of the IRE* 32.7. Conference Name: Proceedings of the IRE, pp. 419–422. ISSN: 2162-6634. DOI: 10.1109/JRPROC.1944.232049 (cit. on p. 56).

Frisk Kockum, Anton, Adam Miranowicz, Simone De Liberato, Salvatore Savasta, and Franco Nori (Jan. 2019). "Ultrastrong coupling between light and matter". en. In: *Nature Reviews Physics* 1.1, pp. 19–40. ISSN: 2522-5820. DOI: 10.1038/s42254-018-0006-2 (cit. on p. 5).

Gardiner, Crispin and Peter Zoller (2004). *Quantum noise - A Handbook of Markovian and Non-Markovian Quantum Stochastic Methods with Applications to Quantum Optics*. Springer Berlin, Heidelberg. ISBN: 978-3-540-22301-6 (cit. on pp. 33, 34, 41).

Garziano, Luigi, Roberto Stassi, Vincenzo Macrì, Anton Frisk Kockum, Salvatore Savasta, and Franco Nori (Dec. 2015). "Multiphoton quantum Rabi oscillations in ultrastrong cavity QED". en. In: *Physical Review A* 92.6, p. 063830. ISSN: 1050-2947, 1094-1622. DOI: 10.1103/PhysRevA.92.063830 (cit. on pp. 5, 87).

Gely, Mario F., Marios Kounalakis, Christian Dickel, Jacob Dalle, Rémy Vatré, Brian Baker, Mark D. Jenkins, and Gary A. Steele (Mar. 2019). "Observation and stabilization of photonic Fock states in a hot radio-frequency resonator". en. In: *Science* 363.6431, pp. 1072–1075. ISSN: 0036-8075, 1095-9203. DOI: 10.1126/science.aaw3101 (cit. on p. 39).

Gheeraert, Nicolas, Xin H. H. Zhang, Théo Sépulcre, Soumya Bera, Nicolas Roch, Harold U. Baranger, and Serge Florens (Oct. 2018). "Particle production in ultrastrong-coupling waveguide QED". en. In: *Physical Review A* 98.4, p. 043816. ISSN: 2469-9926, 2469-9934. DOI: 10.1103/PhysRevA.98.043816 (cit. on p. 9).

Goldstein, Moshe, Michel H. Devoret, Manuel Houzet, and Leonid I. Glazman (Jan. 2013). "Inelastic Microwave Photon Scattering off a Quantum Impurity in a Josephson-Junction Array". en. In: *Physical Review Letters* 110.1, p. 017002. ISSN: 0031-9007, 1079-7114. DOI: 10.1103/PhysRevLett.110.017002 (cit. on p. 9).

Gorini, Vittorio, Alberto Frigerio, Maurizio Verri, Andrzej Kossakowski, and E. C. G. Sudarshan (Apr. 1978). "Properties of quantum Markovian master equations". In: *Reports on Mathematical Physics* 13.2, pp. 149–173. ISSN: 0034-4877. DOI: 10.1016/0034-4877(78)90050-2 (cit. on p. 39).

Gottesman, Daniel, Alexei Kitaev, and John Preskill (June 2001). "Encoding a qubit in an oscillator". In: *Physical Review A* 64.1. Publisher: American Physical Society, p. 012310. DOI: 10.1103/PhysRevA.64.012310 (cit. on p. 12).

Grimm, A., N. E. Frattini, S. Puri, S. O. Mundhada, S. Touzard, M. Mirrahimi, S. M. Girvin, S. Shankar, and M. H. Devoret (Aug. 2020). "Stabilization and operation of a Kerr-cat qubit". en. In: *Nature* 584.7820. Number: 7820 Publisher: Nature Publishing Group, pp. 205–209. ISSN: 1476-4687. DOI: 10.1038/s41586-020-2587-z (cit. on p. 11).

Groszkowski, Peter, A Di Paolo, A L Grimsmo, A Blais, D I Schuster, A A Houck, and Jens Koch (Apr. 2018). "Coherence properties of the 0- {\textbackslashpi\ qubit". en. In: *New Journal of Physics* 20.4, p. 043053. ISSN: 1367-2630. DOI: 10.1088/1367-2630/aab7cd (cit. on p. 44).

Hamilton, Clark A. (2000). "Josephson voltage standards". en. In: *Review of Scientific Instruments* 71.10, p. 3611. ISSN: 00346748. DOI: 10.1063/1.1289507 (cit. on p. 16).

Hofheinz, Max, E. M. Weig, M. Ansmann, Radoslaw C. Bialczak, Erik Lucero, M. Neeley, A. D. O'Connell, H. Wang, John M. Martinis, and A. N. Cleland (July 2008). "Generation of Fock states in a superconducting quantum circuit". en. In: *Nature* 454.7202.

Number: 7202 Publisher: Nature Publishing Group, pp. 310–314. ISSN: 1476-4687. DOI: 10.1038/nature07136 (cit. on p. 10).

Houzet, M. and L. I. Glazman (Dec. 2020). "Critical Fluorescence of a Transmon at the Schmid Transition". In: *Physical Review Letters* 125.26, p. 267701. DOI: 10.1103/PhysRevLett.125.267701 (cit. on p. 9).

Hriscu, A. M. and Yu. V. Nazarov (Feb. 2011). "Model of a Proposed Superconducting Phase Slip Oscillator: A Method for Obtaining Few-Photon Nonlinearities". In: *Physical Review Letters* 106.7. Publisher: American Physical Society, p. 077004. DOI: 10.1103/PhysRevLett.106.077004 (cit. on p. 84).

Ithier, G., E. Collin, P. Joyez, P. J. Meeson, D. Vion, D. Esteve, F. Chiarello, A. Shnirman, Y. Makhlin, J. Schriefl, and G. Schön (Oct. 2005). "Decoherence in a superconducting quantum bit circuit". en. In: *Physical Review B* 72.13, p. 134519. ISSN: 1098-0121, 1550-235X. DOI: 10.1103/PhysRevB.72.134519 (cit. on p. 44).

Johansson, J, S Saito, T Meno, H Nakano, M Ueda, K Semba, and H Takayanagi (2006). "Vacuum Rabi Oscillations in a Macroscopic Superconducting Qubit LC Oscillator System". en. In: *PHYSICAL REVIEW LETTERS* (cit. on p. 5).

Josephson, B. D. (1962). "Possible new effects in superconductive tunnelling". In: *Physics Letters* 1.7, pp. 251–253. ISSN: 0031-9163. DOI: https://doi.org/10.1016/0031-9163(62)91369-0 (cit. on p. 16).

Kaur, Kuljeet, Théo Sépulcre, Nicolas Roch, Izak Snyman, Serge Florens, and Soumya Bera (Dec. 2021). "Spin-Boson Quantum Phase Transition in Multilevel Superconducting Qubits". In: *Physical Review Letters* 127.23. Publisher: American Physical Society, p. 237702. DOI: 10.1103/PhysRevLett.127.237702 (cit. on pp. 8, 99).

Knight, Peter (July 2015). "Quantum Machines: Measurement and Control of Engineered Quantum Systems, edited by Michel Devoret, Benjamin Huard, Robert Schoelkopf, and Leticia F. Cugliandolo". In: *Contemporary Physics* 56.3. Publisher: Taylor & Francis _eprint: https://doi.org/10.1080/00107514.2015.1005684, pp. 395–396. ISSN: 0010-7514. DOI: 10.1080/00107514.2015.1005684 (cit. on p. 16).

Koch, Jens, Terri M. Yu, Jay Gambetta, A. A. Houck, D. I. Schuster, J. Majer, Alexandre Blais, M. H. Devoret, S. M. Girvin, and R. J. Schoelkopf (Oct. 2007). "Charge-insensitive qubit design derived from the Cooper pair box". en. In: *Physical Review A* 76.4, p. 042319. ISSN: 1050-2947, 1094-1622. DOI: 10.1103/PhysRevA.76.042319 (cit. on p. 44).

Kockum, Anton Frisk, Adam Miranowicz, Vincenzo Macrì, Salvatore Savasta, and Franco Nori (June 2017). "Deterministic quantum nonlinear optics with single atoms and virtual photons". en. In: *Physical Review A* 95.6, p. 063849. ISSN: 2469-9926, 2469-9934. DOI: 10.1103/PhysRevA.95.063849 (cit. on p. 5).

Koshino, Kazuki, Tomohiro Shitara, Ziqiao Ao, and Kouichi Semba (Jan. 2022). "Deterministic three-photon down-conversion by a passive ultrastrong cavity-QED system". In: *Physical Review Research* 4.1. Publisher: American Physical Society, p. 013013. DOI: 10.1103/PhysRevResearch.4.013013 (cit. on p. 35).

Kreikebaum, J. M., K. P. O'Brien, A. Morvan, and I. Siddiqi (Apr. 2020). "Improving wafer-scale Josephson junction resistance variation in superconducting quantum coherent circuits". en. In: *Superconductor Science and Technology* 33.6. Publisher: IOP Publishing, 06LT02. ISSN: 0953-2048. DOI: 10.1088/1361-6668/ab8617 (cit. on p. 48).

Krupko, Yu., V. D. Nguyen, T. Weißl, É. Dumur, J. Puertas, R. Dassonneville, C. Naud, F. W. J. Hekking, D. M. Basko, O. Buisson, N. Roch, and W. Hasch-Guichard (Sept. 2018). "Kerr nonlinearity in a superconducting Josephson metamaterial". en. In: *Physical Review B* 98.9, p. 094516. ISSN: 2469-9950, 2469-9969. DOI: 10.1103/PhysRevB.98.094516 (cit. on p. 26).

Kuzmin, R., N. Grabon, N. Mehta, A. Burshtein, M. Goldstein, M. Houzet, L. I. Glazman, and V. E. Manucharyan (May 2021). "Inelastic Scattering of a Photon by a Quantum Phase Slip". In: *Physical Review Letters* 126.19. Publisher: American Physical Society, p. 197701. DOI: 10.1103/PhysRevLett.126.197701 (cit. on p. 9).

Kuzmin, Roman, Nitish Mehta, Nicholas Grabon, Raymond Mencia, and Vladimir E. Manucharyan (Feb. 2019). "Superstrong coupling in circuit quantum electrodynamics". en. In: *npj Quantum Information* 5.1. Number: 1 Publisher: Nature Publishing Group, pp. 1–6. ISSN: 2056-6387. DOI: 10.1038/s41534-019-0134-2 (cit. on p. 8).

Lamb, Willis E. and Robert C. Retherford (Aug. 1947). "Fine Structure of the Hydrogen Atom by a Microwave Method". In: *Physical Review* 72.3. Publisher: American Physical Society, pp. 241–243. DOI: 10.1103/PhysRev.72.241 (cit. on p. 2).

– (Jan. 1951). "Fine Structure of the Hydrogen Atom. Part II". In: *Physical Review* 81.2. Publisher: American Physical Society, pp. 222–232. DOI: 10.1103/PhysRev.81.222 (cit. on p. 2).

Landau, L. D. and Lifshitz, E. M. (1976). *Mechanics, Third Edition: Volume 1 (Course of Theoretical Physics)*. ISBN: 0-7506-2896-0 (cit. on p. 24).

Lang, C., D. Bozyigit, C. Eichler, L. Steffen, J. M. Fink, A. A. Abdumalikov, M. Baur, S. Filipp, M. P. da Silva, A. Blais, and A. Wallraff (June 2011). "Observation of Resonant Photon Blockade at Microwave Frequencies Using Correlation Function Measurements". In: *Physical Review Letters* 106.24. Publisher: American Physical Society, p. 243601. DOI: 10.1103/PhysRevLett.106.243601 (cit. on p. 104).

Lang, Christian (2014). "Quantum Microwave Radiation and its Interference Characterized by Correlation Function Measurements in Circuit Quantum Electrodynamics". en. Artwork Size: 1 Band Medium: application/pdf Pages: 1 Band. PhD thesis. ETH Zurich. DOI: 10.3929/ETHZ-A-010245903 (cit. on p. 78).

Lecocq, F., I. M. Pop, I. Matei, E. Dumur, A. K. Feofanov, C. Naud, W. Guichard, and O. Buisson (Mar. 2012). "Coherent Frequency Conversion in a Superconducting Artificial Atom with Two Internal Degrees of Freedom". en. In: *Physical Review Letters* 108.10, p. 107001. ISSN: 0031-9007, 1079-7114. DOI: 10.1103/PhysRevLett.108.107001 (cit. on p. 87).

Lecocq, Florent (2011). "Dynamique quantique dans un dcSQUID: du qubit de phase à l'oscillateur quantique bidimensionnel". fr. In: p. 166 (cit. on p. 48).

Lecocq, Florent, Ioan M Pop, Zhihui Peng, Iulian Matei, Thierry Crozes, Thierry Fournier, Cécile Naud, Wiebke Guichard, and Olivier Buisson (Aug. 2011). "Junction fabrication by shadow evaporation without a suspended bridge". en. In: *Nanotechnology* 22.31, p. 315302. ISSN: 0957-4484, 1361-6528. DOI: 10.1088/0957-4484/22/31/315302 (cit. on pp. 16, 48).

Léger, Sébastien (2021). "Quantum electrodynamics of a Josephson Junction coupled to a strongly dissipative environment". PhD Thesis. Université Grenoble Alpes (cit. on pp. 28, 67).

Léger, Sébastien, Javier Puertas-Martínez, Karthik Bharadwaj, Rémy Dassonneville, Jovian Delaforce, Farshad Foroughi, Vladimir Milchakov, Luca Planat, Olivier Buisson, Cécile Naud, Wiebke Hasch-Guichard, Serge Florens, Izak Snyman, and Nicolas Roch (Dec. 2019). "Observation of quantum many-body effects due to zero point fluctuations in superconducting circuits". en. In: *Nature Communications* 10.1, p. 5259. ISSN: 2041-1723. DOI: 10.1038/s41467-019-13199-x (cit. on pp. 8, 20).

Léger, Sébastien, Théo Sépulcre, Dorian Fraudet, Olivier Buisson, Cécile Naud, Wiebke Hasch-Guichard, Serge Florens, Izak Snyman, Denis M. Basko, and Nicolas Roch (May 2023). "Revealing the finite-frequency response of a bosonic quantum impurity". en. In: *SciPost Physics* 14.5, p. 130. ISSN: 2542-4653. DOI: 10.21468/SciPostPhys.14.5.130 (cit. on pp. 8, 9, 13, 20).

Leggett, A J, S Chakravarty, A T Dorsey, Matthew P A Fisher, Anupam Garg, and W Zwerger (1987). "Dynamics of the dissipative two-state system". en. In: *Rev. Mod. Phys.* 59.1 (cit. on p. 6).

Leghtas, Z., S. Touzard, I. M. Pop, A. Kou, B. Vlastakis, A. Petrenko, K. M. Sliwa, A. Narla, S. Shankar, M. J. Hatridge, M. Reagor, L. Frunzio, R. J. Schoelkopf, M. Mirrahimi, and M. H. Devoret (Feb. 2015). "Confining the state of light to a quantum manifold by engineered two-photon loss". In: *Science* 347.6224. Publisher: American Association for the Advancement of Science, pp. 853–857. DOI: 10.1126/science.aaa2085 (cit. on p. 10).

Leppäkangas, Juha, Michael Marthaler, Dibyendu Hazra, Salha Jebari, Romain Albert, Florian Blanchet, Göran Johansson, and Max Hofheinz (Jan. 2018). "Multiplying and detecting propagating microwave photons using inelastic Cooper-pair tunneling". en.

In: *Physical Review A* 97.1, p. 013855. ISSN: 2469-9926, 2469-9934. DOI: 10.1103/PhysRevA.97.013855 (cit. on pp. 33, 35).

Likharev, K. K. and A. B. Zorin (May 1985). "Theory of the Bloch-wave oscillations in small Josephson junctions". en. In: *Journal of Low Temperature Physics* 59.3-4, pp. 347–382. ISSN: 0022-2291, 1573-7357. DOI: 10.1007/BF00683782 (cit. on p. 18).

Likharev, K.K. and V.K. Semenov (Mar. 1991). "RSFQ logic/memory family: a new Josephson-junction technology for sub-terahertz-clock-frequency digital systems". en. In: *IEEE Transactions on Applied Superconductivity* 1.1, pp. 3–28. ISSN: 1051-8223, 1558-2515, 2378-7074. DOI: 10.1109/77.80745 (cit. on p. 16).

Maclay, G. Jordan (Apr. 2020). "History and Some Aspects of the Lamb Shift". en. In: *Physics* 2.2, pp. 105–147. ISSN: 2624-8174. DOI: 10.3390/physics2020008 (cit. on p. 3).

Manucharyan, Vladimir E., Jens Koch, Leonid I. Glazman, and Michel H. Devoret (Oct. 2009). "Fluxonium: Single Cooper-Pair Circuit Free of Charge Offsets". In: *Science* 326.5949, pp. 113–116. DOI: 10.1126/science.1175552 (cit. on p. 88).

Mehta, Nitish, Cristiano Ciuti, Roman Kuzmin, and Vladimir E. Manucharyan (2022). *Theory of strong down-conversion in multi-mode cavity and circuit QED*. en. Tech. rep. arXiv:2210.14681 (cit. on p. 9).

Mehta, Nitish, Roman Kuzmin, Cristiano Ciuti, and Vladimir E. Manucharyan (Jan. 2023). "Down-conversion of a single photon as a probe of many-body localization". en. In: *Nature* 613.7945. Number: 7945 Publisher: Nature Publishing Group, pp. 650–655. ISSN: 1476-4687. DOI: 10.1038/s41586-022-05615-y (cit. on pp. 10, 87).

Meiser, D. and P. Meystre (Dec. 2006). "Superstrong coupling regime of cavity quantum electrodynamics". In: *Physical Review A* 74.6. Publisher: American Physical Society, p. 065801. DOI: 10.1103/PhysRevA.74.065801 (cit. on p. 8).

Mermin, N. David (Aug. 1990). "Quantum mysteries revisited". en. In: *American Journal of Physics* 58.8, pp. 731–734. ISSN: 0002-9505, 1943-2909. DOI: 10.1119/1.16503 (cit. on p. 12).

Michelson, Albert A and Edward W Morley (1887). "ART. XLVII.– On a Method of making the Wave-length of Sodium Light the actual and practical standard of length". In: *American Journal of Science (1880-1910)* 34.204. Publisher: American Periodicals Series II, p. 427 (cit. on p. 1).

Miloni, Peter W. (1994). *The Quantum Vacuum*. Academic Press. ISBN: 978-0-08-057149-2 (cit. on p. 3).

Minev, Zlatko K., Zaki Leghtas, Shantanu O. Mundhada, Lysander Christakis, Ioan M. Pop, and Michel H. Devoret (Aug. 2021). "Energy-participation quantization of

Josephson circuits". en. In: *npj Quantum Information* 7.1. Number: 1 Publisher: Nature Publishing Group, pp. 1–11. ISSN: 2056-6387. DOI: 10.1038/s41534-021-00461-8 (cit. on p. 25).

Niemczyk, T., F. Deppe, H. Huebl, E. P. Menzel, F. Hocke, M. J. Schwarz, J. J. Garcia-Ripoll, D. Zueco, T. Hümmer, E. Solano, A. Marx, and R. Gross (Oct. 2010). "Beyond the Jaynes-Cummings model: circuit QED in the ultrastrong coupling regime". en. In: *Nature Physics* 6.10, pp. 772–776. ISSN: 1745-2473, 1745-2481. DOI: 10.1038/nphys1730 (cit. on p. 6).

Nyquist, H. (July 1928). "Thermal Agitation of Electric Charge in Conductors". In: *Physical Review* 32.1. Publisher: American Physical Society, pp. 110–113. DOI: 10.1103/PhysRev.32.110 (cit. on p. 55).

Peropadre, B., D. Zueco, D. Porras, and J. J. García-Ripoll (Dec. 2013). "Nonequilibrium and Nonperturbative Dynamics of Ultrastrong Coupling in Open Lines". In: *Physical Review Letters* 111.24. Publisher: American Physical Society, p. 243602. DOI: 10.1103/PhysRevLett.111.243602 (cit. on p. 9).

Planat, Luca (2020). "Resonant and traveling-wave parametric amplification near the quantum limit". fr. PhD Thesis. Université Grenoble Alpes (cit. on pp. 10, 47, 57).

Planat, Luca, Remy Dassonneville, Javier Puertas Martinez, Farshad Foroughi, Olivier Buisson, Wiebke Hasch-Guichard, Cecile Naud, R. Vijay, Kater Murch, and Nicolas Roch (Mar. 2019). "Understanding the saturation power of Josephson Parametric Amplifiers made from SQUIDs arrays". en. In: *Physical Review Applied* 11.3, p. 034014. ISSN: 2331-7019. DOI: 10.1103/PhysRevApplied.11.034014 (cit. on p. 57).

Pozar, D.M. (2011). *Microwave Engineering, 4th Edition*. Wiley. ISBN: 978-1-118-21363-6 (cit. on p. 66).

Probst, S., F. B. Song, P. A. Bushev, A. V. Ustinov, and M. Weides (Feb. 2015). "Efficient and robust analysis of complex scattering data under noise in microwave resonators". In: *Review of Scientific Instruments* 86.2, p. 024706. ISSN: 0034-6748. DOI: 10.1063/1.4907935 (cit. on p. 72).

Puertas, Javier (2018). "Probing light-matter interaction in the many-body regime of superconducting quantum circuits". en. PhD Thesis. Université Grenoble Alpes (cit. on pp. 21, 47).

Puertas Martínez, Javier, Sébastien Léger, Nicolas Gheeraert, Rémy Dassonneville, Luca Planat, Farshad Foroughi, Yuriy Krupko, Olivier Buisson, Cécile Naud, Wiebke Hasch-Guichard, Serge Florens, Izak Snyman, and Nicolas Roch (Dec. 2019). "A tunable Josephson platform to explore many-body quantum optics in circuit-QED". en. In: *npj Quantum Information* 5.1, p. 19. ISSN: 2056-6387. DOI: 10.1038/s41534-018-0104-0 (cit. on pp. 8, 21).

Raimond, J M, M Brune, S Haroche, and Laboratoire Kastler Brossel (2001). "Colloquium: Manipulating quantum entanglement with atoms and photons in a cavity". en. In: *Rev. Mod. Phys.* 73.3 (cit. on p. 5).

Ranadive, Arpit (2022). "Nonlinear quantum optics with Josephson metamaterials". PhD thesis. Université Grenoble Alpes (cit. on pp. 57, 58).

Ridolfo, A., J. Rajendran, L. Giannelli, E. Paladino, and G. Falci (June 2021). "Probing ultrastrong light–matter coupling in open quantum systems". en. In: *The European Physical Journal Special Topics* 230.4, pp. 941–945. ISSN: 1951-6401. DOI: 10.1140/epjs/s11734-021-00070-8 (cit. on p. 6).

Rieger, D., S. Günzler, M. Spiecker, A. Nambisan, W. Wernsdorfer, and I.M. Pop (July 2023). "Fano Interference in Microwave Resonator Measurements". In: *Physical Review Applied* 20.1. Publisher: American Physical Society, p. 014059. DOI: 10.1103/PhysRevApplied.20.014059 (cit. on p. 72).

Roy, Ananda and Michel Devoret (July 2018). "Quantum-limited Parametric Amplification with Josephson Circuits in the Regime of Pump Depletion". en. In: *Physical Review B* 98.4, p. 045405. ISSN: 2469-9950, 2469-9969. DOI: 10.1103/PhysRevB.98.045405 (cit. on pp. 33, 34).

Sanchez-Burillo, E., D. Zueco, J. J. Garcia-Ripoll, and L. Martin-Moreno (Dec. 2014). "Scattering in the Ultrastrong Regime: Nonlinear Optics with One Photon". In: *Physical Review Letters* 113.26. Publisher: American Physical Society, p. 263604. DOI: 10.1103/PhysRevLett.113.263604 (cit. on p. 9).

Schlosshauer, Maximilian (2007). *Decoherence and the quantum-to-classical transition.* en. The frontiers collection. Berlin: Springer. ISBN: 978-3-540-35773-5 (cit. on p. 7).

Schmid, Albert (Oct. 1983). "Diffusion and Localization in a Dissipative Quantum System". en. In: *Physical Review Letters* 51.17, pp. 1506–1509. ISSN: 0031-9007. DOI: 10.1103/PhysRevLett.51.1506 (cit. on p. 9).

Schrieffer, J. R. and P. A. Wolff (Sept. 1966). "Relation between the Anderson and Kondo Hamiltonians". en. In: *Physical Review* 149.2, pp. 491–492. ISSN: 0031-899X. DOI: 10.1103/PhysRev.149.491 (cit. on p. 31).

Sépulcre, Théo (2021). "Superconducting simulators for quantum impurity models". en. PhD Thesis. Université Grenoble Alpes (cit. on pp. 18, 72).

Shapiro, Sidney (July 1963). "Josephson Currents in Superconducting Tunneling: The Effect of Microwaves and Other Observations". en. In: *Physical Review Letters* 11.2, pp. 80–82. ISSN: 0031-9007. DOI: 10.1103/PhysRevLett.11.80 (cit. on p. 16).

Silbey, Robert and Robert A. Harris (Mar. 1984). "Variational calculation of the dynamics of a two level system interacting with a bath". In: *The Journal of Chemical Physics* 80.6, pp. 2615–2617. ISSN: 0021-9606. DOI: 10.1063/1.447055 (cit. on p. 7).

Sundaresan, Neereja M., Yanbing Liu, Darius Sadri, László J. Szőcs, Devin L. Underwood, Moein Malekakhlagh, Hakan E. Türeci, and Andrew A. Houck (June 2015). "Beyond Strong Coupling in a Multimode Cavity". In: *Physical Review X* 5.2. Publisher: American Physical Society, p. 021035. DOI: 10.1103/PhysRevX.5.021035 (cit. on p. 8).

Svensson, Ida-Maria, Andreas Bengtsson, Jonas Bylander, Vitaly Shumeiko, and Per Delsing (July 2018). "Period multiplication in a parametrically driven superconducting resonator". en. In: *Applied Physics Letters* 113.2, p. 022602. ISSN: 0003-6951, 1077-3118. DOI: 10.1063/1.5026974 (cit. on p. 11).

Tinkham, Michael (2004). *Introduction to superconductivity*. Dover Publication (cit. on p. 16).

Vakhtel, T. (2023). *Private communication* (cit. on p. 104).

Vasa, Parinda, Wei Wang, Robert Pomraenke, Melanie Lammers, Margherita Maiuri, Cristian Manzoni, Giulio Cerullo, and Christoph Lienau (Feb. 2013). "Real-time observation of ultrafast Rabi oscillations between excitons and plasmons in metal nanostructures with J-aggregates". en. In: *Nature Photonics* 7.2. Number: 2 Publisher: Nature Publishing Group, pp. 128–132. ISSN: 1749-4893. DOI: 10.1038/nphoton.2012.340 (cit. on p. 5).

Vrajitoarea, Andrei, Ron Belyansky, Rex Lundgren, Seth Whitsitt, Alexey V. Gorshkov, and Andrew A. Houck (Sept. 2022). "Ultrastrong light-matter interaction in a photonic crystal". en. In: arXiv:2209.14972 (cit. on p. 10).

Walls, Daniel F. and Gerard J. Milburn (2008). *Quantum optics*. en. 2. ed. OCLC: 254897076. Berlin: Springer. ISBN: 978-3-540-28573-1 978-3-540-28574-8 (cit. on p. 10).

Weiss, Ulrich (2012). *Quantum Dissipative Systems*. en. Google-Books-ID: qgfuFZxvGKQC. World Scientific. ISBN: 978-981-4374-91-0 (cit. on p. 6).

Weißl, T., B. Küng, E. Dumur, A. K. Feofanov, I. Matei, C. Naud, O. Buisson, F. W. J. Hekking, and W. Guichard (Sept. 2015). "Kerr coefficients of plasma resonances in Josephson junction chains". In: *Physical Review B* 92.10. Publisher: American Physical Society, p. 104508. DOI: 10.1103/PhysRevB.92.104508 (cit. on p. 68).

Zelaya, Kevin, Sanjib Dey, and Véronique Hussin (Nov. 2018). "Generalized squeezed states". en. In: *Physics Letters A* 382.47, pp. 3369–3375. ISSN: 03759601. DOI: 10.1016/j.physleta.2018.10.003 (cit. on p. 10).

Zhang, Qi, Minhan Lou, Xinwei Li, John L. Reno, Wei Pan, John D. Watson, Michael J. Manfra, and Junichiro Kono (Nov. 2016). "Collective non-perturbative coupling of 2D electrons with high-quality-factor terahertz cavity photons". en. In: *Nature Physics* 12.11. Number: 11 Publisher: Nature Publishing Group, pp. 1005–1011. ISSN: 1745-2481. DOI: 10.1038/nphys3850 (cit. on p. 5).